The role of structural disorder in increasing the activity of cobalt oxide and manganese oxide water oxidation catalysts

by

Hannah Jayne King

Bachelor of Science (Honours)

Supervisors: Dr. Rosalie K. Hocking (primary)
Prof. Peter Junk (secondary)

Thesis submitted for the degree of Doctor of Philosophy (Natural and Physical Sciences)
Thesis submitted in December 2019

James Cook University
Division of Tropical Environments and Societies
College of Science and Engineering
School of Chemistry

Copyright Notice and Plagiarism Declaration

This thesis contains no material which has been accepted for the award of any other degree or diploma at any university or equivalent institution and that, to the best of my knowledge and belief, this thesis contains no material previously published or written by another person, except where due reference is made in the text of the thesis.

Abstract

This thesis consists of an introduction (Chapter 1) and three subsequent research chapters (Chapters 2, 3 and 4). Chapter 2 examines disorder in heterogenite-like cobalt oxides, Chapter 3 examines disorder in birnessite-like manganese oxides, and Chapter 4 examines heterogenite-like cobalt oxides in an *in situ* XAS-electrochemical study.

Chapter 2 presents a structure *versus* function study for a series of phosphate doped heterogenite-like cobalt oxides with the aim of explaining the mechanistic importance of disorder in Kanan and Nocera's highly efficient 'Co-Pi' (heterogenite-like cobalt oxide with phosphate) electrocatalyst. The phosphate doped heterogenite-like cobalt oxide series was synthesised *ex situ* to allow an in-depth structural characterisation of the materials by X-ray absorption spectroscopy (XAS) and transmission electron microscopy (TEM). The relationship between thermodynamic stability and catalytic activity was examined by measuring the oxidative strength of each material in a reaction with hydrogen peroxide (H_2O_2).

It was concluded from this study that phosphate doping systematically transitioned the nanocrystalline undoped cobalt oxide material into a highly disordered amorphous material with significant bond-length disorder at 9 wt% phosphate doping. Disorder decreased the thermodynamic stability of the heterogenite-like phase and caused the material with 9 wt% phosphate doping to become a stronger chemical oxidant but less efficient catalyst. This finding challenged the contemporary understanding that disorder in cobalt oxide water oxidation catalysts was beneficial to catalytic activity, and instead proposed that disorder was beneficial to oxidative activity. This chapter is based on a peer-reviewed and published manuscript titled "Engineering disorder into heterogenite-like cobalt oxides by phosphate doping: Implications for the design of water-oxidation catalysts" (ChemCatChem, 2017).

Chapter 3 presents a structure *versus* function study for disordered and ordered birnessite-like manganese (III,IV) oxides with the aim of explaining why disordered birnessite phases are more catalytically active than ordered birnessite phases. The two disordered birnessite-like phases (one with 2D stacking disorder and one with no crystalline order) and an ordered birnessite-like phase were comprehensively structurally characterised by X-ray diffraction (XRD), XAS and TEM. The thermodynamic stability of each material was quantified by examining how each material functioned in the competitive 'direct oxidation' / 'catalytic disproportionation' reaction with H_2O_2. The disordered materials degraded to Mn^{2+} during the H_2O_2 reaction and during *quasi in situ* and *ex situ* (with Ce^{IV} as a chemical oxidant) water oxidation catalysis, which strongly suggested that the disordered materials were acting as direct oxidants in both reactions.

This study suggested that the disordered manganese oxides were more efficient catalysts because they were stronger chemical oxidants and functioned in a redox geochemical-like cycle between the $Mn^{2+}_{(aq)}$ and $MnO_{x(s)}$ states. Consequently, this suggested that the cobalt oxide materials were also functioning in a redox-type cycle and that amorphous metal oxides form a class of redox-type catalysts. Therefore, disorder in heterogeneous metal oxide catalysts was beneficial to non-catalytic oxidative activity, and caused the bulk of the metal oxide material to be involved in the water oxidation reaction and not just the surface material. This chapter is based on 4 peer-reviewed and published manuscripts investigating manganese oxide water oxidation catalysts.

Chapter 4 presents the design and utilisation of a new spectroelectrochemical cell for the investigation of electrochemical and photoelectrochemical reaction mechanisms during *in situ* XAS-electrochemical experiments. Specifically, the cell was used to study the reaction mechanisms of two heterogenite-like cobalt oxides and to quantify X-ray beam-induced phenomenon associated with the *in situ* characterisation of these samples.

The study concluded that either high oxidation states of cobalt (>4+) are not involved in the catalytic cycle of heterogenite-like cobalt oxides or that the possible Co^{V} intermediate is too short lived to ever be detected by XAS. In addition, the study characterised photooxidation, photoreduction and photodeposition phenomenon which occurred in parallel with the mechanistic study. This chapter is based on a peer-reviewed and published manuscript titled "Photon-induced, timescale and electrode effects critical for the *in situ* X-ray spectroscopic analysis of electrocatalysts: the water oxidation case" (J. Phys. Chem. C, 2019).

Table of Contents

Publication Record

Title:	Engineering disorder at a nanoscale: A combined TEM and XAS investigation of amorphous *versus* nanocrystalline sodium birnessite
Publisher:	Australian Journal of Chemistry
Year:	2015
Details:	volume 68, issue 11, pages 1715-1722
Authors:	Rosalie K. Hocking, Hannah J. King, Aimee Hesson, Shannon A. Bonke, Bernt Johannessen, Monika Fekete, Leone Spiccia, Shery L.Y. Chang

Title:	Engineering disorder into heterogenite-like cobalt oxides by phosphate doping: Implications for the design of water oxidation catalysts
Publisher:	ChemCatChem
Year:	2017
Details:	volume 9, issue 3, pages 511-521
Authors:	Hannah J. King, Shannon A. Bonke, Shery L.Y. Chang, Leone Spiccia, Bernt Johannessen, Rosalie K. Hocking

Title:	Tunable Biogenic Manganese Oxides
Publisher:	Chemistry: A European Journal
Year:	2017
Details:	volume 23, issue 54, pages 13482-13492
Authors:	Alexandr N. Simonov, Rosalie K. Hocking, Lizhi Tao, Thomas Gengenbach, Timothy Williams, Xi-Ya Fang, Hannah J. King, Shannon A. Bonke, Dijon A. Hoogeveen, Christine A. Romano, Bradley M. Tebo, Lisandra L. Martin, William H. Casey, and Leone Spiccia

Title:	Direct formation of 2D-MnO_x under conditions of water oxidation catalysis
Publisher:	American Chemical Society - Applied Nano Materials
Year:	2018
Details:	volume 1, issue 4, pages 1603-1611
Authors:	Rosalie K. Hocking, Rosalind Gummow, Hannah J. King, Mayada Sabri, Peter Kappen, Christian Dwyer, Shery L.Y. Chang

Title:	The oxidation of peroxide by disordered metal oxides: A measurement of thermodynamic stability "by proxy"
Publisher:	ChemPlusChem
Year:	2018
Details:	volume 83, issue 7, pages 620-629
Authors:	Mayada Sabri, Hannah J. King, Rosalind J. Gummow, François Malherbe, Rosalie K. Hocking

Title:	Oxidant or catalyst for oxidation? A study of how structure and disorder change the selectivity for direct versus catalytic oxidation mediated by manganese (III,IV) oxides
Publisher:	American Chemical Society – Chemistry of Materials
Year:	2018
Details:	volume 30, issue 22, pages 8244-8256
Authors:	Mayada Sabri, Hannah J. King, Rosalind J. Gummow, Xunyu Lu, Chuan Zhao, Michael Oelgemöller, Shery L. Y. Chang, Rosalie K. Hocking

Title:	Photon-induced, timescale and electrode effects critical for the *in situ* X-ray spectroscopic analysis of electrocatalysts: the water oxidation case
Publisher:	Journal of Physical Chemistry C
Year:	2019
Details:	volume 123, issue 47, pages 28533-28549
Authors:	Hannah J. King, Maxime Fournier, Shannon A. Bonke, Enrico Seeman, Manjunath Chatti, Askhat N. Jumabekov, Bernt Johannessen, Peter Kappen, Alexandr N. Simonov, Rosalie K. Hocking

Statement Acknowledging the Contribution of Others

This thesis is based on 7 published manuscripts. The ideas, development and authorship of this thesis was the principal responsibility of myself (the candidate) working under the supervision of Dr. Rosalie Hocking. The inclusion of co-authors reflects the collaborative nature of scientific research, and I hereby acknowledge their contributions. My authorship, intellectual and technical contributions to each of the 7 manuscripts is described as follows:

Chapter #	**Publication title**	**Publication status**	**Extent (%) and nature of student contribution**
2	Engineering disorder into heterogenite-like cobalt oxides by phosphate doping: Implications for the design of water-oxidation catalysts	Published: ChemCatChem 2017	70% Completed all syntheses and characterisations. Primary manuscript author.
3	Engineering disorder at a nanoscale: A combined TEM and XAS investigation of amorphous versus nanocrystalline sodium birnessite	Published: Aust. J. Chem 2015	50% Partially completed structural characterisations. Primary manuscript editor.
	Direct formation of 2D-MnO_x under conditions of water oxidation catalysis	Published: ACS Appl. Nano Mater. 2018	30% Partially completed structural characterisations. Primary manuscript editor.

	The oxidation of peroxide by disordered metal oxides: A measurement of thermodynamic stability "by proxy"	Published: ChemPlusChem 2018	30% Partially completed structural characterisations. Intellectual contributions. Primary manuscript editor.
	Oxidant or catalyst for oxidation? A study of how structure and disorder change the selectivity for direct versus catalytic oxidation mediated by manganese (III,IV) oxides	Published: ACS Chem. Mater. 2018	30% Collaboratively collected XAS data and provided interpretations. Provided intellectual contributions. Primary manuscript editor.
4	Photon-induced, timescale and electrode effects critical for the *in situ* X-ray spectroscopic analysis of electrocatalysts: the water oxidation case	Published: J. Phys. Chem. C 2019	70% Collaboratively completed all structural characterisations. Primary manuscript author.
N/A	Tunable Biogenic Manganese Oxides	Published: Chem: Eur. J. 2017	5% Collaboratively collected XAS data and provided interpretations.

The undersigned certifies that the above declaration correctly reflects the extent and nature of the student and co-authors' contributions to this work.

Student Signature: Supervisor Signature: Date: 19/12/19

Hannah J. King Rosalie K. Hocking

Personal Acknowledgments

I sincerely thank those who have provided guidance and support during the completion of this doctorate.

I want to thank my supervisor Dr. Rosalie Hocking for the opportunity to complete a PhD, and for being a moral support throughout the years.

I would also like to thank our electrochemist collaborators at Monash University;
Dr. Alexandr ‘Sasha’ Simonov, Dr. Shannon Bonke and Dr. Maxime ‘Max’ Fournier.

I extend my many thanks to Dr. Rosalind Gummow and Dr. Shery Chang for all their intellectual and technical assistance.

To the XAS beamline scientists at the Australian Synchrotron and to our remaining collaborators I would like to thank you for your expertise and generous donation of your time.

I would like to thank James Cook University and Swinburne University for supporting this research project.

I finally thank my family for their support during my PhD.

Acknowledgments for Grants, Awards and Technical Support

The work in this thesis was supported by an Australian Postgraduate Award from the Australian Government.

I gratefully acknowledge the research funding and financial awards provided by the Graduate Research School (GRS) at James Cook University.

I extend my appreciation to the Australian Synchrotron for providing instrument access and extend additional thanks for financially supporting travel costs and providing multiple opportunities to attend user meetings and workshops.

I thank the James Cook University Advance Analytical Centre and its staff for technical assistance with instruments.

I gratefully acknowledge the receipt of a scholarship to attend the Cheiron School in Japan.

I extend my thanks to the Royal Australian Chemical Institute (RACI) for providing a travel grant to attend the RACI Centenary Conference.

I thank James Cook University and Swinburne University for providing workspaces and access to technical instruments.

List of Figures

CHAPTER 1

CHAPTER 2

CHAPTER 3

CHAPTER 4

List of Tables

CHAPTER 2

CHAPTER 3

CHAPTER 4

List of Schemes

CHAPTER 2

CHAPTER 3

CHAPTER 4

Chapter 1 –

Introduction

1.1 Fossil fuels & renewable energy sources

Fossil fuels are non-renewable energy resources that formed naturally over millions of years from organic matter trapped in geologic deposits during the Carboniferous period (~ 359.2 to 299 million years ago).[1-2] Fossil fuels are the world's primary energy source,[3-4] however, their extraction and combustion is unsustainable due to dwindling reserves and the adverse effects on the environment, such as carbon dioxide (CO_2) emissions, deforestation, acidic precipitation, and ozone depletion.[3-6] To ensure the economic and environmental security of our planet, we need to substantially diminish our reliance on fossil fuels and transition to energy sources that are carbon-neutral, sustainable and economically viable. Renewable energy sources generate power from natural sources or processes and are generally considered to be clean and inexhaustible sources of energy.[6-8] The principle renewable energy resources are solar, wind, waves, bioenergy, hydro, geothermal, and tidal.[6, 9] As a stable and reliable supply of energy is imperative for a functional society, a successful transition to a solely renewable energies future would realistically require multiple renewable energy technologies to be implemented globally.[4, 10-14]

1.2 Solar power & solar fuels

The Sun is by far the largest exploitable renewable energy source with a global energy potential of 23000 Terawatt (TW) per annum.[11, 15] More energy is provided by the Sun in one hour than consumed globally in an entire year (approximately 20 TW per annum).[10-11, 15-16] The heat and light energy from the Sun can be converted directly or indirectly into electricity, or be used to heat air, water or other substances.[17] **Figure 1.1** depicts the power available from remaining finite reserves and renewable energy resources in Terawatt per annum. Solar technologies typically have lower capital costs (per unit of energy produced) than other renewables[17-18], and are usually less geographically dependent,[4, 19-20] are more predictable in comparison to other renewables,[21] require less infrastructure and maintenance,[22] and can be scaled in size from localised systems to solar farms[23]. However, solar power production is seasonally dependent, and the supply of energy is intermittent due to the diurnal cycle of the Sun and weather conditions (*e.g.* clouds) which limit solar irradiance at the Earth's surface.

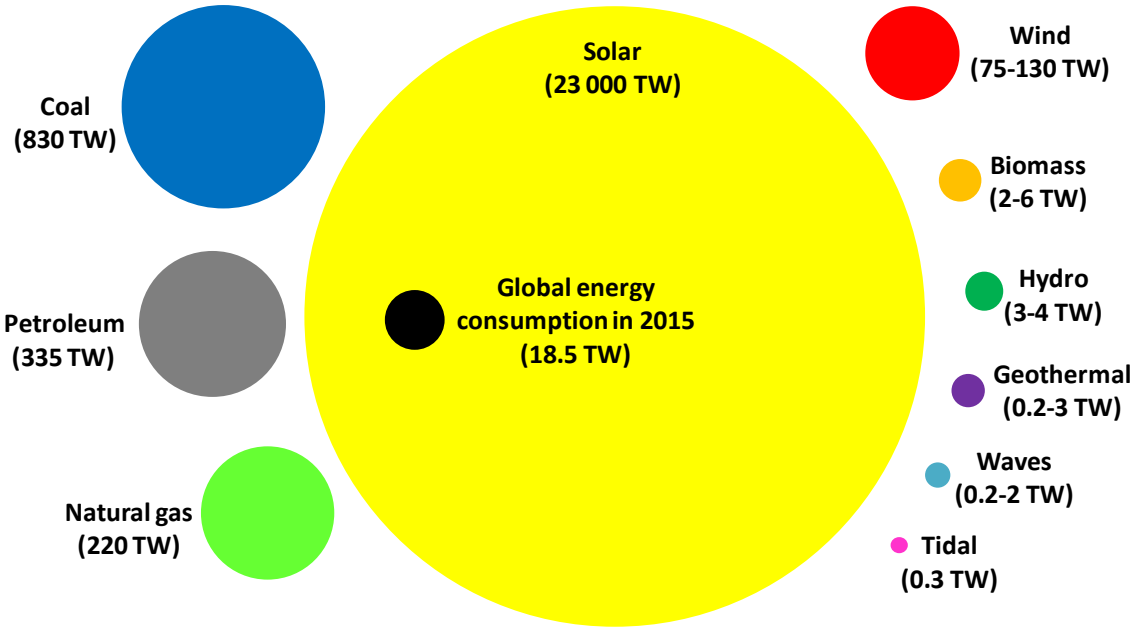

Figure 1.1: An infographic illustrating the power available from finite and renewable energy reserves (in TW per annum). The diagram shows the energy available from recoverable finite reserves and the yearly capacity from renewable energy sources. The surface area of each sphere is scaled to the total amount of recoverable energy from the energy source. This figure was reproduced from reference 15.

To overcome the intermittent nature of the Sun, solar power production can be coupled to energy storage technologies such as fuels or battery storage.[4, 10-13] The conversion of solar energy into chemical fuels (so called 'solar fuels') is particularly advantageous as fuels have a high energy density, are transportable, can be easily stored, and are long-lived.[11-12, 16, 24] Examples of solar fuels include hydrogen (H_2 *via* water splitting), ammonia (NH_3 *via* N_2 reduction), as well as carbonous fuels such as methanol (CH_3OH), carbon monoxide (CO) and methane (CH_4) (ideally synthesised *via* CO_2 reduction).[16, 24-25] As fuels release energy *via* exothermic oxidation reactions, the synthesis of a solar fuel proceeds *via* the endothermic reduction of a suitable substrate (*e.g.* H^+, N_2 or CO_2). The amount of energy required to synthesise a fuel is greater than the amount of energy stored in the fuel, and as such, it is imperative that solar fuel syntheses proceed *via* catalysed reactions.

1.3 Water splitting

Water splitting is a redox process involving the oxidation of water to produce protons, electrons and oxygen, followed by the reduction of these protons to produce hydrogen fuel.[11, 26-28] The water splitting reactions and the associated thermodynamics are presented in r**eactions 1.1**, **1.2** and **1.3**.[29-30] The half-cell equilibrium potentials (E) shift with pH on the standard hydrogen electrode (SHE) scale due to the contribution of H^+ ions to the Nernst equation (**reaction 1.4**) (*i.e.* the half-cell potentials are decreased by 59 mV for each pH unit increase).[26, 28, 30-31] An electrochemical cell driven by renewable electricity can be used to performed the water splitting reaction, as shown schematically in **Figure 1.2**.

Ox: $2H_2O_{(l)} \rightleftharpoons O_{2(g)} + 4H^+_{(aq)} + 4e^-$ $E_{anode} = 1.23\ V - (0.059 \times pH)\ V$ *vs.* SHE **(1.1)**

Red: $2H^+_{(aq)} + 2e^- \rightleftharpoons H_{2(g)}$ $E_{cathode} = 0\ V - (0.059 \times pH)\ V$ *vs.* SHE **(1.2)**

Redox: $2H_2O_{(l)} \rightleftharpoons O_{2(g)} + 2H_{2(g)}$ $E_{cell} = -1.23\ V$ *vs.* SHE, * **(1.3)**

* Gibbs free energy and enthalpy for $H_2O \rightleftharpoons \frac{1}{2}O_2 + H_2$ is $\Delta G° = 237\ kJ\ mol^{-1}$ and $\Delta H^0 = 286\ kJ\ mol^{-1}$, respectively.

Nernst Equation: $$E_{eq} = E^0 - \frac{RT}{nF} \ln \frac{oxidised}{reduced} \quad \textbf{(1.4)}$$

where E_{eq} = equilibrium potential (V), R = universal gas constant = $8.314\ \frac{J}{mol\ K}$,
T = temperature (K), n = moles of electrons per mole of products (unitless),
F = Faraday's constant = $9.648 \times 10^4\ \frac{C}{mol}$

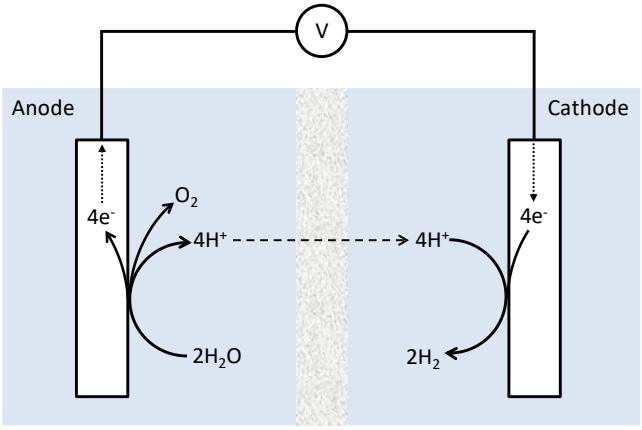

Figure 1.2: Schematic of electrochemical water splitting. Water is oxidised at the anode (left) to produce molecular oxygen (O_2), protons (H^+) and electrons (e^-). The protons are subsequently reduced at the cathode (right) to evolve molecular hydrogen (H_2). The *grey* membrane prevents the transport of oxygen and hydrogen between the compartments.

Although both the water oxidation and proton reduction reactions need to be catalysed for water splitting to proceed at appreciable rates, the water oxidation reaction is the most energetically unfavourable and has therefore attracted the focus of the catalysis community.[32] The water oxidation reaction is kinetically and thermodynamically unfavourable owing to high energy transition states associated with the complexity of removing 4 protons and 4 electrons from 2 water molecules and the work required to break stable H_2O molecules to form the O_2 double bond.[33]

The kinetic penalty for the water oxidation reaction is depicted as a single large activation energy barrier ($E_{A,ox}$) in the Gibbs free energy diagram in **Figure 1.3**, and the thermodynamic penalty is quantified in the stated thermodynamic energy value (ΔG_{ox}). The difference between the thermodynamic energy minimum for water oxidation (1.23 V *vs.* SHE at pH 0) and the experimentally required potential is defined as the *overpotential* (η).[34] Catalysts lower the required overpotential by facilitating the multiple electron and proton transfer processes of a reaction.[35-36]

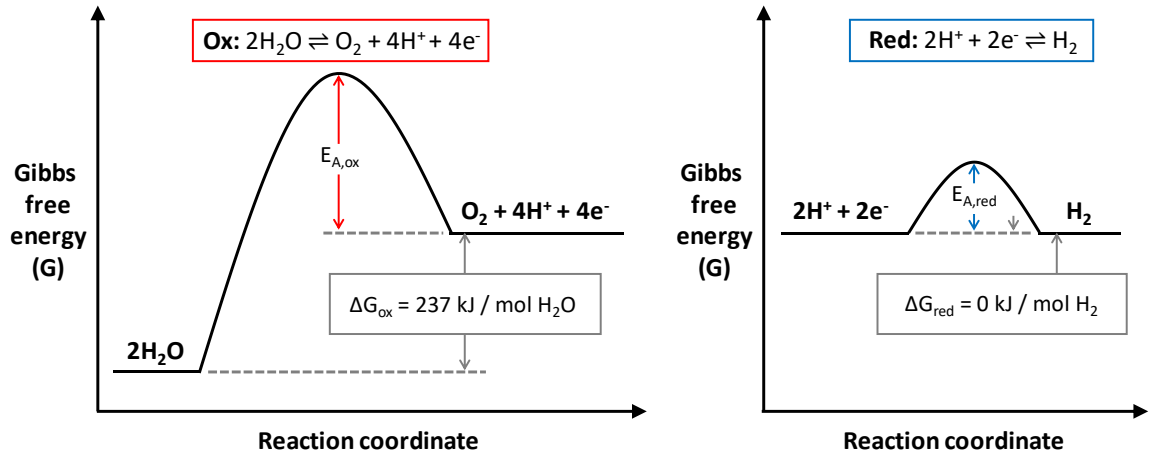

Figure 1.3: Gibbs free energy diagram of electrochemical water splitting. Symbols represent: $E_{A,redox}$ = activation energy, and G = Gibbs free energy.

1.4 Water oxidation catalysts

An ideal water oxidation catalyst is efficient, inexpensive, non-toxic, elementally abundant, environmentally benign, cheap to operate, and stable. 'Efficiency' can be loosely defined by the overpotential of a catalyst and the potentials required to produce current densities of 10 mA cm^{-2} and 100 mA cm^{-2}. Note that onset potential is typically not used as its exact value can be difficult to distinguish. An ideal catalyst has an overpotential between 200 and 300 mV, but overpotentials between 300 and 400 mV are excellent.[37] A catalyst is generally considered highly active if it achieves a current density of 10 mA cm^{-2} at approximately 1.47 V (η = 240 mV), and a current density of 100 mA cm^{-2} at approximately 1.63 V (η = 400 mV) in 1 M KOH (pH 14).[32]

RuO_2 and IrO_2 nanoparticles are benchmark electrocatalysts as they have some of the highest efficiencies for the water oxidation reaction in aqueous acidic and alkaline media. These electrocatalysts require overpotentials between 300 and 315 mV to drive a current density of 10 mA cm^{-2} in 0.1 M KOH.[28, 32] However, the high cost and scarcity of the Ir and Ru metals prevents these catalysts from being implemented in large-scale industrial applications, and requires that cheaper catalysts be developed.[11]

There are three main types of water oxidation catalysts: (i) biological, (ii) homogeneous (aqueous state), and (iii) heterogeneous (solid state). Although there are many subcategories of catalyst types (*e.g.* transition metal complexes[38], nanoparticles[28], cocatalysts[39], metal-organic frameworks (MOFs)[40], etc.), all water oxidation catalysts are driven by some combination of electro-, photo- or chemical catalysis. **Figure 1.4** presents a flowchart of the catalyst types relevant to this thesis. The structural and functional interplay between the catalyst types is described using manganese-based electrocatalysts as examples.

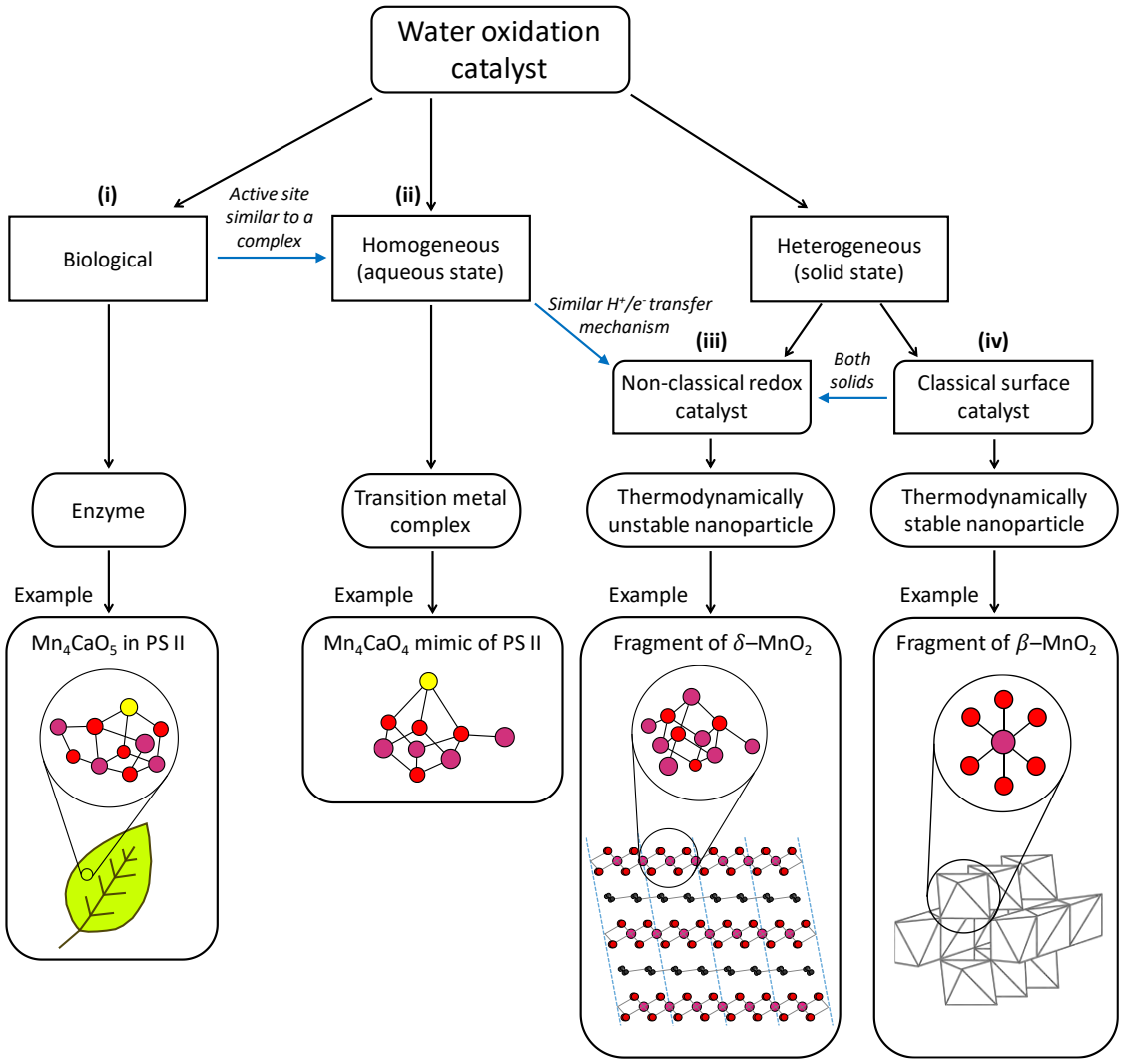

Figure 1.4: Flowchart depicting the three main types of water oxidation catalysts. References are made to the following: **(i)** biological catalysts,[41] **(ii)** homogeneous catalysts,[42] **(iii)** heterogeneous catalysts – non-classical,[43] and **(iv)** heterogeneous catalysts – classical.[44-45]

Manganese-based catalysts are historically important to the catalysis community as photosystem II (PS II) has an oxo-bridged tetra-manganese calcium cluster (Mn_4CaO_5) at its active site.[46-48] PS II is one of two multi-subunit proteins required for oxygenic photosynthesis in plants, algae, and cyanobacteria, and is the only biological catalyst to perform water oxidation in nature (**Figure 1.4-i**).[49]

Since the 1990s, many synthetic analogues of the photosynthetic system and the Mn_4CaO_5 active site have been synthesised.[50-52] However, the exact composition and shape of the PS II active site was unknown until 2004 when the research groups of Barber and Iwata provided

evidence for a Mn_3Ca-cubane model with a distanced fourth Mn.[47, 53] As the active site of PS II resembles a molecular metal complex with organic ligands, many biomimetic homogeneous analogues of mono-, di-, tri- and tetra-nuclear manganese complexes have been synthesised (**Figure 1.4-ii**).[49-51, 54] Other molecular metal complexes of ruthenium[33, 55], iridium[56], cobalt[57], nickel[58], copper[59] and iron[60-61] have been developed as water oxidation catalysts, with ruthenium catalysts being the most active and widely studied.[62]

Heterogeneous nanosized materials (1-10 nm) may also be good structural and functional models of the active site within PS II, which has a dimension of approximately 0.5 nm.[50, 53] Examples of nanosized catalysts include metal oxide nanoparticles, metal clusters, colloids, and nanostructured materials.[53] Nanosized materials blur the clear distinction between homogenous (**Figure 1.4-ii**) and heterogenous-classical (**Figure 1.4-iv**) classifications due to their unique physiochemical properties. As examples; (i) some suspensions of these solid-state catalysts can appear transparent to the naked eye (*i.e.* homogeneous), (ii) their mechanism can differ significantly from classical solid-state catalysis, and (iii) unstable molecular Mn-complexes can transform into nanoparticulate heterogeneous manganese oxides/hydroxides under the harsh oxidative conditions of water oxidation catalysis.[50, 53, 63-64] More specifically, some nanosized catalysts operate *via* a homogenous-like proton and electron transfer mechanism rather than a classical surface-mediated mechanism, and have been termed 'redox catalysts' by some research groups.[65-69] First row transition metal oxides of Mn[63, 70-81], Co[31, 34-35, 68, 82-93] and Ni[94-96] have demonstrated high catalytic activity for water oxidation and are promising cheap alternatives to precious metal catalysts.[97-98]

1.5 A brief history of heterogenous metal oxide synthesis

Prior to the mid-1990s, metal oxides were commonly prepared through 'ceramic' methods.[66, 99-100] 'Ceramic' or 'solid-state' methods involved; (i) finely grinding crystalline powders of oxides, carbonates, oxalates or other compounds containing the relevant metals, (ii) pelletizing the mixture with a hydraulic press such that the homogenized solid-state reactants were in close proximity to each other, and (ii) heating the pelletized mixture at the desired high temperature, typically to at least two thirds (⅔) of the melting point of one or more of the reactants (Tamman's Rule)[101] such that the reaction occurred in the solid-state.[99-100, 102] Very high temperatures (500-2000°C) were required to overcome the crystal lattice energies and allow the interdiffusion of ions through the solid-state mixture.[99-100]

Ceramic methods yielded thermodynamically stable bulk-crystalline and polycrystalline metal oxides with particle sizes on the micrometre (μm)-scale (approximately 1-10 μm) (**Figure 1.5**).[66, 99-100] The ceramic method was unable to produce nanosized particles as the high temperatures used in the synthesis caused particles to agglomerate to micrometre-scale particles. Although the ordered metal oxides could be characterised relatively easily by diffraction (a widely available characteristic technique since the 1920s), the reduced overall surface area of the metal oxides was inherently detrimental to their reactivity in chemical and physical applications.[101] *Metastable* (*i.e.* thermodynamically unstable) nanosized materials were predicted to be more functionally active due to their large surface areas, unique physiochemical properties, interesting structural features, and their non-equilibrium state.[66-67, 101-104]

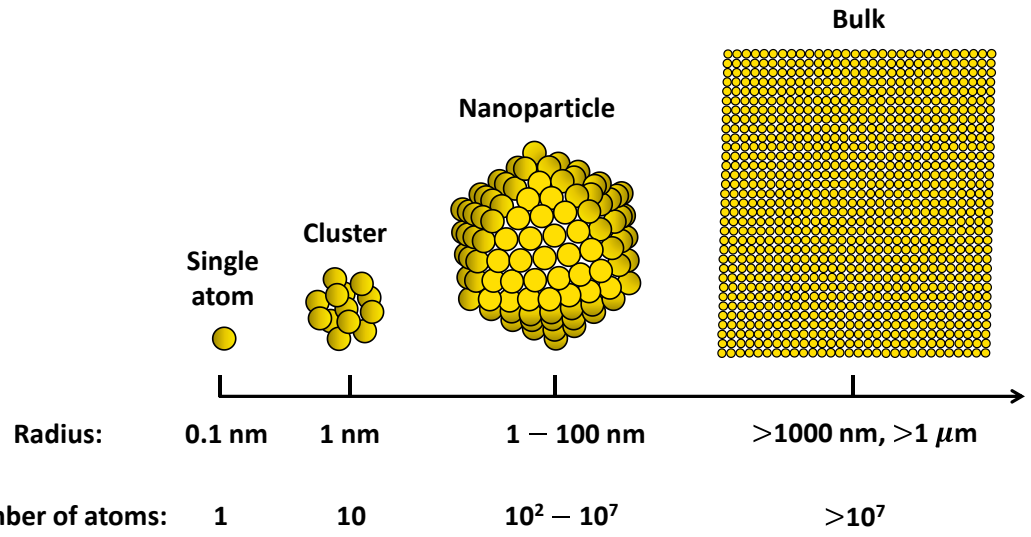

Figure 1.5: Graphic showing the scale of particle sizes. Scale regions are not well-defined, and bulk crystalline materials can be as small as 10 nm.[105]

'Chimie douce' or 'soft chemistry' synthetic techniques use low temperature (often room temperature) conditions to prepare inorganic materials that are not accessible by thermodynamically controlled high temperature methods.[66-67, 103-104] The term chimie douce was introduced in the 1970s by French scientists who were interested in synthesising bioinspired nanostructured materials under 'softer' reaction conditions (*e.g.* biological conditions of low temperatures and pressures).[103] Early research was particularly focussed on mimicking the chemistry of diatoms (living organisms found in water environments) as they can synthesise thermodynamically unstable silica glasses (SiO_2) at room temperature while the industrial synthesis of silica requires temperatures higher than 1000°C.[103]

Chimie douce methods focus on synthesising metastable nanosized materials that are typically nanostructured, nanoparticulate and/or porous. Nanosized materials are generally defined as having particle sizes between 1 − 100 nm, which corresponds to approximately 10^2 – 10^7 atoms.[66] Nanoparticles may be amorphous or consist of only a few unit cells of crystalline material.[106] In general, a Chimie douce method involves dissolving the starting materials in a liquid phase then tuning reaction parameters such as pH, concentration, temperature and reaction time to obtain the desired product.[101] Specific chimie douce methods include electrochemical, sol-gel, and ion exchange reactions.[107]

Electrochemical methods can be used to synthesize metastable metal oxides as thin films on electrode surfaces.[102] Metal oxides can be electrodeposited by anodic oxidation techniques wherein aqueous metal ions in a lower oxidation state are anodically oxidized to a higher oxidation state where they readily undergo hydrolysis to yield the metal oxide or hydroxide product.[102] The applied cell potential is used to control the oxidising power of the anodic electrodeposition and to thereby control the product yielded. Many metal oxides that have been electrochemically synthesised at room temperature are nanoparticulate, poorly ordered (*i.e.* disordered), diffraction amorphous, or have structural defects which make unequivocal structural characterization of the materials difficult.[102]

1.6 Metastability and particle size effects in nanosized materials

Nanosized catalysts have unique physical structures that are typically described by particle size, surface area, morphology, elemental composition, surface chemistry, porosity, structural defects, and crystallinity.[65-67] These unique structural features govern the thermodynamic, acid-base, and redox properties of the nanosized catalyst.[53, 65, 105, 108-110] As outlined by Maier *et al.* in references 111 and 112, particle size has two effects at the nanoscale; (i) a trivial effect where reactivity is increased due to an increase in the surface-to-volume ratio which causes a larger fraction of atoms (*i.e.* active sites) to sit at the surface interface, and (ii) a true effect where nanoparticles have distinct properties from their bulk counterparts.[111-112] Maier discusses two true size effects in detail; the difference in electrical properties (*e.g.* space charge overlap) and changes to internal structure (*e.g.* bond-length distortions in nanocrystals).[111-112]

Navrotsky's research group have also extensively characterised the differences between nanoparticulate materials and their bulk counterparts. As explained in references 106 and 105; nanomaterials may differ in their structure (*e.g.* internal stain, defects, disorder), crystallographic symmetry and lower surface energies (the Ostwald step rule), and may be more susceptible to polymorphism or amorphization. As a consequence of these true particle size effects, Navrotsky's group have reported that the redox potentials (*i.e.* the thermodynamic stability) of nanoparticles significantly differ from those of their bulk counterparts, with large thermodynamically driven shifts in reduction-oxidation (redox) equilibria.[110] Additionally, their research has illustrated the importance of wet chemistry chimie douce methods in synthesising metastable phases that are microporous and thereby resist particle coarsening.[105-106, 110, 113]

1.7 Characterisation of nanoparticulate disordered metal oxides

It is generally understood that nanoscale metastable materials are more catalytically active for water oxidation and that, by extension, amorphous and disordered phases make better catalysts.[15, 23, 26-27, 36, 38-39] In manganese (MnO_x), cobalt (CoO_x) and nickel oxide (NiO_x) materials, a lack of crystallinity could be caused by structural defects, poor intra- or interlayer order, and/or lack of basic repeat 'molecular unit'.[66-67, 74-76, 87, 91, 101-102, 114] Specific types of structural disorder include; a turbostratic layer structure (*i.e.* disordered layer stacking along the *c*-axis)[44, 75, 115-118], limited interlayer sheet stacking (*i.e.* 2-dimensional (2D) materials)[75, 119-122], atomic intralayer vacancies (*i.e.* missing metal and/or oxygen atoms in the intralayer of MnO_x[53, 75, 114, 116, 123-125], CoO_x[126-127], and NiO_x[128] materials), lattice strain (*i.e.* bond-length and bond-angle distortion)[87, 114, 116, 129], curled nanosheets[122, 130], and anion defects (including missing, substituted anion dopant/impurity, or interstitial ions)[87, 131-134]. **Figure 1.6** graphically illustrates each of these types of structural disorder using a layered MnO_2 similar to K^+ birnessite (δ-MnO_2) as a base structure.

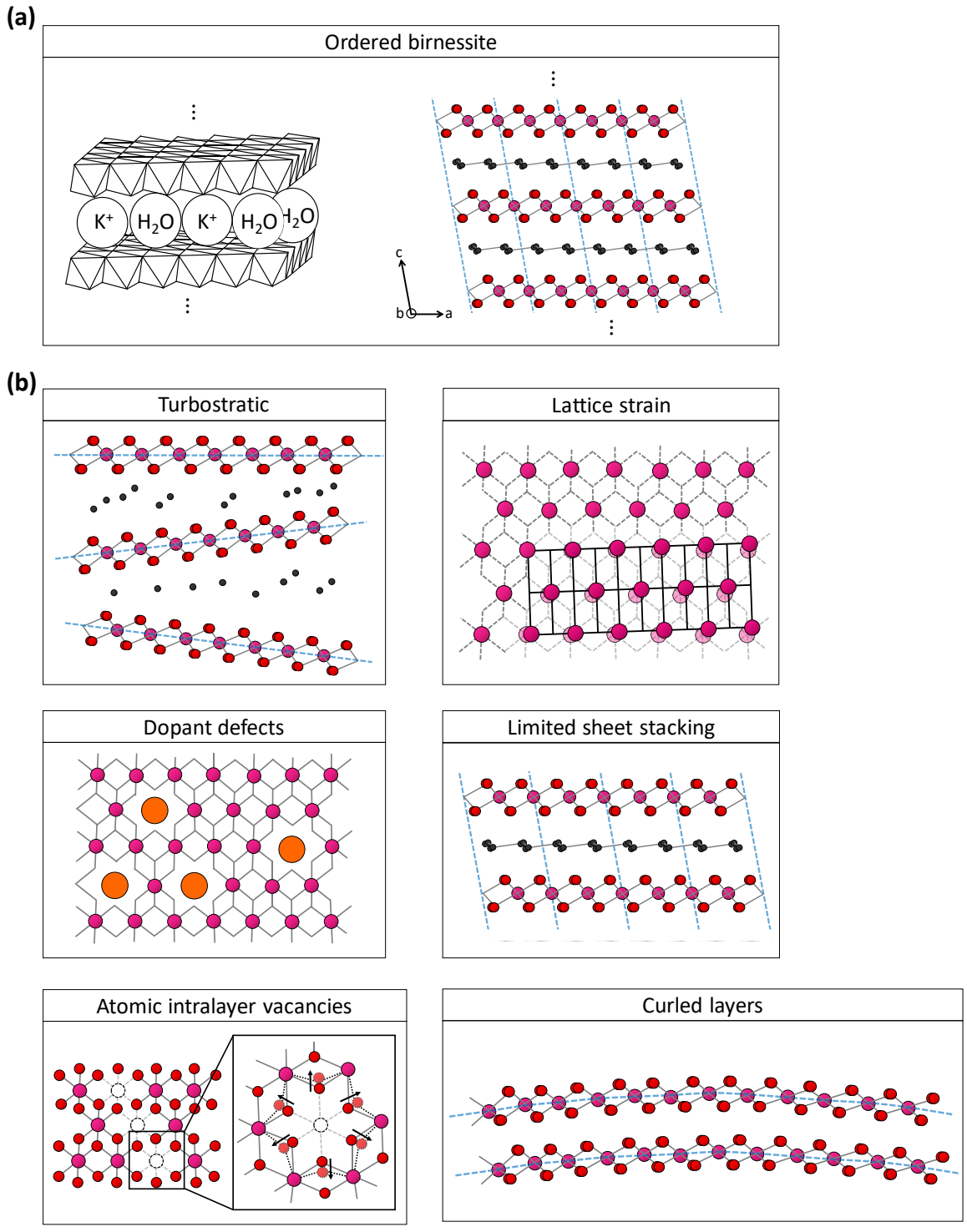

Figure 1.6: (a) Ordered crystal structure of K^+ birnessite (δ-MnO_2).[44-45] **(b)** Types of structural disorder occurring in transition metal oxides as exemplified for a birnessite-like structure with crystallite dimensions of $a \times b \times c$; where a and b are the crystallographic dimensions of the intralayer planes, and c is the interlayer crystallographic dimension. The 6 types of structural disorder depicted are: turbostratic layer structure, lattice strain, dopant defects, limited interlayer stacking or '2D', atomic intralayer vacancies, and curled layers.

Structurally characterising catalysts before, during and after catalysis is integral to improving our understanding of catalytic mechanisms and modes of catalyst deactivation.[135-140] However, nanosized and/or disordered materials are challenging to structurally characterise and require a multi-technique and multi-disciplinary analytical approach.[137-140] Traditional analytical methods are best suited to characterising molecular and crystalline materials (**Figure 1.7**), but the structures of many highly active catalysts fall between these two limits. At the atomic end of the size scale, molecular samples are amenable to inorganic spectroscopic techniques (*e.g.* electron paramagnetic resonance (EPR),[141] Mössbaur,[142] and UV-Vis near infrared[143]), and at the micrometre end of the size scale, bulk single crystals are amenable to X-ray diffraction (XRD) techniques.[138-139]

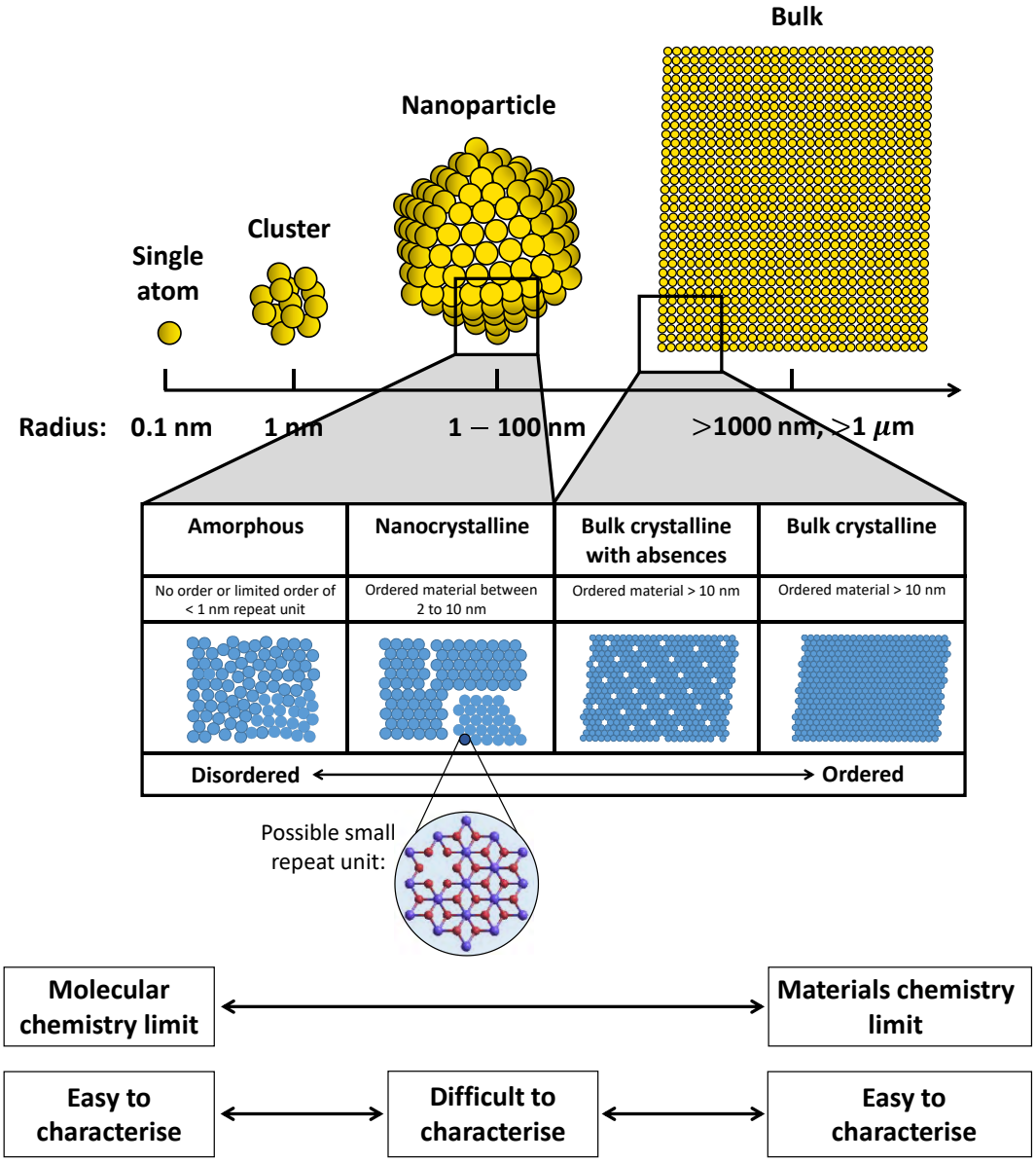

Figure 1.7: Particle size and disorder scale from molecular to bulk crystalline. Scale regions are not well-defined, and bulk crystalline materials can be as small as 10 nm.[139]

Nanosized disordered materials are commonly studied with a complementary set of analytical techniques, frequently XRD, X-ray absorption spectroscopy (XAS), and transmission electron microscopy (TEM). Typically, XRD is used to identify crystalline phases if present and determine the crystalline grain size using the Scherrer equation, XAS provides information of the electronic, coordination and bonding environment (distances < 6 Å) of the metal in the metal oxide, and TEM is used to characterise the size, shape and crystallinity of the particles.[135-140]

The *in situ* or *quasi in situ* characterisation of materials during catalysis is particularly important for determining the catalytically active phase, the catalytic mechanism, and modes of catalyst degradation. As previously stated in **§1.4 Water oxidation catalysts**, unstable molecular Mn-complexes can transform into nanoparticulate heterogeneous manganese oxides/hydroxides under the harsh oxidative conditions of water oxidation catalysis.[50, 53, 63-64] Therefore, knowing the catalytically active phase requires spectroscopic characterisation under catalytic conditions. While electrochemistry is a very powerful technique to decipher reaction mechanisms involving electrons, electrochemical signal is an indirect measure of structure and direct characterisation techniques such as XAS are required for unambiguous structural determination.[144,145,146]

1.8 Birnessite-like manganese oxide water oxidation catalysts

Birnessite and birnessite-like minerals are manganese (III,IV) oxides that are ubiquitous in a wide variety of geological settings and are often characterised as being poorly crystalline or completely amorphous.[44, 147-148] Mineral birnessite has the general chemical formula $(Na,Ca,K)_x(Mn^{4+},Mn^{3+})_2O_4 \cdot 1.5(H_2O)$ and consists of edge-sharing MnO_6 octahedra sheets with intralayer Mn and O vacancies (**Figure 1.6a)**.[149] Cations such as H^+, Na^+, K^+, Ca^{2+}, Mg^{2+}, and Mn^{2+} are typically found in the interlayer where they act to compensate negative charges from intralayer Mn vacancies.[149] Birnessite-like minerals are geochemically active species and participate in light-induced geochemical cycling *via* reductive decomposition to Mn^{2+}.[44, 63, 150-151]

Birnessite is structurally similar to the Mn_4CaO_5 active site within PS II (**Figure 1.8**), and many birnessite-like manganese oxides and manganese-calcium oxides have been developed as water oxidation catalysts.[28, 63, 70, 72-73, 76, 152-154] In part, manganese oxides are considered excellent water oxidation catalysts because manganese is a multivalent metal with common oxidation states of Mn^{2+}, Mn^{3+} and Mn^{4+}.[37, 44] The disordered forms of birnessite are much more catalytically active than their more ordered hexagonal and triclinic birnessite counterparts.[155-156] Highly disordered birnessite phases can be synthesized with a high concentration of Mn vacancies and random sheet-stacking (*i.e.* turbostratic stacking, **Figure 1.6b**). [157-158] Research by the Kwon (theoretical) and Sasaki (experimental) research groups demonstrated that disorder increased birnessite reactivity by showing that Mn intralayer vacancies promoted the photoreduction of natural birnessite phases in aquatic systems.[158-159]

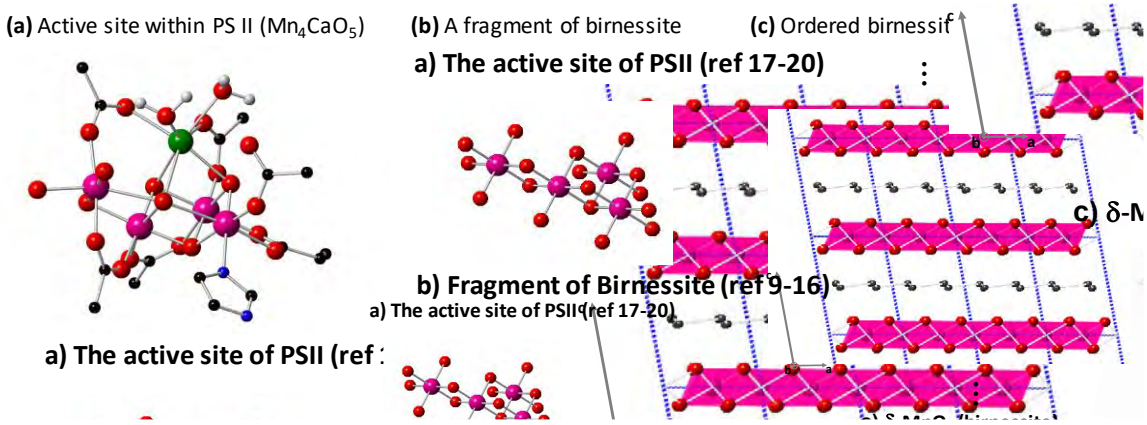

Figure 1.8: (a) The Mn_4CaO_5 active site within PS II, **(b)** a single layer fragment of birnessite, and **(c)** the layer structure of ordered birnessite.[44, 117]

1.9 Heterogenite-like cobalt oxide water oxidation catalysts

Heterogenite-like (CoOOH) cobalt oxides have received significant attention as water oxidation catalysts since 2008 when Kanan and Nocera reported an amorphous heterogenite-like cobalt oxide with phosphate catalyst (so called 'Co-Pi') that was highly active in neutral pH conditions.[31] Co-Pi was electrodeposited (*i.e.* a chimie douce method) from a phosphate buffered Co^{2+} solution at positive potentials both below or above that required for water oxidation.[31, 83-85] The high activity and stability of this catalyst at neutral

pH prompted the development of other 'transition metal − anion' type materials, including Ni-Bi (where 'Bi' denotes borate),[94] Co-Bi,[90] and Mn-Pi. [160] Catalysts of this type are typically synthesised *in situ* through oxidative electrodeposition from a solution of the transition metal cation in a proton accepting pH buffering electrolyte, where the electrolyte anion becomes incorporated into the electrodeposited material.[74, 82]

The catalytic mechanism of heterogenite-like cobalt oxides has been studied by many research groups (particularly those of Nocera[31, 35, 83-85, 161-162] and Dau[28, 68, 74, 82]) using a range of analytical techniques including electrochemical analyses[35], *in situ* electron paramagnetic resonance[86] and *in situ* XAS[68, 88]. The catalytic mechanism has been hypothesised by several groups to be of the kind depicted in **Figure 1.9**, where there is a proton coupled electron transfer (PCET) prior to a chemical turnover limiting step.[35, 163-165] Specifically, it has been hypothesised that the oxidation of $Co^{III}(OH)$ to $Co^{IV}(O)$ or even Co^{V} (reaction **G** ⇄ **A** in **Figure 1.9**) is coupled to proton withdrawal by dissolved base (reaction **A** + **R** → **G** + **P** in **Figure 1.9**) prior to the onset of the rate limiting oxygen-oxygen bond formation step.[35-36, 88, 166]

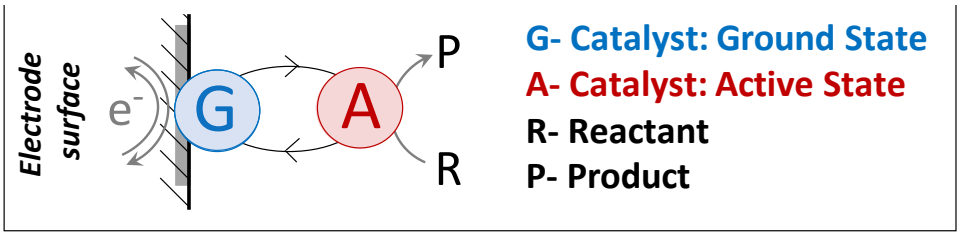

Figure 1.9: A simplified heterogeneous electrocatalytic mechanism. **G** and **A** are the ground and active states of the electrocatalyst, respectively. **R** is a reactant, and **P** is a product. This figure was reproduced from reference 167.

In 2014, Dau *et al.* proposed that the bulk (*i.e.* material below the surface) of the amorphous heterogenite-like catalyst was undergoing oxidation state changes during catalysis, and consequently concluded that water oxidation was taking place throughout the hydrated catalyst material and not exclusively at the catalyst/electrolyte interface (*i.e.* the surface).[69] Although redox catalysts are solid-state materials, they demonstrated molecular-like behaviour by undergoing structural, chemical and redox transitions during catalysis.[68-69] This mode of operation was termed 'volume catalysis' in reference to the 3D volume or bulk

of the material being involved in the reaction, and the class of catalysts that participated in this mechanistic mode were termed 'redox catalysts'.[68] NiO_x and MnO_x amorphous metal oxides were also suggested to operate as redox catalysts owing to their similar structural motifs to amorphous Co-Pi.[68-69]

Metal oxides are basic in the Lux classification of bases (a classification often used in geochemistry)[168], and therefore readily react with protons generated from the water oxidation reaction ($H_2O \rightleftharpoons ½O_2 + 2H^+ + 2e^-$). This reaction degrades first row transition metal oxide catalysts in a process called 'corrosion' (*e.g.* $CoO_x \rightarrow Co^{2+} + 2e^-$). As such, the catalytic turnover of Co-Pi is accompanied by the dissolution of the catalyst and the presence of free $Co^{2+}_{(aq)}$ ions in the electrolyte of the electrochemical cell. However, there exists a 'self-healing' mechanism for Co-Pi as the material can be re-electrosynthesised (*i.e.* $Co^{2+} + 2e^- \rightarrow CoO_x$) from the $Co^{2+}_{(aq)}$ state in the phosphate buffered electrolyte at potentials where water oxidation catalysis occurs.[169] Thus, Co-Pi is able to 'self-heal' while simultaneously catalysing the water oxidation reaction. This self-healing mechanism is known for Co, Mn and Ni catalysts in phosphate and borate buffered solutions.[169] The self-healing mechanism highlights an important characteristic of amorphous transmission metal oxides synthesised at room temperature; the equilibrium for self-assembly (*i.e.* initial generation and regeneration) lies energetically within that the water oxidation catalysis.[169]

1.10 Thesis research objectives

The overall aim of this thesis is to determine the role of structural disorder in increasing the activity of amorphous metal oxides for water oxidation catalysis. This thesis examines heterogenite-like cobalt oxides and birnessite-like manganese oxides and compares disordered phases to their more ordered counterparts in structure *versus* function studies. The aims of the following 3 chapters can be described as follows:

Chapter 2 | Disorder in heterogenite-like cobalt oxides

Systematically dope a heterogenite-like phase with phosphate and characterise the structural and functional effects of this phosphate doping at low (1 %P), medium (3 %P) and high (9 %P) dopant loadings. Conclusions from this study contribute to the functional understanding of Kanan and Nocera's Co-Pi benchmark electrocatalyst.

Chapter 3 | Disorder in birnessite-like manganese oxides

Comprehensively structurally characterise ordered and disordered birnessite-like materials and determine why disordered birnessite phases are more catalytically active than ordered birnessite. This study further investigates the link between the geochemical cycling of mineral birnessite and the functionality of synthetic birnessite catalysts by examining the role of metastability in birnessite reactivity.

Chapter 4 | *In situ* XAS/electrochemical analysis of heterogenite-like cobalt oxides

Develop a gas- and liquid-tight spectroelectrochemical cell that produces high quality XAS and electrochemical data, outline a good experimental protocol for the *in situ* characterisation of electrocatalysts, and undertake a mechanistic study of amorphous heterogenite-like cobalt oxides with consideration of photoeffects and the timescales of XAS/electrochemical events.

1.11 Chapter 1 references

1. Berner, R. A., The long-term carbon cycle, fossil fuels and atmospheric composition. *Nature* **2003,** *426* (6964), 323-326.
2. Feulner, G., Formation of most of our coal brought Earth close to global glaciation. *Proc. Natl. Acad. Sci.* **2017,** *114* (43), 11333-11337.
3. Leung, D. Y. C.; Caramanna, G.; Maroto-Valer, M. M., An overview of current status of carbon dioxide capture and storage technologies. *Renew. Sustain. Energy Rev.* **2014,** *39*, 426-443.
4. Dresselhaus, M. S.; Thomas, I. L., Alternative energy technologies. *Nature* **2001,** *414* (6861), 332-337.
5. Chmielewski, A. G., *Interactions: Energy / environment*. Eolss Publishers Co. Ltd.: Oxford, United Kingdom, 2009; p 105.
6. Dincer, I., Renewable energy and sustainable development: A crucial review. *Renew. Sustain. Energy Rev.* **2000,** *4* (2), 157-175.
7. Lund, H., Renewable energy strategies for sustainable development. *Energy* **2007,** *32* (6), 912-919.
8. Turner, J. A., A realizable renewable energy future. *Science* **1999,** *285* (5428), 687-689.
9. Panwar, N. L.; Kaushik, S. C.; Kothari, S., Role of renewable energy sources in environmental protection: A review. *Renew. Sustain. Energy Rev.* **2011,** *15* (3), 1513-1524.
10. Gür, T. M., Review of electrical energy storage technologies, materials and systems: challenges and prospects for large-scale grid storage. *Energy Environ. Sci.* **2018,** *11* (10), 2696-2767.
11. Lewis, N. S.; Nocera, D. G., Powering the planet: chemical challenges in solar energy utilization. *Proc. Natl. Acad. Sci.* **2006,** *103* (43), 15729-15735.
12. Nocera, D. G., Chemistry of personalized solar energy. *Inorg. Chem.* **2009,** *48* (21), 10001-10017.
13. Arvizu, D.; Balaya, P.; Cabeza, L. F.; Hollands, K. G. T.; Jäger-Waldau, A.; Kondo, M.; Konseibo, C.; Meleshko, V.; Stein, W.; Tamaura, Y. *et al.* IPCC Special report on renewable energy sources and climate change mitigation. In *Renewable energy sources and climate change mitigation*, Edenhofer, O.; Pichs-Madruga, R.; Sokona, Y.; Seyboth, K.; Matschoss, P.; Kadner, S.; Zwickel, T.; Eickemeier, P.; Hansen, G.; Schlömer, S. *et al.* Eds. Cambridge University Press: Cambridge, United Kingdom and New York, NY, USA, 2011.
14. Johansson, T. B.; Kelly, H.; Reddy, A. K. N.; Burnham, L.; Williams, R. H., *Renewable energy: Sources for fuels and electricity*. Island Press: 1993.
15. Perez, R.; Perez, M., *A fundamental look at energy reserves for the planet*. The international Energy Agency: 2009; Vol. 50, p 3.
16. Dahl, S.; Chorkendorff, I., Towards practical implementation. *Nat. Mater.* **2012,** *11*, 100-101.
17. Mekhilef, S.; Saidur, R.; Safari, A., A review on solar energy use in industries. *Renew. Sustain. Energy Rev.* **2011,** *15* (4), 1777-1790.
18. Administration, U. S. E. I. *Cost and performance characteristics of new generating technologies, annual energy outlook 2019* Washington, DC, United States of America, 2019.
19. El-Shimy, M., Viability analysis of PV power plants in Egypt. *Renew. Energy* **2009,** *34* (10), 2187-2196.

20. Perez, R.; Zweibel, K.; Hoff, T. E., Solar power generation in the US: Too expensive, or a bargain? *Energy Policy* **2011,** *39* (11), 7290-7297.
21. Tsuchiya, H., Electricity supply largely from solar and wind resources in Japan. *Renew. Energy* **2012,** *48*, 318-325.
22. Jacobson, M. Z.; Delucchi, M. A., Providing all global energy with wind, water, and solar power, Part I: Technologies, energy resources, quantities and areas of infrastructure, and materials. *Energy Policy* **2011,** *39* (3), 1154-1169.
23. Hernandez, R. R.; Easter, S. B.; Murphy-Mariscal, M. L.; Maestre, F. T.; Tavassoli, M.; Allen, E. B.; Barrows, C. W.; Belnap, J.; Ochoa-Hueso, R.; Ravi, S. *et al.* Environmental impacts of utility-scale solar energy. *Renew. Sustain. Energy Rev.* **2014,** *29*, 766-779.
24. Tran, P. D.; Wong, L. H.; Barber, J.; Loo, J. S. C., Recent advances in hybrid photocatalysts for solar fuel production. *Energy Environ. Sci.* **2012,** *5* (3), 5902-5918.
25. Wang, L.; Xia, M.; Wang, H.; Huang, K.; Qian, C.; Maravelias, C. T.; Ozin, G. A., Greening ammonia toward the solar ammonia refinery. *Joule* **2018,** *2* (6), 1055-1074.
26. Bard, A. J.; Fox, M. A., Artificial photosynthesis: Solar splitting of water to hydrogen and oxygen. *Acc. Chem. Res.* **1995,** *28* (3), 141-145.
27. Lewis, N. S., Research opportunities to advance solar energy utilization. *Science* **2016,** *351* (6271), 353-362.
28. Dau, H.; Limberg, C.; Reier, T.; Risch, M.; Roggan, S.; Strasser, P., The mechanism of water oxidation: From electrolysis *via* homogeneous to biological catalysis. *ChemCatChem* **2010,** *2* (7), 724-761.
29. Haynes, W. M., Lide, D. R., CRC Handbook of chemistry and physics 92nd ed.; Taylor and Francis: Boca Raton, FL, 2011.
30. Shinagawa, T.; Takanabe, K., Towards versatile and sustainable hydrogen production through electrocatalytic water splitting: Electrolyte engineering. *ChemSusChem* **2017,** *10* (7), 1318-1336.
31. Kanan, M. W.; Nocera, D. G., *In situ* formation of an oxygen-evolving catalyst in neutral water containing phosphate and Co^{2+}. *Science* **2008,** *321* (5892), 1072-1075.
32. Joya, K. S.; Ehsan, M. A.; Babar, N.-U.-A.; Sohail, M.; Yamani, Z. H., Nanoscale palladium as a new benchmark electrocatalyst for water oxidation at low overpotential. *J. Mater. Chem. A* **2019,** *7* (15), 9137-9144.
33. Kamdar, J. M.; Grotjahn, D. B., An overview of significant achievements in ruthenium-based molecular water oxidation catalysis. *Molecules* **2019,** *24* (3), 494.
34. Nocera, D., The artificial leaf. *Acc. Chem. Res.* **2011,** *45* (5), 767-776.
35. Surendranath, Y.; Kanan, M. W.; Nocera, D. G., Mechanistic studies of the oxygen evolution reaction by a cobalt-phosphate catalyst at neutral pH. *J. Am. Chem. Soc.,* **2010,** *132* (46), 16501-16509.
36. Deng, X.; Tüysüz, H., Cobalt-oxide-based materials as water oxidation catalyst: Recent progress and challenges. *ACS Catal.* **2014,** *4* (10), 3701-3714.
37. Tahir, M.; Pan, L.; Idrees, F.; Zhang, X.; Wang, L.; Zou, J.-J.; Wang, Z. L., Electrocatalytic oxygen evolution reaction for energy conversion and storage: A comprehensive review. *Nano Energy* **2017,** *37*, 136-157.
38. Dey, S.; Mondal, B.; Chatterjee, S.; Rana, A.; Amanullah, S.; Dey, A., Molecular electrocatalysts for the oxygen reduction reaction. *Nat. Rev. Chem.* **2017,** *1*, 0098.
39. Yang, J.; Wang, D.; Han, H.; Li, C., Roles of cocatalysts in photocatalysis and photoelectrocatalysis. *Acc. Chem. Res.* **2013,** *46* (8), 1900-1909.
40. Shao, Q.; Yang, J.; Huang, X., The design of water oxidation electrocatalysts from nanoscale metal–organic frameworks. *Chem.: Eur. J* **2018,** *24* (57), 15143-15155.

41. Umena, Y.; Kawakami, K.; Shen, J.-R.; Kamiya, N., Crystal structure of oxygen-evolving photosystem II at a resolution of 1.9 Å. *Nature* **2011,** *473*, 55-60.
42. Zhang C.; Chen C.; Dong H.; Shen J-R.; Dau H.; Zhao J., A synthetic Mn_4Ca-cluster mimicking the oxygen-evolving centre of photosynthesis. *Science* **2015,** *348*, 690-693.
43. Yang, J.; An, H.; Zhou, X.; Li, C., Water oxidation mechanism on alkaline-earth-cation containing birnessite-like manganese oxides. *J. Phys. Chem. C* **2015,** *119* (32), 18487-18494.
44. Post, J. E., Manganese oxide minerals: Crystal structures and economic and environmental significance. *Proc. Natl. Acad. Sci.* **1999,** *96* (7), 3447-3454.
45. Feng, Q.; Kanoh, H.; Ooi, K., Manganese oxide porous crystals. *J. Mater. Chem.* **1999,** *9* (2), 319-333.
46. Najafpour, M. M.; Heidari, S.; Balaghi, S. E.; Hołyńska, M.; Sadr, M. H.; Soltani, B.; Khatamian, M.; Larkum, A. W.; Allakhverdiev, S. I., Proposed mechanisms for water oxidation by Photosystem II and nanosized manganese oxides. *BBA Bioenergetics* **2017,** *1858* (2), 156-174.
47. Ferreira, K. N.; Iverson, T. M.; Maghlaoui, K.; Barber, J.; Iwata, S., Architecture of the photosynthetic oxygen-evolving center. *Science* **2004,** *303* (5665), 1831-1838.
48. Yano, J.; Yachandra, V., Mn_4Ca cluster in photosynthesis: Where and how water is oxidized to dioxygen. *Chem. Rev.* **2014,** *114* (8), 4175-4205.
49. Najafpour, M. M.; Renger, G.; Hołyńska, M.; Moghaddam, A. N.; Aro, E.-M.; Carpentier, R.; Nishihara, H.; Eaton-Rye, J. J.; Shen, J.-R.; Allakhverdiev, S. I., Manganese compounds as water-oxidizing catalysts: From the natural water-oxidizing complex to nanosized manganese oxide structures. *Chem. Rev.* **2016,** *116* (5), 2886-2936.
50. Kärkäs, M. D.; Verho, O.; Johnston, E. V.; Åkermark, B., Artificial photosynthesis: Molecular systems for catalytic water oxidation. *Chem. Rev.* **2014,** *114* (24), 11863-12001.
51. Yachandra, V. K.; Sauer, K.; Klein, M. P., Manganese cluster in photosynthesis: Where plants oxidize water to dioxygen. *Chem. Rev.* **1996,** *96* (7), 2927-2950.
52. Hammarström, L.; Sun, L.; Åkermark, B.; Styring, S., Artificial photosynthesis: Towards functional mimics of photosystem II? *BBA Bioenergetics* **1998,** *1365* (1), 193-199.
53. Najafpour, M. M.; Rahimi, F.; Aro, E.-M.; Lee, C.-H.; Allakhverdiev, S. I., Nano-sized manganese oxides as biomimetic catalysts for water oxidation in artificial photosynthesis: a review. *J. R. Soc. Interface* **2012,** *9* (75), 2383-2395.
54. Debus, R. J., The manganese and calcium ions of photosynthetic oxygen evolution. *BBA Bioenergetics* **1992,** *1102* (3), 269-352.
55. Concepcion, J. J.; Jurss, J. W.; Brennaman, M. K.; Hoertz, P. G.; Patrocinio, A. O. T.; Murakami Iha, N. Y.; Templeton, J. L.; Meyer, T. J., Making oxygen with ruthenium complexes. *Acc. Chem. Res.* **2009,** *42* (12), 1954-1965.
56. Thomsen, J. M.; Huang, D. L.; Crabtree, R. H.; Brudvig, G. W., Iridium-based complexes for water oxidation. *Dalton Trans.* **2015,** *44* (28), 12452-12472.
57. Huang, Z.; Luo, Z.; Geletii, Y. V.; Vickers, J. W.; Yin, Q.; Wu, D.; Hou, Y.; Ding, Y.; Song, J.; Musaev, D. G. *et al.* Efficient light-driven carbon-free cobalt-based molecular catalyst for water oxidation. *J. Am. Chem. Soc.* **2011,** *133* (7), 2068-2071.
58. Singh A.; Spiccia L., Water oxidation catalysts based on abundant 1st row transition metals. *Coord. Chem. Rev.* **2013,** *257* (17), 2607-2622.
59. Zhang, T.; Wang, C.; Liu, S.; Wang, J.-L.; Lin, W., A biomimetic copper water oxidation catalyst with low overpotential. *J. Am. Chem. Soc.* **2014,** *136* (1), 273-281.

60. Fillol, J. L.; Codolà, Z.; Garcia-Bosch, I.; Gómez, L.; Pla, J. J.; Costas, M., Efficient water oxidation catalysts based on readily available iron coordination complexes. *Nat. Chem.* **2011,** *3* (10), 807-813.
61. Ellis, W. C.; McDaniel, N. D.; Bernhard, S.; Collins, T. J., Fast water oxidation using iron. *J. Am. Chem. Soc.* **2010,** *132* (32), 10990-10991.
62. Liu, T.; Zhang, B.; Sun, L., Iron-based molecular water oxidation catalysts: Abundant, cheap, and promising. *Chem. Asian J.* **2019,** *14* (1), 31-43.
63. Hocking, R. K.; Brimblecombe, R.; Chang, L.-Y.; Singh, A.; Cheah, M. H.; Glover, C.; Casey, W. H.; Spiccia, L., Water-oxidation catalysis by manganese in a geochemical-like cycle. *Nat. Chem.* **2011,** *3* (6), 461-466.
64. Crabtree R. H., Resolving heterogeneity problems and impurity artifacts in operationally homogeneous transition metal catalysts. *Chem. Rev.* **2011,** *112* (3), 1536-1554.
65. Védrine, J. C., Metal oxides in heterogeneous oxidation catalysis: State of the art and challenges for a more sustainable world. *ChemSusChem* **2019,** *12* (3), 577-588.
66. Gopalakrishnan, J., Chimie douce approaches to the synthesis of metastable oxide materials. *Chem. Mater.* **1995,** *7* (7), 1265-1275.
67. Sanchez, C.; Rozes, L.; Ribot, F.; Laberty-Robert, C.; Grosso, D.; Sassoye, C.; Boissiere, C.; Nicole, L., "Chimie douce": A land of opportunities for the designed construction of functional inorganic and hybrid organic-inorganic nanomaterials. *Cr. Chim.* **2010,** *13* (1), 3-39.
68. Risch, M.; Ringleb, F.; Kohlhoff, M.; Bogdanoff, P.; Chernev, P.; Zaharieva, I.; Dau, H., Water oxidation by amorphous cobalt-based oxides: *In situ* tracking of redox transitions and mode of catalysis. *Energy Environ. Sci.* **2015,** *8*, 661-674.
69. Klingan, K.; Ringleb, F.; Zaharieva, I.; Heidkamp, J.; Chernev, P.; Gonzalez-Flores, D.; Risch, M.; Fischer, A.; Dau, H., Water oxidation by amorphous cobalt-based oxides: Volume activity and proton transfer electrolyte bases. *ChemSusChem* **2014,** *7* (5), 1301-1310.
70. Najafpour, M. M.; Ehrenberg, T.; Wiechen, M.; Kurtz, P., Calcium manganese (III) oxides ($CaMn_2O_4.xH_2O$) as biomimetic oxygen-evolving catalysts. *Angew. Chemie. Int. Ed.* **2010,** *49* (12), 2233-2237.
71. Zaharieva, I.; Najafpour, M. M.; Wiechen, M.; Haumann, M.; Kurz, P.; Dau, H., Synthetic manganese–calcium oxides mimic the water-oxidizing complex of photosynthesis functionally and structurally. *Energy Environ. Sci.* **2011,** *4* (7), 2400-2408.
72. Wiechen, M.; Zaharieva, I.; Dau, H.; Kurz, P., Layered manganese oxides for water-oxidation: alkaline earth cations influence catalytic activity in a photosystem II-like fashion. *Chem. Sci.* **2012,** *3* (7), 2330-2339.
73. Frey, C. E.; Wiechen, M.; Kurz, P., Water-oxidation catalysis by synthetic manganese oxides – systematic variations of the calcium birnessite theme. *Dalton Trans.* **2014,** *43* (11), 4370-4379.
74. Zaharieva, I.; Chernev, P.; Risch, M.; Klingan, K.; Kohlhoff, M.; Fischer, A.; Dau, H., Electrosynthesis, functional, and structural characterization of a water-oxidizing manganese oxide. *Energy Environ. Sci.* **2012,** *5*, 7081-7089.
75. Iyer, A.; Del-Pilar, J.; King'ondu, C. K.; Kissel, E.; Garces, H. F.; Huang, H.; El-Sawy, A. M.; Dutta, P. K.; Suib, S. L., Water oxidation catalysis using amorphous manganese oxides, octahedral molecular sieves (OMS-2), and octahedral layered (OL-1) manganese oxide structures. *J. Phys. Chem. C* **2012,** *116* (10), 6474-6483.
76. Najafpour, M. M.; Nayeri, S.; Pashaei, B., Nano-size amorphous calcium–manganese oxide as an efficient and biomimetic water oxidizing catalyst for artificial photosynthesis: back to manganese. *Dalton Trans.* **2011,** *40* (37), 9374-9378.

77. Zhou, F.; Izgorodin, A.; Hocking, R. K.; Spiccia, L.; MacFarlane, D. R., Electrodeposited MnO_x films from ionic liquid for electrocatalytic water oxidation. *Adv. Energy Mater.* **2012,** *2* (8), 1013-1021.
78. Zhou, F.; Izgorodin, A.; Hocking, R. K.; Armel, V.; Spiccia, L.; MacFarlane, D. R., Improvement of catalytic water oxidation on MnO_x films by heat treatment. *ChemSusChem* **2013,** *6* (4), 643-651.
79. Najafpour, M. M.; Moghaddam, A. N., Nano-sized manganese oxide: A proposed catalyst for water oxidation in the reaction of some manganese complexes and cerium(IV) ammonium nitrate. *Dalton Trans.* **2012,** *41* (34), 10292-10297.
80. Jiao, F.; Frei, H., Nanostructured cobalt and manganese oxide clusters as efficient water oxidation catalysts. *Energy Environ. Sci.* **2010,** *3* (8), 1018-1027.
81. Gorlin, Y.; Lassalle-Kaiser, B.; Benck, J. D.; Gul, S.; Webb, S. M.; Yachandra, V. K.; Yano, J.; Jaramillo, T. F., *In situ* X-ray absorption spectroscopy investigation of a bifunctional manganese oxide catalyst with high activity for electrochemical water oxidation and oxygen reduction. *J. Am. Chem. Soc.* **2013,** *135* (23), 8525-8534.
82. Risch, M.; Khare, V.; Zaharieva, I.; Gerencser, L.; Chernev, P.; Dau, H., Cobalt−oxo core of a water-oxidizing catalyst film. *J. Am. Chem. Soc.* **2009,** *131* (20), 6936-6937.
83. Lutterman, D. A.; Surendranath, Y.; Nocera, D. G., A self-healing oxygen-evolving catalyst. *J. Am. Chem. Soc.* **2009,** *131* (11), 3838-3839.
84. Kanan, M. W.; Surendranath, Y.; Nocera, D. G., Cobalt–phosphate oxygen-evolving compound. *Chem. Soc. Rev.* **2009,** *38* (1), 109-114.
85. Surendranath, Y.; Dinca, M.; Nocera, D. G., Electrolyte-dependent electrosynthesis and activity of cobalt-based water oxidation catalysts. *J. Am. Chem. Soc.* **2009,** *131* (7), 2615-2620.
86. McAlpin, J. G.; Surendranath, Y.; Dinca, M.; Stich, T. A.; Stoian, S. A.; Casey, W. H.; Nocera, D. G.; Britt, R. D., EPR evidence for Co(IV) species produced during water oxidation at neutral pH. *J. Am. Chem. Soc.* **2010,** *132* (20), 6882-6883.
87. King, H. J.; Bonke, S. A.; Chang, S. L. Y.; Spiccia, L.; Johannessen, B.; Hocking, R. K., Engineering disorder into heterogenite-like cobalt oxides by phosphate doping: Implications for the design of water-oxidation catalysts. *ChemCatChem* **2017,** *9* (3), 511-521.
88. Kanan, M. W.; Yano, J.; Surendranath, Y.; Dinca, M.; Yachandra, V. K.; Nocera, D. G., Structure and valency of a cobalt-phosphate water oxidation catalyst determined by *in situ* X-ray spectroscopy. *J. Am. Chem. Soc.* **2010,** *132* (39), 13692-13701.
89. Gerken, J. B.; McAlpin, J. G.; Chen, J. Y. C.; Rigsby, M. L.; Casey, W. H.; Britt, R. D.; Stahl, S. S., Electrochemical water oxidation with cobalt-based electrocatalysts from pH 0-14: The thermodynamic basis for catalyst structure, stability and activity. *J. Am. Chem. Soc.* **2011,** *133* (36), 14431-14442.
90. Esswein, A. J.; Surendranath, Y.; Reece, S. Y.; Nocera, D. G., Highly active cobalt phosphate and borate based oxygen evolving catalysts operating in neutral and natural waters. *Energy Environ. Sci.* **2011,** *4* (2), 499-504.
91. Risch, M.; Klingan, K.; Ringleb, F.; Chernev, P.; Zaharieva, I.; Fischer, A.; Dau, H., Water oxidation by electrodeposited cobalt oxides - Role of anions and redox-inert cations in structure and function of the amorphous catalyst. *ChemSusChem* **2012,** *5* (3), 542-549.
92. Cobo, S.; Heidkamp, J.; Jacques, P.-A.; Fize, J.; Fourmond, V.; Guetaz, L.; Jousselme, B.; Ivanova, V.; Dau, H.; Palacin, S. *et al.* A Janus cobalt-based catalytic material for electro-splitting of water. *Nat. Mater.* **2012,** *11*, 802-807.

93. Bediako, D. K.; Costentin, C.; Jones, E. C.; Nocera, D. G.; Savéant, J.-M., Proton–electron transport and transfer in electrocatalytic films. Application to a cobalt-based O_2-evolution catalyst. *J. Am. Chem. Soc.* **2013,** *135* (28), 10492-10502.
94. Dinca, M.; Surendranath, Y.; Nocera, D., Nickel-borate oxygen-evolving catalyst that functions under benign conditions. *Proc. Natl. Acad. Sci.* **2010,** *23*, 10337-10341.
95. Singh, A.; Chang, S. L. Y.; Hocking, R. K.; Bach, U.; Spiccia, L., Highly active nickel oxide water oxidation catalysts deposited from molecular complexes. *Energy Environ. Sci.* **2013,** *6* (2), 579-586.
96. Risch, M.; Klingan, K.; Heidkamp, J.; Ehrenberg, D.; Chernev, P.; Zaharieva, I.; Dau, H., Nickel-oxido structure of a water-oxidizing catalyst film. *ChemComm* **2011,** *47* (43), 11912-11914.
97. Seo, H.; Cho, K. H.; Ha, H.; Park, S.; Hong, J. S.; Jin, K.; Nam, K. T., Water oxidation mechanism for 3d transition metal oxide catalysts under neutral condition. *J. Korean Ceram. Soc.* **2017,** *54* (1), 1-8.
98. McCrory, C. C. L.; Jung, S.; Peters, J. C.; Jaramillo, T. F., Benchmarking heterogeneous electrocatalysts for the oxygen evolution reaction. *J. Am. Chem. Soc.* **2013,** *135* (45), 16977-16987.
99. Rao, C. N. R.; Biswas, K., Ceramic methods. In *Essentials of inorganic materials synthesis*, John Wiley & Sons, Inc.: 2015; pp 17-21.
100. Rao, C. N. R., Chemical synthesis of solid inorganic materials. *Mater. Sci. Eng. B* **1993,** *18* (1), 1-21.
101. Melghit, K., *Soft chemistry routes to new nanosize materials*. 2007; Vol. 12, p 87-100.
102. Therese, G. H. A.; Kamath, P. V., Electrochemical synthesis of metal oxides and hydroxides. *Chem. Mater.* **2000,** *12* (5), 1195-1204.
103. Livage, J., Chimie douce: From shake-and-bake processing to wet chemistry. *New J. Chem.* **2001,** *25* (1), 1-1.
104. Schleich, D. M., Chimie douce: Low temperature techniques for synthesizing useful compounds. *Solid State Ion.* **1994,** *70-71*, 407-411.
105. Navrotsky, A., Energetic clues to pathways to biomineralization: Precursors, clusters, and nanoparticles. *Proc. Natl. Acad. Sci.* **2004,** *101* (33), 12096-12101.
106. Navrotsky, A., Thermochemistry of nanomaterials. *Rev. Mineral. Geochem.* **2001,** *44* (1), 73-103.
107. Rao, C. N. R.; Biswas, K., Soft chemistry routes. In *Essentials of inorganic materials synthesis*, John Wiley & Sons, Inc.: 2015; pp 57-95.
108. Baer, D. R.; Engelhard, M. H.; Johnson, G. E.; Laskin, J.; Lai, J.; Mueller, K.; Munusamy, P.; Thevuthasan, S.; Wang, H.; Washton, N. *et al.* Surface characterization of nanomaterials and nanoparticles: Important needs and challenging opportunities. *J. Vac. Sci. Technol. A* **2013,** *31* (5), 50820-50820.
109. Levar, C. E.; Hoffman, C. L.; Dunshee, A. J.; Toner, B. M.; Bond, D. R., Redox potential as a master variable controlling pathways of metal reduction by Geobacter sulfurreducens. *ISME J.* **2017,** *11* (3), 741-752.
110. Navrotsky, A.; Ma, C.; Lilova, K.; Birkner, N., Nanophase transition metal oxides show large thermodynamically driven shifts in oxidation-reduction equilibria. *Science* **2010,** *330* (6001), 199-201.
111. Jamnik, J.; Maier, J., Nanocrystallinity effects in lithium battery materials Aspects of nano-ionics. Part IV. *Phys. Chem. Chem. Phys.* **2003,** *5* (23), 5215-5220.
112. Maier, J., Thermodynamic aspects and morphology of nano-structured ion conductors: Aspects of nano-ionics Part I. *Solid State Ion.* **2002,** *154-155*, 291-301.

113. Navrotsky, A., Energetics of nanoparticle oxides: interplay between surface energy and polymorphism†. *Geochem. Trans.* **2003,** *4*, 34-34.
114. Chang, S. L. Y.; Singh, A.; Hocking, R. K.; Dwyer, C.; Spiccia, L., Nanoscale structural disorder in manganese oxide particles embedded in Nafion. *J. Mater. Chem. A* **2014,** *2* (11), 3730-3733
115. Albering, J. H., *Handbook of battery materials*. 2nd ed.; Wiley-VCH Verlag GmbH: 2011; p330.
116. Zhang, B.; Li, Y.; Valvo, M.; Fan, L.; Daniel, Q.; Zhang, P.; Wang, L.; Sun, L., Electrocatalytic water oxidation promoted by 3D nanoarchitectured turbostratic δ-MnO_x on carbon nanotubes. *ChemSusChem* **2017,** *10* (22), 4472-4478.
117. Hirata, K.; Shinzawa-Itoh, K.; Yano, N.; Takemura, S.; Kato, K.; Hananaka, M.; Muramoto, K.; Kawahara, T.; Tsukihara, T.; Yamashita, E. *et al.* Determination of damage-free crystal structure of an X-ray sensitive protein using an XFEL. *Nat. Methods* **2014,** *11* (7), 734-736.
118. Bergmann, A.; Zaharieva, I.; Dau, H.; Strasser, P., Electrochemical water splitting by layered and 3D cross-linked manganese oxides: correlating structural motifs and catalytic activity. *Energy Environ. Sci.* **2013,** *6* (9), 2745-2755.
119. Hocking, R. K.; Gummow, R. J.; King, H. J.; Sabri, M.; Kappen, P.; Dwyer, C.; Chang, S. L. Y., Direct formation of 2D-MnO_x under conditions of water oxidation catalysis. *ACS Appl. Nano Mater.* **2018**.
120. Geng, Z.; Sun, Y.; Zhang, Y.; Wang, Y.; Li, L.; Huang, K.; Wang, X.; Liu, J.; Yuan, L.; Feng, S., Architecture of biomimetic water oxidation catalyst with Mn_4CaO_5 clusterlike structure unit. *ACS Appl. Mater. Interfaces* **2018,** *10* (44), 37948-37954.
121. Ida, S.; Ishihara, T., Recent progress in two-dimensional oxide photocatalysts for water splitting. *J. Phys. Chem. Lett.* **2014,** *5* (15), 2533-2542.
122. Liu, H.; Gao, X.; Yao, X.; Chen, M.; Zhou, G.; Qi, J.; Zhao, X.; Wang, W.; Zhang, W.; Cao, R., Manganese(II) phosphate nanosheet assembly with native out-of-plane Mn centres for electrocatalytic water oxidation. *Chem. Sci.* **2019,** *10* (1), 191-197.
123. Wiechen, M.; Najafpour, M. M.; Allakhverdiev, S. I.; Spiccia, L., Water oxidation catalysis by manganese oxides: Learning from evolution. *Energy Environ. Sci.* **2014,** *7* (7), 2203-2212.
124. Zhang, G.; Dong, W.; Huang, X.; Zou, J., Oxygen vacancy induced enhancement of photochemical water oxidation on calcium manganese oxide catalyst. *Catal. Commun.* **2017,** *89*, 117-120.
125. Kwon, K. D.; Refson, K.; Sposito, G., Defect-induced photoconductivity in layered manganese oxides: A density functional theory study. *Phys. Rev. Lett.* **2008,** *100* (14), 146601.
126. Zhang, R.; Zhang, Y.-C.; Pan, L.; Shen, G.-Q.; Mahmood, N.; Ma, Y.-H.; Shi, Y.; Jia, W.; Wang, L.; Zhang, X. *et al.* Engineering cobalt defects in cobalt oxide for highly efficient electrocatalytic oxygen evolution. *ACS Catal.* **2018,** *8* (5), 3803-3811.
127. Wang, J.; Liu, J.; Zhang, B.; Cheng, F.; Ruan, Y.; Ji, X.; Xu, K.; Chen, C.; Miao, L.; Jiang, J., Stabilizing the oxygen vacancies and promoting water-oxidation kinetics in cobalt oxides by lower valence-state doping. *Nano Energy* **2018,** *53*, 144-151.
128. Tian, T.; Gao, H.; Zhou, X.; Zheng, L.; Wu, J.; Li, K.; Ding, Y., Study of the active sites in porous nickel oxide nanosheets by manganese modulation for enhanced oxygen evolution catalysis. *ACS Energy Lett.* **2018,** *3* (9), 2150-2158.
129. Chan, M. Z.; Kitchaev, D. A.; Weker, J. N.; Schnedermann, C.; Lim, K.; Ceder, G.; Tumas, W.; Toney, M. F.; Nocera, D. G., Electrochemical trapping of metastable Mn^{3+} ions for activation of MnO_2 oxygen evolution catalysts. *Proc. Natl. Acad. Sci.* **2018,** *115* (23), E5261-E5268.

130. Chen, L.; Zhang, Y.; Li, D.; Wang, Y.; Duan, C., Magnesium-regulated oxygen vacancies of nickel layered double hydroxides for electrocatalytic water oxidation. *J. Mater. Chem. A* **2018,** *6* (38), 18378-18383.
131. Zhu, Y.; Liu, X.; Jin, S.; Chen, H.; Lee, W.; Liu, M.; Chen, Y., Anionic defect engineering of transition metal oxides for oxygen reduction and evolution reactions. *J. Mater. Chem. A* **2019,** *7* (11), 5875-5897.
132. Védrine, J. C., Heterogeneous catalysis on metal oxides. *Catalysts* **2017,** *7* (11), 341.
133. Mavrokefalos, C. K.; Patzke, G. R., Water oxidation catalysts: The quest for new oxide-based materials. *Inorganics* **2019,** *7* (3), 29.
134. Menezes, P. W.; Indra, A.; Gutkin, V.; Driess, M., Boosting electrochemical water oxidation through replacement of OH Co sites in cobalt oxide spinel with manganese. *ChemComm* **2017,** *53* (57), 8018-8021.
135. Cook, T. R.; Dogutan, D. K.; Reece, S. Y.; Surendranath, Y.; Teets, T. S.; Nocera, D. G., Solar energy supply and storage for the legancy and nonlegacy worlds. *Chem. Rev.* **2010,** *110* (11), 6474-6502.
136. Blankenship, R. E.; Tiede, D. M.; Barber, J.; Brudvig, G. W.; Fleming, G.; Ghirardi, M.; Gunner, M. R.; Junge, W.; Kramer, D. M.; Melis, A. *et al.* Comparing photosynthetic and photovoltaic efficiencies and recognising the potential for improvement. *Science* **2011,** *332*, 805-809.
137. Montoro Bustos, A. R.; Pettibone, J. M.; Murphy, K. E., Chapter 2: Characterization of nanoparticles: Advances. In *Nanoparticle design and characterization for catalytic applications in sustainable chemistry*, The Royal Society of Chemistry: 2019; pp 37-83.
138. Mourdikoudis, S.; Pallares, R. M.; Thanh, N. T. K., Characterization techniques for nanoparticles: comparison and complementarity upon studying nanoparticle properties. *Nanoscale* **2018,** *10* (27), 12871-12934.
139. Hocking, R. K.; Chang, S. L. Y.; MacFarlane, D. R.; Spiccia, L., Preparation and characterization of catalysts for clean energy: A challenge for X-rays and electrons. *Aust. J. Chem.* **2012,** *65* (6), 608-614.
140. Winnischofer, H.; Rocha, T. C. R.; Nunes, W. C.; Socolovsky, L. M.; Knobel, M.; Zanchet, D., Chemical synthesis and structural characterization of highly disordered Ni colloidal nanoparticles. *ACS Nano* **2008,** *2* (6), 1313-1319.
141. Walker F. A., Magnetic spectroscopic (EPR, ESEEM, Mossbauer, MCD and NMR) studies of low-spin ferriheme centres and their correspondning heme proteins. *Coord. Chem. Rev.* **1999,** *185-186*, 471-534.
142. Murad E.; Cashion J., *Mossbauer spectroscopy of environmental materials and their industrial utilization*. Kluwer Academic Publishers: 2003.
143. Ballhausen C. J., *Molecular electronic structures of transition metal complexes*. McGraw-Hill: 1979.
144. Pastor, E.; Le Formal, F.; Mayer, M. T.; Tilley, S. D.; Francàs, L.; Mesa, C. A.; Grätzel, M.; Durrant, J. R., Spectroelectrochemical analysis of the mechanism of (photo)electrochemical hydrogen evolution at a catalytic interface. *Nat. Commun.* **2017,** *8* (14280).
145. Bard, A. J.; Faulkner, L. R., *Electrochemical methods: Fundamentals and applications*. 2nd ed.; John Wiley & Sons, Inc.: 2000; p 864.
146. Binninger, T.; Fabbri, E.; Patru, A.; Garganourakis, M.; Han, J.; Abbott, D. F.; Sereda, O.; Kötz, R.; Menzel, A.; Nachtegaal, M. *et al.* Electrochemical flow-cell setup for *in situ* X-ray investigations: I. Cell for SAXS and XAS at synchrotron facilities. *J. Electrochem. Soc.* **2016,** *163* (10), H906-H912.

147. Golden, D.; Dixon, J.; Kanehiro, Y., The manganese oxide mineral, lithiophorite, in an oxisol From Hawaii. *Soil Res.* **1993,** *31* (1), 51-66.
148. Taylor, R.; McKenzie, R.; Norrish, K., The mineralogy and chemistry of manganese in some Australian soils. *Soil Res.* **1964,** *2* (2), 235-248.
149. Onac, B. P., Minerals. In *Encyclopedia of caves 2nd Edition*, White, W. B.; Culver, D. C., Eds. Academic Press: Amsterdam, 2012; pp 499-508.
150. Sunda, W. G.; Huntsman, S. A.; Harvey, G. R., Photoreduction of manganese oxides in seawater and its geochemical and biological implications. *Nature* **1983,** *301* (5897), 234-236.
151. Sunda, W. G.; Huntsman, S. A., Photoreduction of manganese oxides in seawater. *Mar. Chem.* **1994,** *46*, 133-152.
152. Najafpour M. M., Mixed-valence manganese calcium oxides as efficient catalysts for water oxidation. *Dalton Trans.* **2011,** *40*, 3793-3795.
153. Lee, S. Y.; Gonzalez-Flores, D.; Ohms, J.; Trost, T.; Dau, H.; Zaharieva, I.; Kurz, P., Screen-printed calcium-birnessite electrodes for water oxidation at neutral pH and an "electrochemical harriman series". *ChemSusChem* **2014,** *7* (12), 3442-3451.
154. Sauer K.; Yachandra V. K., A possible evolutionary origin for the Mn_4 cluster of the photosynthetic water oxidation complex from natural MnO_2 precipitates in the early ocean. *Proc. Natl. Acad. Sci.* **2002,** *99* (13), 8631-8636.
155. Birkner, N.; Nayeri, S.; Pashaei, B.; Najafpour, M. M.; Casey, W. H.; Navrotsky, A., Energetic basis of catalytic activity of layered nanophase calcium manganese oxides for water oxidation. *Proc. Natl. Acad. Sci.* **2013,** *110* (22), 8801-8806.
156. Huynh M.; Chi C.; Billinge S. J.; Nocera D. G., Nature of activated manganese oxide for oxygen evolution. *J. Am. Chem. Soc.* **2015,** *137* (47), 14887-14904.
157. Villalobos, M.; Toner, B.; Bargar, J.; Sposito, G., Characterization of the manganese oxide produced by pseudomonas putida strain MnB1. *Geochim. Cosmochim. Acta* **2003,** *67* (14), 2649-2662.
158. Kwon, K. D.; Refson, K.; Sposito, G., On the role of Mn(IV) vacancies in the photoreductive dissolution of hexagonal birnesite. *Geochim. Cosmochim. Acta* **2009,** *73* (14), 4142-4150.
159. Sakai, N.; Ebina, Y.; Takada, K.; Sasaki, T., Photocurrent generation from semiconducting manganese oxide nanosheets in response to visible light. *J. Phys. Chem. B* **2005,** *109* (19), 9651-9655.
160. Huynh, M.; Bediako, D. K.; Liu, Y.; Nocera, D. G., Nucleation and growth mechanisms of an electrodeposited manganese oxide oxygen evolution catalyst. *J. Phys. Chem. C* **2014,** *118* (30), 17142-17152.
161. Brodsky, C. N.; Bediako, D. K.; Shi, C.; Keane, T. P.; Costentin, C.; Billinge, S. J. L.; Nocera, D. G., Proton–electron conductivity in thin films of a cobalt–oxygen evolving catalyst. *ACS Appl. Energy Mater.* **2019,** *2* (1), 3-12.
162. Bediako, D. K.; Ullman, A. M.; Nocera, D. G., Catalytic oxygen evolution by cobalt oxido thin films. In *Solar energy for fuels*, Tüysüz, H.; Chan, C. K., Eds. Springer International Publishing: Cham, 2016; pp 173-213.
163. Ahn, H. S.; Bard, A. J., Surface interrogation of CoPi water oxidation catalyst by scanning electrochemical microscopy. *J. Am. Chem. Soc.,* **2015,** *137* (2), 612-615.
164. Costentin, C.; Porter, T. R.; Savéant, J.-M., Conduction and reactivity in heterogeneous-molecular catalysis: New insights in water oxidation catalysis by phosphate cobalt oxide films. *J. Am. Chem. Soc.* **2016,** *138* (17), 5615-5622.
165. Zaharieva, I.; Gonzalez-Flores, D.; Asfari, B.; Pasquini, C.; Mohammadi, M. R.; Klingan, K.; Zizak, I.; Loos, S.; Chernev, P.; Dau, H., Water oxidation catalysis— Role of

redox and structural dynamics in biological photosynthesis and inorganic manganese oxides. *Energy Environ. Sci.* **2016,** *9*, 2433-2443.
166. Ullman, A. M.; Nocera, D. G., Mechanism of cobalt self-exchange electron transfer. *J. Am. Chem. Soc.* **2013,** *135* (40), 15053-15061.
167. King, H. J.; Fournier, M.; Bonke S. A.; Seeman E.; Chatti, M.; Jumabekov A. N.; Johannessen B.; Kappen P.; Simonov A. N.; Hocking R. K.; Photon-induced, timescale, and electrode effects critical for the in situ X-ray spectroscopic analysis of electrocatalysts: The water oxidation case. *J. Phys Chem. C*. **2019**, 123 (47), 28533-28549.
168. Lux, H., "Säuren" und "basen" im schmelzfluss: Die bestimmung der sauerstoffionen-konzentration. *Zeitschrift für Elektrochemie und angewandte physikalische Chemie* **1939,** *45* (4), 303-309.
169. Costentin, C.; Nocera, D. G., Self-healing catalysis in water. *Proc. Natl. Acad. Sci.* **2017,** *114* (51), 13380-13384.

Chapter 2 –

Engineering disorder into heterogenite-like cobalt oxides by phosphate doping: Implications for the design of water oxidation catalysts

ABSTRACT

Amongst the most promising materials for economical water oxidation catalysis are manganese (MnO_x), nickel (NiO_x), and cobalt oxides (CoO_x). Despite extensive research into metal oxide catalysts of this kind, the relationship between structure and function is not fully understood. However, it is known that many metal oxide catalysts function best in a proton accepting electrolyte (such as borate or phosphate buffer), and that electrodeposition from these electrolytes significantly alters the structure of the material by imparting a 'molecular nature' or form of internal 'disorder'. Arguably, the most well-known case for this phenomenon is Kanan and Nocera's 'Co-Pi' (cobalt oxide with phosphate) catalyst.

In this study, we synthesized a series of heterogenite-like cobalt oxides with different levels of phosphate doping (0, 1, 3 and 9 wt% phosphate) to mimic the structural and functional properties of the electrodeposited Co-Pi catalyst. The systematic structural changes within the CoO_x series were directly correlated with activity for water oxidation catalysis and with CoO_x oxidative strength. It was determined that the most disordered materials were the most active as sacrificial oxidants but were the least active as water oxidation catalysts. Furthermore, this research suggested that phosphate introduced bond-length structural disorder into Co-Pi and that this consequently decreased the thermodynamic stability and changed the mechanistic functionality of the material for the water oxidation reaction.

Chapter 2 – Publications

This chapter is an extended version of the first author peer-reviewed and published manuscript described below:

Title: Engineering disorder into heterogenite-like cobalt oxides by phosphate doping: Implications for the design of water oxidation catalysts

Publisher: ChemCatChem

Year: 2017

Details: volume 9, issue 3, pages 511-521

Authors: Hannah J. King, Shannon A. Bonke, Shery L.Y. Chang, Leone Spiccia, Bernt Johannessen, Rosalie K. Hocking

Chapter 2 – Table of contents

2.1 Introduction

One of the biggest challenges of the 21st century is to develop methods of producing cheap, carbon-neutral, clean energy.[1-4] The Sun is the Earth's most powerful and abundant source of renewable energy, with more energy radiated onto the Earth in one hour than consumed globally (from all energy sources) in an entire year.[5-8] While this makes the Sun ideal as a renewable energy source, its diurnal and intermittent nature limits its capacity as a dominant energy provider. Electrochemical water splitting is one method by which electromagnetic energy from the Sun can be stored as chemical energy (in so-called 'solar fuels').[9-11] The overall and half-cell reactions for electrochemical water splitting are given in **Scheme 2.1**:[5-6, 12-14]

Oxidation:	$2H_2O \rightleftharpoons O_2 + 4H^+ + 4e^-$	$E_{anode} = 1.23\ V - (0.059 \times pH)\ V$	*vs.* SHE
Reduction:	$4H^+ + 4e^- \rightleftharpoons 2H_2$	$E_{cathode} = 0\ V - (0.059 \times pH)\ V$	*vs.* SHE
Overall:	$2H_2O \rightleftharpoons 2H_2 + O_2$	$E_{rxn} = -1.23\ V$, $\Delta G = 237\ kJ\ mol^{-1}$ of H_2	

Scheme 2.1: Water splitting redox half reactions. The standard reaction potentials (at 25°C, pH 0, *vs*. standard hydrogen electrode (SHE)) vary according to the Nernst equation, whereby the half-cell potentials are decreased by 59 mV for each pH unit increase.[5, 15-16]

The water oxidation reaction is the most kinetically and thermodynamically demanding of the two redox reactions shown in **Scheme 2.1**.[9] The kinetics of the water oxidation reaction are slow due to the many intermediates required to complete the $4H^+/4e^-$ oxidation of water to molecular oxygen.[15-17] The slow kinetics cause high overpotentials (η), and necessitate the use of catalysts to stabilise kinetic intermediates and lower the required overpotential.[18-19] The large financial costs associated with electrolytic water splitting can be reduced by catalysing the water oxidation half-reaction.[1-4] Transition metal oxides have shown excellent potential as cheap and efficient water oxidation catalysts, particularly manganese (MnO_x), nickel (NiO_x), and cobalt oxides (CoO_x).[15-16, 20-21]

The amorphous cobalt oxide with phosphate catalyst reported by Kanan and Nocera in 2008 is one of the most widely studied materials for the water oxidation reaction.[15, 18, 22-25] The so-called 'Co-Pi' catalyst (where 'Pi' denotes inorganic phosphate) is mostly heterogenite-like (CoOOH) cobalt oxide by composition, with approximately 7.7 wt% phosphate incorporated into the material.[15] The high activity of this catalyst at neutral pH prompted the development of other 'transition metal − anion' type materials, including Ni-Bi (where 'Bi' denotes borate),[26] Co-Bi,[23] and Mn-Pi.[27-28] Catalysts of this type are typically synthesised *in situ* through oxidative electrodeposition from a solution of the transition metal cation in a proton accepting pH buffering electrolyte, where the electrolyte anion becomes incorporated into the electrodeposited material.[29-30]

Co-Pi further inspired studies into a range of related catalysts including substrate and nanoparticle supported metal oxide catalysts,[25, 31-35] *ex situ* synthesised screen-printed materials,[36-40] materials precipitated from ionic liquids,[41] and anodised metal oxides.[26,23] Many of these metal oxide catalysts have shown some improved efficiency when operated in neutral phosphate buffer (pH 7) or mildly basic borate buffer (pH 9.2).[23, 26-28]

Extensive research into the mechanism of Co-Pi has revealed several important functions of the phosphate anion in the electrodeposition and operation of the material.[15, 22-23] Firstly, phosphate is said to promote catalyst formation by allowing Co-Pi to be electrodeposited from low Co^{2+} concentrations at moderate potentials greater than 1.05 V *versus* Ag|AgCl.[23] Secondly, phosphate facilitates the re-deposition of Co-Pi from the Co^{2+} and phosphate degradation products during catalytic operation in a so-called 'self-healing' mechanism.[15,22] Thirdly, XAS and TEM studies have revealed that phosphate is important for forming an amorphous, structurally disordered material. Specifically, studies by the Nocera and Dau research groups have suggested that phosphate terminates 'molecular sized' CoO_x clusters, and thereby limits the atomic level order of the Co-Pi material.[24, 29-30, 42] Finally, mechanistic studies have shown that phosphate acts as a proton acceptor during proton coupled electron transfer (PCET) steps during catalytic operation.[18, 43-44] This function is important for maintaining the local and bulk pH environments, as well as preventing catalyst corrosion by reducing proton accumulation at the catalyst surface.[22-23, 45]

Although heterogeneous catalytic reactions are often considered to be surface mediated, cobalt oxide catalysts of the type described above have shown a dependence on the amount of cobalt present in the material and have, therefore, shown that material below the surface nano-layer is functional in the catalytic mechanism.[46-48] This deviation from classical heterogeneous behaviour has been investigated by Klingan et al., where it was shown that catalytic current increased linearly with film thickness[45, 49], and has been supported by González-Flores et al., where kinetic studies determined that the overall activity of a cobalt oxide catalyst was explained by both surface and bulk catalytic activity.[50] The involvement of both the surface and bulk in the catalytic reaction has important implications for the mechanism, activity and thermodynamic stability of transition metal oxide materials.

To better understand the structure and function of heterogenite-like cobalt oxide electrocatalysts such as Co-Pi, we developed a heterogenite-like cobalt oxide series with different levels of phosphate doping (0, 1, 3, and 9 wt% phosphate) and subsequently correlated the systematic changes in structure with activity for the water oxidation reaction. The phosphate doped series was chemically and structurally characterised using powder X-ray diffraction (XRD), X-ray absorption spectroscopy (XAS), transmission electron microscopy (TEM), inductively coupled plasma – atomic emission spectroscopy (ICP-AES), Fourier transform infrared (FTIR), scanning electron microscopy (SEM) and Brunauer-Emmett-Teller (BET) analyses. The catalytic efficiency of the materials for water oxidation was analysed using electrochemical methods and *ex situ* reactions with hypochlorite (ClO^-) as a sacrificial oxidant. Finally, the oxidative strength of the CoO_x materials was measured with reductive dissolution experiments using hydrogen peroxide (H_2O_2).

2.2 Experimental

2.2.1 Synthesis of CoO_x (*x* %P) series

The heterogenite-like cobalt oxide samples were synthesised in a 'one-pot' reaction procedure in which $Co_3(PO_4)_2$ was initially precipitated from diluted stock solutions of Co^{2+} (cobalt sulfate heptahydrate, 0.2 M) and phosphate buffer (sodium dihydrogen orthophosphate dihydrate, 1 M or 0.1 M, pH 7), and subsequently oxidised with sodium hypochlorite (NaOCl, 4 w/v%, pH 12, 50% by volume). Oxygen gas was evolved during the hypochlorite addition and was measured using an O_2 probe (*Presens* GmbH, Germany, *Microx 4* monitoring system with Pst7 probe). The resulting dark brown cobalt oxide precipitate was isolated and washed (10 ×) with distilled water using a centrifuge, then washed with acetone. The CoO_x samples were dried in an oven (at 110°C for ~10 h) in preparation for analysis. Herein, we define the incorporation of phosphate as *doping*. A systematically doped CoO_x (*x* %P) series was developed by varying the amount of phosphate (by a factor of 10) used in the 8mM Co^{2+} synthesis. A high cobalt concentration series (**§ 2.3.1.1**) was synthesised from an 80mM Co^{2+} solution.

2.2.2 Synthesis of bulk heterogenite

Bulk heterogenite (β-CoOOH) was synthesised using a methodology outlined by Myers and Penn[51] in which sodium hydroxide (NaOH, 200 mL, 1 M, 60°C) was added at a rate of 8 mL min^{-1} to a Co^{2+} solution (cobalt sulfate heptahydrate, 200 mL, 0.1 M, 60°C) followed by the dropwise addition of sodium hypochlorite (NaOCl, 80mL, 4 w/v%, pH 12). The suspension was stirred and heated for 2 h.[51] The precipitate was separated and washed as described in **§ 2.2.1**.

2.2.3 Inductively coupled plasma – atomic emission spectroscopy (ICP-AES)

ICP-AES was used to measure the cobalt and phosphorus content of the CoO_x materials. The CoO_x solid was dissolved for ICP-AES analysis by heating (90 ± 5°C) the CoO_x (*ca*. 0.1 g accurately weighed) in nitric acid (HNO_3, 10 mL, 70 %) for 2 h. The solution was cooled and diluted 1 in 10. The ICP-AES analysis was carried out using a Varian Liberty Series II and a calibration curve (R = 0.999) generated from 3 standards (5, 25 and 50 ppm).

2.2.4 Powder X-ray diffraction (XRD)

The cobalt oxide samples were prepared as (*ca*. 1 g) pressed powder mounts for XRD analysis. The powder XRD analyses were carried out using a Siemens D5000 Diffractometer θ:2θ goniometer, with a copper anode X-ray tube (λ = 0.154 nm). The effects of particle size on the cobalt oxide spectra were simulated from a *.cif file for heterogenite[52] using the *CrystalDiffract*[53] program. Particle sizes were estimated based on the Scherrer equation[54].

2.2.5 X-ray absorption spectroscopy (XAS)

Co K-edge XAS spectra were collected on the multipole wiggler XAS beamline (12-ID) at the Australian Synchrotron (ANSTO), Melbourne, operating with an electron beam energy of 3.0 GeV and beam current of 200 mA. The XAS beamline was operated in mode 1 (top-up mode) using a Si(111) monochromator and focusing optics. All samples were pressed pellets (7-10 mg CoO_x with 100 mg of cellulose, 3 tonnes for 10 seconds) that were analysed in a liquid helium cryostat (held below 10 K). The data were collected in both fluorescence (solid state 100-element Ge detector) and transmission (OKEN ionisation chambers) modes. The edge energy (E, defined as the first inflection point of the main absorption peak) of each collected spectrum was aligned to a Co foil reference that was calibrated to 7709 eV. The raw data collected from the beamline was converted in *Average*[55] or *Sakura*[56], and analysed in *Athena*[57] (normalise, background subtraction, E calibration) and *Artemis*[57] (data fitting).

The extended X-ray absorption fine structure (EXAFS) data was analysed in two ways. In the first method, each data set was fitted with an identical set of 7 parameters (from the heterogenite crystal structure[58]) that were chosen to best represent the data. The parameters correlate with each of the 7 peaks shown in **Figure 2.7**. In this case, the co-ordination number of each vector was fixed, and the distance and Debye-Waller (σ^2) factors were floated. In the second method, the EXAFS were back-calculated (into q-space) from different regions of the Fourier transform (R′-space). In basic EXAFS data interpretation, the collected EXAFS spectrum (k-space) is split into its Fourier components and combined to give the Fourier transform. If the EXAFS are well-described in a given region in R′-space, then the k-space EXAFS will match the q-space EXAFS. However, if the data is under-described in R′-space then the k-space and q-space EXAFS will differ. Therefore, back-calculating different regions of the Fourier transform will give an indication of long range order by identifying which EXAFS regions contribute significantly to the Fourier transform.

2.2.6 Transmission electron microscopy (TEM)

In preparation for analysis, the cobalt oxide samples were drop cast directly onto amorphous carbon film coated copper TEM grids. The TEM images were taken using an aberration-corrected Titan (FEI Company) operated at 300 kV.

2.2.7 Fourier transform infrared (FTIR) spectroscopy

The ground cobalt oxide samples were analysed by FTIR without further preparation. FTIR data was collected using a Nicolet 6700 Fourier transform infrared spectrometer as attenuated total reflection (ATR) spectra (using OMNIC 8.2 computer program) in the region of 4000-525 cm^{-1}.

2.2.8 Scanning electron microscopy (SEM)

The cobalt oxide samples were analysed by SEM as: (i) a finely ground powder adhered to a SEM pin stub with an adhesive double-sided graphite tab, and (ii) an electrode directly adhered on a SEM pin stub with an adhesive double-sided graphite tab. All samples were gold sputter coated. In preparation (ii), graphite tape was used to bridge the conductive sample surface to the pin stub. The SEM images were taken using a Jeol JSM5410LV.

2.2.9 Brunauer-Emmett-Teller (BET)

The specific surface area of each CoO_x material was determined using multipoint BET.[59] In preparation for BET analysis; the metal oxides powders where degassed at 150°C for 12 h. The N_2 adsorption and desorption isotherms (at 77 K) were obtained using a TriStar II Series Micrometrics instrument.

2.2.10 Inductively coupled plasma – mass spectroscopy (ICP-MS)

Inductively coupled plasma – mass spectrometry (ICP-MS) was used to measure the cobalt content of the CoO_x materials screen-printed or electrodeposited onto fluorine-doped tin oxide (FTO) coated glass (FTO/glass). In preparation for analysis, the CoO_x solid was dissolved off the electrode by heating (90 ± 5°C) in nitric acid (HNO_3, 10 mL, 70 %) for 30 mins, then cooled and diluted 1 in 10. Triplicate electrodes were analysed. The ICP-MS analysis was carried out using a Varian ICP-MS 820 series instrument, with a calibration curve (R = 0.999) generated from 3 standard solutions (5, 25 and 50 ppm).

2.2.11 Screen-printing CoO_x onto electrodes

In this procedure, the CoO_x sample (500 mg) was ball-milled (250 rpm for 4 h) into a fine powder and oven dried (110°C, 2 h) to remove water which is immiscible with the solvents used in the printing paste. To make the printing paste (2.5 w/v% suspension of CoO_x in ethanol); terpineol (solvent; 10 g) and ethyl cellulose (binding agent; 1 g dispersed in 20 mL ethanol) were added to the CoO_x (in the ball mill jar) and the milling step (250 rpm for 4 h) was repeated to give a uniform paste or 'ink'. The sample was ready to screen-print once the optimal viscosity was obtained by *in vacuo* removal of the ethanol solvent (175 mbar, 60°C). Each sample was screen-printed inside the designated laser engraved area (6 × 6 mm, electroactive area = 0.36 cm^2) of a large FTO/glass sheet (8 Ω/sq., *Dyesol TEC8 Glass Plates*). The screen-printed large FTO/glass sheet was initially dried on a hotplate (120°C, < 15 mins), then sintered at 500°C (< 10 mins) on a sintering hotplate. In preparation for electrochemical experiments, individual electrodes were cut from the large FTO/glass sheet. The electroactive area was isolated by masking with a polyimide tape (Kapton) to ensure the measured activity was due solely to the cobalt oxide material.

It is additionally noted from the above that: (i) fluorine-doped tin oxide coated glass is also typically abbreviated as F:SnO_2. (ii) 20 squares (4 × 4 mm, electroactive area = 0.16 cm^2) of screen-printed sample were pasted per large FTO/glass sheet, with each square of CoO_x material corresponding to one electrode. (iii) Heating to 500°C incinerates the ethyl cellulose and terpineol components and leaves pores in the printed thin film.

2.2.12 Electrochemical experiments

All electrochemical experiments were conducted on a Voltalab PGZ301 potentiostat, using a two-compartment electrochemical H-cell (with a P4 (10−16 μm) ceramic frit), and a 3-electrode system. The anodic H-cell compartment contained the Ag|AgCl (3 M NaCl) reference electrode and the working electrode, and the cathodic compartment contained the platinum mesh auxiliary electrode. A 3D printed electrode holder kept the working and reference electrodes a constant 3-4 mm distance apart. The cobalt oxide materials were analysed/operated in phosphate buffer (sodium dihydrogen orthophosphate dihydrate, 0.1 M, pH 7), which was stirred using a magnetic stirrer bar (550 rpm). All experimental potential differences are reported against the experimental reference electrode (Ag|AgCl, 3 M NaCl). Other potential differences quoted herein are reported against the explicitly stated reference electrode.

2.2.12.1 Cyclic voltammetry (CV)

Cyclic voltammetry (CV) data was collected in triplicate (*i.e.* 3 different electrodes of the same sample) and the first cycle of the median scan is presented. The CV data was measured at a scan rate of 20 mV sec^{-1}. The background current was measured using a blank FTO/glass electrode.

2.2.12.2 Tafel plot

Tafel data was collected in duplicate and averaged in preparation for analysis. The Tafel slopes were generated by plotting the log of current density (*abscissa*) *versus* the overpotential (*ordinate*), and calculating the slope of the linear regression over the optimal domain (over the region of current onset).[14,60] For ease of comparison, the Tafel slopes were calculated over a similar domain region (0.98 to 1.10 V, or 1.00 to 1.12 V).

2.2.13 *Ex situ* measurement of water oxidation catalysis by reaction with hypochlorite (ClO^-)

Hypochlorite is a commonly used sacrificial reagent in *ex situ* tests for water oxidation catalysis.[61-62] Herein, a gas burette was used to measure the quantity of gas evolved from the hypochlorite and CoO_x reaction. In this set-up, the CoO_x sample (*ca.* 300 mg) was transferred into a small Quickfit conical flask with phosphate buffer (sodium dihydrogen orthophosphate dihydrate, 5 mL; 1 M, pH 7), a magnetic stirrer bar was added to the suspension, the flask was connected to the gas burette using the available Quickfit connection, and the flask was placed on a magnetic stirrer plate to enable stirring. Whilst the suspension was being stirred, a needle was used to inject sodium hypochlorite (NaOCl, 20mL, 4 w/v%, pH 12) through the septum into the flask. The volume of gas evolved was incrementally measured for 6 mins. Each reaction solution was between pH 7.5 and 8.5.

2.2.14 Measurement of CoO_x oxidative strength by reaction with hydrogen peroxide (H_2O_2)

The oxidative strength of each cobalt oxide sample was measured using a novel experiment involving hydrogen peroxide and a gas burette set-up similar to that described in **§ 2.2.13**. In this experiment, the CoO_x (approximately 0.2 mmol Co) was suspended in either nitric acid (HNO_3, 0.1 M, 7 mL; pH 1), acetate buffer (sodium acetate, 0.1 M, 7 mL; pH 3, pH 5) or phosphate buffer (sodium hydrogen phosphate, 0.1 M, 7 mL; pH 7, pH 10 or pH 13), and then mixed with hydrogen peroxide (H_2O_2, 25 %, 2 mL, 0.0164 mol). The volume of gas evolved was incrementally measured for 30 mins. In some pH conditions, the dark brown CoO_x solid dissolved to produce a pale red solution.

2.3 Results and analysis

2.3.1 Structural characterisation of the CoO_x (*x* %P) series

This study examined a series of heterogenite-like cobalt oxide materials which had been systematically doped with 0, 1, 3, and 9 wt% phosphate. The CoO_x (*x* %P) series was structurally characterised using XRD, TEM, and XAS. These three techniques provided complimentary information about atomic-level and nanoscale structure. Additional chemical, structural and morphological information was provided by ICP-AES, FTIR, SEM, and BET analyses.

2.3.1.1 ICP-AES

Table 2.1 presents the ICP-AES data and the synthesis conditions for each CoO_x (*x* %P) sample. The mol ratio of cobalt and phosphate in the synthesis solution and in the final product is also provided.

Table 2.1: ICP-AES data and synthesis conditions for the systematically doped CoO_x (*x* %P) series. This data is also provided for a supplementary CoO_x (*x* %P) series with 0.2, 2 and 5 wt% phosphate as selected analyses were conducted on these samples.

Synthesis solution			**CoO_x product**			
Co^{2+} (mM)	**Pi*** (mM)	**Mol ratio** (Co:Pi*)	**Co** (wt% ± σ) †	**Pi*** (wt% ± σ) †	**Mol ratio** (Co:Pi*)	**CoO_x (*x* %P) name**
8	**100**	1 : 12.5	29.3 ± 0.3	8.6 ± 0.1	3 : 1	**CoO_x (9 %P)**
	10	1 : 1.25	32.1 ± 0.2	3.1 ± 0.02	9 : 1	**CoO_x (3 %P)**
	1	1 : 0.125	33.4 ± 0.2	0.8 ± 0.007	42 : 1	**CoO_x (1 %P)**
	0	1 : 0	34.6 ± 0.3	< 0.07		**CoO_x (0 %P)**
80	**100**	1 : 1.25	32.1 ± 0.1	5.4 ± 0.1	6 : 1	**CoO_x (5 %P)**
	10	1 : 0.125	35.6 ± 0.1	1.7 ± 0.01	21 : 1	**CoO_x (2 %P)**
	1	1 : 0.0125	41.7 ± 0.4	0.2 ± 0.003	278 : 1	**CoO_x (0.2 %P)**
Bulk heterogenite			37.2 ± 0.3	0.0 ± 0.001		

* Pi = inorganic phosphate

† σ refers to the standard deviation of the triplicate measurements taken of each sample

2.3.1.2 XRD

Figure 2.1 presents the XRD patterns obtained from bulk heterogenite, CoO_x (0 %P) and CoO_x (9 %P). While the XRD peaks of CoO_x (0 %P) and CoO_x (9 %P) are substantially weaker and boarder than the peaks of bulk heterogenite, the characteristic {003} and {012} heterogenite reflections are present in the CoO_x (*x* %P) samples. Note that XAS was used to confirm that the CoO_x (*x* %P) samples are heterogenite--like.[39] The sharp but weak {200} reflection present in the CoO_x (*x* %P) samples is attributed to NaCl, which is a by-product of hypochlorite oxidation and can be a minor contaminant if the materials are not sufficiently washed during the isolation step in the synthesis.

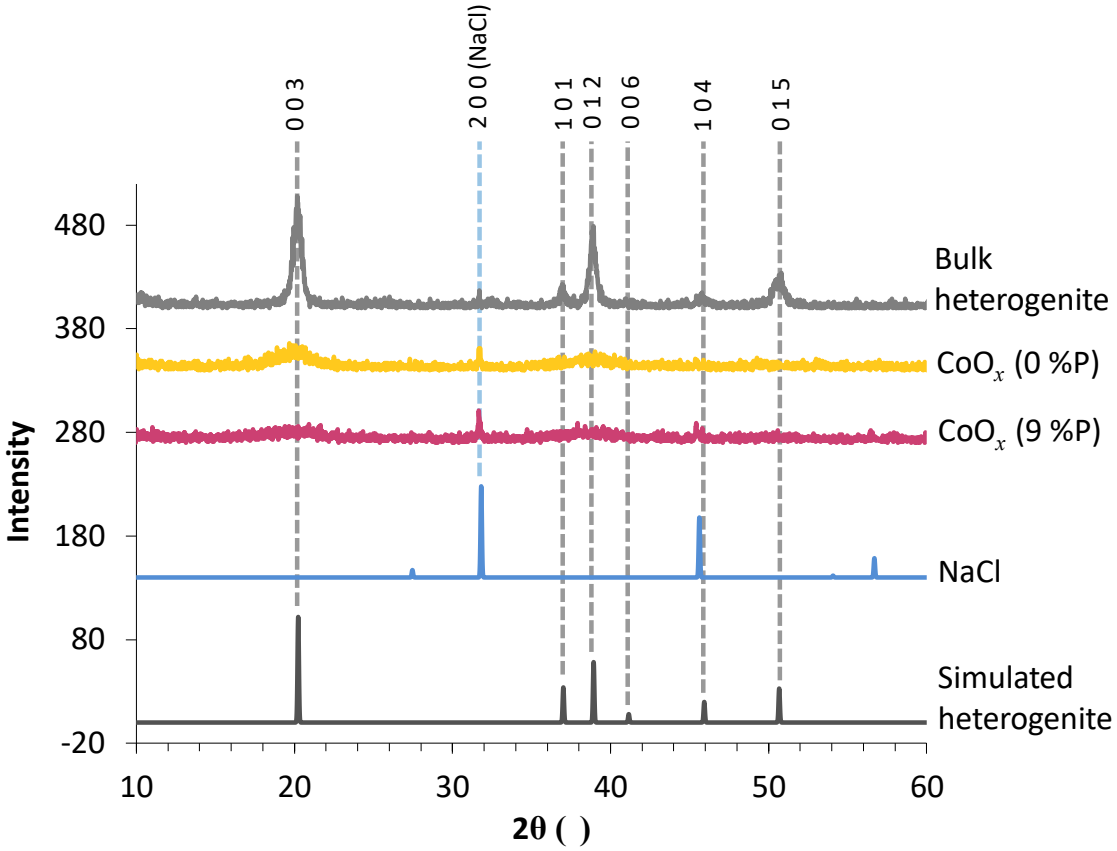

Figure 2.1: Powder XRD spectra collected on bulk heterogenite, CoO_x (0 %P), and CoO_x (9 %P). Data was collected on: bulk heterogenite (*grey*), CoO_x (0 %P) (*yellow*), CoO_x (9 %P) (*pink*), NaCl (*blue*)[65], and simulated crystalline heterogenite (*dark grey*)[53]. The simulated crystalline heterogenite spectrum is based on the crystal structure reported in reference 58. The crystalline heterogenite space group is $R\bar{3}m$ [166], and the lattice constants are a = 2.855 Å and c = 13.156 Å.

Figure 2.2 presents the XRD simulations generated using the Scherrer equation[54, 63-64] for the estimation of average crystallite cluster size for CoO_x (0 %P) and CoO_x (9 %P). The simulations indicated that the CoO_x (0 %P) and CoO_x (9 %P) samples have average cluster sizes of 1.5 and 1 nm, respectively. This estimation relies on the assumption that the internal structure of the nanoparticle is similar to the structure of the bulk. However, this assumption is possibly inadequate as subsequent XAS analysis indicates that the cobalt oxide materials are structurally disordered and as such, the bulk structures may differ from the surface structures within these materials (**§2.3.1.4 XAS**).[54, 63-64]

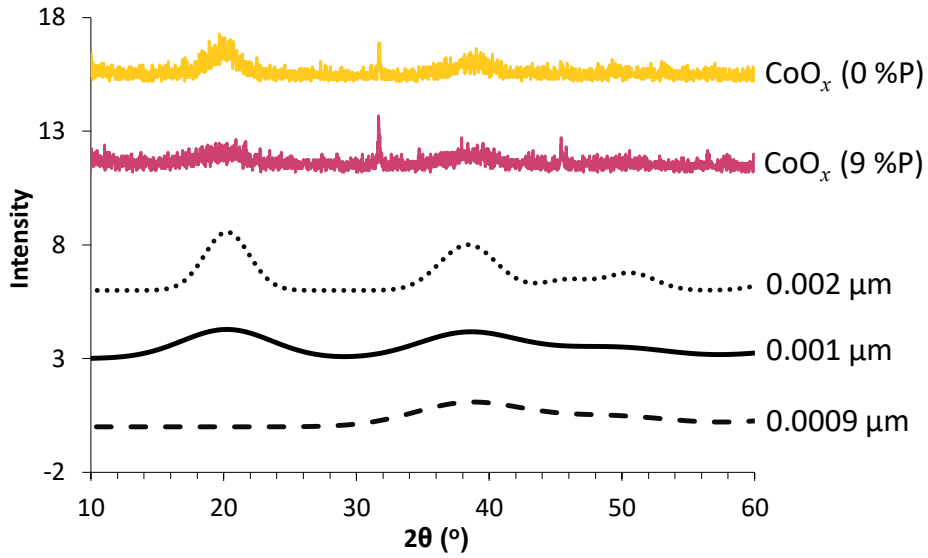

Figure 2.2: XRD simulations of single crystal heterogenite. Data was collected on: CoO_x (0 %P) (*yellow*), CoO_x (9 %P) (*pink*), simulated heterogenite cluster size 2 nm (*black dotted*), simulated heterogenite cluster size 1 nm (*black solid*), simulated heterogenite cluster size 0.9 nm (*black dashed*).

2.3.1.3 TEM

Figure 2.3 presents the TEM images collected on the CoO_x (*x* %P) series. The TEM images indicate that polycrystalline CoO_x (0 %P) (**Figure 2.3 i**) was transitioned into an amorphous material containing nanocrystalline regions at 1 %P and 3 %P phosphate doping (**Figure 2.3 ii** and **iii**), and was further transitioned into a completely amorphous material at 9 %P phosphate doping (**Figure 2.3 iv**). That is, the number of crystalline regions decreased as a function of increased phosphate doping, and that there was a systematic increase in nanoscale disorder with increased phosphate doping. The average crystallite cluster size for CoO_x (0 %P), CoO_x (1 %P) and CoO_x (3 %P) was estimated to be 3-4 nm, 2 nm and 2 nm, respectively.

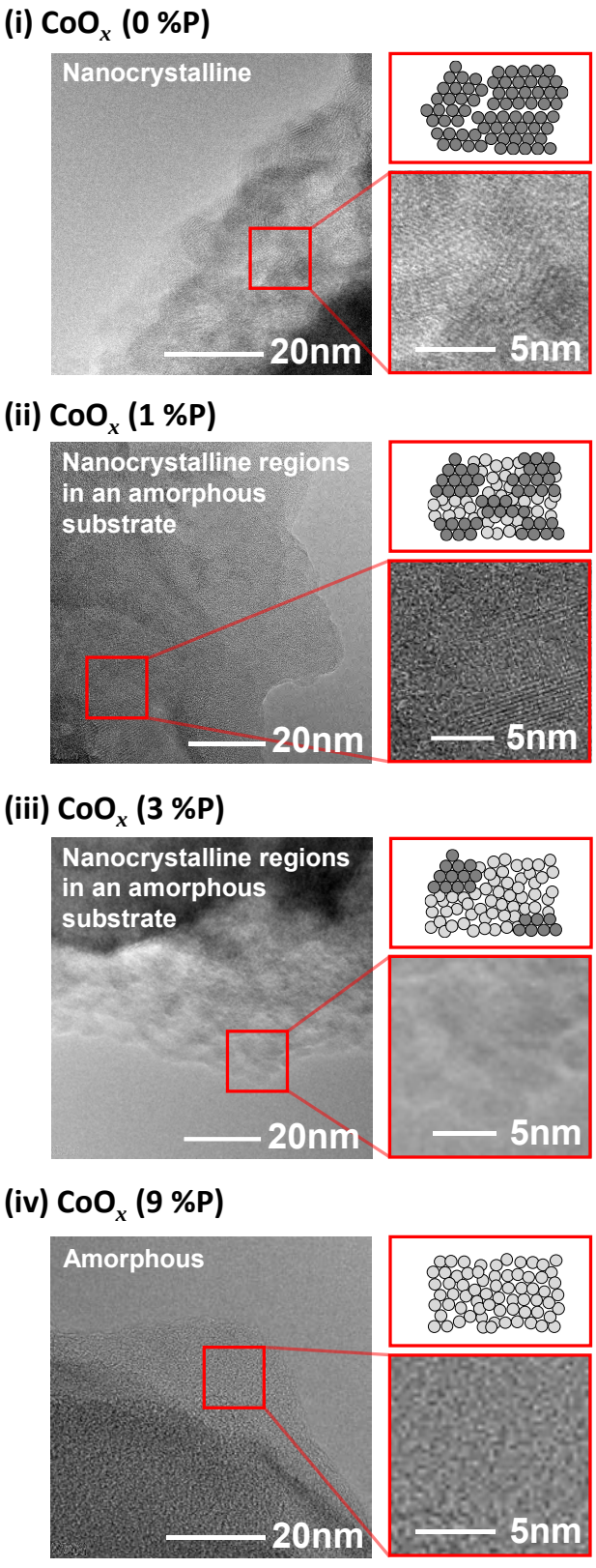

Figure 2.3: TEM images of the CoO_x (*x* %P) series. Data is presented as: **(i)** CoO_x (0 %P), **(ii)** CoO_x (1 %P), **(iii)** CoO_x (3 %P), and **(iv)** CoO_x (9 %P). CoO_x (0 %P) is described as nano/polycrystalline, CoO_x (9%P) is described as amorphous, and CoO_x (1 %P) and CoO_x (3 %P) are described as having nanocrystalline regions in an amorphous substrate.

2.3.1.4 XAS

Figure 2.4 presents the transmission mode cobalt (Co) K-edge XAS data collected on the CoO_x (*x* %P) series and bulk heterogenite (a Co^{3+} reference). **Figure 2.5** presents the fluorescence mode Co K-edge XAS data collected on CoO_x (0 %P), CoO_x (9 %P), Co-Pi and multiple cobalt oxide reference samples (CoO is a Co^{2+} reference, Co_3O_4 is a $Co^{2+/3+}$ reference, CoOOH is a Co^{3+} reference, and $LiCoO_2$ is a Co^{3+} reference).

The X-ray absorption near edge structure (XANES) and EXAFS regions for CoO_x (9 %P) and Co-Pi (containing approximately 7.7 %P)[15] (**Figure 2.5**) are nearly indistinguishable; both as collected herein and as reported elsewhere[15-16, 24, 30, 66]. This is consistent with CoO_x (9 %P) and Co-Pi being electronically and structurally similar, and indicates that CoO_x (9 %P) may be a good structural and functional mimic of Co-Pi.

The XANES features (*i.e.* edge shape, edge position and pre-edge peak) of the CoO_x (*x* %P) series are broadly consistent with heterogenite, **Figure 2.5a**.[52, 67] This provides evidence for the cobalt oxide samples having an average +3 cobalt oxidation state (determined from the edge position) and a near-octahedral coordination geometry that is bound to six oxo- ligands (determined from the pre-edge region).[30,24, 66] The Co(III) centres have a low spin electronic configuration[22, 24, 68], as evidenced by the pre-edge having only one peak corresponding to the 1s → e_g (3d orbital) transition to the ^2E final state.[24, 69] There are no inflections or differences in the XANES that may indicate contamination with a secondary phase (*e.g.* a small loading of $Co_3(PO_4)_2$ in the CoO_x (9 %P) sample).

The EXAFS of the CoO_x (*x* %P) materials are very similar to the EXAFS of heterogenite (**Figure 2.5c**), which indicates that the CoO_x (*x* %P) materials have a very similar intralayer structure to heterogenite. In theory, EXAFS analysis could further be used to locate the doped phosphate within the CoO_x (*x* %P) materials. If the doped phosphate anion ($H_xPO_4^{3-x}$) was bound to the cobalt oxide intralayer either through cobalt as a Co-(O-PO_3) bond or through oxygen as a Co-O-(O-PO_3) bond (*i.e.* 'phosphate-intralayer' bonds), then this bonding interaction would appear as an additional peak/s in the EXAFS Fourier transform data that would increase systematically with increased phosphate doping. The Fourier transform data of the CoO_x (*x* %P) series (**Figure 2.5d**) provides no evidence for phosphate-intralayer bonds, and the omission of these interactions at 9 % phosphate doping and k = 15 transmission EXAFS suggests that there is no direct phosphate-intralayer bond.

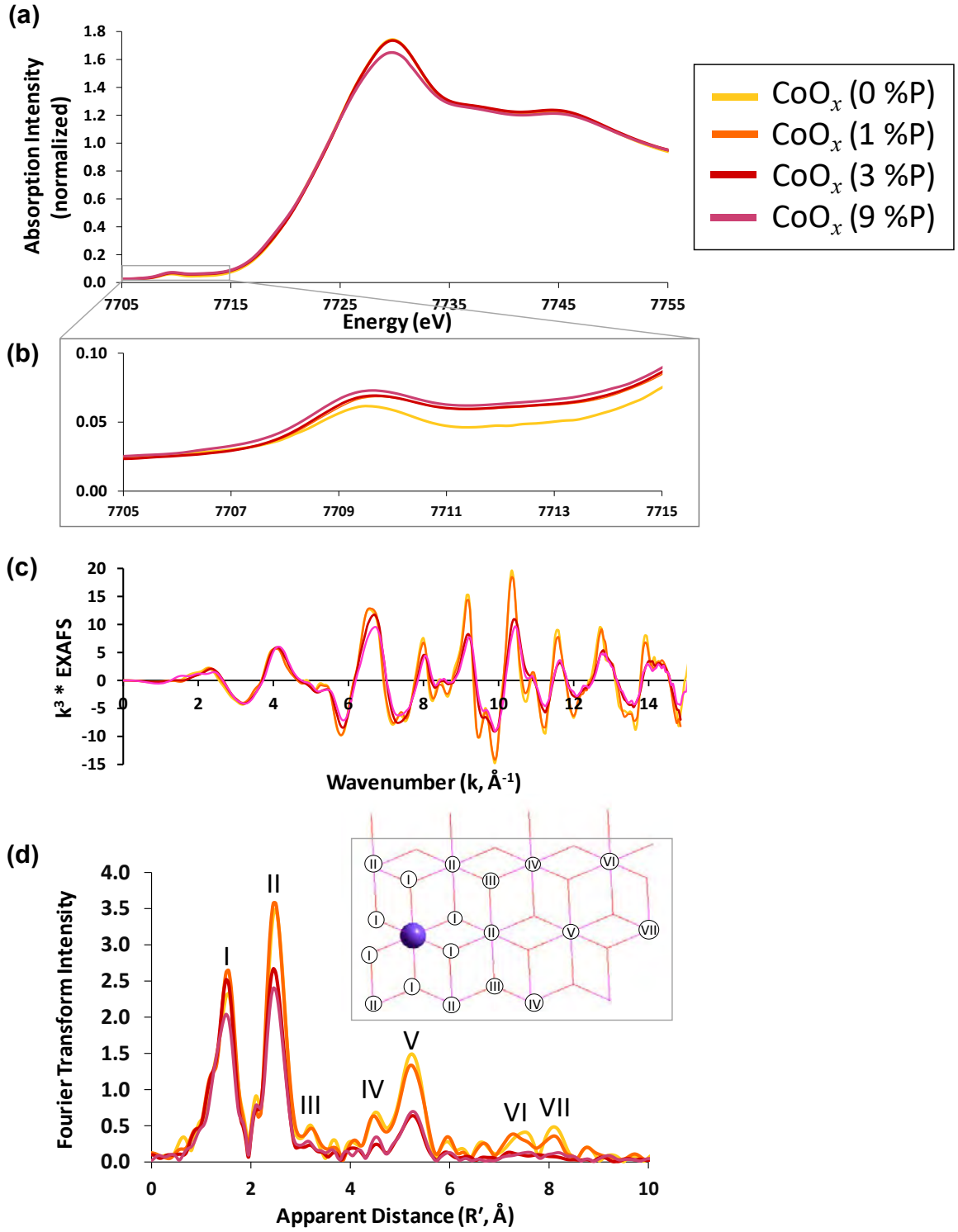

Figure 2.4: Co K-edge XAS spectra collected on the CoO_x (*x* %P) series in transmission mode. Data is presented as: **(a)** XANES, **(b)** pre-edge, **(c)** k^3-weighted EXAFS and **(d)** Fourier transform of the EXAFS (k = 2 to 15). Data was collected on: CoO_x (0 %P) (*yellow*), CoO_x (1 %P) (*orange*), CoO_x (3%P) (*red*), CoO_x (9 %P) (*pink*).

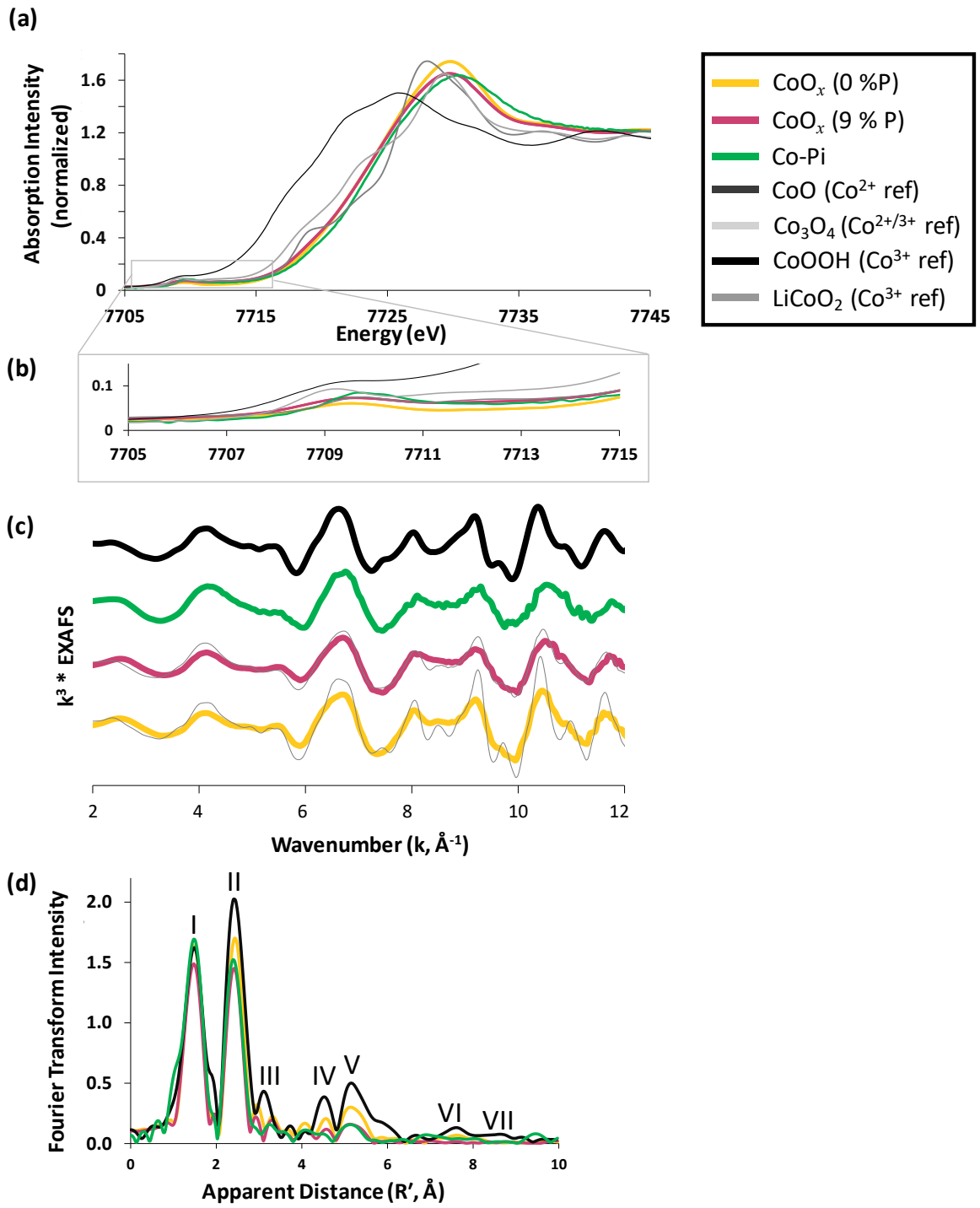

Figure 2.5: Co K-edge XAS spectra collected on CoO_x (9 %P), Co-Pi, and cobalt oxide reference samples in fluorescence mode. Data is presented as: **(a)** XANES, **(b)** pre-edge, **(c)** k^3-weighted EXAFS with transmission mode EXAFS data superposed in *grey*, and **(d)** Fourier transform of the EXAFS (k = 2 to 12). The data was collected on: CoO_x (0 %P) (*yellow*), CoO_x (9 %P) (*pink*), Co-Pi (*green*), CoO (Co^{2+} reference, *dark grey*), Co_3O_4 ($Co^{2+/3+}$ reference, *light grey*), CoOOH (Co^{3+} reference, *black*), $LiCoO_2$ (Co^{3+} reference, *medium grey*).

Phosphorus (P) K-edge soft XAS data (**Figure 2.6**) was subsequently collected on an analogous phosphate doped series (containing 0.2, 2 and 5 %P) to determine whether the phosphate-intralayer bonds could be identified through the P edge. Evidence of phosphate-intralayer bonds would appear as a small (low intensity) peak between 2148 and 2150 eV as indicated by the *red* box in **Figure 2.6**.[70-71] The CoO_x (*x* %P) samples do not have this characteristic pre-edge peak (**Figure 2.6**). Therefore, both the soft XAS and hard XAS data suggest that there is no direct phosphate-intralayer bond, and that the doped phosphate may be located in the interlayer (or equivalent) of the CoO_x (*x* %P) materials.

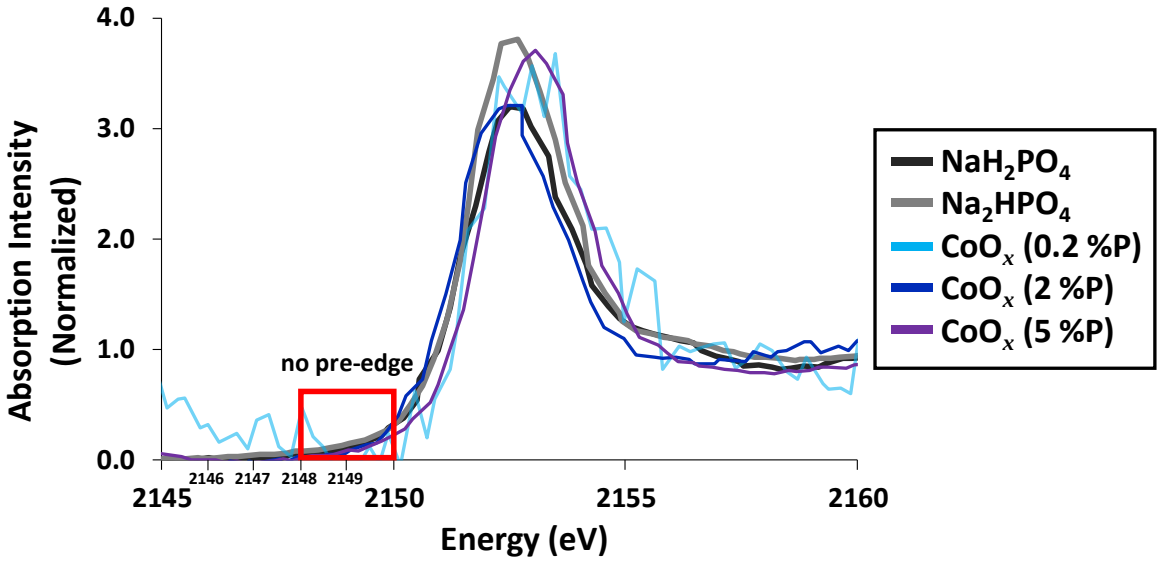

Figure 2.6: P K-edge soft XAS spectra collected on an analogous CoO_x (*x* %P) series. Data was collected on: CoO_x (0.2 %P) (*light blue*), CoO_x (2 %P) (*dark blue*), CoO_x (5 %P) (*purple*), NaH_2PO_4 (*black*), and Na_2HPO_4 (*grey*). Note that the data has not been calibrated in absolute energy.

EXAFS analysis was further used to characterise the structural order within the intralayer of the CoO_x (*x* %P) materials. From the transmission data given in **Figure 2.4d**, it is seen that the high range Fourier transform peaks IV through VII, which are associated with longer range structural order, show a substantial systematic dampening in their intensity as phosphate doping is increased. This EXAFS dampening is also seen to a lesser extent in the fluorescence Fourier transform data in **Figure 2.5d**. Before the cause of this EXAFS dampening can be evaluated, it is important to discuss why the transmission and fluorescence data varies and to determine which data set should be used to evaluate the EXAFS dampening phenomenon. This discussion is presented below.

A comparison between the Fourier transform transmission and fluorescence data in **Figures 2.4d** and **2.5d**, respectively, shows that the high R′ range peaks VI and VII are overall less intense in the fluorescence data than in the transmission data. This intensity difference illustrates that meaningfully different spectra can be generated from the same sample using different detector modes, and consequently indicates that the fluorescence data is dampened due to effects beyond the sample structure.

The intensity difference between the transmission and fluorescence detector modes in **Figures 2.4d** and **2.5d** can be understood by examining how the Fourier transform deconvolutes the EXAFS into its constituent frequencies. In simple terms; higher frequency EXAFS vectors in k-space are associated with longer R′-space distances in the Fourier transform. This is clear from **Figure 2.7** where each of the EXAFS vectors used in the EXAFS fit of CoO_x (3 %P) are correlated with Fourier transform peaks. As such, the dampening of high range Fourier transform peaks in R′-space is associated with higher frequency EXAFS dampening in k-space. Higher frequency k-space EXAFS contributions are more susceptible to not only structural interferences (*e.g.* disorder or molecular sized clusters[15-16, 24, 30, 66]) but also to experimental variables (*e.g.* sample concentration, a small vibration from a monochromator, and sample inhomogeneity).[73]

For the XAS data collected herein, it is likely that the high R′ range fluorescence peaks are less intense than the associated transmission peaks because 'self-absorption' within the sample attenuated the high k-range oscillations and dampened the high k-range EXAFS signal. Self-absorption is a well-understood phenomenon in fluorescence EXAFS and involves the emitted fluorescent X-rays being reabsorbed by the material before they can be measured by the fluorescence detector. The phenomenon relates to the point at which the proportionality between the fluorescence signal and transmission fails.[72] This usually occurs as a function of the material, where a sample may be too thick or have a high-Z matrix (*e.g.* a soil sample). Due to the difficulty in deconvoluting the dampening effects of self-absorption and structural disorder, the EXAFS analysis herein utilised the transmission EXAFS data and not the fluorescence data.

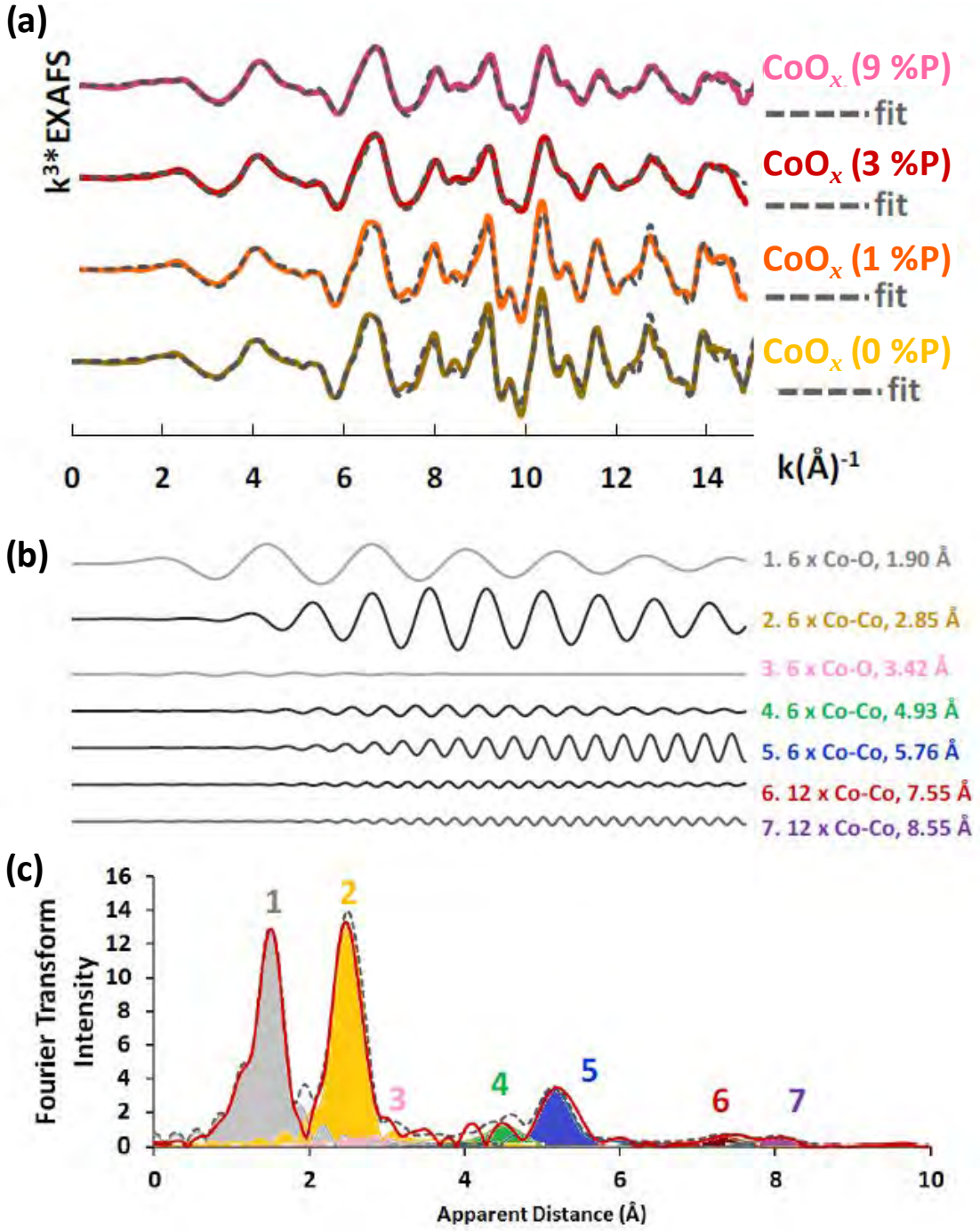

Figure 2.7: Graphical representation of the 7 parameter EXAFS fit for the CoO_x (*x* %P) series. Data is presented as: **(a)** each fit overlaying the original k^3-weighted EXAFS, **(b)** deconvoluted EXAFS frequencies used in the CoO_x (3 %P) fit, **(c)** Fourier transform of each frequency used in the CoO_x (3 %P) fit, with the original Fourier transform data in *black dashed*. The trace colours in **(a)** represent: CoO_x (0 %P) (*yellow*), CoO_x (1 %P) (*orange*), CoO_x (3 %P) (*red*), CoO_x (9 %P) (*pink*), and fit (*black dashed*). The trace colours in **(b)** correlate with the colours used in **(c)**.

The dampening of the high range Fourier transform peaks IV through VII (**Figure 2.4d**) generally suggests that the Co-Pi and CoO_x (*x* %P) materials lack long range order. Although this dampening effect has been attributed to the presence of molecular sized CoO_x clusters by the Nocera and Dau research groups (*viz.* in their XAS characterisation of Co-Pi),[24,30] this dampening effect could equally be explained by structural disorder. The following specifically evaluates the effects structural disorder has on the EXAFS.

To better understand the general differences in structural order across the phosphate doped series, the transmission mode EXAFS data was analysed in two ways: (i) EXAFS fitting, and (ii) comparing the k-space EXAFS to the back-calculated q-space EXAFS. In the first method; each data set was fit with the same set of 7 parameters (chosen to best represent the data) that approximately correlate with each of the 7 peaks shown in **Figure 2.4d**. In these fits, the co-ordination number (N) of each vector was fixed, and the distance and Debye-Waller factors were floated. The Debye-Waller factor and the co-ordination number are two highly correlated parameters; where the Debye-Waller factor acts to decrease EXAFS intensity through disorder, and the co-ordination number acts to decrease EXAFS intensity through a change in metal co-ordination number. As such, it is often difficult to distinguish the effects of co-ordination number from the effects of disorder owing to higher frequency vectors being more susceptible to subtle structural changes caused by interference (**Figure 2.7**).

The details of the EXAFS fits are presented in **Table 2.2** and a graphical representation of the fit for CoO_x (3 %P) is presented in **Figure 2.7**. From **Table 2.2** it is observed that the Debye-Waller and S_0^2 values increase proportionally with phosphate doping when N is fixed, and thereby suggest that structural disorder is systematically increasing with phosphate doping. Herein, it is suggested that this increase in structural disorder is due primarily to bond-length disorder. This effect is evaluated below.

Bond-length disorder occurs when there is a small variation in the bond-length of a single contribution.[74] This effect is demonstrated in **Figure 2.8** for the 2.85 and 5.76 Å Co-Co vectors used in the CoO_x (*x* %P) fits. **Figure 2.8** compares the effects of splitting the shorter 2.85 Å Co-Co vector (**Figure 2.8a**) and the longer 5.76 Å Co-Co vector (**Figure 2.8c**, *black dashed*) by 0.05 Å, as well as the longer 5.76 Å Co-Co vector (**Figure 2.8b**) by 0.1 Å.

Table 2.2: Summary of the parameters for the EXAFS fit of the transmission data.

Heterogenite[52] Shell	**Scatterer distance (Å), Debye-Waller (Å^2)**			
N, Bond, Scatterer distance	**CoO_x (0 %P)**	**CoO_x (1 %P)**	**CoO_x (3 %P)**	**CoO_x (9 %P)**
6, Co-O, 1.89 Å	1.90, (0.0026)	1.90, (0.0021)	1.90, (0.0025)	1.88, (0.0031)
6, Co-Co, 2.85 Å	2.85, (0.0028)	2.85, (0.0025)	2.85, (0.0043)	2.83, (0.0052)
6, Co-O, 3.42 Å	3.64, (0.028)	3.51, (0.016)	3.56, (0.0184)	3.44, (0.019)
6, Co-Co, 4.93 Å	4.96, (0.004)	4.96, (0.004)	4.94, (0.0094)	4.87, (0.014)
6, Co-Co, 5.76 Å	5.55, (-0.00064)ł	5.55, (-0.00062)ł	5.54, (0.0024)	5.51, (0.003)
12, Co-Co, 7.55 Å	7.53, (0.0048)	7.54, (0.0047)	7.82, (0.0171)	7.50, (0.016)
6, Co-Co, 8.55 Å	8.51, (0.0012)	8.51, (0.0018)	8.51, (0.0086)	8.46, (0.0066)
S_0^2, ΔE_0	0.607, -4.308	0.607, -4.308	0.607, -4.308	0.609, -4.308
χ^2	858	1313	1828	1157
R-factor	0.053	0.056	0.028	0.042
ΔR	0.00082	0.00023	0.00019	0.00048
Δk	0.00028	0.00068	0.00050	0.00016

ł A negative Debye-Waller factor is not considered reasonable. However, negatives have been permitted as this is a comparative fit, not independent fits. The negative value implies an additional contribution is needed in that frequency range to adequately describe the data.

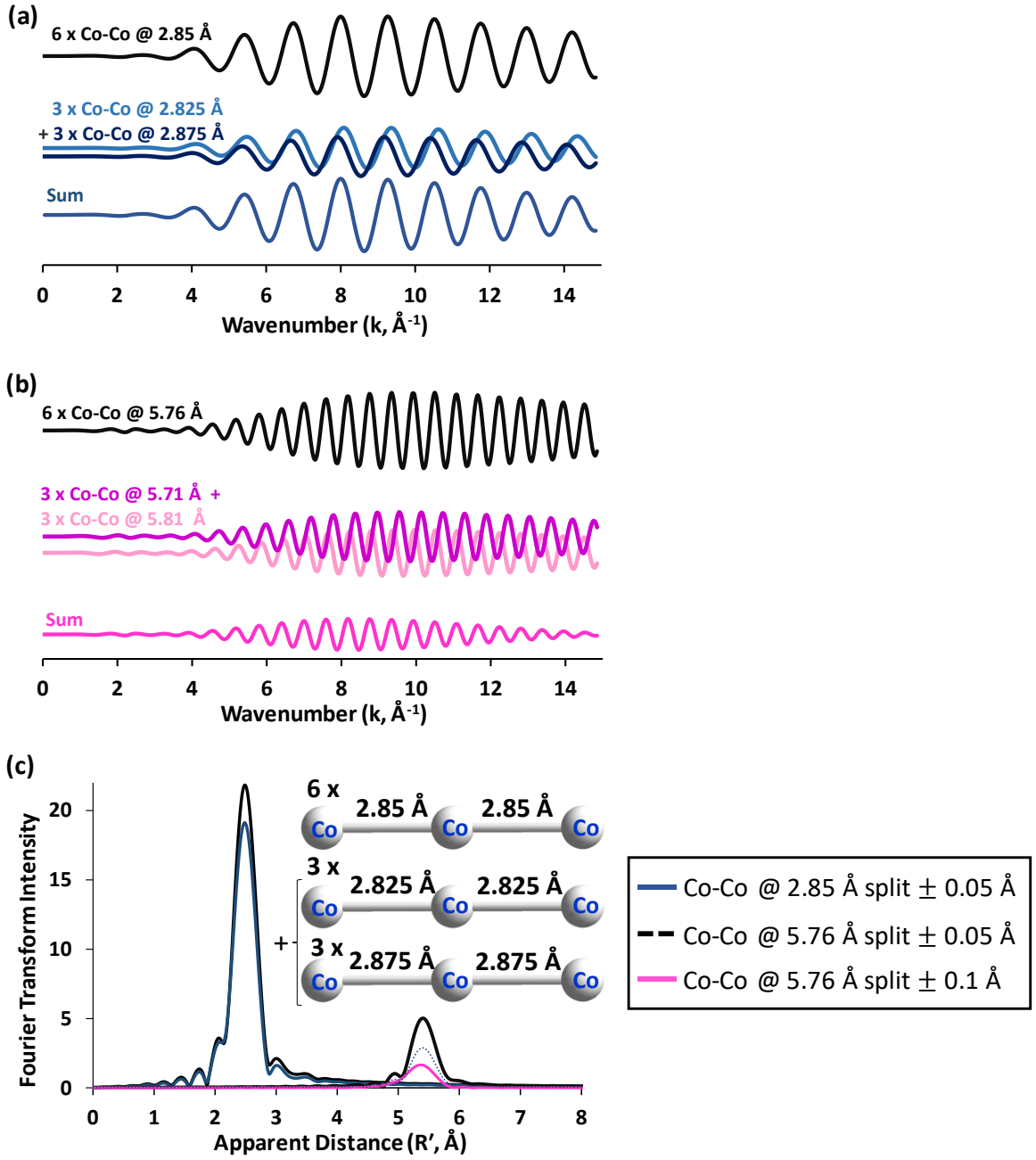

Figure 2.8: EXAFS simulations illustrating the effects of bond-length disorder on the EXAFS intensity. Data is presented as: **(a)** Co-Co vector at 2.85 Å split 50/50 by 0.05 Å (*medium blue*), **(b)** Co-Co vector at 5.76 Å split 50/50 by 0.1 Å (*medium pink*), **(c)** the Fourier transform of the EXAFS from ordered bond-lengths (*black*) and disordered bond-lengths (**a** = *medium blue*, and **b** = *medium pink*), with the additional 0.05 Å splitting of the 5.76 Å Co-Co vector (*black dashed*). The inset in **(c)** shows a graphical representation of the Co-Co vector at 2.85 Å split 50/50 by 0.05 Å.

Figure 2.8 demonstrates that bond-length disorder reduces the overall intensity of the EXAFS by offsetting the phase of the sinusoidal EXAFS wave rather than affecting the frequency of the wave. This reduction in EXAFS intensity is transferred to the peak intensity in the Fourier transform domain (**Figure 2.8c**). The effects of disorder were more pronounced in the longer higher frequency Co-Co vector (5.76 Å, 0.1 Å split), where more than 75% of the EXAFS intensity was lost (**Figure 2.8b** and **c**). When the splitting was reduced to 0.05 Å (**Figure 2.7c**, *black dashed*), approximately 50% of the intensity was lost in the Fourier transform peak (R′ = 5.4 Å). However, the equivalent splitting in the shorter Co-Co vector (2.85 Å, 0.05 Å split) only resulted in a 10% reduction in the Fourier transform peak (R′ = 2.5 Å). Therefore, the EXAFS of the longer, higher frequency vectors were more sensitive to slight changes in order and were thus more likely to show the effects of disorder.

In the second method of EXAFS analysis, the k-space EXAFS were compared to the back-calculated q-space EXAFS for CoO_x (0 %P) and CoO_x (3 %P) (**Figure 2.9**). In **Figure 2.9**, the CoO_x (0 %P) sample required the full R′ = 1 to 9 Å Fourier transform region to be back-calculated for the q-space EXAFS to closely match the k-space EXAFS. However, the CoO_x (3 %P) sample only required the Fourier transform to be back-calculated from R′ = 1 to 6 Å for the q- and k-space EXAFS to match. This provides further evidence for the link between dampening and disorder by showing that CoO_x (3 %P) can be sufficiently described without a higher frequency Fourier transform component. That is, dampening at high R′ range makes spectral information beyond R′ = 6 superfluous to describing CoO_x (3 %P).

Either molecular sized CoO_x clusters[24,30] or bond-length structural disorder could be the cause of the high range Fourier transform peak dampening observed in the phosphate doped materials (including Co-Pi). However, the CoO_x (*x* %P) series demonstrated that the EXAFS intensity systematically decreased as the level of phosphate doping was systematically increased, which suggests that bond-length structural disorder may better explain the observed systematic changes in the spectra. The increase in structural disorder with increased phosphate doping is also more consistent with the TEM images collected on the CoO_x (*x* %P) samples, which indicated the growth of an amorphous material rather than the presence of molecular level clusters.

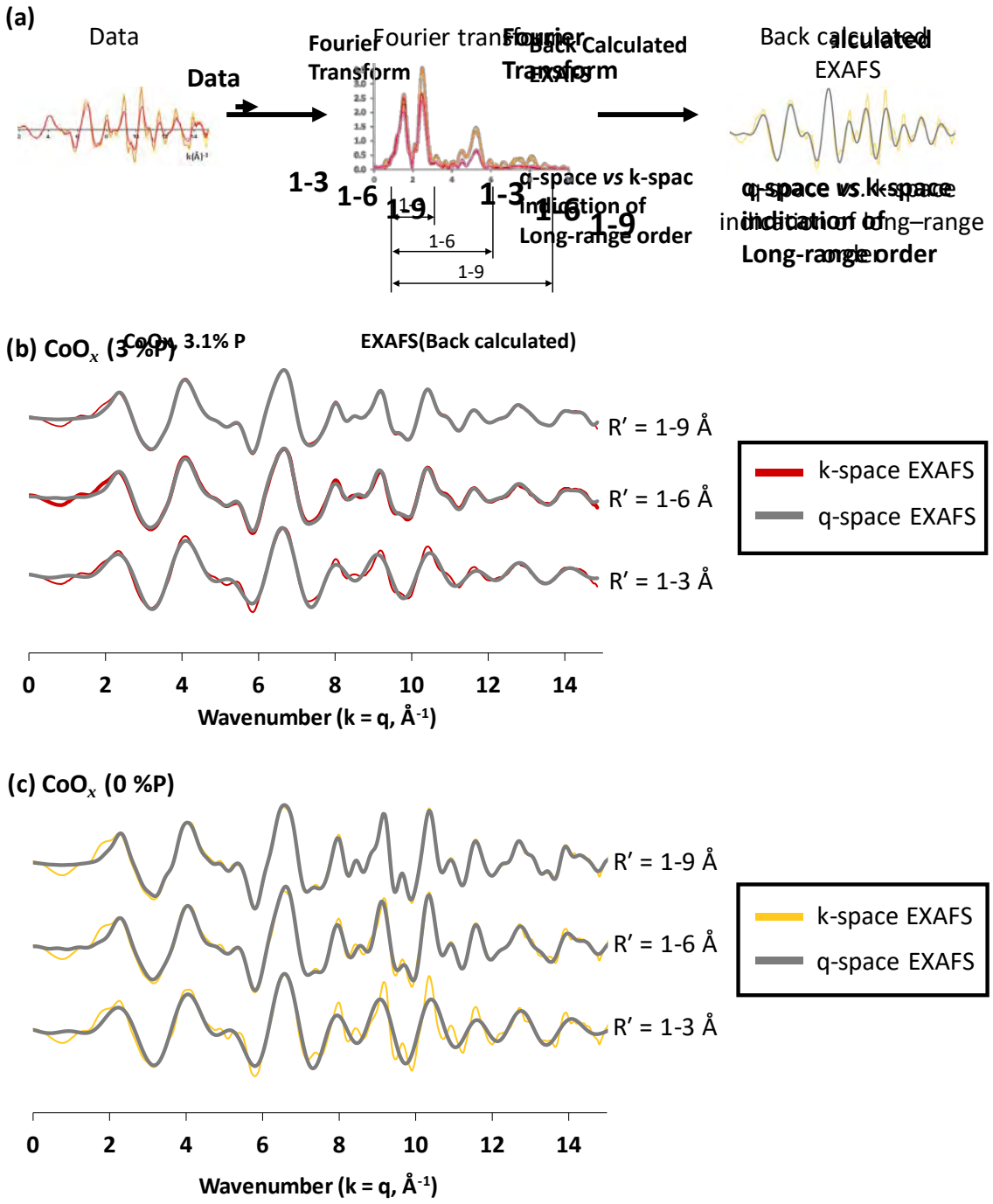

Figure 2.9: Analysis of the EXAFS by back transformation of the Fourier transform data**.** Data is presented as: **(a)** a scheme of the back-calculation process, **(b)** the original k-space EXAFS (*red*) overlayed with the back-calculated q-space EXAFS (*grey*) for CoO_x (3% P), **(c)** the original k-space EXAFS (*yellow*) overlayed with the back-calculated q-space EXAFS (*grey*) for CoO_x (0% P). In **(b)** and **(c)**, the R' regions for which the transforms were taken are indicated to the right of the trace.

2.3.1.5 FTIR

FTIR spectroscopy was used in combination with Co K-edge XAS and P K-edge XAS to attempt to locate phosphate in the cobalt oxide structure. Although the CoO_x (*x* %P) samples contain the characteristic Co-O stretches in the *ca.* 600 to 700 band, the multiple phosphate peaks in the *ca.* 800 to 1200 cm^{-1} band are not clearly identifiable in the CoO_x (*x* %P) samples (**Figure 2.10**). However, the general increase in absorption intensity in the phosphate band as a function of phosphate doping does suggest that phosphate is present in the samples despite no confirmation of phosphate-intralayer bonding.

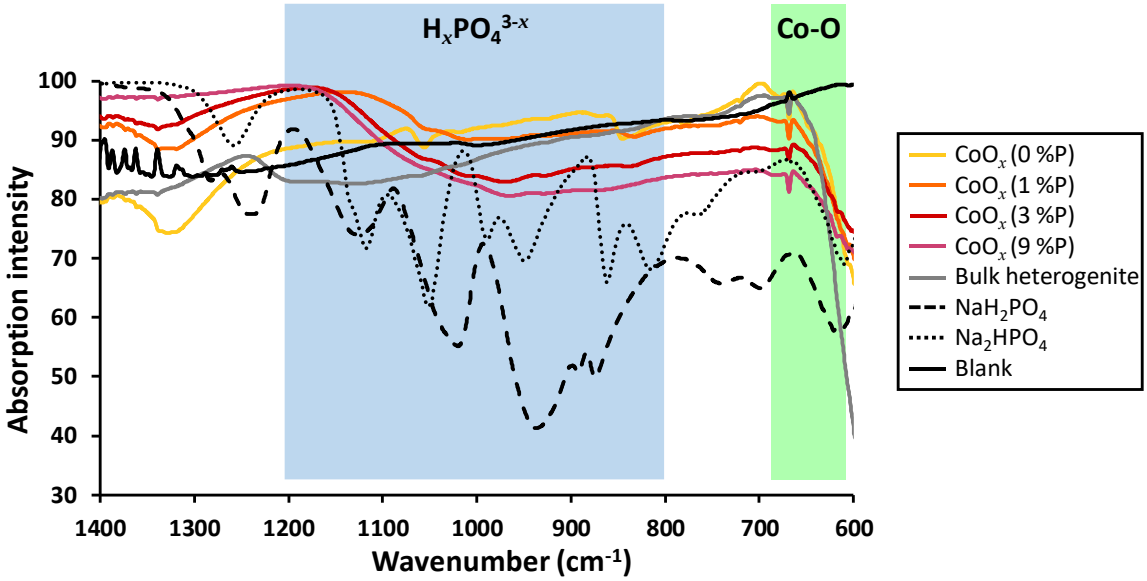

Figure 2.10: FTIR data collected on the CoO_x (*x* %P) series. Data was collected on: CoO_x (0 %P) (*yellow*), CoO_x (1 %P) (*orange*), CoO_x (3 %P) (*red*), CoO_x (9 %P) (*pink*), bulk heterogenite (*grey*), blank (*black*), NaH_2PO_4 (*black dotted*), and Na_2HPO_4 (*black dashed*).

2.3.1.6 SEM

The SEM images of the oven dried CoO_x (0 %P) and CoO_x (9 %P) samples are presented in **Figure 2.11**. The images show irregular shaped larger particles surrounded by finer material. The average large particle size in CoO_x (0 %P) was approximately 50 μm and was approximately 5 μm in the CoO_x (9 %P) sample.

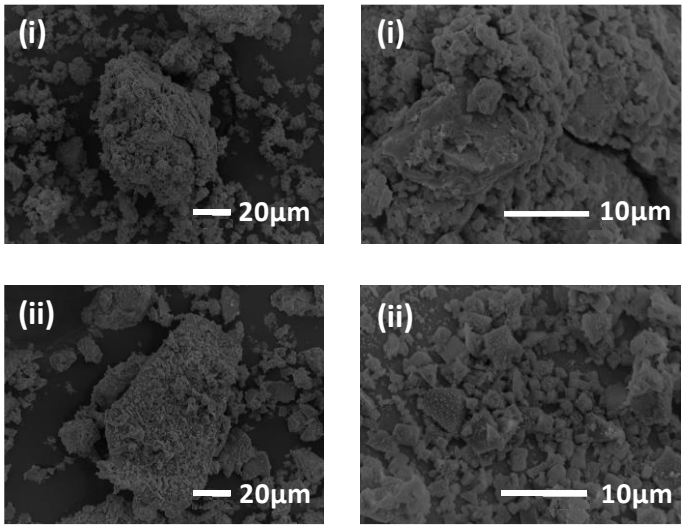

Figure 2.11: SEM images collected on CoO_x (0 %P) and CoO_x (9 %P) at 2 magnification levels. Data is presented as: **(i)** CoO_x (0 %P) and **(ii)** CoO_x (9 %P).

2.3.1.7 BET

Figure 2.12 presents the specific surface areas of the CoO_x (*x* %P) materials as determined using multipoint BET.[59] It is illustrated in **Figure 2.12** that the surface area systematically decreases as a function of phosphate doping. This is a strong indication that the phosphate dopant plays a role in blocking accessibility to interstitial pores, and thereby limits the total surface area. This assessment is consistent with the phosphate ion being located in the interlayer.[75-77]

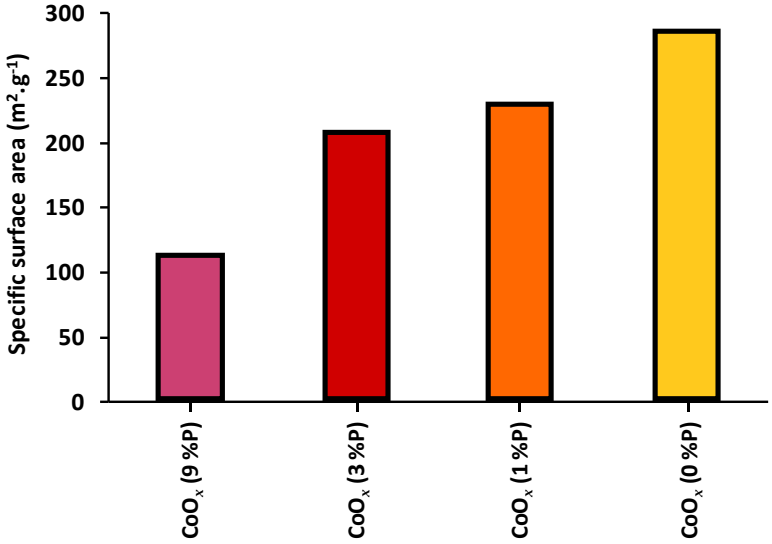

Figure 2.12: BET surface area measurements for the CoO_x (*x* %P) series. Data was collected on: CoO_x (0 %P) (*yellow*), CoO_x (1 %P) (*orange*), CoO_x (3 %P) (*red*), and CoO_x (9 %P) (*pink*).

2.3.2 Water oxidation catalysis

The catalytic activity of the CoO_x (*x* %P) series was characterised using electrochemical methods and gas evolution experiments using hypochlorite as a sacrificial oxidant. As the cobalt oxide materials were synthesised *ex situ* (*i.e.* off an electrode surface), the materials were adhered to FTO/glass substrates (**§ 2.2.11**) for electrochemical analyses.

2.3.2.1 Characterisation of the screen-printed CoO_x materials

While screen-printing is highly beneficial for uniformly adhering a consistent amount of material to an electrode, the process involves mechanically and chemically treating a sample and could thereby change the nature of the sample.[36, 39-40] Selected screen-printed electrodes were examined using TEM to ensure the nanoscale nature of the CoO_x (*x* %P) series was maintained through the screen-printing process. **Figure 2.13** presents the TEM images of CoO_x (0 %P), CoO_x (1 %P) and CoO_x (9 %P) after being screen-printed onto FTO/glass. TEM confirmed that the samples maintained their structural character through the screen-printing process.

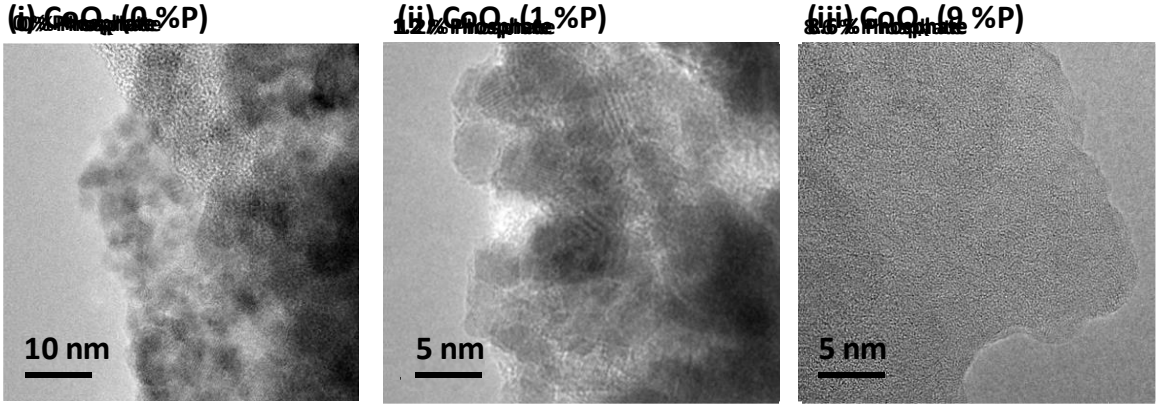

Figure 2.13: TEM images collected on CoO_x (0 %P), CoO_x (1 %P), and CoO_x (9 %P) after screen-printing. Data is presented as: **(i)** CoO_x (0 %P), **(ii)** CoO_x (1 %P), and **(iii)** CoO_x (9 %P).

To ensure the materials were uniformly adhered to the electrode surface, the screen-printed electrodes were examined using SEM and ICP-MS. **Figure 2.14** presents the SEM images of CoO_x (0 %P) and CoO_x (1 %P) after being screen-printed onto FTO/glass. **Table 2.3** presents the average mass of cobalt adhered to a single electrode as measured by ICP-MS analysis. Both the SEM images and ICP-MS results confirmed that the materials were uniformly adhered to the electrode surface.

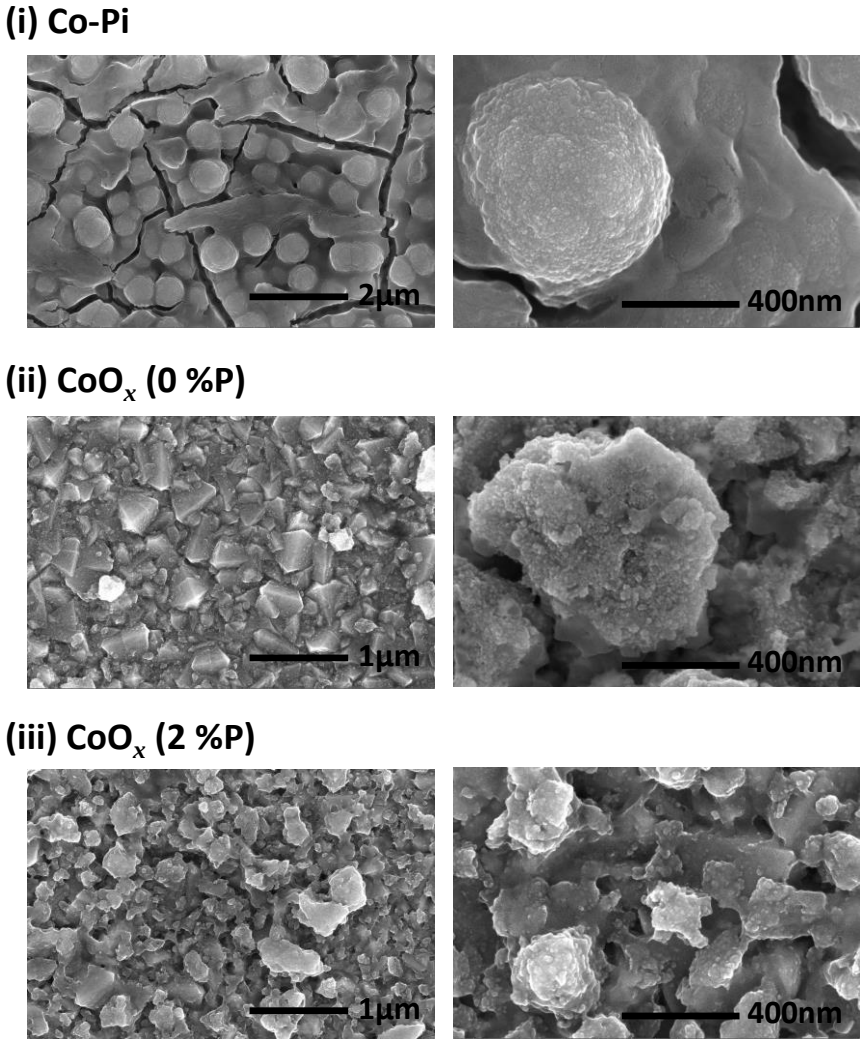

Figure 2.14: SEM images collected on selected cobalt oxide materials after screen-printing at 2 magnification levels. Data is presented as: **(i)** Co-Pi, **(ii)** CoO_x (0 %P) and **(iii)** CoO_x (2 %P).

Table 2.3: The average mass of cobalt adhered to a single FTO/glass electrode.

Sample	**Mass ± σ (µg)**
CoO_x (9 %P)	3.8 ± 0.08
CoO_x (3 %P)	2.0 ± 0.02
CoO_x (1 %P)	3.5 ± 0.04
CoO_x (0 %P)	3.7 ± 0.03

2.3.2.2 Electrochemical analysis of the screen-printed CoO_x materials

The screen-printed cobalt oxide materials were analysed by the electrochemical methods of CV and Tafel analysis. **Figure 2.15** presents the CV analysis of the CoO_x (*x* %P) series conducted in phosphate buffer (0.1 M, pH 7) between 0.2 and 1.4 V (*vs* Ag|AgCl). All members of the CoO_x (*x* %P) series acted as efficient water oxidation catalysts, with the maximum current density of each catalytic wave significantly exceeding the negligible current from the blank electrode (**Figure 2.15**). The most active materials were CoO_x (0 %P) and CoO_x (1 %P), which achieved the same (within experimental error, **Figure 2.16**) maximum current density of approximately 9.2 mA cm^{-2}. The CoO_x (3 %P) sample was the next most active catalyst, followed by CoO_x (9 %P). Therefore, catalytic activity decreased as phosphate doping increased.

The longevity of the CoO_x (0 %P) catalyst was analysed by cycling the material for 50 cycles (in 0.1 M, pH 7 phosphate buffer) (**Figure 2.17**). **Figure 2.17** shows a successive decrease in current, which was likely associated with the loss of CoO_x (0 %P) material from the electrode surface.

The catalytic efficiencies of the CoO_x materials was compared with Co-Pi by evaluating the activity per square cm of catalyst material (mA cm^{-2} at 1.4 V *vs.* normal hydrogen electrode (NHE)). The current densities of the screen-printed electrodes fell between 3.1 and 4.3 mA cm^{-2} at 1.4 V *vs.* NHE, and Co-Pi had a current density measure of 5.3 mA cm^{-2} at 1.4 V *vs.* NHE (using 0.07 cm^{-2} glassy carbon disc). All samples in this comparison were analysed in 0.1 M, pH 7 phosphate buffer, but were examined on different electrode types.

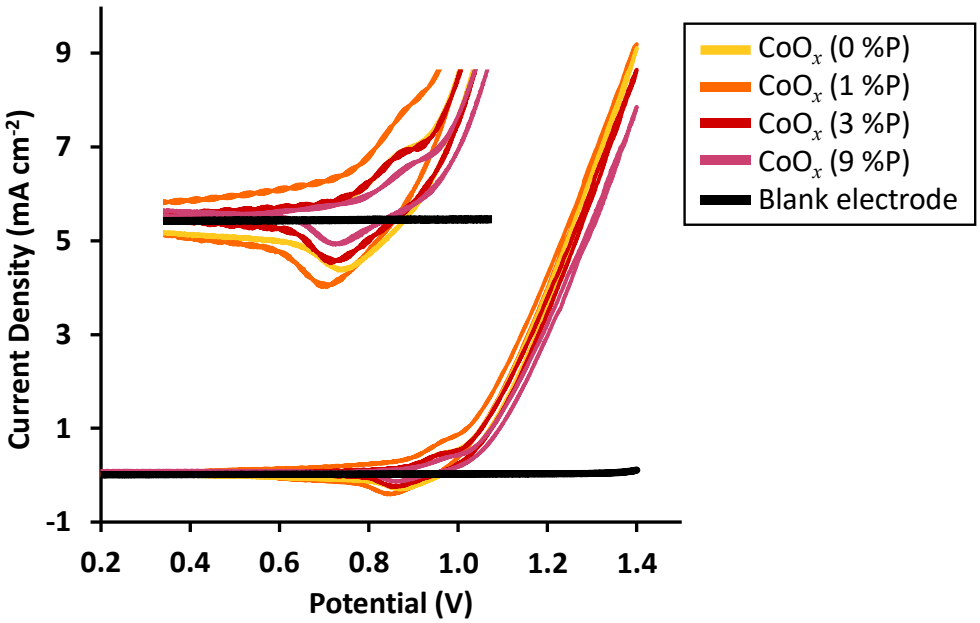

Figure 2.15: Cyclic voltammetry of the CoO_x (*x* %P) series (analysed in 0.1 M, pH 7 phosphate buffer). Inset shows expansion of peak prior to the onset of water oxidation. Data was collected on: CoO_x (0 %P) (*yellow*), CoO_x (1 %P) (*orange*), CoO_x (3 %P) (*red*), CoO_x (9 %P) (*pink*), and blank electrode (*black*). Potential scale *vs.* Ag|AgCl.

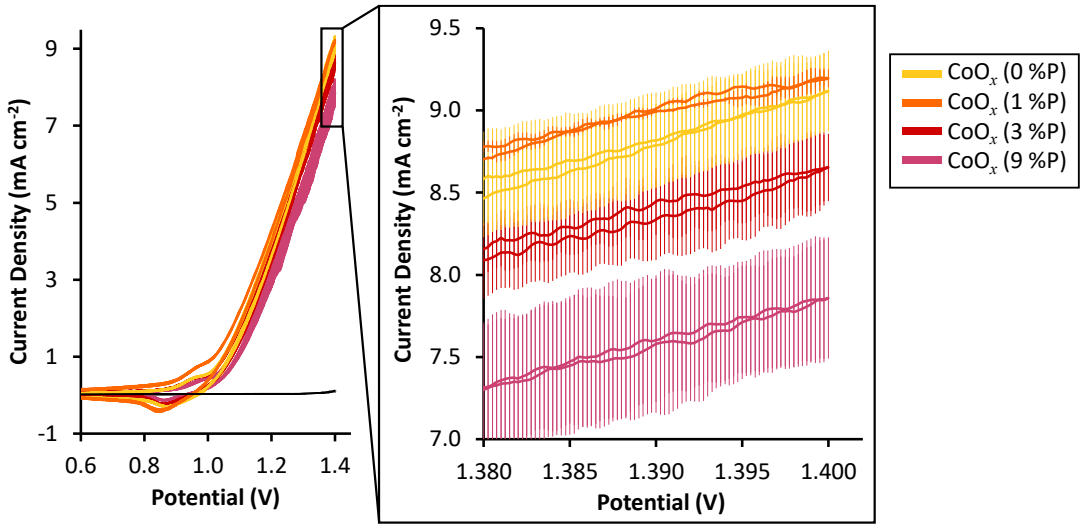

Figure 2.16: Cyclic voltammetry of the CoO_x (*x* %P) series (analysed in 0.1 M, pH 7 phosphate buffer), with 1 standard deviation error shown. Maximum current density achieved by each sample is shown in the expansion. Data was collected on: CoO_x (0 %P) (*yellow*), CoO_x (1 %P) (*orange*), CoO_x (3 %P) (*red*), CoO_x (9 %P) (*pink*), and blank electrode (*black*). Potential scale *vs.* Ag|AgCl.

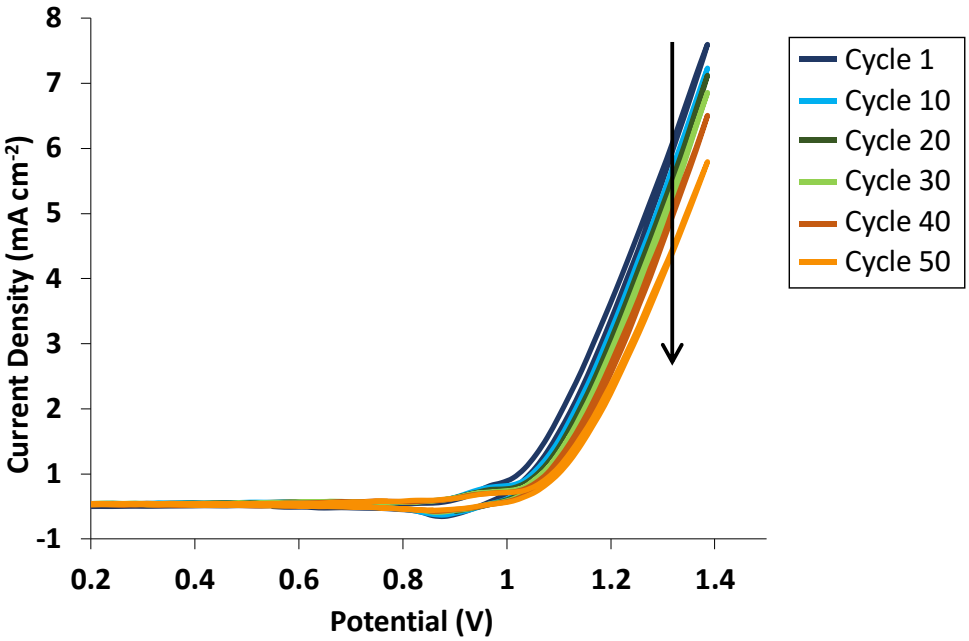

Figure 2.17: Cyclic voltammetry analysis of CoO_x (0 %P) (analysed in 0.1 M, pH 7 phosphate buffer) for 50 cycles. Inset shows expansion of peak prior to the onset of water oxidation. Data is presented as: cycle 1 (*dark blue*), cycle 10 (*light blue*), cycle 20 (*dark green*), cycle 30 (*light green*), cycle 40 (*dark orange*), and cycle 50 (*light orange*). Potential scale *vs.* Ag|AgCl.

The CoO_x materials were also analysed by a series of chronoamperometric, *quasi* steady-state measurements through the potential range of exponentially increasing current. From this data, a Tafel plot was constructed by plotting the overpotential (V) against the current density (mA cm^{-2}) on a logarithmic scale.[14, 60] The Tafel data is independent of the electrode sample loading and is a measure of solely catalytic current (*i.e.* the analysis removes surface confined oxidation processes and capacitive contributions to current).

Figure 2.18 presents the Tafel plot containing the Tafel slopes for the CoO_x (*x* %P) series and bulk heterogenite. The Tafel slopes were calculated over the region of exponentially increasing current (*i.e.* from 980 to 1180 mV with some variation between each material, **Table 2.4**). The Tafel slopes have similar gradients, which suggests that the CoO_x (*x* %P) materials act by a similar water oxidation mechanism. The most active sample is CoO_x (0 %P), followed by CoO_x (1 %P). These samples are significantly more efficient than the higher phosphate doped samples of CoO_x (3 %P) and CoO_x (9 %P). Between these two pairs of samples lies the bulk heterogenite sample.

The Tafel analysis shows a systematic decrease in efficiency with increasing phosphate doping. As the CoO_x (3 %P) and CoO_x (9 %P) samples are the most disorder within the series, the systematic decrease in efficiency also correlates with increasing structural disorder. This suggests that phosphate itself does not contribute to efficiency for water oxidation catalysis.

Table 2.4: The regions over which the Tafel slopes were calculated for the CoO_x (*x* %P) series.

Sample name	Slope (V)	Tafel plot region (V)
CoO_x (9 %P)	0.1522	1.00-1.12
CoO_x (3 %P)	0.1620	1.00-1.12
CoO_x (1 %P)	0.1679	0.98-1.10
CoO_x (0 %P)	0.1822	0.98-1.10
Bulk heterogenite	0.1778	1.00-1.12

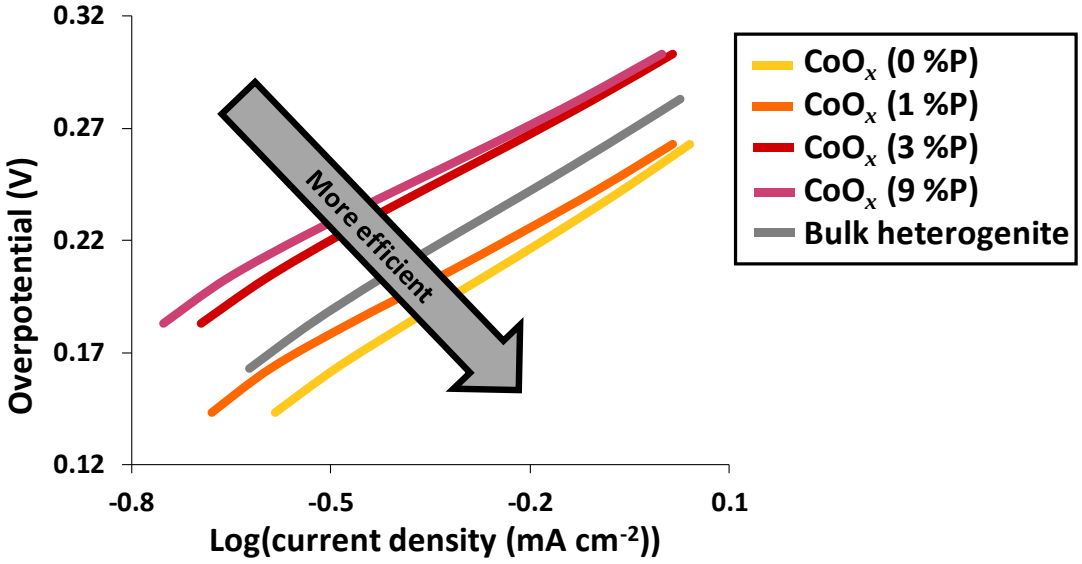

Figure 2.18: Tafel plot containing the Tafel slopes for the CoO_x (*x* %P) series and bulk heterogenite. Data was collected on: CoO_x (0 %P) (*yellow*), CoO_x (1 %P) (*orange*), CoO_x (3 %P) (*red*), CoO_x (9 %P) (*pink*), and bulk heterogenite (*grey*). Overpotential scale *vs* Ag|AgCl.

2.3.2.3 *Ex situ* measurement of water oxidation catalysis by reaction with hypochlorite (ClO^-)

The electrochemical analyses have been complimented with an *ex situ* measure of water oxidation catalysis. In this *ex situ* analysis; the cobalt oxides were reacted with hypochlorite (a sacrificial oxidant) and the resulting O_2 gas evolution was measured. Despite no evidence being found for changes during the screen-printing process, the *ex situ* analysis allows the catalytic activity of the CoO_x materials to be examined as prepared. While tests with sacrificial oxidants can be controversial[61-62], the hypochlorite test provides an important comparison with the electrochemical analyses as the *ex situ* experiment is an independent measurement of water oxidation efficiency (per mol of Co).[61-62, 78]

Figures 2.19 and **2.20** present the results from the *ex situ* water oxidation analysis using hypochlorite as a sacrificial oxidant. In this experiment, the best catalytic materials evolve the most gas. **Figure 2.19** shows that catalytic activity systematically decreased as phosphate doping systematically increased. It is noted that particle size will greatly influence the measured efficiency of each material; with efficiency increasing proportionally with surface area and inversely with particle size. From the BET analysis, it was determined that surface area increased as phosphate doping decreased (**Figure 2.12**). As such, it is difficult to deconvolute the results of the *ex situ* water oxidation experiment from surface area effects.

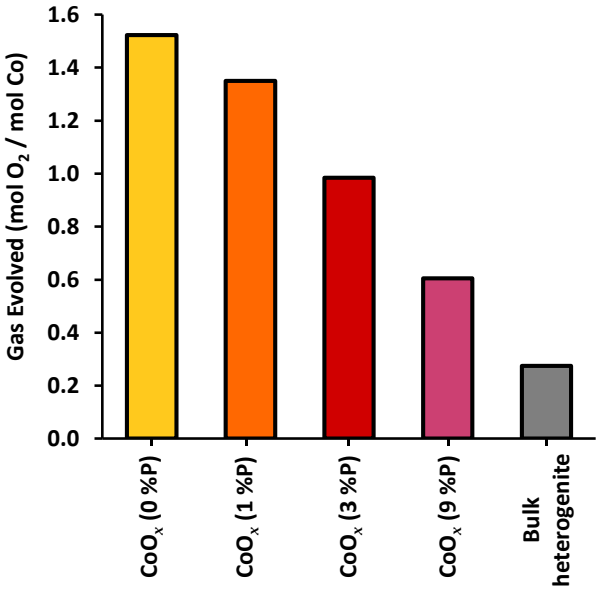

Figure 2.19: *Ex situ* measure of water oxidation catalysis using hypochlorite as a sacrificial oxidant. Gas evolution is presented as a total after 5 mins of reaction. Data was collected on: CoO_x (0 %P) (*yellow*), CoO_x (1 %P) (*orange*), CoO_x (3 %P) (*red*), CoO_x (9 %P) (*pink*), and bulk heterogenite (*grey*).

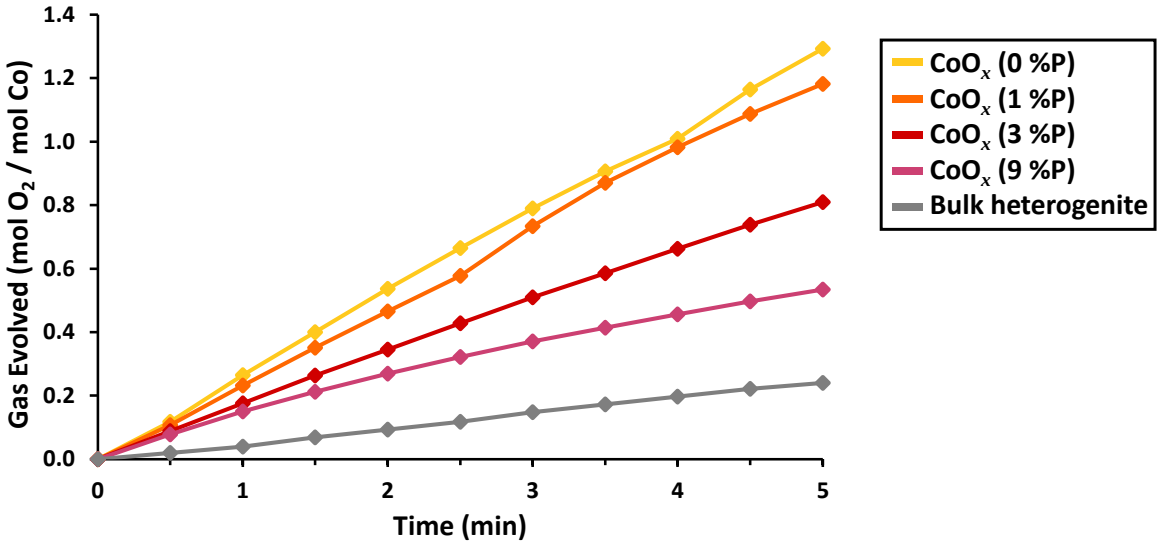

Figure 2.20: *Ex situ* measure of water oxidation catalysis using hypochlorite as a sacrificial oxidant. Gas evolution is presented as a function of time. Data was collected on: CoO_x (0 %P) (*yellow*), CoO_x (1 %P) (*orange*), CoO_x (3 %P) (*red*), CoO_x (9 %P) (*pink*), and bulk heterogenite (*grey*).

The structural and catalytic analyses have thus far determined that phosphate doping introduces structural disorder into heterogenite-like cobalt oxides and that catalytic activity decreases as phosphate doping increases. However, amorphous materials are generally considered to be more active for water oxidation catalysis as they are structurally destabilised relative to their ordered bulk phase counterparts.[15, 23, 26-27, 36, 38-39] To study the chemical effect structural destabilisation had on the cobalt oxide materials, the CoO_x (*x* %P) series was studied by hydrogen peroxide reductive dissolution whereby the oxidative strength of the CoO_x materials was determined.

2.3.3 Measurement of CoO_x oxidative strength by reaction with H_2O_2

Research by Ulrich et al. as well as Lee-Penn and Veblen et al. has noted that certain classes of destabilised CoO_x materials should be more prone to reductive dissolution.[79-80] It was noted during these studies that the cobalt oxides were sufficiently strong oxidising agents to directly oxidise hydrogen peroxide. As such, this reaction was used to monitor the ease with which the CoO_x materials were reduced and thereby determine the oxidative strength of the CoO_x (*x* %P) materials. Subsequently, this was used to evaluate the effect structural destabilisation had on the activity of the materials as oxidants and as catalysts. The heterogenite family of CoO_x materials can catalyse the disproportionation of H_2O_2 and/or directly oxidise H_2O_2 as described in **reactions 2.1** and **2.2**:[81-83]

Catalyse the disproportionation of H_2O_2:

$$H_2O_{2\,(aq)} \rightarrow H_2O_{\,(aq)} + \tfrac{1}{2}O_{2\,(g)} \qquad \textbf{(2.1)}$$

Directly oxidise H_2O_2:

$$CoO_{x\,(s)} + 2H^+_{\,(aq)} + H_2O_{2\,(aq)} \rightarrow O_{2\,(g)} + Co^{2+}_{\,(aq)} + 2H_2O_{\,(aq)} \qquad \textbf{(2.2)}$$

Reaction 2.1 preserves the CoO_x solid (as it is acting as a catalyst) and many mols of gas can be evolved per mol of Co. **Reaction 2.2** results in the dissolution of the CoO_x, (*i.e.* the dark brown CoO_x solid decomposes to the pale red Co^{2+} solution) and can evolve only 1 mol of O_2 per mol of Co. The propensity of a material to mediate one reaction *versus* the other can be found by measuring the gas evolved from the decomposition of hydrogen peroxide. As the oxidation reaction will become more spontaneous at low pH due to protons being consumed in the reaction,[84] it was important to evaluate the effect pH had on the CoO_x / H_2O_2 reaction. As such, the hydrogen peroxide experiment was performed at pH 1, 3, 5, 7, 10 and 13.

Figure 2.21 presents the quantity of gas evolved between each CoO_x and H_2O_2 at pH 1, 3, 5, 7, 10 and 13 (measured as mol O_2 per mole Co). The CoO_x (*x* %P) series demonstrated a systematic increase in gas evolution and decrease in reductive dissolution as phosphate doping decreased. That is, CoO_x (9 %P) (*i.e.* the most disordered material) evolved the least gas and was the most easily reduced, and CoO_x (0 %P) (*i.e.* the most ordered material) evolved the most gas and was the least easily reduced. This trend provides strong evidence that oxidative strength increases proportionally with phosphate doping.

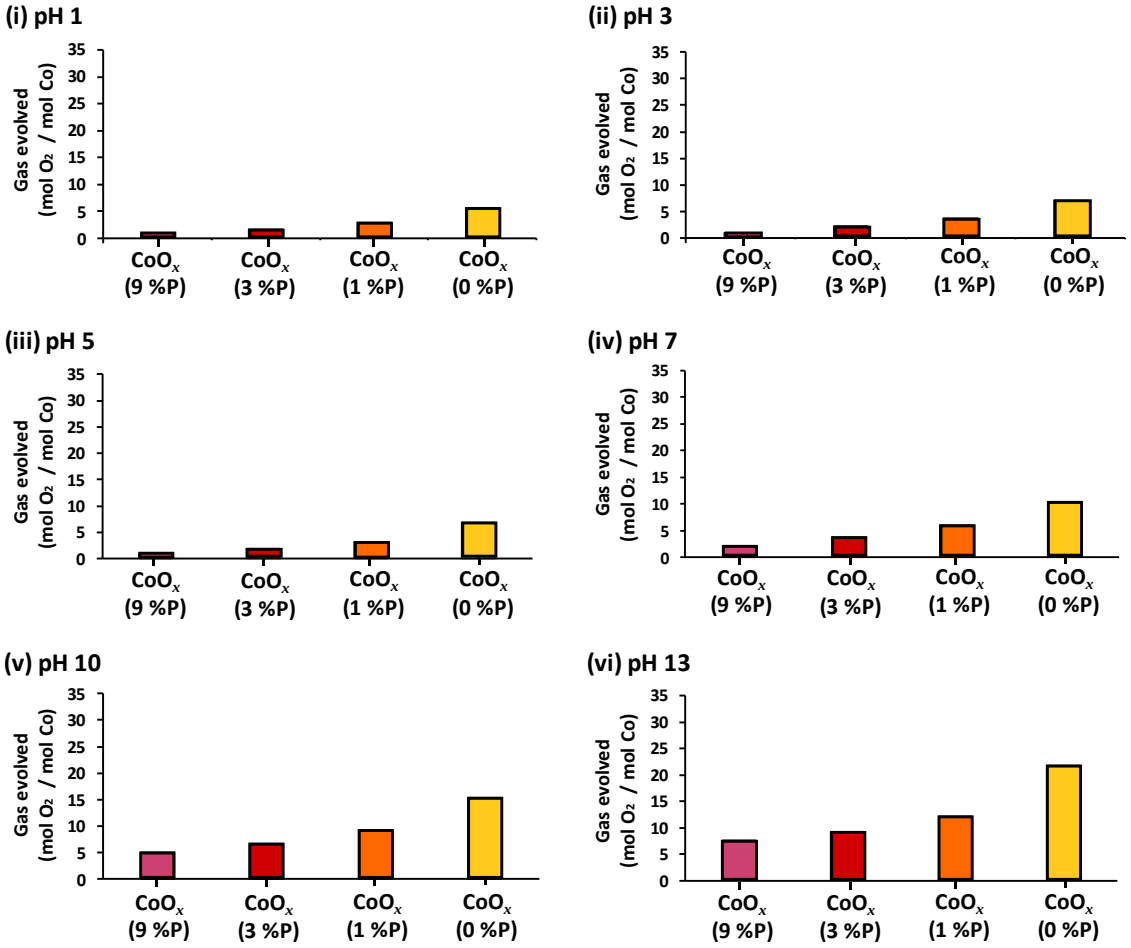

Figure 2.21: Measurement of CoO_x (x %P) oxidative strength by reaction with hydrogen peroxide. Gas evolution (mol O_2 per mole Co) was measured after 30 mins of reaction. Data was collected at: **(i)** pH 1, **(ii)** pH 3, **(iii)** pH 5, **(iv)** pH 7, **(v)** pH 10, and **(vi)** pH 13. Data was collected on: CoO_x (0 %P) (*yellow*), CoO_x (1 %P) (*orange*), CoO_x (3 %P) (*red*), and CoO_x (9 %P) (*pink*). All CoO_x (x %P) materials dissolved in all pH conditions during this experiment.

2.4 Discussion

This study utilised a novel synthetic method and advanced analytical techniques to systematically characterise the functional effects of structural disorder in heterogenite-like cobalt oxides. In summary; the systematic increase in phosphate doping caused a systematic increase in bond-length and nanoscale disorder, a systematic decrease in thermodynamic stability, a systematic decrease in catalytic activity, and a systematic increase in oxidative strength. While the general understanding in the catalysis community is that amorphous and disordered phases are more 'active' than their ordered counterparts,[15, 23, 26-27, 36, 38-39] the findings herein indicate that disordered phases are more 'redox active' and ordered phases are more 'catalytically active'. The systematic nature of the functional changes across the CoO_x (*x* %P) series indicates that redox and catalytic functionality may be tuneable by controlling disorder and thermodynamic properties (**Scheme 2.2**). That is, the functionality of a material towards catalyst or oxidant behaviour can be controlled by tuning structural disorder such that the thermodynamic stability of a material is tuned.

This understanding is important to the design of new catalytic materials as the catalytic mechanism suggests that a material needs to have both catalyst and oxidant properties to be optimally active for the water oxidation reaction.[85] That is, for the self-healing mechanism (i.e. the material is consumed and reformed through redox changes in the catalytic cycle) to operate, a material needs to be thermodynamically stable enough to participate as a catalyst in the water oxidation reaction but thermodynamically destabilised enough to be redeposited under the potentiometric conditions of the reaction.

The cobalt oxide materials studied herein mimic the structure of the electrodeposited Co-Pi catalyst and provide three key insights into the structural and functional characterisation of this catalyst. Firstly, the dampening of high range EXAFS may be a function of bond-length disorder rather than CoO_x cluster size. Secondly, phosphate does not appear to play a role in the water oxidation mechanism, but rather acts to thermodynamically destabilise the CoO_x phase and allow the self-healing mechanism to operate. Finally, the preceding conclusion suggests that sacrificial oxidation may be an important part of a catalytic mechanism.

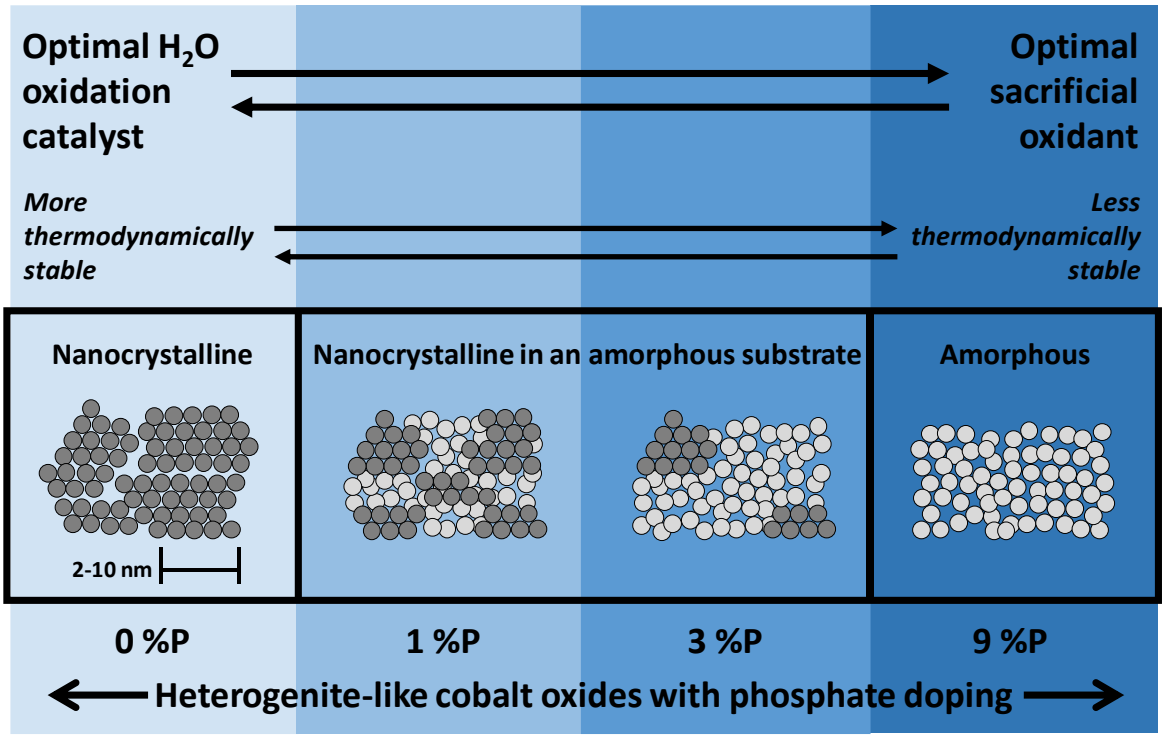

Scheme 2.2: Summary of the key findings into phosphate doped heterogenite-like cobalt oxides. Firstly, phosphate doping systematically increased the structural disorder within the CoO_x (*x* %P) materials through an increase in both bond-length disorder and nanoscale disorder. Secondly, phosphate doping systematically decreased the thermodynamic stability of the cobalt oxide phase. Finally, phosphate doping systematically decreased catalytic activity and systematically increased oxidative activity. As such, phosphate doping tunes the structure, stability and activity of the heterogenite-like cobalt oxide phase towards a more disordered and destabilised material that reacts more favourably as a sacrificial oxidant.

2.5 Conclusion

This study examined the structural and functional effects phosphate doping had on a heterogenite-like cobalt oxide phase, such as Co-Pi. It was determined from TEM and XAS characterisations that phosphate doping increased nanoscale and atomic-level structural disorder within the base heterogenite-like structure. More specifically, phosphate doping transitioned the bulk heterogenite-like phase into a truly amorphous phase with bond-length disorder. It was determined that phosphate doping made the heterogenite-like phase a less thermodynamically stable and a less catalytically active material.

It is suggested that phosphate within the Co-Pi catalyst destabilises the catalytic heterogenite-like phase and thereby allows this catalytic phase to form and re-form with the application of potential during catalysis at low overpotentials. This study further suggests that phosphate is located in the interlayer and does not play a direct role in increasing the activity of the heterogenite-like phase. Thus, the catalytic efficiency of a cobalt oxide material may be optimised by tuning the disorder within the material such that thermodynamic instability allows the self-healing mechanism to function at low overpotentials.

2.6 Chapter 2 references

1. Stern, N., *Stern review on the economics of climate change*. Cambridge University Press Cambridge, United Kingdom, 2006.
2. International student energy summit. 10 Unsolvables - Energy problems the world must solve. http://10unsolvables.org/ (accessed 16/08/14).
3. Nakagawa, T.; Beasley, C. A.; Murray, R. W., Efficient electro-oxidation of water near its reversible potential by a mesoporous IrO_x nanoparticle film. *J. Phys. Chem. C* **2009,** *113* (30), 12958-12961.
4. Kamat, P. V., Meeting the clean energy demand: Nanostructure architectures for solar energy conversion. *J. Phys. Chem. C* **2007,** *111* (7), 2834-2860.
5. Bard, A. J.; Fox, M. A., Artificial photosynthesis: solar splitting of water to hydrogen and oxygen. *Acc. Chem. Res.* **1995,** *28* (3), 141-145.
6. Lewis, N. S.; Nocera, D. G., Powering the planet: Chemical challenges in solar energy utilization. *Proc. Natl. Acad. Sci.* **2006,** *103* (43), 15729-15735.
7. Faunce, T.; Styring, S.; Wasielewski, M. R.; Brudvig, G. W.; Rutherford, A. W.; Messinger, J.; Lee, A. F.; Hill, C. L.; deGroot, H.; Fontecave, M., et al. Artificial photosynthesis as a frontier technology for energy sustainability. *Energy Environ. Sci.* **2013,** *6*, 1074-1076.
8. Lewis, N. S., Research opportunities to advance solar energy utilization. *Science* **2016,** *351* (6271), 353-362.
9. Lewis, N. S., Toward cost-effective solar energy use. *Science* **2007,** *315* (5813), 798-801.
10. Cook, T. R.; Dogutan, D. K.; Reece, S. Y.; Surendranath, Y.; Teets, T. S.; Nocera, D. G., Solar energy supply and storage for the legacy and nonlegacy worlds. *Chem. Rev.* **2010,** *110* (11), 6474-6502.
11. Gust, D.; Moore, T. A.; Moore, A. L., Solar fuels *via* artificial photosynthesis. *Acc. Chem. Res.* **2009,** *42* (12), 1890-1898.
12. Arvizu, D.; Balaya, P.; Cabeza, L. F.; Hollands, K. G. T.; Jäger-Waldau, A.; Kondo, M.; Konseibo, C.; Meleshko, V.; Stein, W.; Tamaura, Y., et al. IPCC Special report on renewable energy sources and climate change mitigation. In *Renewable energy sources and climate change mitigation*, Edenhofer, O.; Pichs-Madruga, R.; Sokona, Y.; Seyboth, K.; Matschoss, P.; Kadner, S.; Zwickel, T.; Eickemeier, P.; Hansen, G.; Schlömer, S. et al. Eds. Cambridge University Press: Cambridge, United Kingdom and New York, NY, USA, 2011.
13. Maeda, K.; Domen, K., Photocatalytic water splitting: Recent progress and future challenges. *J. Phys. Chem. Lett* **2010,** *1* (18), 2655-2661.
14. Bard, A. J.; Faulkner, L. R., *Electrochemical methods: Fundamentals and applications*. John Wiley & Sons, Inc.: United States of America, 2000; p 864.
15. Kanan, M. W.; Nocera, D. G., *In situ* formation of an oxygen-evolving catalyst in neutral water containing phosphate and Co^{2+}. *Science* **2008,** *321* (5892), 1072-1075.
16. Dau, H.; Limberg, C.; Reier, T.; Risch, M.; Roggan, S.; Strasser, P., The mechanism of water oxidation: From electrolysis *via* homogeneous to biological catalysis. *ChemCatChem* **2010,** *2* (7), 724-761.
17. Balzani, V.; Armaroli, N., *Energy for a sustainable world: From the oil age to a sun-powered future*. Wiley: 2010.
18. Surendranath, Y.; Kanan, M. W.; Nocera, D. G., Mechanistic studies of the oxygen evolution reaction by a cobalt-phosphate catalyst at neutral pH. *J. Am. Chem. Soc.,* **2010,** *132* (46), 16501-16509.
19. Deng, X.; Tüysüz, H., Cobalt-oxide-based materials as water oxidation catalyst: Recent progress and challenges. *ACS Catal.* **2014,** *4* (10), 3701-3714.

20. Singh, A.; Hocking, R. K.; Chang, S. L. Y.; George, B. M.; Fehr, M.; Lips, K.; Schnegg, A.; Spiccia, L., Water oxidation catalysis by nanoparticulate manganese oxide thin films: Probing the effect of the manganese precursors. *Chem. Mater.* **2013,** *25* (7), 1098-1108.
21. Shaner S. E.; Hooker P. D.; Nickel A-M.; Leichtfuss A. R.; Adams C. S.; de la Cerda D.; She Y.; Gerken J. B.; Pokhrel R.; Ambrose N. J., et al. Discovering inexpensive, effective catalysts for solar energy conversion: An authentic research laboratory experience. *J. Chem. Ed.,* **2016,** *93*, 650-657.
22. Lutterman, D. A.; Surendranath, Y.; Nocera, D. G., A self-healing oxygen-evolving catalyst. *J. Am. Chem. Soc.* **2009,** *131* (11), 3838-3839.
23. Surendranath, Y.; Dinca, M.; Nocera, D. G., Electrolyte-dependent electrosynthesis and activity of cobalt-based water oxidation catalysts. *J. Am. Chem. Soc.* **2009,** *131* (7), 2615-2620.
24. Kanan, M. W.; Yano, J.; Surendranath, Y.; Dinca, M.; Yachandra, V. K.; Nocera, D. G., Structure and valency of a cobalt-phosphate water oxidation catalyst determined by *in situ* X-ray spectroscopy. *J. Am. Chem. Soc.* **2010,** *132* (39), 13692-13701.
25. Nocera, D., The artificial leaf. *Acc. Chem. Res.* **2011,** *45* (5), 767-776.
26. Dinca, M.; Surendranath, Y.; Nocera, D., Nickel-borate oxygen-evolving catalyst that functions under benign conditions. *Proc. Natl. Acad. Sci.* **2010,** *23*, 10337-10341.
27. Huynh, M.; Bediako, D. K.; Liu, Y.; Nocera, D. G., Nucleation and growth mechanisms of an electrodeposited manganese oxide oxygen evolution catalyst. *J. Phys. Chem. C* **2014,** *118* (30), 17142-17152.
28. Huynh, M.; Bediako, D. K.; Nocera, D. G., A functionally stable manganese oxide oxygen evolution catalyst in acid. *J. Am. Chem. Soc.* **2014,** *136* (16), 6002-6010.
29. Zaharieva, I.; Chernev, P.; Risch, M.; Klingan, K.; Kohlhoff, M.; Fischer, A.; Dau, H., Electrosynthesis, functional, and structural characterization of a water-oxidizing manganese oxide. *Energy Environ. Sci.* **2012,** *5* (5), 7081-7089.
30. Risch, M.; Khare, V.; Zaharieva, I.; Gerencser, L.; Chernev, P.; Dau, H., Cobalt-oxo core of a water-oxidizing catalyst film. *J. Am. Chem. Soc.* **2009,** *131* (20), 6936-6937.
31. Hou, H. J. M., Structural and mechanistic aspects of Mn-oxo and Co-based compounds in water oxidation catalysis and potential applications in solar fuel production. *J. Integr. Plant Biol.* **2010,** *52* (8), 704-711.
32. Lin, Y.-G.; Hsu, Y.-K.; Chen, Y.-C.; Lee, B.-W.; Hwang, J.-S.; Chen, L.-C.; Chen, K.-H., Cobalt-phosphate-assisted photoelectrochemical water oxidation by arrays of molybdenum-doped zinc oxide nanorods. *ChemSusChem* **2014,** *7* (9), 2748-2754.
33. Pilli, S. K.; Janarthanan, R.; Deutsch, T. G.; Furtak, T. E.; Brown, L. D.; Turner, J. A.; Herring, A. M., Efficient photoelectrochemical water oxidation over cobalt-phosphate (Co-Pi) catalyst modified $BiVO_4$/1D-WO_3 heterojunction electrodes. *Phys. Chem. Chem. Phys.* **2013,** *15* (35), 14723-14728.
34. Pihosh, Y.; Turkevych, I.; Mawatari, K.; Asai, T.; Hisatomi, T.; Uemura, J.; Tosa, M.; Shimamura, K.; Kubota, J.; Domen, K.; Kitamori, T., Nanostructured WO_3/$BiVO_4$ photoanodes for efficient photoelectrochemical water splitting. *Small* **2014,** *10* (18), 3692-3699.
35. Pilli, S. K.; Deutsch, T. G.; Furtak, T. E.; Turner, J. A.; Brown, L. D.; Herring, A. M., Light induced water oxidation on cobalt-phosphate (Co-Pi) catalyst modified semi-transparent, porous SiO_2-$BiVO_4$ electrodes. *Phys. Chem. Chem. Phys.* **2012,** *14* (19), 7032-7039.
36. Fekete, M.; Hocking, R. K.; Chang, S. L. Y.; Italiano, C.; Patti, A. F.; Arena, F.; Spiccia, L., Highly active screen-printed electrocatalysts for water oxidation based on [small beta]-manganese oxide. *Energy Environ. Sci.* **2013,** *6* (7), 2222-2232.

37. Indra, A.; Menezes, P. W.; Zaharieva, I.; Baktash, E.; Pfrommer, J.; Schwarze, M.; Dau, H.; Driess, M., Active mixed-valent MnO_x water oxidation catalysts through partial oxidation (corrosion) of nanostructured MnO particles. *Angew. Chem. Int. Ed. Engl.* **2013,** *52* (50), 13206-13210.
38. Singh, A.; Fekete, M.; Gengenbach, T.; Simonov, A. N.; Hocking, R. K.; Chang, S. L. Y.; Rothmann, M.; Powar, S.; Fu, D.; Hu, Z. et al. Catalytic activity and impedance behavior of screen-printed nickel oxide as efficient water oxidation catalysts. *ChemSusChem* **2015,** *8* (24), 4266-4274.
39. Hocking, R. K.; King, H. J.; Hesson, A.; Bonke, S. A.; Johannessen, B.; Fekete, M.; Spiccia, L.; Chang, S. L. Y., Engineering disorder at a nanoscale: A combined TEM and XAS investigation of amorphous *versus* nanocrystalline sodium birnessite. *Aus. J. Chem* **2015,** *68* (11), 1715-1722.
40. Lee, S. Y.; González-Flores, D.; Ohms, J.; Trost, T.; Dau, H.; Zaharieva, I.; Kurz, P., Screen-printed calcium-birnessite electrodes for water oxidation at neutral pH and an "electrochemical harriman series". *ChemSusChem* **2014,** *7* (12), 3442-51.
41. Zhou, F.; Izgorodin, A.; Hocking, R. K.; Spiccia, L.; MacFarlane, D. R., Electrodeposited MnO_x films from ionic liquid for electrocatalytic water oxidation. *Adv. Energy Mater.* **2012,** *2* (8), 1013-1021.
42. Hu, X. L.; Piccinin, S.; Laio, A.; Fabris, S., Atomistic structure of cobalt-phosphate nanoparticles for catalytic water oxidation. *ACS Nano* **2012,** *6* (12), 10497-10504.
43. Bediako, D. K.; Surendranath, Y.; Nocera, D. G., Mechanistic studies of the oxygen evolution reaction mediated by a nickel-borate thin film electrocatalyst. *J. Am. Chem. Soc.* **2013,** *135* (9), 3662-3674.
44. Costentin, C.; Porter, T. R.; Savéant, J.-M., Conduction and reactivity in heterogeneous-molecular catalysis: New insights in water oxidation catalysis by phosphate cobalt oxide films. *J. Am. Chem. Soc.* **2016,** *138* (17), 5615-5622.
45. Klingan K.; Ringleb F.; Zaharieva I.; Heidkamp J.; Chernev P.; González-Flores D.; Risch M.; Fischer A.; Dau H., Water oxidation by amorphous cobalt-based oxides: Volume activity and proton transfer electrolyte bases. *ChemSusChem* **2014,** *7* (5), 1301-1310.
46. Bond G. C., *Heterogeneous catalysis*. 2nd ed.; Clarendon Press: Oxford, 1987; Vol. 8.
47. Davis, M. E.; Davis, R. J., *Fundamentals of chemical reaction engineering* McGraw-Hill Higher Education New York, NY, 2003.
48. Bell, A. T., The impact of nanoscience on heterogeneous catalysis. *Science* **2003**, 1688-1691.
49. Esswein, A. J.; Surendranath, Y.; Reece, S. Y.; Nocera, D. G., Highly active cobalt phosphate and borate based oxygen evolving catalysts operating in neutral and natural waters. *Energy Environ. Sci.* **2011,** *4* (2), 499-504.
50. González-Flores, D.; Sánchez, I.; Zaharieva, I.; Klingan, K.; Heidkamp, J.; Chernev, P.; Menezes, P. W.; Driess, M.; Dau, H.; Montero, M. L., Heterogeneous water oxidation: Surface activity *versus* amorphization activation in cobalt phosphate catalysts. *Angew. Chem. Int.* **2015,** *127* (8), 2502-2506.
51. Myers, J. C.; Penn, R. L., Controlling heterogenite particle morphology and microstructure by varying synthetic conditions. *Mater. Res. Bull.* **2011,** *46* (5), 649-657.
52. Deliens, M.; Goethals, H., Polytypism of heterogenite. *Mineralog. Mag.* 1973, pp 152-157.
53. *CrystalDiffract*, 6.0.5 (200); Oxford, UK, 2014.
54. Patterson, A. L., The Scherrer formula for X-ray particle size determination. *Phys. Rev.* **1939,** *56* (10), 978-982.
55. Ellis P. J.; Freeman J. C., *Average*. *J. Synchrotron Radiat.* **1995,** *2*, 190-195.

56. Kappen, P.; Ruben, G. *Sakura*, Australian Synchrotron: 2013.
57. Ravel, B.; Newville, M. *Athena, Artemis, Hephaestus: Data analysis for X-ray Absorption Spectroscopy using IFEFFIT*, J. Synchrotron Radiat.: 2005.
58. Yang, J.; Yao, L.; Sun, J.; Sun, B., Coordination self-assembly of heterogenite nanosheets into uniform nanospheres through an ultrasonic-assisted process. *J. Inorg. Organomet. Polym. Mater.* **2013,** *23* (6), 1240-1246.
59. Brunauer S.; Emmett P. H.; Teller E., Absorption of gases in mulimolecular layers. *J. Am. Chem. Soc.* **1938,** *60* (2), 309-319.
60. Burstein, G. T., A hundred years of Tafel's Equation: 1905-2005. *Corros. Sci.* **2005,** *47*, 2858-2859.
61. Macounová, K. M.; Simic, N.; Ahlberg, E.; Krtil, P., Electrochemical water-splitting based on hypochlorite oxidation. *J. Am. Chem. Soc.* **2015,** *137* (23), 7262-7265.
62. Parent, A. R.; Crabtree, R. H.; Brudvig, G. W., Comparison of primary oxidants for water-oxidation catalysis. *Chem. Soc. Rev.* **2013,** *42*, 2247-2252.
63. Dorofeev, G. A.; Streletskii, A. N.; Povstugar, I. V.; Protasoc, A. V.; Elsukov, E. P., Determination of nanoparticle sizes by X-ray diffraction. *Colloid J.* **2012,** *74*, 675-685.
64. Yan, W.; Petkov, V.; Mahurin, S. M.; Overbury, S. H.; Dai, S., Powder XRD analysis and catalysis characterization of ultra-small gold nanoparticles deposited on titania-modified SBA-15 •. *Catal. Commun.* **2005,** *6*, 404-408.
65. Kiel, S.; Grinberg, O.; Perkas, N.; Charmet, J.; Kepner, H.; Gedanken, A., Forming nanoparticles of water-soluble ionic molecules and embedding them into polymer and glass substrates. *J. Nanotechnol.* **2012,** *3*, 267-276.
66. Risch, M.; Ringleb, F.; Khare, V.; Chernev, P.; Zaharieva, I.; Dau, H., Characterisation of a water-oxidising Co-film by XAFS. *J. Phys.* **2009,** *190*, 1-4.
67. Delaplane, R. G.; Ibers, J. A.; Ferraro, J. R.; Rush, J. J., Diffraction and spectroscopic studies of the cobaltic acid system $HCoC_2$–$DCoO_2$. *J. Chem. Phys.* **1969,** *50* (5), 1920-1927.
68. Klaeui, W.; Eberspach, W.; Guetlich, P., Spin-crossover cobalt(III) complexes: steric and electronic control of spin state. *Inorg. Chem.* **1987,** *26* (24), 3977-3982.
69. Westre T. E.; Kennepohl P.; DeWitt J. G.; Hedman B.; Hodgson K. O.; Solomon E. I., A multiplet analysis of Fe K-edge 1s to 3d pre-edge features of iron complexes. *J. Am. Chem. Soc.* **1997,** *119* (27), 6297-6314.
70. Ingall, E. D.; Brandes, J. A.; Diaz, J. M.; de Jonge, M. D.; Paterson, D.; McNulty, I.; Crawford Elliott, W.; Northrup, P., Phosphorus K-edge XANES spectroscopy of mineral standards. *J. Synchrotron Radiat.* **2011,** *18* (2), 189-197.
71. Vantelon, D.; Hofmann, A.; Hanselmann, K.; Flank, A. M. In *Speciation of phosphate in iron rich mineral deposit in a high mountain lake environment: A study at the micron scale at the LUCIA beamline*, 2007/02/1; pp 232-234.
72. Pickering, I. J.; George, G. N.; Yu, E. Y.; Brune, D. C.; Tuschak, C.; Overmann, J.; Beatty, J. T.; Prince, R. C., Analysis of sulfur biochemistry of sulfur bacteria using X-ray absorption spectroscopy. *Biochem.* **2001,** *40* (27), 8138-8145.
73. Calvin, S., *XAFS for everyone*. CRC Press: Florida, U.S.A, 2013.
74. Ressler T.; Brock S. L.; Wong J.; Suib S. L., Multiple-scattering EXAFS analysis of tetraalykylammonium manganese oxide colloids. *J. Phys. Chem. B.* **1999,** *103*, 6407-6420.
75. King H. J.; Bonke S. A.; Chang S.; Spiccia L.; Johannesson B.; Hocking R. K., Engineering disorder into heterogenite-like cobalt oxides by phosphate doping: Implications for the design of water oxidation catalysts. *ChemCatChem* **2017,** *9* (3), 511-521.
76. Risch M.; Ringleb F.; Kohlhoff M.; Bogdanoff P.; Chernev P.; Zaharieva I.; Dau H., Water oxidation by amorphous cobalt-based oxides: *In situ* tracking of redox transitions and mode of catalysis. *Energy Environ. Sci.* **2015,** *2*, 661-674.

77. Gerken, J. B.; McAlpin, J. G.; Chen, J. Y.; Rigsby, M. L.; Casey, W. H.; Britt, R. D.; Stahl, S. S., Electrochemical water oxidation with cobalt-based electrocatalysts from pH 0-14: The thermodynamic basis for catalyst structure, stability and activity. *J. Am. Chem. Soc.* **2011,** *133* (36), 14431-14442.
78. Limburg, J.; Vrettos, J. S.; Liable-Sands, L. M.; Rheingold, A. L.; Crabtree, R. H.; Brudvig, G. W., A functional model for O-O bond formation by the O_2-evolving complex in photosystem II. *Science* **1999,** *283*, 1524-1527.
79. Stone, A. T.; Ulrich, H.-J., Kinetics and reaction stoichiometry in the reductive dissolution of manganese(IV) dioxide and Co(III) oxide by hydroquinone. *J. Colloid Interface Sci.* **1989,** *132* (2), 509-522.
80. Penn R. L.; Stone A. T.; Veblen D. R., Defects and disorder: Probing the surface chemistry of heterogenite using hydroquinone and iminodiacetic acid. *J. Phys. Chem. B.* **2001,** *105* (20), 4690-4697.
81. Gelasco, A.; Askenas, A.; Pecoraro, V. L., Catalytic disproportionation of hydrogen peroxide by the tetranuclear manganese complex $[Mn^{II}(2\text{-}OHpicpn)]_4$. *Inorg. Chem.* **1996,** *35* (6), 1419-1420.
82. Prasad, R. V.; Thakkar, N. V., Study of cobalt complexes as catalysts in the decomposition of hydrogen peroxide. *J. Mol. Catal.* **1994,** *92*, 9-20.
83. Salem, I. A.; El-Maazawi, M.; Zaki, A. B., Kinetics and mechanisms of decomposition reaction of hydrogen peroxide in presence of metal complexes. *Int. J. Chem. Kinet.* **2000,** *32*, 643-666.
84. Frey, C. E.; Wiechen, M.; Kurz, P., Water-oxidation catalysis by synthetic manganese oxides – Systematic variations of the calcium birnessite theme. *Dalton Trans.* **2014,** *43* (11), 4370-4379.
85. Sabri, M.; King, H. J.; Gummow, R. J.; Lu, X.; Zhao, C.; Oelgemöller, M.; Chang, S. L. Y.; Hocking, R. K.; Oxidant or catalyst for oxidation? A study of how structure and disorder change the selectivity for direct versus catalytic oxidation mediated by manganese(III,IV) oxides. *Chem. Mater*. 2018, 30 (22), 8244-8256.

Chapter 3 –

Elucidating the role of structural disorder in increasing the activity of birnessite-like manganese oxides

ABSTRACT

The natural water-oxidising complex of Photosystem II (Mn_4CaO_5) has inspired the development of many synthetic manganese oxides (MnO_x) as inexpensive and efficient catalysts for the water oxidation reaction. However, elucidating the key structural features important for high catalytic activity has been challenging as many active manganese oxides are amorphous and/or disordered and are thereby challenging to characterise with traditional analytical approaches.

In this study, we investigate the role of structural disorder in increasing the efficiency of birnessite-like manganese oxides for the water oxidation reaction. Two distinctively disordered birnessite-like manganese oxides (*viz.* one with 2D stacking disorder, and one with no crystallinity) were synthesised and compared with highly ordered K^+ birnessite in a comprehensive structure *versus* function characterisation. Like the heterogenite-like cobalt oxide series examined in Chapter 2, it was found that the disordered birnessite phases were less thermodynamically stable and were stronger chemical oxidants but not necessarily better catalysts. The relationship between disorder and metastability was examined, with its broader importance to the functionality of transition metal oxide catalysts discussed in detail.

Chapter 3 – Publications

This chapter contains unpublished research as well as components by the author which appear in the following peer-reviewed and published manuscripts:

Title: Engineering disorder at a nanoscale: A combined TEM and XAS investigation of amorphous *versus* nanocrystalline sodium birnessite
Publisher: Australian Journal of Chemistry
Year: 2015
Details: volume 68, issue 11, pages 1715-1722
Authors: Rosalie K. Hocking, Hannah J. King, Aimee Hesson, Shannon A. Bonke, Bernt Johannessen, Monika Fekete, Leone Spiccia, Shery L.Y. Chang

Title: Direct formation of 2D-MnO_x under conditions of water oxidation catalysis
Publisher: American Chemical Society - Applied Nano Materials
Year: 2018
Details: volume 1, issue 4, pages 1603-1611
Authors: Rosalie K. Hocking, Rosalind Gummow, Hannah J. King, Mayada Sabri, Peter Kappen, Christian Dwyer, Shery L.Y. Chang

Title: The oxidation of peroxide by disordered metal oxides: A measurement of thermodynamic stability "by proxy"
Publisher: ChemPlusChem
Year: 2018
Details: volume 83, issue 7, pages 620-629
Authors: Mayada Sabri, Hannah J. King, Rosalind J. Gummow, François Malherbe, Rosalie K. Hocking

Title: Oxidant or catalyst for oxidation? A study of how structure and disorder change the selectivity for direct versus catalytic oxidation mediated by manganese (III,IV) oxides

Publisher: American Chemical Society – Chemistry of Materials

Year: 2018

Details: volume 30, issue 22, pages 8244-8256

Authors: Mayada Sabri, Hannah J. King, Rosalind J. Gummow, Xunyu Lu, Chuan Zhao, Michael Oelgemöller, Shery L. Y. Chang, Rosalie K. Hocking

Chapter 3 – Table of contents

3.1 Introduction

Hydrogen (H_2) production *via* electrochemical water splitting is considered one of the most promising methods to store renewable energy.[1-3] A major challenge to achieving economic water splitting is the significant overpotential required to drive the four-electron water oxidation reaction ($2H_2O \rightleftharpoons O_2 + 4H^+ + 4e^-$) and a lack of efficient, robust, cheap, and easily manufactured catalysts to mediate this reaction.[4-8] While most commercial electrolysers utilise electrocatalysts based on precious metals (such as Pt[9], RuO_2[10] and IrO_2[11]), the high cost and scarcity of precious metals prevents their use in large-scale applications. Water oxidation catalysts based on the oxides of more abundant transition metals, such as manganese (MnO_x)[3, 9, 12-22], nickel (NiO_x)[23-25], and cobalt (CoO_x)[26-41] have been developed as efficient and cheap alternatives to precious metal based catalysts.[42-43]

Highly active MnO_x, NiO_x and CoO_x materials are most commonly synthesised through oxidative electrodeposition at ambient temperature and pressure from electrolyte solutions containing simple salts of the respective transition-metal ions.[7, 44] Unlike traditional high-temperature chemical methods which yield thermodynamically stable products,[44-48] an electrochemical system allows the precipitation of metastable phases (*i.e.* materials with a higher free energy than a corresponding thermodynamically stable phase) under ambient conditions by providing a means of controlling the kinetics and thermodynamics of the reaction (**Figure 3.1**).[44-45, 49] In an electrochemical system, the kinetics of a reaction is controlled by regulating the current passed through the cell and the thermodynamics is controlled by governing the potential applied across the cell. The chimie douce ('soft chemistry') conditions of an electrodeposition provide an integral link to the chemistry in nature by allowing synthetic reaction conditions to mimic those present in biological and natural systems.[45, 49]

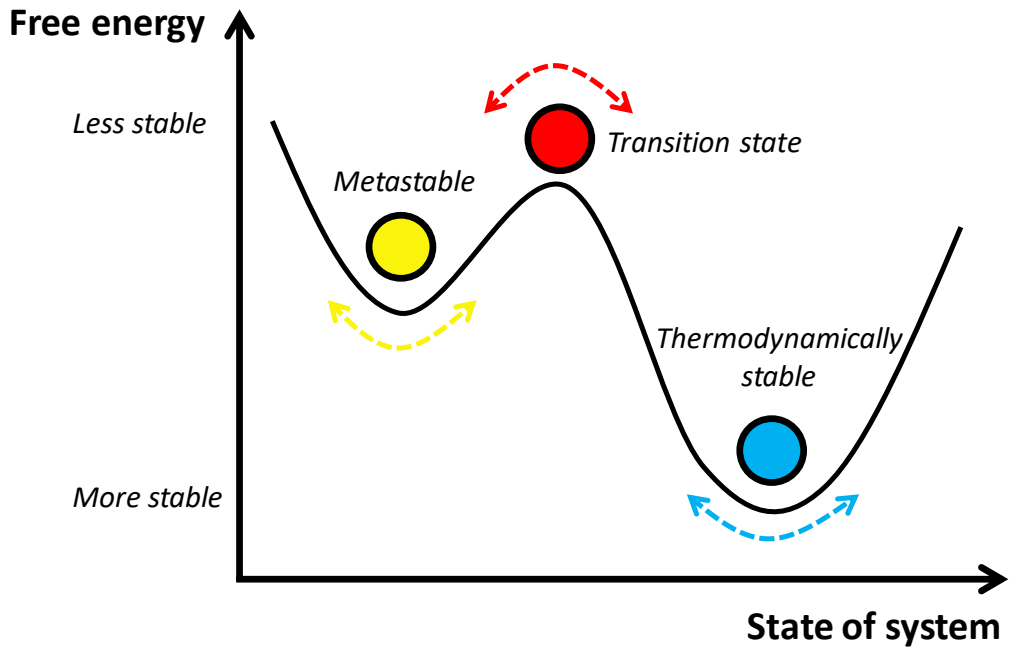

Figure 3.1: Free energy diagram illustrating the comparative free energy levels of the metastable, transition, and thermodynamically stable states. The metastable and thermodynamically stable states are at energy minima, and the least stable transition state is at an energy maximum.

Chimie douce electrochemical methods can be used to synthesise amorphous and/or disordered transition metal oxide catalysts. Materials are generally characterised as 'amorphous' and /or 'disordered' if they cannot be characterised by X-ray diffraction and are demonstrated to lack order by electron microscopy. However, this definition of order is somewhat dependent on the discipline using it (*e.g.* geology, biology, physics or chemistry). A lack of crystallinity could be caused by structural defects, poor intra- or interlayer order, and/or lack of basic repeat 'molecular unit'.[3-4, 18, 32, 37, 44-45, 49-51] Specific types of structural disorder include; a turbostratic layer structure (*i.e.* disordered layer stacking along the *c*-axis)[18, 52-56], limited interlayer sheet stacking (*i.e.* 2-dimensional (2D) materials)[18, 57-60], atomic intralayer vacancies (*i.e.* missing metal and/or oxygen atoms in the intralayer of MnO_x[4, 18, 54, 61-64], CoO_x[65-66], and NiO_x[67] materials), lattice strain (*i.e.* bond-length and bond-angle distortion)[4, 32, 54, 68], curled nanosheets[60, 69], and anion defects (including missing, substituted (anion dopant/impurity), or interstitial ions)[32, 70-73]. **Figure 3.2b** graphically illustrates each type of structural disorder using a layered MnO_2 similar to birnessite (δ-MnO_2) as a base structure.

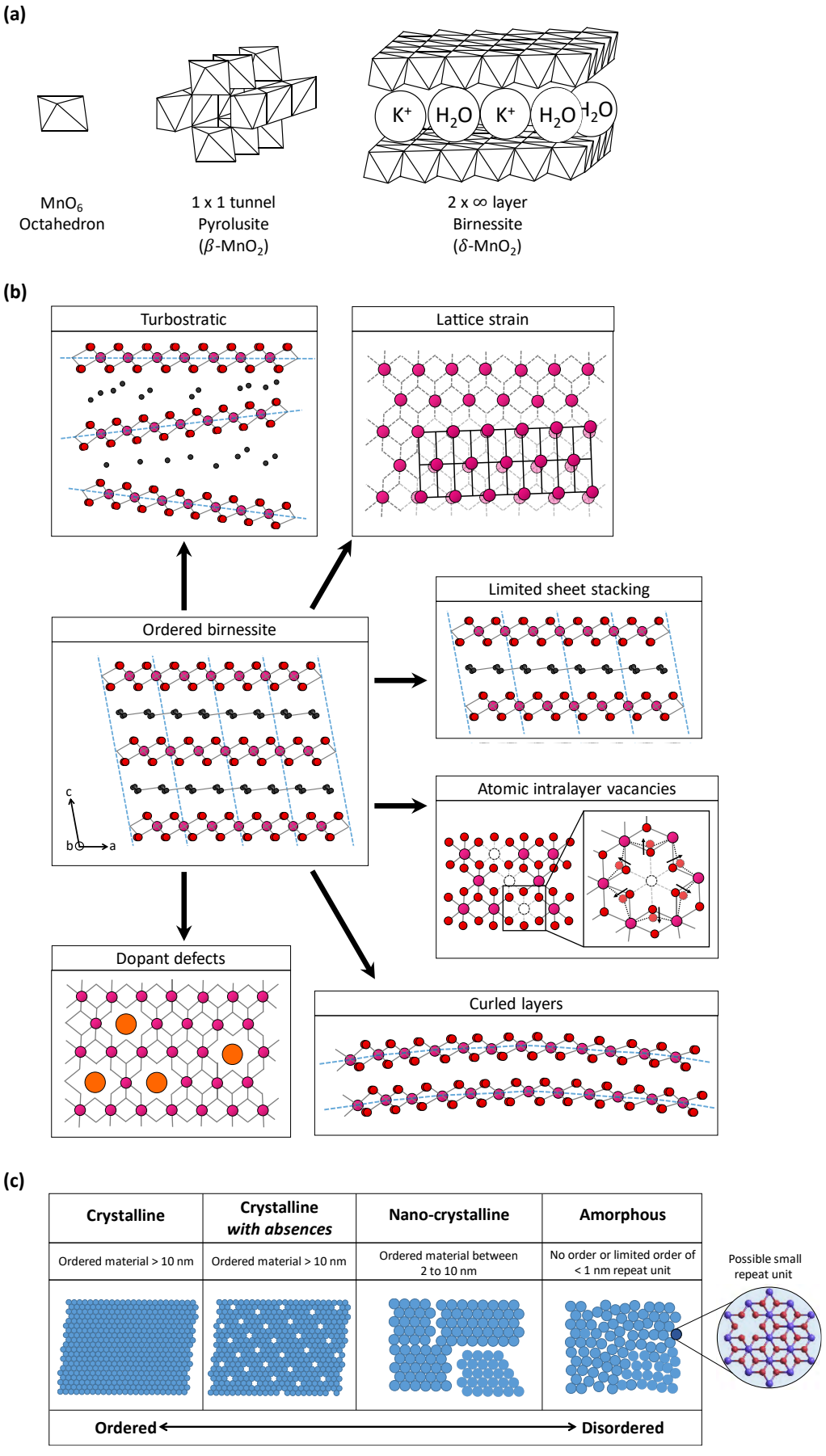

(Figure caption over page)

Figure 3.2: (a) Polyhedron representation of the crystal structures of pyrolusite (β-MnO_2) and K^+ birnessite (δ-MnO_2).[74-75] **(b)** Types of structural disorder occurring in transition metal oxides as exemplified for a birnessite structure with crystallite dimensions of $a \times b \times c$; where a and b are the crystallographic dimensions of the intralayer planes, and c is the interlayer crystallographic dimension (*i.e.* the stacking axis). The 6 types of structural disorder depicted are: turbostratic layer structure, lattice strain, limited interlayer stacking or '2D', atomic intralayer vacancies, curled layers, and dopant defects. **(c)** A simplified model showing an increase in structural disorder from 'crystalline' (ordered) to 'crystalline with absences' to 'nanocrystalline' to 'amorphous' (disordered).

Birnessite and birnessite-like minerals are ubiquitous in a wide variety of geological settings and are often characterised as being poorly crystalline or completely amorphous.[74, 76-77] Mineral birnessite has the general chemical formula $(Na,Ca,K)_x(Mn^{4+},Mn^{3+})_2O_4 \cdot 1.5(H_2O)$ and consists of edge-sharing MnO_6 octahedra sheets with intralayer Mn and O vacancies (**Figure 3.2a**).[78] Cations such as Na^+, K^+, Ca^{2+}, Mg^{2+}, and Mn^{2+} are typically found in the interlayer where they act to compensate negative charges from intralayer vacancies.[78] Birnessite-like minerals are geochemically active species and participate in geochemical cycling *via* photoreductive decomposition to Mn^{2+}.[56, 79-81]

Many heterogenous manganese oxides and molecular manganese complexes convert to a layered birnessite-like structure under the *in situ* (*i.e.* in an electrochemical cell) and *ex situ* (*i.e.* in the presence of cerium (IV), Ce^{IV}) conditions of water oxidation catalysis.[13, 82-84] In this protocol; the original manganese cluster dissociates or reduces to a Mn(II) state which is then reoxidized to form a disordered birnessite-like phase.[13, 82] This protocol forms the basis of a so-called 'self-healing' mechanism (as described by Kanan and Nocera et al.[26, 85]), where the active birnessite-like material decomposes to Mn^{2+} during the catalytic cycle and is reformed under the conditions of water oxidation catalysis.[86] The distinction between molecular-like and heterogeneous-like behaviours is further blurred by the general understanding that solid-state amorphous manganese oxide electrocatalysts exhibit molecular-like behaviour by undergoing structural, chemical and redox transitions during catalysis.[41, 87] The self-healing mechanism provides long-term stability to the catalyst and has an important conceptual link to the oxidative chemistry of mineral birnessite in nature.[13, 74, 78, 80-82]

Herein, we compare the structure and reactivity of ordered birnessite (K^+ birnessite) to two disordered birnessite-like manganese oxides (0%Pi-MnO_x and 1.5%Pi-MnO_x) and examine the relationship between structural order, catalytic activity for water oxidation, and thermodynamic stability. Additional comparisons are made to pyrolusite (β-MnO_2), which is a well-studied manganese oxide that is structurally ordered and thermodynamically stable. The structural order of the materials was analysed by X-ray absorption spectroscopy (XAS), powder X-ray diffraction (XRD), and transmission electron microscopy (TEM). The catalytic efficiency of the materials was analysed by cyclic voltammetry (CV) and gas evolution experiments using Ce^{IV} as a sacrificial chemical oxidant. The thermodynamic stability of the manganese oxides was qualitatively measured using hydrogen peroxide (H_2O_2) as a test assay, and *via* XAS analysis of the manganese oxides at progressive stages of the water oxidation reaction.

3.2 Experimental

3.2.1 Synthesis of manganese oxide materials

Four MnO_x samples were utilised in this study: nanoparticulate birnessite with 0% phosphate doping (termed herein as 0%Pi-MnO_x), nanoparticulate birnessite with 1.5% phosphate doping (termed herein as 1.5%Pi-MnO_x), potassium birnessite (termed herein as K^+ birnessite), and pyrolusite. The nomenclature of 'Pi' is used for the *x*%Pi-MnO_x samples to denote inorganic phosphate, which exists in the forms of PO_4^{3-}, HPO_4^{2-}, $H_2PO_4^-$, or H_3PO_4. This nomenclature is used because the protonation state of the phosphate is unknown. The term 'doping' is used to describe the addition of phosphate into a material.

The empirical formulas of the birnessite-like manganese oxides were determined using a combination of ion chromatography (IC), inductively coupled plasma – atomic emission spectroscopy (ICP-AES), X-ray absorption near edge structure (XANES) analysis of redox state and weight changes upon heating to different temperatures. The formulations of the materials are described as follows: 0%Pi-MnO_x is $Mn^{2+}_{0.16}Na_{0.12}(H_2O)_{0.9}[Mn^{4+}_{0.90},(Mn_v)_{0.10}O_2]$, 1.5%Pi-$MnO_x$ is $Mn^{2+}_{0.16}Na_{0.12}(H_2O)_{0.9}(HPO_4^{2-})_{0.0159}[Mn^{4+}_{0.90},(Mn_v)_{0.10}O_2]$, and K^+ birnessite is $K^+_{0.231}(Mn^{4+}_{0.885}Mn^{3+}_{0.077}(Mn_v)_{0.033})O_2.(0.6)H_2O$; where (Mn_v) is a Mn vacancy.

3.2.1.1 Synthesis of 0%Pi-MnO_x

The synthesis of 0%Pi-MnO_x involved rapidly oxidising a Mn(II) solution (0.2 M, $Mn(CH_3COO)_2.4H_2O$, 500 mL) with hypochlorite (4 w/v%, NaOCl, 400 mL). The MnO_x material was isolated and washed with water using a centrifuge, and then rinsed once with acetone. The isolated sample was dried in an oven (at 110°C for approximately 12 h) in preparation for analysis.

The 0%Pi-MnO_x sample was found to have a 2D structure by XRD and TEM analysis.[57] Samples of 0%Pi-MnO_x were heated to 100°C, 200°C, 500°C and 800°C in a muffle furnace and analysed by XRD to examine the effects of temperature on the structure. When kept below 200°C, 0%Pi-MnO_x retained its 2D structure but was noted to reversibly absorb and desorb water.

The formulation of unheated 0%Pi-MnO_x is $Mn^{2+}_{0.16}Na_{0.12}(H_2O)_{3.0}$ $[Mn^{4+}_{0.9}(Mn_v)_{0.1}O_2]$, and the formulation of 0%Pi-MnO_x heated to 100°C is $Mn^{2+}_{0.16}Na_{0.12}(H_2O)_{0.9}$ $[Mn^{4+}_{0.9}(Mn_v)_{0.1}O_2]$, where (Mn_v) is a Mn vacancy. When heated to 500°C, 0%Pi-MnO_x decomposed to hollandite with sodium in the interlayer. When heated further to 800°C, the material decomposed to Mn_2O_3.

3.2.1.2 Synthesis of 1.5%Pi-MnO_x

The 1.5%Pi-MnO_x sample was synthesised by hypochlorite oxidation in a similar manner to the 0%Pi-MnO_x sample. In this procedure, a Mn(II) solution (0.2 M, $(CH_3COO)_2Mn.4H_2O$, 500 mL) was mixed with sodium phosphate buffer (0.1 M, pH 7, $NaH_2PO_4.2H_2O$, 100 mL), and then the precipitate was rapidly oxidised with hypochlorite (4 w/v%, NaOCl, 400 mL). The MnO_x material was isolated and washed 10 × with water using a centrifuge, and then rinsed once with acetone. The isolated sample was oven dried (at 110°C for approximately 12 h) in preparation for analysis.

Replicate samples of 1.5%Pi-MnO_x contained the same phosphate content (by ICP-AES, within experimental error), which indicated that phosphate could be reproducibly integrated into the MnO_x structure. The amount of phosphate doped into a manganese oxide sample could be altered based on the phosphate concentration in the synthesis. However, at phosphate concentrations higher than those required to make 1.5%Pi-MnO_x, the extended X-ray absorption fine structure (EXAFS) showed a phase change (**Figure 3.3 b** and **c**) from the required birnessite-like structure and consequently placed the materials outside the scope of this work. This phase change is exemplified in the comparative XAS spectra of 1.5%-MnO_x and 10%P-MnO_x (*i.e.* a MnO_x sample with 10% phosphate doping) in **Figure 3.3**.

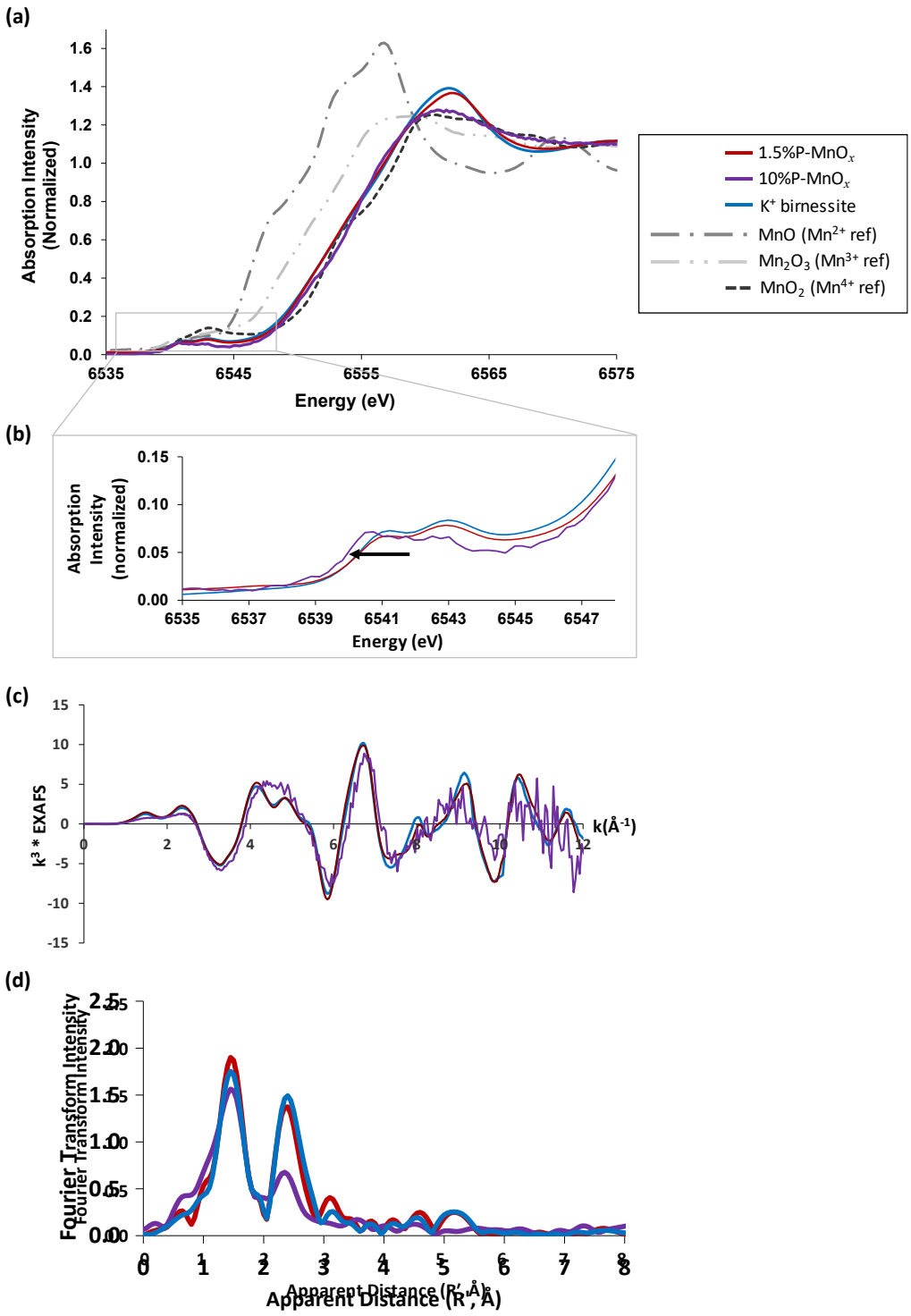

Figure 3.3: Mn K-edge XAS data comparing 10%P-MnO_x to birnessite structures. Data is presented as: **(a)** XANES, **(b)** expanded pre-edge region with an arrow indicating the peak shift in 10%P-MnO_x, **(c)** k^3-weighted EXAFS, and **(d)** Fourier Transform of the EXAFS. Data was collected on: K^+ birnessite (*blue*), 1.5%Pi-MnO_x (*red*), 10%P-MnO_x (*purple*), MnO (*medium grey*, a Mn^{2+} reference), Mn_2O_3 (*light grey*, a Mn^{3+} reference), and MnO_2 (*dark grey*, a Mn^{4+} reference). Materials with > 1.5 %P doping were significantly different to birnessite, and were therefore not analysed further.

3.2.1.3 Synthesis of K^+ birnessite

Potassium birnessite was prepared according to a method previously described by Galliot[88-89]. The synthesis involved heating potassium permanganate ($KMnO_4$) in a muffle furnace (800°C, 12 h), separating the K^+ birnessite product by filtration using water as an eluent, then drying at room temperature. The phase and chemical composition of the product was confirmed by XRD and elemental analysis to be consistent with the material described by Galliot[88-89].

3.2.1.4 Synthesis of pyrolusite

The synthesis of pyrolusite involved mixing $KMnO_4$ (0.45 g in 40mL of water), HCl (1 mL, 10 M) and titanium foil, and heating in an autoclave (140°C, 12 h). The phase and chemical composition of the pyrolusite product was confirmed by XRD and elemental analysis to be consistent within error of commercially purchased pyrolusite (Sigma-Aldrich, ref: 529664).

3.2.2 Inductively coupled plasma–atomic emission spectroscopy (ICP-AES)

ICP-AES was used to measure the manganese and phosphate content of the MnO_x materials. In preparation for analysis, a known quantity (0.1 g) of each manganese oxide was heated (90±5°C, 2 h) in nitric acid (HNO_3, 70%, 10 mL) and hydrogen peroxide (H_2O_2, 30%, 15 mL).[90] The solution was cooled and diluted 1 in 10. The ICP-AES analysis was carried using a Varian Liberty Series II and a calibration curve (R = 0.999) generated from 3 standards (5, 25 and 50 ppm).

3.2.3 Ion chromatography (IC)

IC was used to measure the manganese and sodium content of the manganese oxide materials. Samples were dissolved using the procedure described in **§ 3.2.2**, and analysed with a Metrohm 930 flex using a standard cation exchange column (METROSEP C6-250/4.0).

3.2.4 X-ray absorption spectroscopy (XAS)

Manganese (Mn) K-edge XAS spectra were collected on the multipole wiggler XAS beamline (12-ID) at the ANSTO Australian Synchrotron, Melbourne. The Australian Synchrotron has an electron beam energy of 3.0 GeV and beam current of 200 mA (maintained in top-up mode). All samples were analysed in a liquid helium cryostat held

below 10 K. Manganese oxide samples were collected in transmission mode using He-filled OKEN ionisation chambers, and the MnO_x/Ce^{IV} samples were collected in fluorescence mode using a solid-state 100-element Ge detector. The edge energy (E, defined as the first inflection point of the main absorption peak) of each collected spectrum was aligned to a manganese foil reference that was calibrated to 6539 eV. The raw data collected from the beamline was converted in *Sakura*[91], and analysed in *Athena*[92] (normalise, background subtraction, E calibration) and *Artemis*[92] (EXAFS data fitting). The oxidation states of the manganese oxide materials were calculated from the relative edge positions of the samples and manganese oxide reference samples.

3.2.4.1 Preparation of manganese oxide samples for XAS

The standard manganese oxide samples were prepared for XAS analysis by grinding the MnO_x (7-10 mg) together with cellulose (100 mg) and sealing the sample into a 1 mm thin Al spacer with 63.5 μM Kapton tape.[93] These samples were analysed by XAS in transmission mode.

3.2.4.2 Preparation of 0%Pi-MnO_x in hypochlorite for XAS

The 0%Pi-MnO_x in hypochlorite sample was prepared for XAS analysis by fast freezing (in liquid nitrogen in a specially designed plastic sample holder) an aliquot of the Mn^{2+} in the hypochlorite synthesis solution after 1.5 min of reaction. Spectra collected on samples freeze quenched at times shorter than 1.5 mins showed substantial Mn^{2+} remaining.

3.2.4.3 Preparation of screen-printed electrodes for XAS

The screen-printed electrodes were mounted directly onto the XAS sample rod using 63.5 μM Kapton tape and analysed in fluorescence mode.

3.2.4.4 Preparation of MnO_x/Ce^{IV} samples for XAS

The reaction of MnO_x with the Ce^{IV} chemical oxidant was studied at different time points (0, 1 and 48 h) by quenching the suspension at the required time in a −20°C freezer and freeze-drying in preparation for XAS analysis. A new suspension was prepared for each time point. Each suspension was prepared in a 50 mL Falcon tube and contained the MnO_x sample (ca. 10 mg for 0%Pi-MnO_x or 0%Pi-MnO_x, and 5 mg for K^+ birnessite), Ce^{IV} oxidant ($(NH_4)_2Ce(NO_3)_6$, 0.2 g) and water (5 mL). After the suspension had completely frozen (∼24 h in the freezer), it was freeze dried using a 'CRYODOS−50' freeze dryer (*ca.* 0.240 mBar, -50°C) until all the solvent had evaporated (∼24 h).

The MnO_x/Ce^{IV} samples were prepared for XAS analysis by grinding the MnO_x/Ce^{IV} together with cellulose (diluted 1 in 3) and sealing the sample into a 1 mm thin Al spacer with 63.5 μM Kapton tape. These samples were analysed by XAS in fluorescence mode.

As the Ce L_1-edge may interfere with the Mn K-edge, samples of Ce^{III} and Ce^{IV} were analysed in the Mn K-edge region to determine the possible extent of Ce spectral interference. The Ce^{IV} sample was prepared for XAS analysis as a 1 in 300 dilution of $(NH_4)_2Ce(NO_3)_6$ in cellulose. The Ce^{III} sample was synthesised by reacting an aqueous solution of $(NH_4)_2Ce(NO_3)_6$ with zinc powder, then freeze quenching the solution in liquid nitrogen. To minimise the interference from the Ce L_1-edge, the Ce^{IV} concentration was reduced from 0.675 g in 5 mL of water (*i.e.* the quantity used in the *ex situ* water oxidation experiments, **§ 3.2.8**) to the reduced concentration of 0.2 g in 5 mL of water, as stated above. The XANES data for the reduced Ce concentration MnO_x/Ce^{IV} samples showed insignificant interference from the Ce L_1 edge (**§**).

3.2.5 Powder X-ray diffraction (XRD)

XRD samples were prepared as pressed powder mounts (*ca.* 1 g). The XRD analyses were carried out using a Siemens D5000 diffractometer θ:2θ goniometer, with a copper anode X-ray tube (λ = 0.154 nm). Samples were scanned between 1.3 and 65.38 (2θ) at 0.028 increments at a rate of 2.4 s per increment. XRD data were analysed with Microsoft Excel.

3.2.6 Transmission electron microscopy (TEM)

High resolution (HR-) and bright field (BF-) TEM was performed using an aberration corrected transmission electron microscope, Titan (FEI Company) at 300 kV at LeRoy Eyring Center for Solid State Science at Arizona State University. The imaging condition was tuned to so-called negative Cs imaging condition. In this case, spherical aberration Cs = -15 μm and the defocus C1 ~ 20 nm. The images were acquired using the single electron detection camera K2 (Gatan, Inc.) under 'counted' mode. The dose rate was kept at 10 electrons/pixel/s to minimize the potential electron beam induced vacancies.

3.2.7 Brunauer-Emmett-Teller (BET)

The specific surface area for each MnO_x was determined using multipoint BET.[94] In this method; the metal oxides powders where degassed at 150°C overnight, then N_2 adsorption and desorption isotherms (at 77 K) were obtained with a TriStar II Series Micrometrics.

3.2.8 Chemical water oxidation using Ce^{IV}

The Frey, Wiechen and Kurtz[16, 95-96] analytical method was used to determine the *ex situ* water oxidation efficiency of the manganese oxides. This method is advantageous as it does not require mechanical, chemical or thermal treatment of the samples in preparation for analysis. The Frey, Wiechen and Kurtz method is considered one of the least ambiguous techniques to test for manganese oxide water oxidation catalysis as Ce^{IV} is a single electron oxidant with a high enough potential for water oxidation (*viz.* oxidation potential of approximately +1.6 V *vs.* normal hydrogen electrode, NHE).[16, 95, 97] Importantly, ^{18}O labelling has shown that the oxygen produced in reactions between manganese oxides and Ce^{IV} originates from the water solvent.[97]

Following the Frey, Wiechen and Kurtz method; each reaction solution consisted of the MnO_x (ca. 10 mg for 0%Pi-MnO_x and 1.5%Pi-MnO_x and 5 mg for K^+ birnessite and pyrolusite) and Ce^{IV} oxidant ($(NH_4)_2Ce(NO_3)_6$, 0.675 g) mixed with water (5 mL) in a Labco Exetainer vial (12 mL, flat bottomed, non-evacuated, double wadded cap). At the time steps of 10, 20 and 60 min; 0.5 mL of the sample vial headspace was hand drawn for gas chromatography (GC) analysis.

Molecular oxygen (O_2) and nitrogen (N_2) were measured using a Shimadzu GC-2014 equipped with a Restek Molesieve 5Å 80/100 column (10 ft × 2.1 mm) and thermal conductivity detector (TCD). The column temperature was 70°C, the injector temperature was 150°C and the TCD was 380°C. Ultrahigh purity He was used as a carrier gas at a flow rate of 30 mL min^{-1}.

3.2.9 Electrochemical experiments

All electrochemical experiments were conducted on a Voltalab PGZ301 potentiostat, using a two-compartment electrochemical H-cell (with a P4 (10−16 μm) ceramic frit), and a 3-electrode system. The anodic H-cell compartment contained the Ag|AgCl (3 M NaCl) reference electrode and the working electrode, and the cathodic compartment contained the platinum mesh auxiliary electrode. A 3D printed electrode holder kept the working and reference electrodes a constant 3-4 mm distance apart. The manganese oxide materials were analysed/operated in phosphate buffer (sodium dihydrogen orthophosphate dihydrate, 0.1 M, pH 7), which was stirred using a magnetic stirrer bar (550 rpm). CV data was

collected in triplicate (*i.e.* 3 different electrodes of the same sample) and the first cycle of the median scan is presented. The CV data was measured at a scan rate of 20 mV sec^{-1}. The background current was measured using a blank electrode. All experimental potential differences are reported against the experimental reference electrode (Ag|AgCl, 3 M NaCl). Other potential differences quoted herein are reported against the explicitly stated reference electrode.

3.2.10 Fabrication of electrodes for electrochemical experiments

The 0%Pi-MnO_x and 1.5%Pi-MnO_x samples were adhered onto fluorine doped tin oxide (FTO) coated glass electrodes (denoted as FTO/glass) using a screen-printing method, and K^+ birnessite was adhered using a drop cast method. The sample loading of each sample onto an electrode was approximately 1.6×10^{-6} mol Mn.

3.2.10.1 Screen-printing

In this procedure, the MnO_x sample (500 mg) was ball-milled (250 rpm for 4 h) into a fine powder and oven dried (110°C, 2 h) to remove water which is immiscible with the solvents used in the printing paste. To make the printing paste (2.5 w/v% suspension of MnO_x in ethanol); terpineol (solvent; 10 g) and ethyl cellulose (binding agent; 1 g dispersed in 20 mL ethanol) were added to the MnO_x (in the ball mill jar) and the milling step (250 rpm for 4 h) was repeated to give a uniform paste or 'ink'. The sample was ready to screen-print once the optimal viscosity was obtained by *in vacuo* removal of the ethanol solvent (175 mbar, 60°C). Each sample was screen-printed inside the designated laser engraved area (6 × 6 mm, electroactive area = 0.36 cm^2) of a large FTO/glass sheet (8 Ω/sq., *Dyesol TEC8 Glass Plates*). The screen-printed large FTO/glass sheet was initially dried on a hotplate (120°C, < 15 mins), then sintered at 500°C (< 10 mins) on a sintering hotplate. In preparation for electrochemical experiments, individual electrodes were cut from the large FTO/glass sheet. The electroactive area was isolated by masking with a polyimide tape (Kapton) to ensure the measured activity was due solely to the cobalt oxide material.

It is additionally noted from the above that: (i) fluorine-doped tin oxide coated glass is also typically abbreviated as F:SnO_2. (ii) 20 squares (4 × 4 mm, electroactive area = 0.16 cm^2) of screen-printed sample were pasted per large FTO/glass sheet, with each square of CoO_x material corresponding to one electrode. (iii) Heating to 500°C incinerates the ethyl cellulose and terpineol components and leaves pores in the printed thin film.

3.2.10.2 Drop casting

The drop cast K^+ birnessite sample was prepared by sonicating a suspension of the MnO_x in solvent (4 mg MnO_x in 200 µL of 50/50 water/isopropanol), micropipetting an aliquot of the suspension (10 µL) onto the electrode, and then drying the electrode at room temperature for at least 30 mins.

3.2.11 Measurement of MnO_x oxidative strength by reaction with hydrogen peroxide (H_2O_2)

MnO_x materials were tested for their reactivity with H_2O_2 as a by-proxy measure of their thermodynamic stability, as described in detail in reference 98. The manganese oxide (*ca.* 0.2 mmol Mn) was suspended in either nitric acid (HNO_3, 0.1 M, 7 mL, pH 1), acetate buffer (sodium acetate, 0.1 M, pH 3, pH 5, 7 mL) or a phosphate buffer (sodium hydrogen phosphate, 0.1 M, pH 7, pH 10 or pH 13, 7 mL), and then mixed with hydrogen peroxide (H_2O_2, 25%, 2 mL, 16.4 mmol). The gas evolved from the reaction was measured (in mL) using a gas burette. Reactions were monitored for a period of 30 mins.

The gas burette is constructed of a standard graduated glass burette tube that has a removable Quickfit glass stopper at the top of the burette, a modular stopcock at the bottom of the burette which leads to the burette tip and the open Quickfit socket joint glass connector, as well as a graduated glass inset that sits within the main burette tube and is used to measure the gas input through the open connector. For the experiments herein, (i) the MnO_x suspension was placed in a Quickfit round bottom flask (100 mL), (ii) the round bottom flask was connected to the gas burette using a custom glass piece with a Quickfit connector to the round bottom flask, a Quickfit ball joint connector to the gas burette, and a silicon septum input for needles, (iii) H_2O_2 was input into the round bottom flask though the silicon septum using a needle and syringe, and (iv) the gas evolution was measured by recording how high the glass inset was pushed within the tube (recorded in mL). A photograph of the experimental set up is given in **Figure 3.4**.

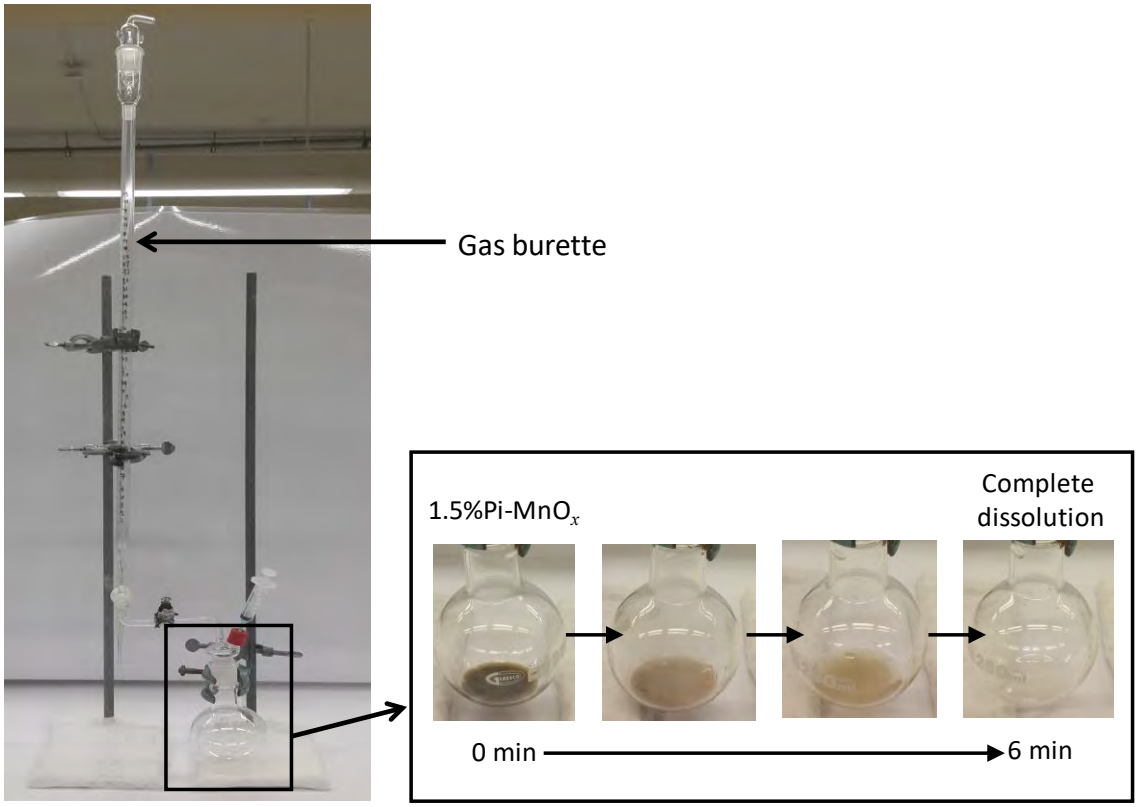

Figure 3.4: Photograph of the gas burette used to quantify the gas evolved from the MnO_x/H_2O_2 reaction, and sequential photographs illustrating the dissolution of 1.5%Pi-MnO_x over the course of 6 mins. Gas evolution was measured for 30 mins despite gas evolution typically ceasing once the manganese oxides dissolved.

3.3 Results and analysis

3.3.1 Structural characterisation of the manganese oxide series

Two distinctively disordered birnessite-like manganese oxides (0%Pi-MnO_x and 1.5%Pi-MnO_x) were synthesised and compared with highly ordered K^+ birnessite and pyrolusite in a comprehensive structure *versus* function characterisation. The empirical formulas of the birnessite-like manganese oxides are given in **§ 3.2.1**. The intra- and interlayer structures of 0%Pi-MnO_x, 1.5%Pi-MnO_x, K^+ birnessite and pyrolusite were characterised using XAS, XRD and TEM. The BET technique for measuring surface area was used to estimate particle size, and subsequently used to correlate particle size with structural disorder.

3.3.1.1 XAS

Figure 3.5 presents the XANES and EXAFS spectra collected on each manganese oxide material. The EXAFS of 0%Pi-MnO_x and 1.5%Pi-MnO_x are very similar to the EXAFS of K^+ birnessite, which indicates that 0%Pi-MnO_x and 1.5%Pi-MnO_x have an intralayer structure of edge-sharing MnO_6 octahedra sheets similar to K^+ birnessite. While the EXAFS of K^+ birnessite and 0%Pi-MnO_x are nearly indistinguishable, there are minor differences between the EXAFS of K^+ birnessite and 1.5%Pi-MnO_x. These differences are indicated by the three arrows in **Figure 3.5b-ii**.

These differences have been quantified using EXAFS fitting, which are provided in **Tables 3.1, 3.2 and 3.3** and are visually represented in **Figure 3.6 a-c** for K^+ birnessite, 0%Pi-MnO_x and 1.5%Pi-MnO_x, respectively. The EXAFS of the three samples have been fit using the same 7 paths to facilitate a structural comparison between the materials. This simplified fit estimates the EXAFS with a limited number of paths for the higher order peaks between 4 Å < R′ < 6 Å (a region which typically requires 20 or more co-dependent paths for a good fit). A simplified 3-path EXAFS fit of pyrolusite has been provided for comparison in **Table 3.4** and **Figure 3.6 d**.

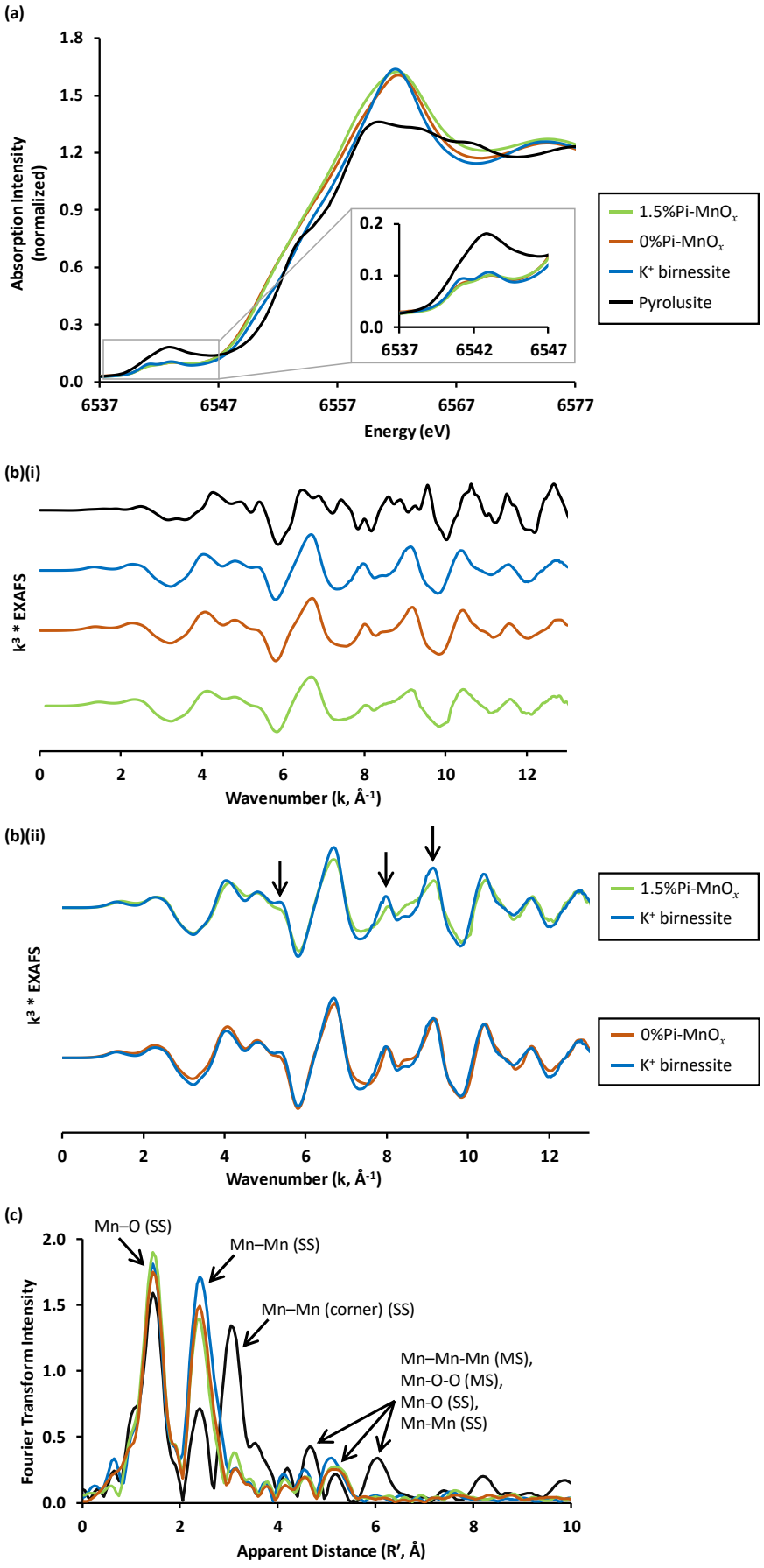

(Figure and caption continued over page)

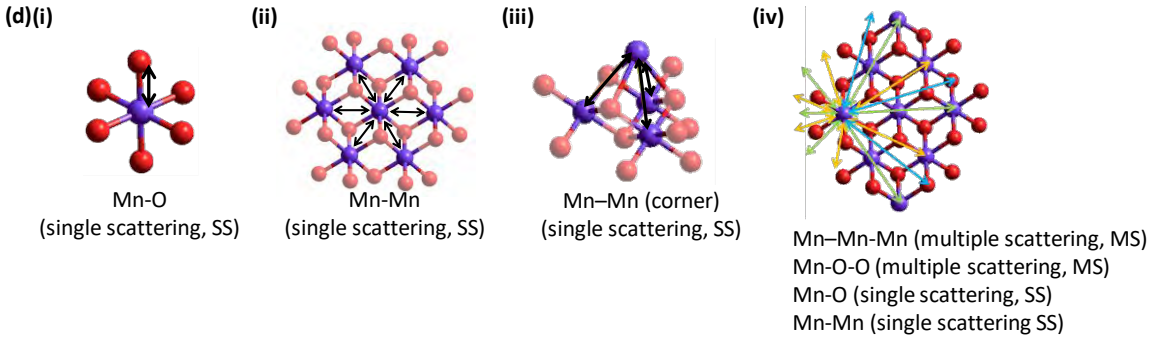

Figure 3.5: Mn K-edge XAS data collected on the manganese oxide samples. Data is presented as: **(a)** XANES with expanded pre-edge inset, **(b)** k^3-weighted EXAFS as **(i)** stack plot and **(ii)** overlapped plot (labelled with arrows identifying EXAFS differences), **(c)** Fourier Transform of the EXAFS (labelled with the bonding interactions responsible for the dominant birnessite peaks), and **(d)** structural models for the bonding interactions labelled in **(c)**. Data was collected on: pyrolusite (*black*), K^+ birnessite (*blue*), 1.5%Pi-MnO_x (*green*), and 0%Pi-MnO_x (*orange*).

Table 3.1: EXAFS fit of K^+ birnessite using 7 paths.

Shell	**Coordination number**	**Scatterer distance (Å)**	**σ^2 (Å^2)**
Mn^{4+}-O	6	1.90	0.0035
Mn^{3+}/Mn^{2+}-O interlayer	1	2.35	0.0052
Mn^{4+}-Mn^{4+} edge	6	2.88	0.006
Mn^{4+}-$Mn^{3+/4+}$ corner	1	3.45	0.0021
Mn^{4+}-O	6	3.58	0.0083
Mn-Mn/Mn-Mn-Mn estimate*	6 estimate*	4.95	0.0129
Mn-Mn/Mn-Mn-Mn estimate*	6 estimate*	5.99	0.0124
Parameters for this fit: $S_0^2 = 0.643^{\dagger}$, ΔE_0 = -2.89 eV, χ^2 = 301, R-factor = 0.015			

*Long-range interactions are difficult to effectively model with a limited number of paths as a larger number of single and multiple scattering paths constructively and destructively interfere to produce the EXAFS at longer ranges.

†This S_0^2 value is smaller than the generally accepted range of 0.7 to 1. However, this small value has been accepted because this is a comparative fit and not an independent fit.

Table 3.2: EXAFS fit of 0%Pi-MnO_x using 7 paths.

Shell	**Coordination number**	**Scatterer distance (Å)**	**σ^2 (Å^2)**
Mn^{4+}-O	6	1.90	0.0024
Mn^{3+}/Mn^{2+}-O interlayer	1	2.41	0.0119
Mn^{4+}-Mn^{4+} edge	6	2.88	0.0048
Mn^{4+}-$Mn^{3+/4+}$ corner	1	3.46	0.0041
Mn^{4+}-O	8	4.61	0.0059
Mn-Mn/Mn-Mn-Mn estimate*	6 estimate	4.94	0.0106
Mn-Mn/Mn-Mn-Mn estimate*	12 estimate*	5.52	0.006
Parameters for this fit: $S_0^2 = 0.509^{\dagger}$, $\Delta E_0 = 8.767$ eV, $\chi^2 = 14774$, R-factor = 0.014			

*Long-range interactions are difficult to effectively model with a limited number of paths as a larger number of single and multiple scattering paths constructively and destructively interfere to produce the EXAFS at longer ranges.

†This S_0^2 value is smaller than the generally accepted range of 0.7 to 1. However, this small value has been accepted because this is a comparative fit and not an independent fit.

Table 3.3: EXAFS fit of 1.5%Pi-MnO_x using 7 paths.

Shell	**Coordination number**	**Scatterer distance (Å)**	**σ^2 (Å^2)**
Mn^{4+}-O	6	1.90	0.0036
Mn^{3+}/Mn^{2+}-O interlayer	1	2.34	0.0054
Mn^{4+}-Mn^{4+} edge	6	2.88	0.0077
Mn^{4+}-$Mn^{3+/4+}$ corner	1	3.44	0.00083‡
Mn^{4+}-O	6	3.58	0.0098
Mn-Mn/Mn-Mn-Mn estimate*	6 estimate	4.92	0.0136
Mn-Mn/Mn-Mn-Mn estimate*	6 estimate*	5.99	0.008
Parameters for this fit: $S_0^2 = 0.608^{\dagger}$, $\Delta E_0 = -2.804$ eV, $\chi^2 = 1035$, R-factor = 0.017			

*Long-range interactions are difficult to effectively model with a limited number of paths as a larger number of single and multiple scattering paths constructively and destructively interfere to produce the EXAFS at longer ranges.

†This S_0^2 value is smaller than the generally accepted range of 0.7 to 1. However, this small value has been accepted because this is a comparative fit and not an independent fit.

‡This Debye-Waller factor is too small for a satisfactory fit. While 1.5%Pi-MnO_x is better fit with a higher coordination number, both K^+ birnessite and 1.5%Pi-MnO_x fits set N = 1 to facilitate a structural comparison between three materials.

Table 3.4: EXAFS fit of pyrolusite using 3 paths.*

Shell	**Coordination number**	**Scatterer distance (Å)**	**σ^2 (Å^2)**
Mn^{4+}-O	6	1.89	0.00057
Mn^{3+}/Mn^{2+}-O interlayer	2	2.87	0.00144
Mn^{4+}-$Mn^{3+/4+}$ corner	8	3.42	0.00203
Parameters for this fit: S_0^2 = 0.459, ΔE_0 = 6.710 eV, χ^2 = 2705, R-factor = 0.058			

*This is a simplified fit intended to fit the first 3 dominant peaks in the Fourier transform at R′ = 1.9, 2.9 and 3.4 Å.

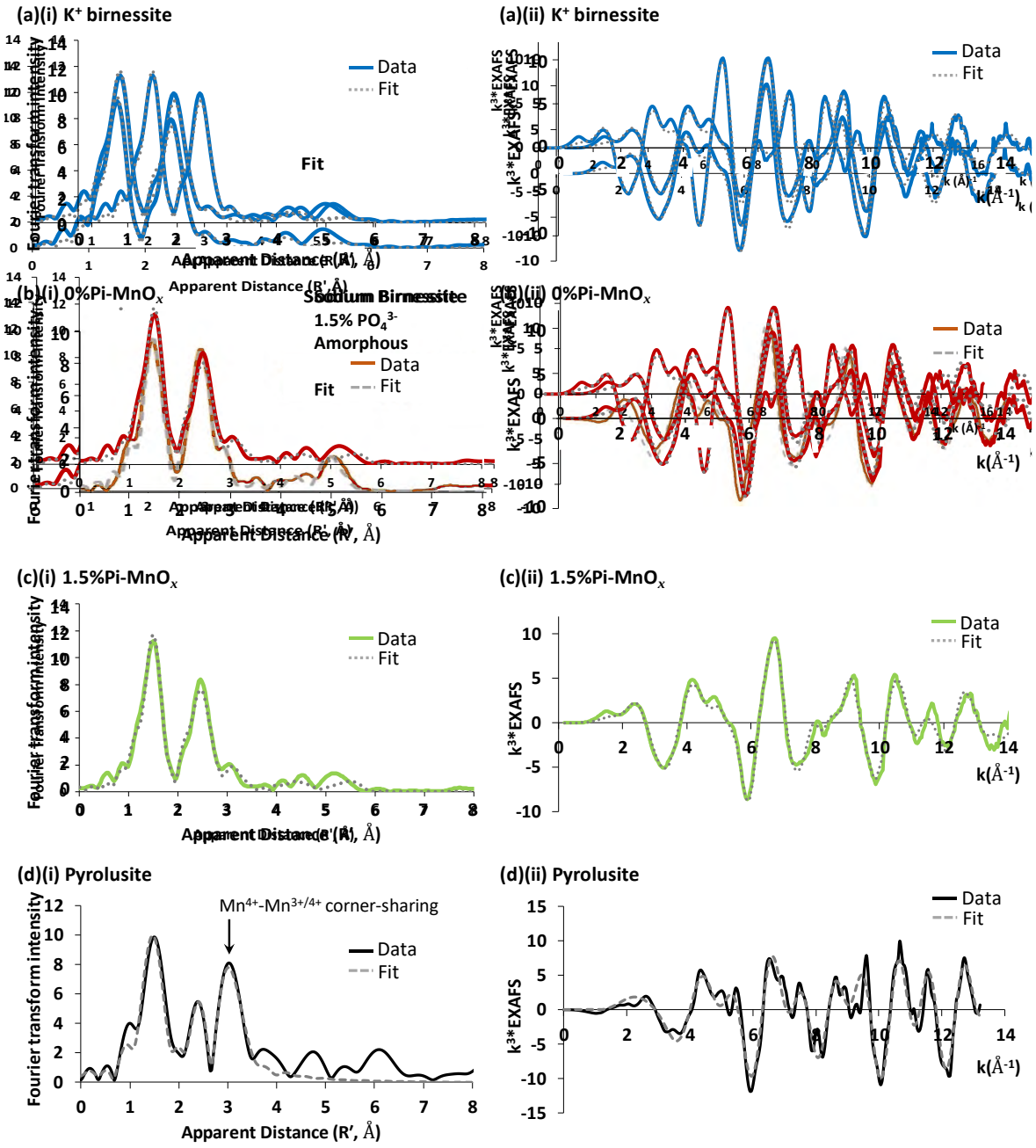

Figure 3.6: Visual representation of the EXAFS fits for the manganese oxides. The fits are associated with the EXAFS fits described in **Tables 3.1**, **3.2**, **3.3** and **3.4**. Data is presented as: **(a)** K^+ birnessite, **(b)** 0%Pi-MnO_x and **(c)** 1.5%Pi-MnO_x, **(d)** pyrolusite, with **(i)** the Fourier transform of the EXAFS in R′-space and **(ii)** the EXAFS in k-space. The arrow in **(d)(i)** indicates the peak attributed to the Mn^{4+}-$Mn^{3+/4+}$ corner-sharing vector.

In **(b)(ii)**, the 0%Pi-MnO_x material exhibits systematic differences between the fit and the data as the sample is less ordered than K^+ birnessite and the EXAFS likely have contributions from Mn^{2+} interlayer ions which interfere and dampen the EXAFS. The parameters of the fit, including S_0^2, reflect these effects.

The EXAFS differences between K^+ birnessite and 1.5%Pi-MnO_x are largely explained by the varying contribution from the Mn^{4+}-$Mn^{3+/4+}$ corner-sharing vector at 3.45 Å (**Figure 3.5d-iii**). The EXAFS fits show that the Debye-Waller factor is lower in 1.5%Pi-MnO_x (**Table 3.3**) than in K^+ birnessite (**Table 3.1**) when the coordination number for the Mn^{4+}-$Mn^{3+/4+}$ corner-sharing vector was fixed to 1 in both samples. This difference suggests that there is variation in the disorder over this vector, and that 1.5%Pi-MnO_x is likely better fit with a higher coordination number. The pyrolusite sample shows the spectroscopic effect the Mn^{4+}-$Mn^{3+/4+}$ corner-sharing vector has on the EXAFS (indicated by the arrow in **Figure 3.6d-i**), with the $R' \approx 3.5$ peak dominant for pyrolusite which has many corner sharing vectors. However, it is difficult to distinguish the exact structural effect increased disorder and higher coordination number have on the structure of 1.5%Pi-MnO_x. One possibility is that phosphate doping has altered the number of Mn centres in the interlayer.

The average oxidation state of the K^+ birnessite, 0%Pi-MnO_x and 1.5%Pi-MnO_x samples was estimated by comparing their respective edge positions in the XANES to those of closely related manganese oxide reference compounds at two absorption intensities of 0.5 and 1.0. An example of this oxidation state calculation is presented in **Figure 3.7** for the normalized absorption intensity of 0.5.[99] While this method does not provide an absolute measurement of oxidation state as many factors influence the position and shape of the edge, it does allow the three materials to be considered relative to each other.

The edge positions for K^+ birnessite, 0%Pi-MnO_x and 1.5%Pi-MnO_x are consistent with each sample having an average Mn oxidation state of +3.9, +3.7 and +3.7, respectively (**Tables 3.5 and 3.6**). Indra and Driess et al. have previously noted that effective water oxidation catalysts likely requires the presence of Mn sites with a mean Mn oxidation state between 3.5 and 3.8.[100] As such, the 0%Pi-MnO_x and 1.5%Pi-MnO_x materials have a good Mn^{III} : Mn^{IV} ratio for catalysis. As the 0%Pi-MnO_x and 1.5%Pi-MnO_x materials are synthesised in oxidising hypochlorite conditions, it was relevant to analyse the oxidation state of these materials under formation conditions. The oxidation state of the 0%Pi-MnO_x material under the oxidising synthetic conditions was calculated to be + 4.0 (**Figure 3.7c**; *red* trace).

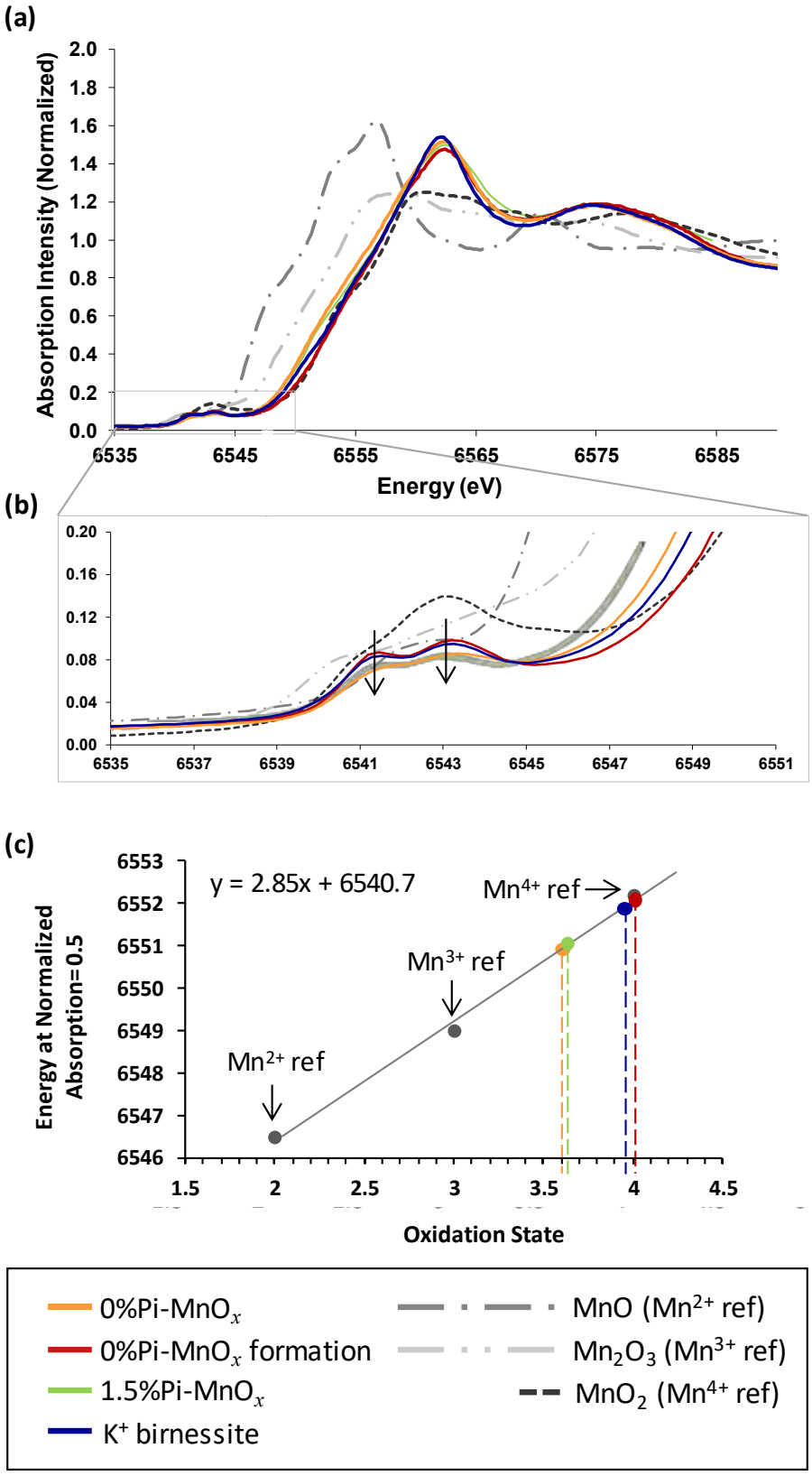

Figure 3.7: Oxidation state calculation for the manganese oxide materials. Data is presented as: **(a)** XANES, **(b)** pre-edge, and **(c)** calibration curve with linear regression. Data was collected on: K^+ birnessite (*blue*), 1.5%Pi-MnO_x (*green*), 0%Pi-MnO_x (*orange*), and 0%Pi-MnO_x formation (*red*).

Table 3.5: Oxidation state calculation for the manganese oxide materials. Energy values (eV) corresponding to the normalized absorption values of 0.5 and 1.0 for the manganese oxide references and samples.

	Energy (eV)						
	Mn 2+ reference	**Mn 3+ reference**	**Mn 4+ reference**	**0%Pi-MnO_x**	**0%Pi-MnO_x formation**	**1.5%Pi-MnO_x**	**K^+ birnessite**
0.5 abs	6546.5	6549.0	6552.2	6551.0	6552.2	6551.1	6552.0
1 abs	6549.8	6553.8	6557.5	6556.6	6557.0	6556.6	6557.0

Table 3.6: Oxidation states calculated from the absorption intensities of 0.5 and 1.0, and an average of these values.

	Oxidation state at 0.5	**Oxidation state at 1.0**	**Average Oxidation state**
0%Pi-MnO_x	3.6	3.8	3.7
0%Pi-MnO_x formation	4.0	3.9	4.0
1.5%Pi-MnO_x	3.6	3.8	3.7
K^+ birnessite	4.0	3.9	3.9

The K^+ birnessite, 0%Pi-MnO_x and 1.5%Pi-MnO_x samples have a pre-edge feature containing two peaks, which is typical of Mn^{IV} in birnessite-like materials (**Figure 3.7b**).[4, 17, 86, 95, 101] However, the pre-edge peak intensities for 1.5%Pi-MnO_x and 0%Pi-MnO_x (**Figure 3.7b**) are slightly reduced relative to K^+ birnessite. This peak dampening is evident in other catalytic materials studied *ex situ*, such as Spiccia's biomimetic birnessite-like catalyst which was made from molecular precursors in Nafion and is described as a manganese–oxo complex with a cubic $\{Mn_4O_4\}^{7+}$ core (**Figure 3.8b**).[13,102] The most likely explanation for the dampening of this feature is the presence of Mn^{2+} in the interlayer where Mn^{2+} has a very weak pre-edge and has a dilution effect on the Mn(III/IV) signal.[103] Cations of K^+ and Mn^{2+} are typically found in the interlayer as they compensate negative charges from intralayer Mn vacancies.[78] Intralayer vacancies are a form of structural disorder (**Figure 3.2b**) which are frequently associated with highly active manganese oxide materials.[4, 18, 54, 61-64, 104-105]

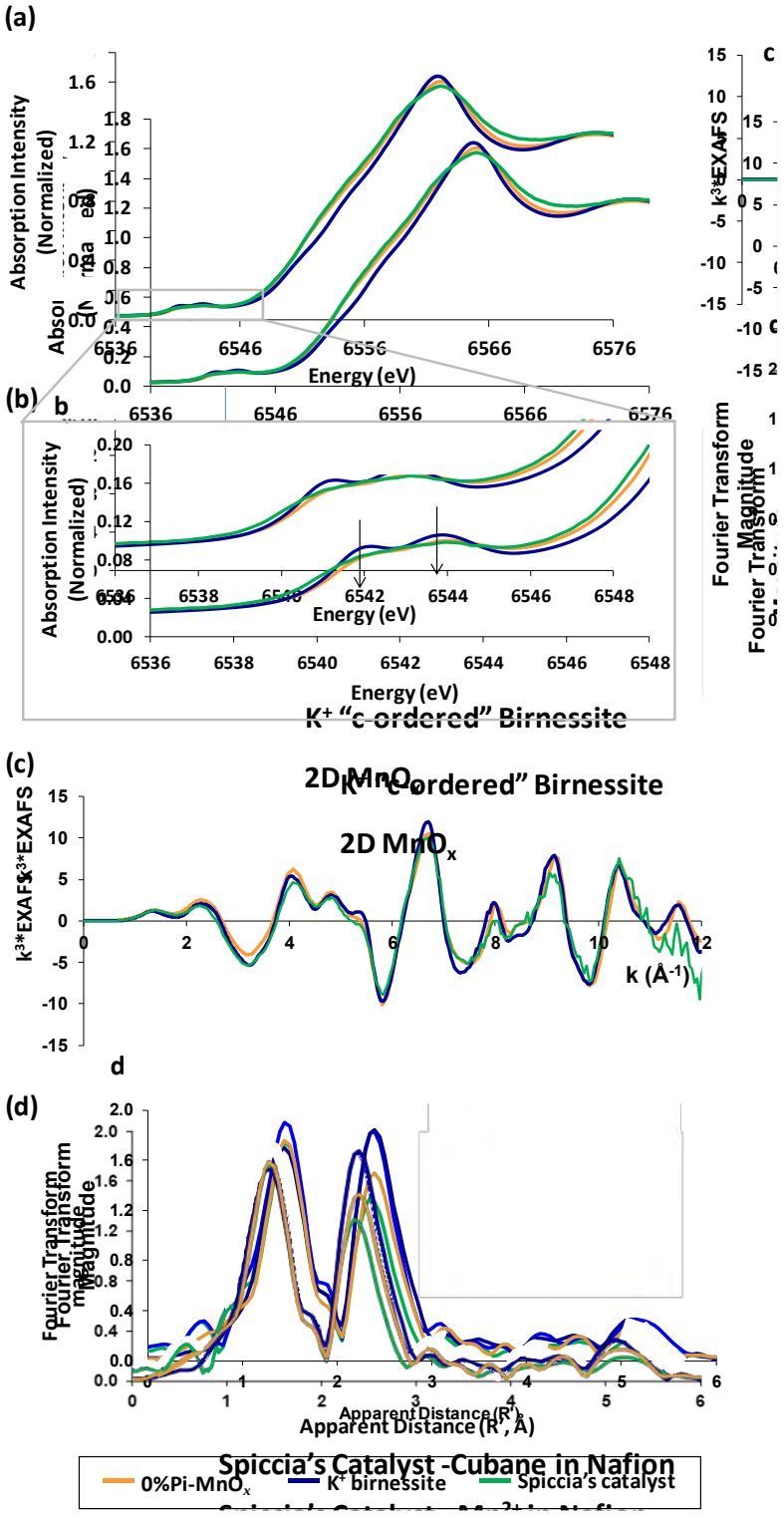

Figure 3.8: Comparison of 0%Pi-MnO_x and K^+ birnessite to Spiccia's catalyst. The data is presented as: **(a)** XANES, **(b)** pre-edge, **(c)** k-weighted EXAFS, and **(d)** Fourier transform of the EXAFS. Data was collected on: K^+ birnessite (*blue*), 0%Pi-MnO_x (*orange*), and Spiccia's catalyst (*green*)[79, 86, 106-111]. While the EXAFS of Spiccia's catalyst are almost indistinguishable from the EXAFS of 0%Pi-MnO_x and K^+ birnessite, the XANES and pre-edges of Spiccia's catalyst more closely resemble 0%Pi-MnO_x than K^+ birnessite.

3.3.1.2 XRD

Although XAS is a key technique for intralayer structural characterization (*i.e.* distances less than 6 Å), the technique needs to be complemented with diffraction and electron microscopy analyses to provide information on nano-structuring, interlayer stacking, and crystallinity. **Figure 3.9** presents the XRD patterns obtained from the K^+ birnessite, 0%Pi-MnO_x, 1.5%Pi-MnO_x, and pyrolusite samples, with a comparison made to a biogenetic MnO_x formed by L. disophora SP6 reported by Jurgenson[104].

The 1.5%Pi-MnO_x sample did not produce any diffraction peaks and is thus described as an amorphous material. Note that the amorphous nature of 1.5%Pi-MnO_x was confirmed by TEM (**§ 3.3.1.3**). The K^+ birnessite sample has a diffraction pattern typical of ordered layered birnessite, with sharp well-defined peaks. The dominant (00l) and (002) peaks are associated with very ordered *c*-directional stacking of the MnO_x sheets.[112] The diffraction patterns of K^+ birnessite and pyrolusite are consistent with multiple previous reports in literature[56, 112-114] and with XRD simulations based on their known crystal structures (**Figure 3.10 g** and **h** for the comparison between experimental K^+ birnessite and its crystalline simulation).

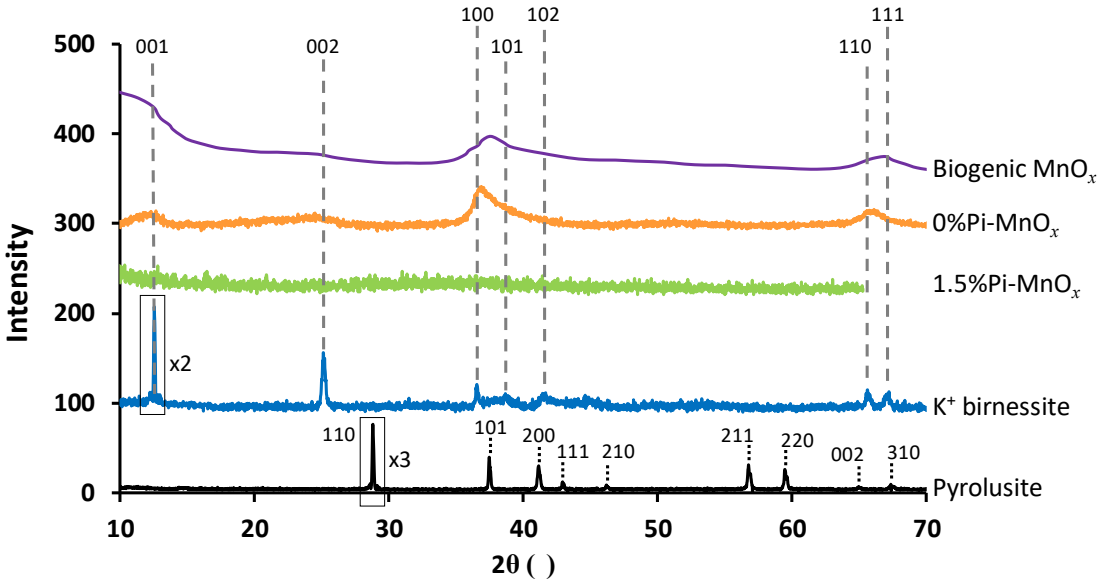

Figure 3.9: XRD spectra for the manganese oxides and a biogenic manganese oxide sample. Data is presented as: pyrolusite (*black*), K^+ birnessite (*blue*), 1.5%Pi-MnO_x (*green*), 0%Pi-MnO_x (*orange*) and a biogenic MnO_x from Jurgenson[104] (*purple*). The boxed peaks in the K^+ birnessite and pyrolusite spectra indicate that the intensity of those peaks have been scaled by half and a third (respectively) such that the shown peaks are 2× and 3× larger than they appear in the figure (respectively).

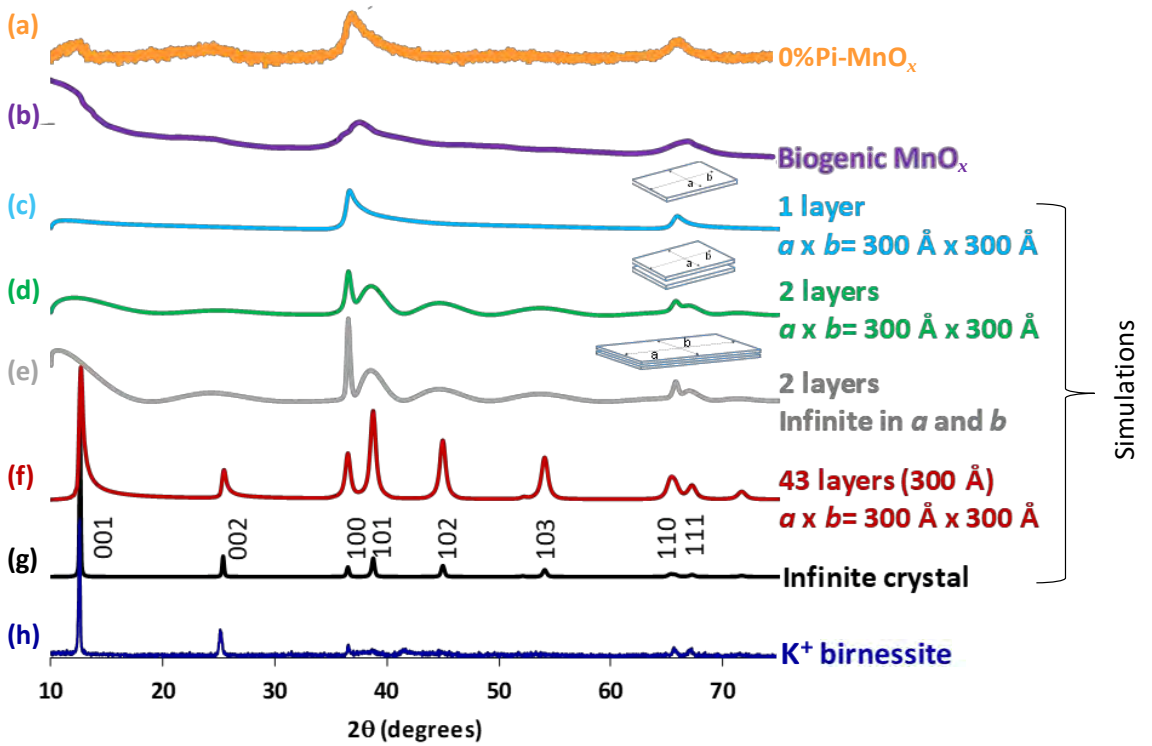

Figure 3.10: XRD spectra for selected manganese oxide samples, with simulated spectra of birnessite with different lattice dimensions. Data was collected on: **(a)** 0%Pi-MnO_x (*orange*), **(b)** biogenic MnO_x from Jurgenson[104] (*purple*), and **(h)** K^+ birnessite (*blue*), with simulations of birnessite with varying lattice dimensions provided in **(c)**, **(d)**, **(e)**, **(f)** and **(g)**.

The 0%Pi-MnO_x and biogenic MnO_x samples have very similar XRD patterns, and both samples are generally consistent with a birnessite structure with absent 00ℓ peaks. Jurgensen et al. have previously noted that the dominant 00ℓ peaks in K^+ birnessite are associated with *c*-directional stacking and that these peaks can be dampened or completely removed if the *c*-directional stacking is limited to a few (2-3) MnO_x layers.[104-105] This effect is supported by the simulations in **Figure 3.10** (comparison between **g** and **e**), which show the 00ℓ peaks become broader when the *c*-directional stacking is limited to 43 layers and are absent when the *c*-directional stacking is limited to 2 layers. Therefore, the 0%Pi-MnO_x and biogenic MnO_x samples likely have reduced interlayer dimensions of < 3 layers and thereby have an approximate 2D structure. The biogenic MnO_x has also previously been characterised by Jurgensen et al. as having Mn intralayer vacancies, which further suggests that 0%Pi-MnO_x Mn intralayer vacancies. Therefore, 0%Pi-MnO_x likely features both intra- and interlayer disorder (**Figure 3.2c**).

The signals for the 0%Pi-MnO_x and biogenic MnO_x samples are weak and broad and indicate that the crystallinity of these materials is perturbed from the highly ordered K^+ birnessite standard. The source of these perturbations can include the finite size of the crystals, the limited stacking coherence in the interlayers due to the finite number of layers, or disordered layer stacking (*i.e.* turbostratic disorder, **Figure 3.2b**).[103-105, 115-116] The cause of the perturbed crystallinity in the 0%Pi-MnO_x and the biogenic MnO_x samples was determined from the series of simulations presented in **Figure 3.10**; where the crystallite dimensions were selectively limited in the $a \times b \times c$ directions.

As stated above, systematically limiting the *c*-directional stacking systematically reduced the relative intensities of the (00ℓ) peaks (comparison of **Figure 3.10g** and **e**). Limiting the crystallite dimensions to 300 Å in *a*, *b* and *c* resulted in peak broadening across the whole spectrum (comparison of **Figure 3.10 g** and **f**). It was determined that the 0%Pi-MnO_x and the biogenic MnO_x samples were best fit with a finite intralayer dimension of approximately 30 nanometers and a reduced interlayer dimension of < 3 layers (*i.e.* a structure like classical 2D materials). The 0%Pi-MnO_x sample is very structurally similar to the biogenic MnO_x sample, and is likely a good functional mimic of this sample.

3.3.1.3 TEM

The XRD analysis could not independently confirm the 2D nature of the 0%Pi-MnO_x material as the analysis could permit disordered or buckled MnO_x layers to be interpreted as a finite number of layers. Thus, TEM was required to confirm that the material was comprised of a few MnO_x layers rather than exhibiting turbostratic stacking (**Figure 3.2b**).

Figure 3.11 presents the BF-TEM and HR-TEM images obtained from pyrolusite, K^+ birnessite, 0%Pi-MnO_x and 1.5%Pi-MnO_x. The TEM images of K^+ birnessite (**Figure 3.11b**) show aggregates of well-defined, highly crystalline, spherical-like particles of sizes around 40 nm. The 0%Pi-MnO_x material (**Figure 3.11c**) shows nanocrystalline aggregates with a curved sheet morphology (**Figure 3.11b**). This curved sheet morphology is known to be characteristic of 2D materials, such as graphene and other 2D metal oxides described in literature[40, 117-122]. The TEM images of 1.5%Pi-MnO_x (**Figure 3.11d**) show no indication of any lattice fringes typical of crystalline or periodic features and is consistent with the sample being described as amorphous.

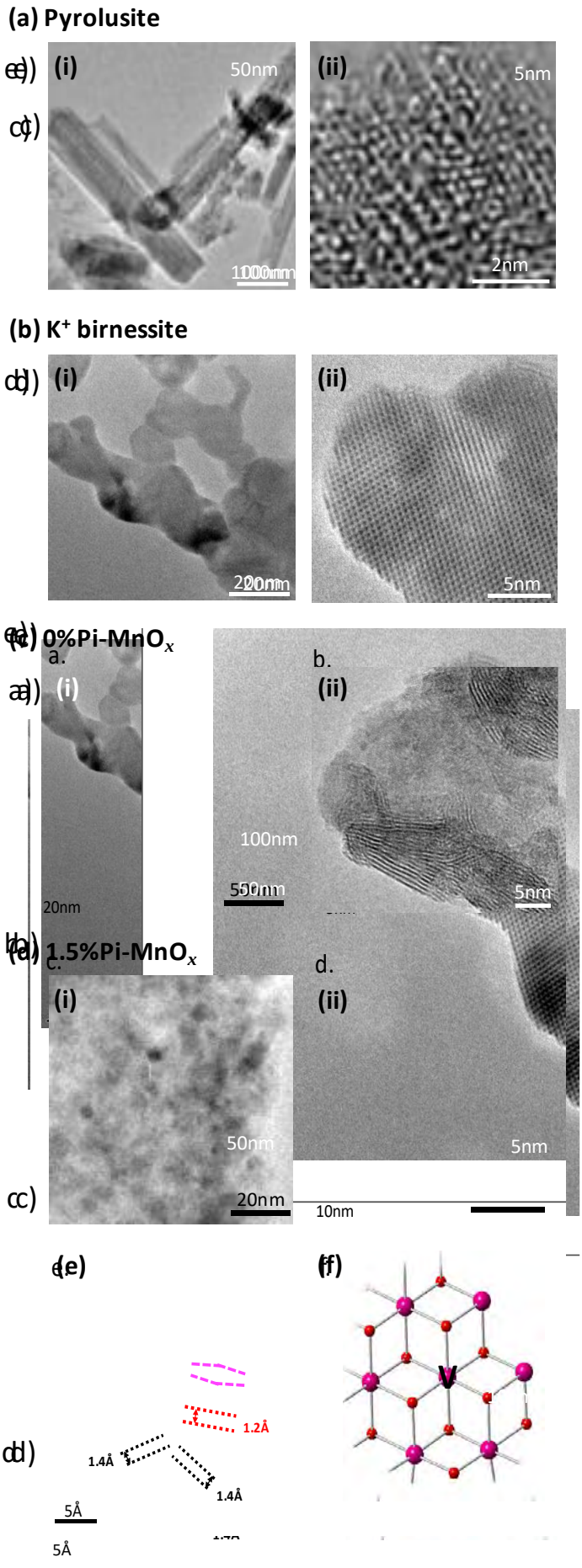

Figure 3.11: TEM images of the manganese oxide samples. Data is presented as: **(i)** BR-TEM and **(ii)** HR-TEM images of **(a)** pyrolusite, **(b)** K^+ birnessite, **(c)** 0%Pi-MnO_x, and **(d)** 1.5%Pi-MnO_x. **(e)** Atomically resolved image of 0%Pi-MnO_x viewed along [001] orientation. **(f)** Ball and stick atomic model of MnO_x with *pink*= manganese, *red* = oxygen. The image illustrates that the original *red* oxygen atoms distort from their shown position to the dashed position due to a Mn vacancy in the structure.

3.3.1.4 BET

Figure 3.12 presents the surface area measurements obtained for the manganese oxide series using the BET technique. It is well-understood that surface area is an important consideration when studying kinetics as increasing the surface area (*i.e.* reducing particle size) will typically increase the reaction rate. However, particle size can also have significant effect on the internal structure and thermodynamic stability of the material as it is typically found that nanosized materials often have high surface energies[123-125] and increased internal structural strain[126-128]. More specifically; a reduction in particle size typically causes a greater energy difference between the bulk of the material and the surface of the material[123-125] and causes significant structural deviations from the ideal bond-length and bond-angles[126-128].

The results in **Figure 3.12** show that 1.5%Pi-MnO_x and 0%Pi-MnO_x have the largest surface areas, with measured surface areas of 291 and 224 $m^2\ g^{-1}$, respectively. As 1.5%Pi-MnO_x and 0%Pi-MnO_x have the largest surface areas, it is likely that these samples have the smallest particle sizes and greatest internal structural disorder. This assumption correlates with the combined XAS, XRD and TEM findings which determined that both samples contain internal structural disorder (*i.e.* bond-length and bond-angle distortions) caused by Mn intralayer vacancies, with 1.5%Pi-MnO_x being a truly amorphous phase and 0%Pi-MnO_x having < 3 MnO_x layers with curled MnO_x lattice fringes.

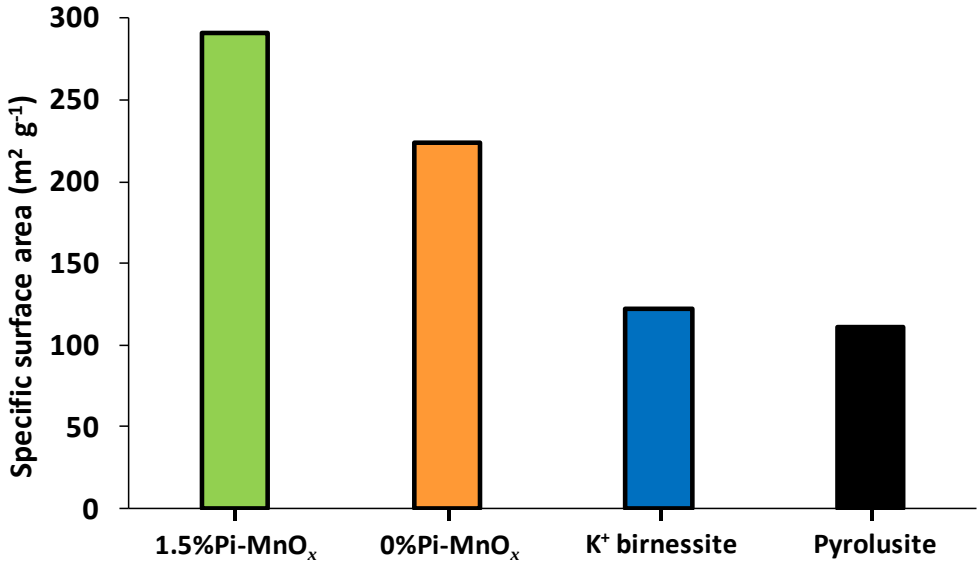

Figure 3.12: BET surface area measurements of the manganese oxide samples. Data was collected on: pyrolusite, K^+ birnessite, 0%Pi-MnO_x, and 1.5%Pi-MnO_x.

3.3.2 Activity for water oxidation

There are two established methods for measuring the 'true' reactivity of heterogeneous water oxidation catalysts: (i) an *ex situ* test implementing a chemical oxidant such as Ce^{IV}, and (ii) *in situ* electrocatalytic studies where the material is immobilized on an electrode.[16, 95-97] Herein, both *ex situ* and *in situ* methods were used to determine the relative water oxidation reactivity of the birnessite series. As 0%Pi-MnO_x is known to decompose to hollandite upon heating to 300°C and reversibly absorb/desorb water below 200°C, it was important to minimize the mechanical, chemical and thermal treatment of this sample during the preparation for activity studies to preserve the 2D nature and manganese ratio in the sample.

3.3.2.1 *Ex situ* measurement of water oxidation catalysis by reaction with Ce^{IV}

The Frey, Wiechen and Kurtz *ex situ* method of measuring water oxidation activity involves reacting a sample with Ce^{IV} and measuring the quantity of oxygen evolved.[16, 95-96] This method allows the 'as synthesised' manganese oxide materials to be analysed without further mechanical or chemical processing. **Figure 3.13** presents the quantity of O_2 evolved after 60 mins of reaction between each manganese oxide and Ce^{IV}. The 0%Pi-MnO_x material performed the largest number of water oxidation turnovers, with an activity 2.2 times more than 1.5%Pi-MnO_x, 23 times more than K^+ birnessite and 15 times more than pyrolusite.

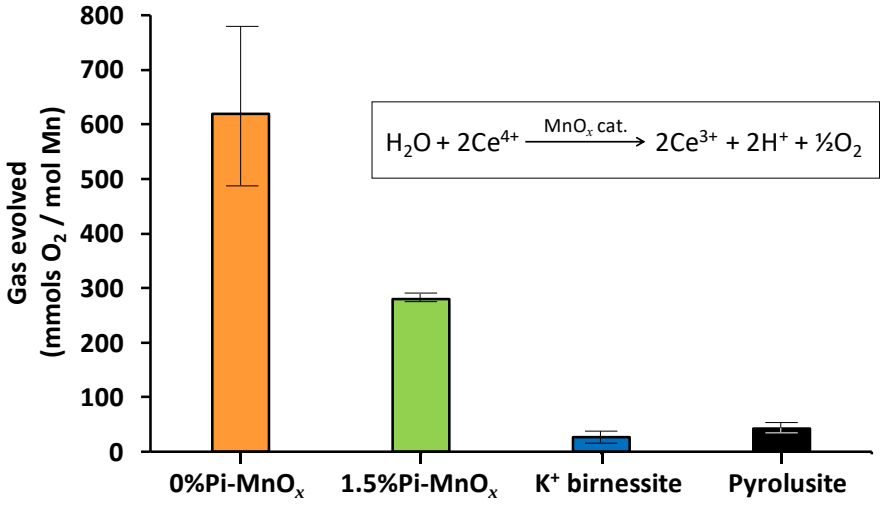

Figure 3.13: Activity of the manganese oxide samples for the *ex situ* water oxidation reaction using Ce^{IV} as a chemical oxidant. The inset chemical equation describes the redox process occurring during the reaction.[16, 95-96] Error bar indicates $\pm$ 1 standard deviation (σ). A relatively large error is associated with the 0%Pi-MnO_x sample as there are inherently

larger errors associated with measuring larger volumes than smaller volumes of gas, and this is reflected in the standard deviation of the data.

3.3.2.2 Electrochemical analysis The manganese oxides were analysed by CV, which is a direct *in situ* electrochemical measurement of water oxidation catalysis. Both XAS (**Figure 3.14**) and TEM (**Figure 3.15**) were performed on the screen-printed 0%Pi-MnO_x material to ensure the material was unchanged in the screen-printing process. The XANES (**Figure 3.14 a** and **b**) and EXAFS (**Figure 3.14c**) spectra were the same before and after screen-printing, which indicates that the manganese oxide phase did not change phase in the screen-printing process.

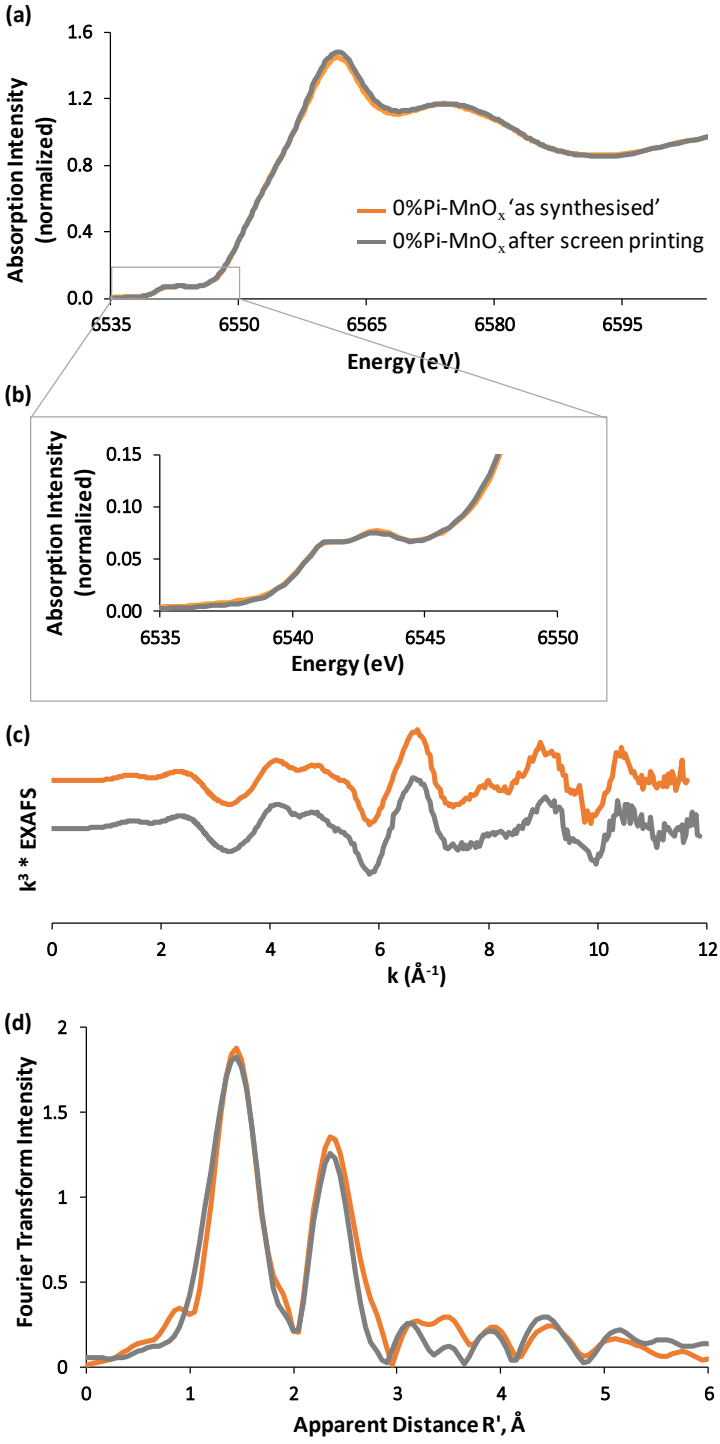

Figure 3.14: Mn K-edge XAS data of screen-printed 0%Pi-MnO_x. Data is presented as: **(a)** XANES, **(b)** expanded pre-edge, **(c)** k^3-weighted EXAFS, **(d)** Fourier transform of the EXAFS. Data was collected on: 0%Pi-MnO_x 'as synthesised' before screen printing (*orange*), and 0%Pi-MnO_x after screen printing (*grey*).

The TEM image (**Figure 3.15a**) before screen-printing shows clearly defined nano-sized polycrystalline regions and the TEM image after screen-printing shows less well-defined polycrystalline regions (**Figure 3.15b**). Although the 0%Pi-MnO_x sample maintained its polycrystalline character, the change in crystallite size indicates that the manganese oxide particles agglomerated on the electrode surface. This likely occurred during the final sintering process (10 min at 500°C), which is required to improve the adhesion between the sample and the electrode. As the manganese oxide phase and the fundamental polycrystalline character of the sample did not change during the adhesion process, screen-printing was accepted as an electrode preparation method.

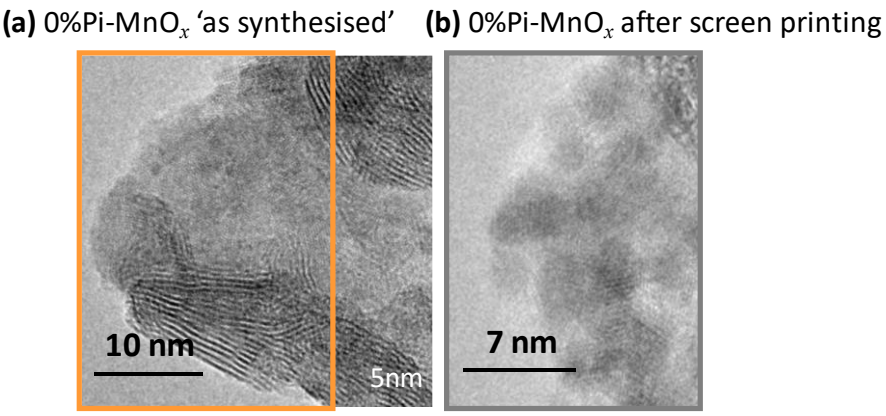

Figure 3.15: HR-TEM images of the manganese oxide samples. Data was collected on: **(a)** 0%Pi-MnO_x 'as synthesised' before screen printing (*orange*), and **(b)** 0%Pi-MnO_x after screen printing (*grey*).

Figure 3.16 presents the CV data collected on 0%Pi-MnO_x, 1.5%Pi-MnO_x and K^+ birnessite in phosphate buffer (0.1 M, pH 7). The 0%Pi-MnO_x and 1.5%Pi-MnO_x materials were both highly active for water oxidation catalysis, with the highest current density and lowest onset overpotential achieved by 0%Pi-MnO_x. While K^+ birnessite was a slightly active water oxidation catalyst (as it produced a higher current density than the blank), the disordered materials were significantly more active than the highly ordered K^+ birnessite counterpart.

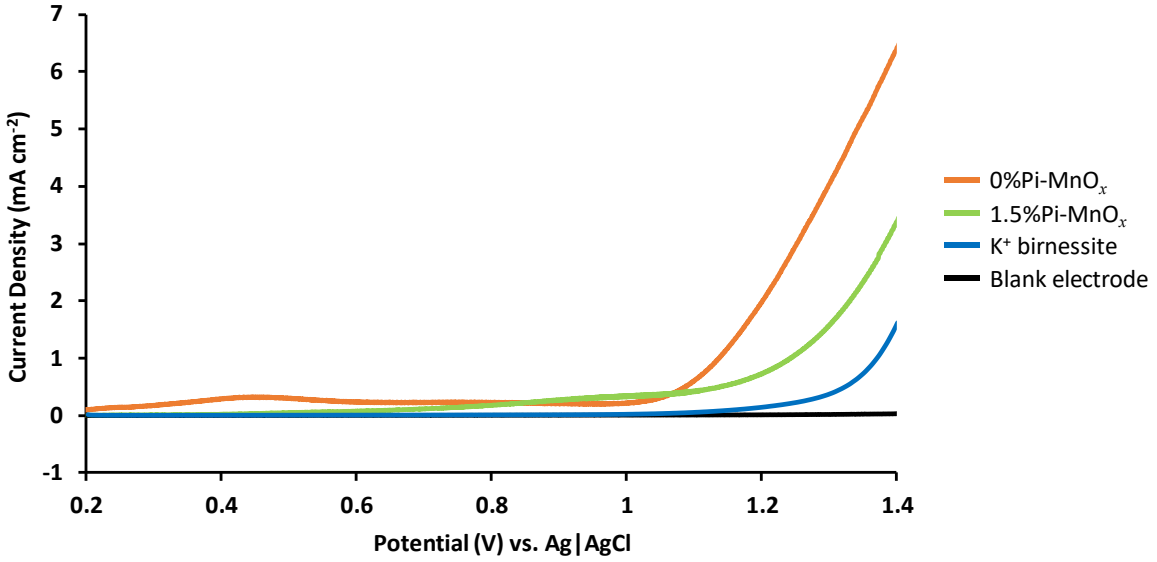

Figure 3.16: CV data collected on the manganese oxide samples. Data is presented as: 0%Pi-MnO_x (*orange*), 1.5%Pi-MnO_x (*green*), and K^+ birnessite (*blue*), with a blank electrode (*black*). The first half of the first CV cycle is shown.

Thus far, the structure *versus* activity study has shown that 0%Pi-MnO_x and 1.5%Pi-MnO_x are both more disordered and more catalytically active than ordered K^+ birnessite. Specifically, 0%Pi-MnO_x has more structural order than 1.5%Pi-MnO_x and is the most catalytically active manganese oxide in the birnessite series. To determine why 0%Pi-MnO_x was the most catalytically active sample, further experiments were conducted to examine the functionality of each manganese oxide in the water oxidation reaction. These experiments investigated the redox properties of the manganese oxides and subsequently correlated redox strength with thermodynamic stability and mode of reactivity (*i.e.* surface catalysis or bulk/volume catalysis).

The rationale for examining redox strength was three-fold. Firstly, 0%Pi-MnO_x and 1.5%Pi-MnO_x were structurally similar to biological and geological manganese oxide samples, which are known to be active in a wide variety of redox and cation-exchange reactions in nature.[56, 129] Secondly, it is generally understood that disordered materials are more easily reduced, which implies that there is a shift in the thermodynamic stability and redox potential ($\Delta G = -nFE^{\circ}_{cell}$) of these materials is association with changes to structural order.[130,98] Thirdly, mechanistic studies on similar metal oxide materials suggested that the bulk of the material was involved in the catalytic mechanism, which implied that reactivity was not solely effected by surface properties.[36, 41, 87]

A simple test using hydrogen peroxide was developed to quantify the propensity for a metal oxide to undergo reduction.[131-134] The catalyzed disproportionation and the direct oxidation of H_2O_2 by MnO_2 are described in **reaction 3.1** and **reaction 3.2**, respectively.[135-136] By measuring the efficiency for the direct oxidation of H_2O_2 (**reaction 3.2**) and the disproportionation of H_2O_2 (**reaction 3.1**) as a function of pH, it is possible to quantify the relative stability of the materials as a 'by proxy' measure of thermodynamic stability and redox potential. The catalytic disproportionation of H_2O_2 will evolve many moles of O_2 per mole of Mn, and the direct oxidation reaction will evolve approximately 1 mole of O_2 for each mole of Mn consumed.[131-133, 137] Herein, the peroxide test was performed at 6 different pH values (pH 1, 3, 5, 7, 10 and 13) to determine the pH dependence of the redox reaction, with the reactions expected to become more spontaneous at low pH as protons are consumed in the direct oxidation reaction.[98]

Catalyzed disproportionation of H_2O_2:

$$2H_2O_{2\,(aq)} \xrightarrow{MnO_x\ cat.} 2H_2O_{\,(aq)} + O_{2\,(g)} \qquad \textbf{(3.1)}$$

Direct oxidation of H_2O_2:

$$MnO_{2\,(s)} + 2e^- + 4H^+_{\,(aq)} \rightleftharpoons Mn^{2+}_{\,(aq)} + 2H_2O_{\,(aq)} \quad E^0 = +1.22\ V \qquad \textbf{(3.2a)}$$

$$O_{2\,(g)} + 2H^+_{\,(aq)} + 2e^- \rightleftharpoons H_2O_{2\,(aq)} \quad E^0 = +0.70\ V \qquad \textbf{(3.2b)}$$

Measurement of MnO_x oxidative strength by reaction with H_2O_2Figure 3.17 presents the quantity of gas evolved (measured as moles of O_2 per mole of Mn) from the reaction of H_2O_2 and MnO_x materials at pH 1, 3 5, 7, 10 and 13. As expected, more gas was evolved across the whole manganese oxide series as the pH was increased from pH 1 to 13, which indicates that the spontaneity of the oxidation reaction increases as proton concentration increased. Halving the peroxide concentration approximately halved the quantity of gas evolved (**Figure 3.18**).[98] This suggests that the disproportionation of H_2O_2 is 1st order (*i.e.* the reaction rate is proportional to H_2O_2 concentration), which is consistent with previous literature reports[131, 136, 138].

The observation that both 1.5%Pi-MnO_x and 0%Pi-MnO_x dissolved under all pH conditions indicates that these materials are stronger oxidants than either K^+ birnessite or pyrolusite. Sequential photographs of the 1.5%Pi-MnO_x dissolution are presented in **Figure 3.4**. The dissolution of 1.5%Pi-MnO_x and 0%Pi-MnO_x is consistent with these samples having evolved the least quantities of O_2 / Mn. Despite dissolving under all pH conditions, it can be seen that all four manganese oxides can act as both an oxidant and a catalyst as the pH is increased towards 13; where the stoichiometric ratio of O_2 : MnO_x indicates how much more favorable the catalytic reaction is *versus* direct oxidation.

For each pH condition, the manganese oxides can be ordered from the least to most O_2 evolved per mole of Mn as: (i) 1.5%Pi-MnO_x, (ii) 0%Pi-MnO_x, (iii) K^+ birnessite, and (iv) pyrolusite. Therefore, the manganese oxide series can be described from strongest to weakest oxidant and from least to most thermodynamically stable as: (i) 1.5%Pi-MnO_x, (ii) 0%Pi-MnO_x, (iii) K^+ birnessite, and (iv) pyrolusite. The determination that 0%Pi-MnO_x is more thermodynamically stable than 1.5%Pi-MnO_x is consistent with the structural analysis in which it was observed that 0%Pi-MnO_x is nanocrystalline and 1.5%Pi-MnO_x is amorphous. This concept is illustrated in **Figure 3.2c**.

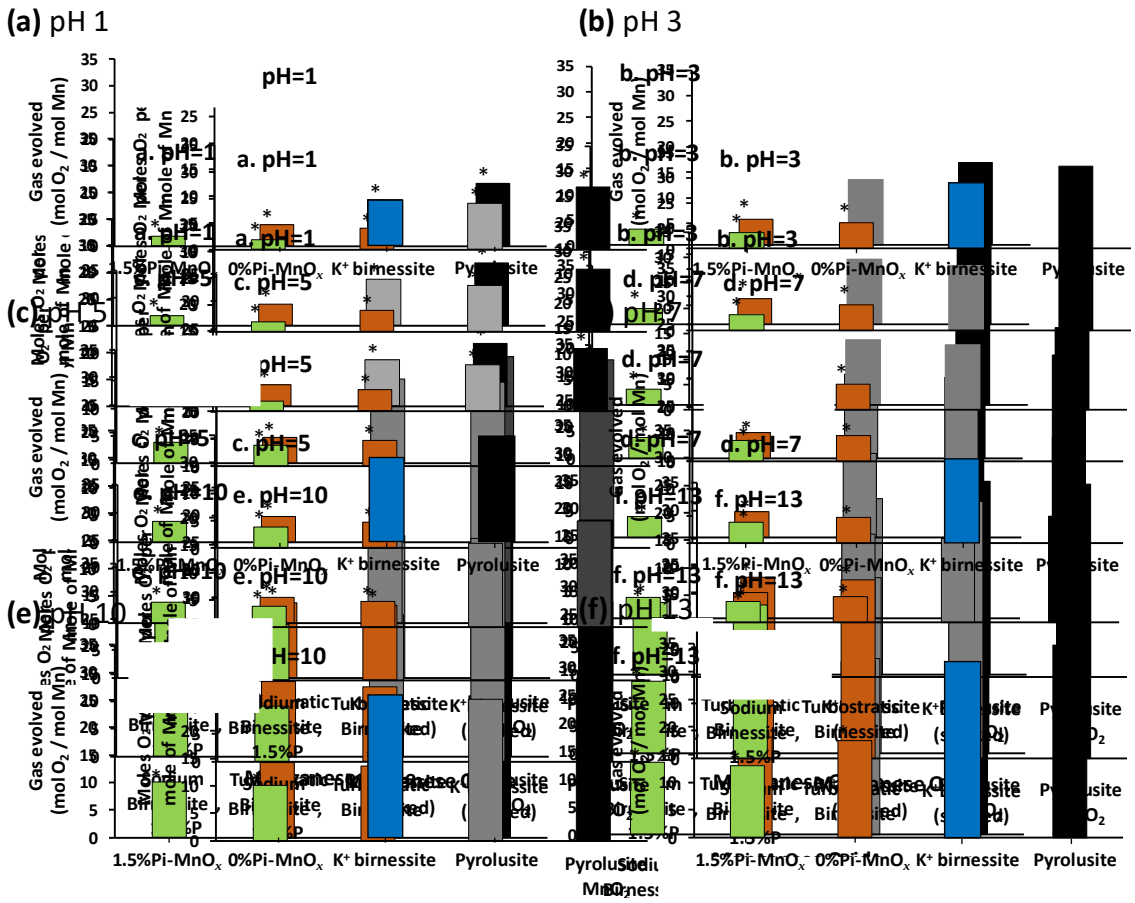

Figure 3.17: The quantity of gas evolved (measured as moles of O_2 per mole of Mn) from the reaction of H_2O_2 and MnO_x materials at pH 1, 3 5, 7, 10 and 13. Data was collected on: 1.5%Pi-MnO_x (*green*), 0%Pi-MnO_x (*orange*), K^+ birnessite (*blue*), and MnO_x (*black*). The '*' above a column indicates that a material dissolved under the test conditions of the 30 min reaction.

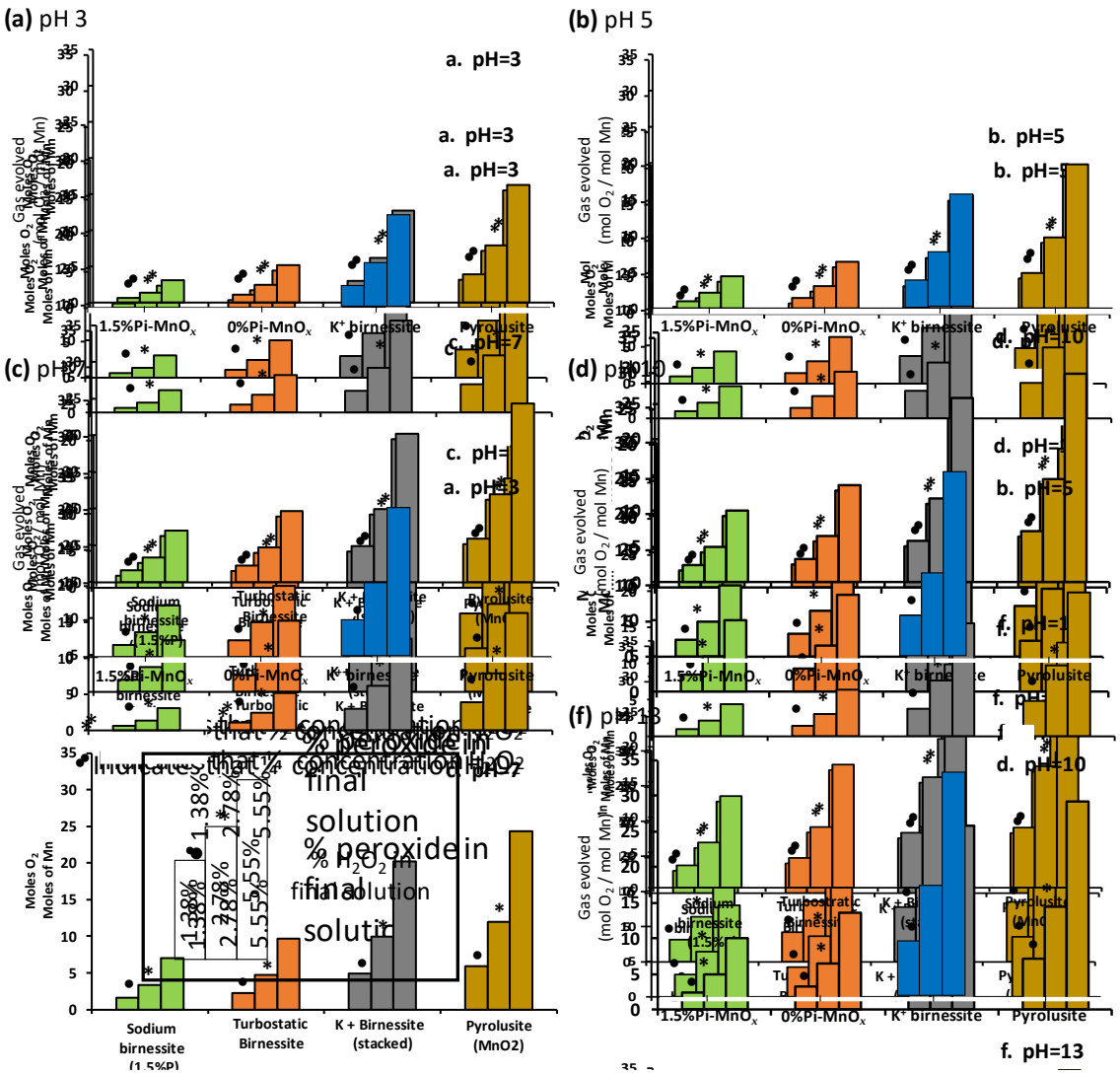

Figure 3.18: The quantity of gas evolved (measured as moles of O_2 per mole of Mn) from a reaction involving half the concentration of H_2O_2 at pH 3, 5, 7, 10 and 13. Data was collected on: 1.5%Pi-MnO_x (*green*), 0%Pi-MnO_x (*orange*), K^+ birnessite (*blue*), and pyrolusite (*gold*).

According to the results of the peroxide test, the disordered 0%Pi-MnO_x and 1.5%Pi-MnO_x samples acted as sacrificial oxidants in their reactions with H_2O_2 (*i.e.* MnO_x dissolved to Mn^{2+}). To determine whether 0%Pi-MnO_x and 1.5%Pi-MnO_x also reacted as oxidants in the water oxidation reaction, the oxidation states of the materials were tracked by XAS during the *quasi in situ* and *ex situ* water oxidation reactions.

The oxidation state conversion between the birnessite-like manganese oxide phase and the completely reduced Mn^{2+} state has previously been characterized using XAS by Hocking et al.[79] The XAS data showing this conversion has been reproduced in **Figure 3.19** with permission from reference 79. The shape and positions of the edges can be used as a fingerprint for identifying the mixed Mn^{2+} and $Mn^{3/4+}$ states in birnessite-like manganese oxides.

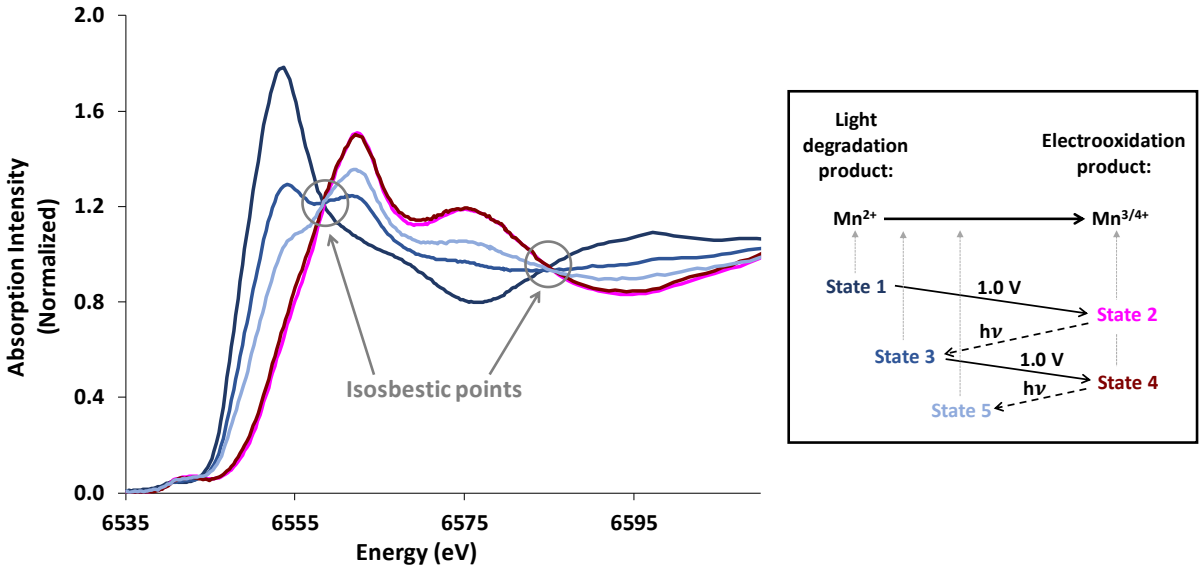

Figure 3.19: Mn K-edge XANES of a single glassy carbon electrode loaded with Nafion-coated $[Mn_4O_4L_6]^+$ (where L = diarylphosphinate) (*i.e.* a tetranuclear Mn^{2+} cluster), which has been measured in different 'states' of photochemical cycling. Data is presented as: *State 1* = the initial Mn^{2+} cluster, *State 2* = electrooxidation of electrode, *State 3* = light irradiation, *State 4* = electrooxidation of electrode, *State 5* = light irradiation. Note that electrooxidation was conducted at 1.0 V vs Ag|AgCl in 0.1 M Na_2SO_4, and light irradiation was conducted in 0.1 M Na_2SO_4 for 40 mins. Two isosbestic points are circled in the XAS data and indicate that repeated cycling between an oxidised birnessite-like state and a reduced Mn^{2+} state can be achieved. Reproduced with permission from reference 79.

In the *quasi in situ* water oxidation experiment, the screen printed 0%Pi-MnO_x material was analysed by XAS before and after CV analysis (**Figure 3.20**). The shift in edge position from a higher to a lower energy value (**Figure 3.20a**) and the general shape of the edge indicates the presence of Mn^{2+} in the screen-printed sample after CV analysis. This suggests that 0%Pi-MnO_x was undergoing a MnO_x to Mn^{2+} conversion during the *in situ* water oxidation reaction.

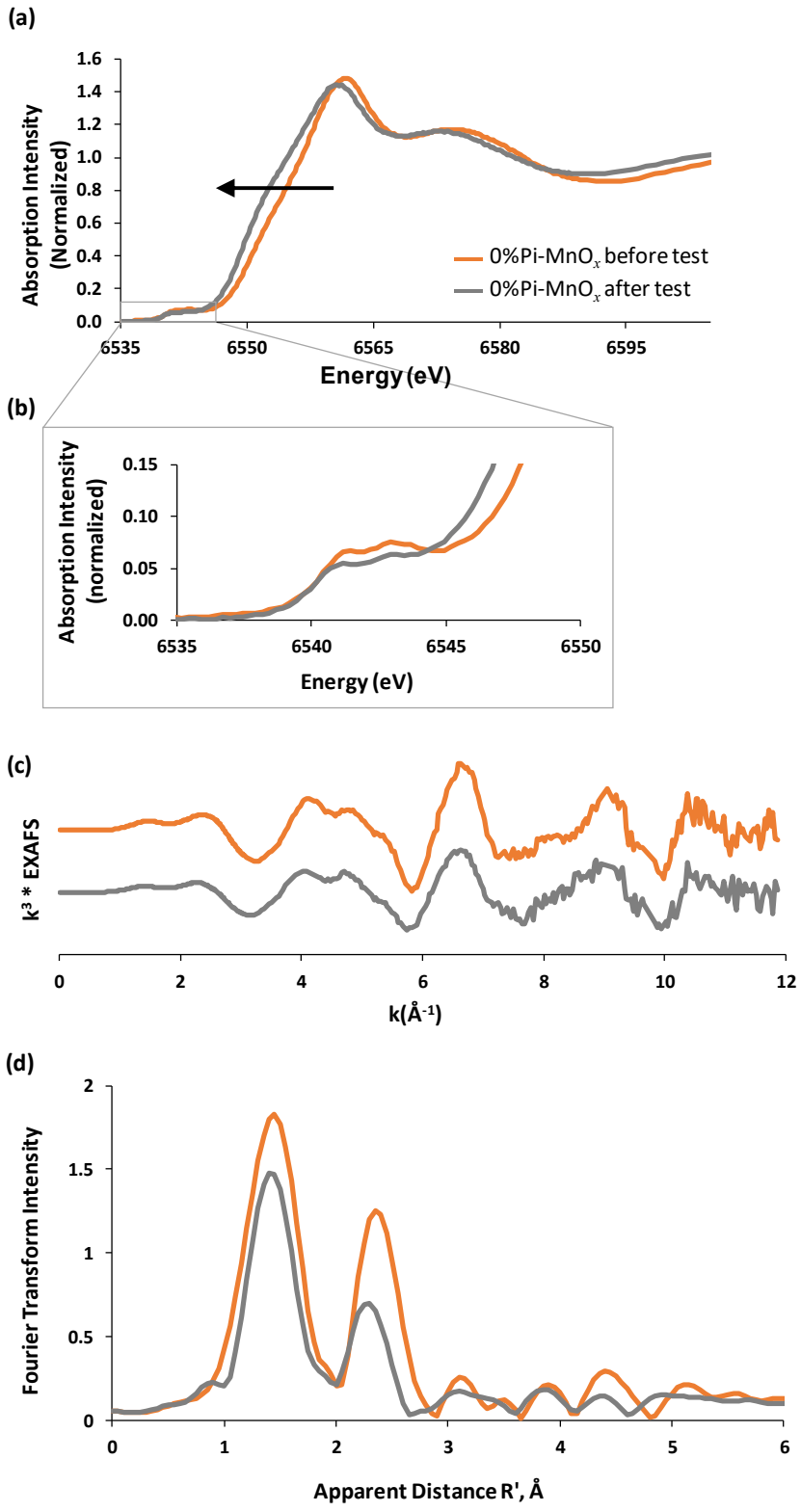

Figure 3.20: Mn K-edge XAS data for the *quasi in situ* water oxidation reaction. Data is presented as: **(a)** XANES, **(b)** expanded pre-edge, **(c)** k^3-weighted EXAFS, **(d)** Fourier transform of the EXAFS. Data was collected on: 0%Pi-MnO_x before CV analysis (*orange*), and 0%Pi-MnO_x after CV analysis (*grey*). The arrow in **(a)** shows the shift in edge position to a lower energy value, which is interpreted as the formation of Mn^{2+}.

In the *ex situ* water oxidation experiment, samples of Ce^{IV}/MnO_x were freeze quenched at time points of 0, 1 and 48 h and freeze dried for analysis by XAS. To determine the extent to which the L_1-edges of Ce^{III} and Ce^{IV} may interfere with the Mn K-edges of the Ce^{IV}/MnO_x samples, the L_1-edge of Ce^{3+} and Ce^{4+} were measured in the Mn K-edge region. **Figure 3.21** presents the raw absorption intensity XANES spectra for Ce^{III} and Ce^{IV}, with the spectra for Ce^{IV}/1.5%Pi-MnO_x added as a comparison. The low signal from the Ce L_1-edges indicates that Ce will not interfere significantly with the Mn K-edge data of the Ce^{IV}/MnO_x samples.

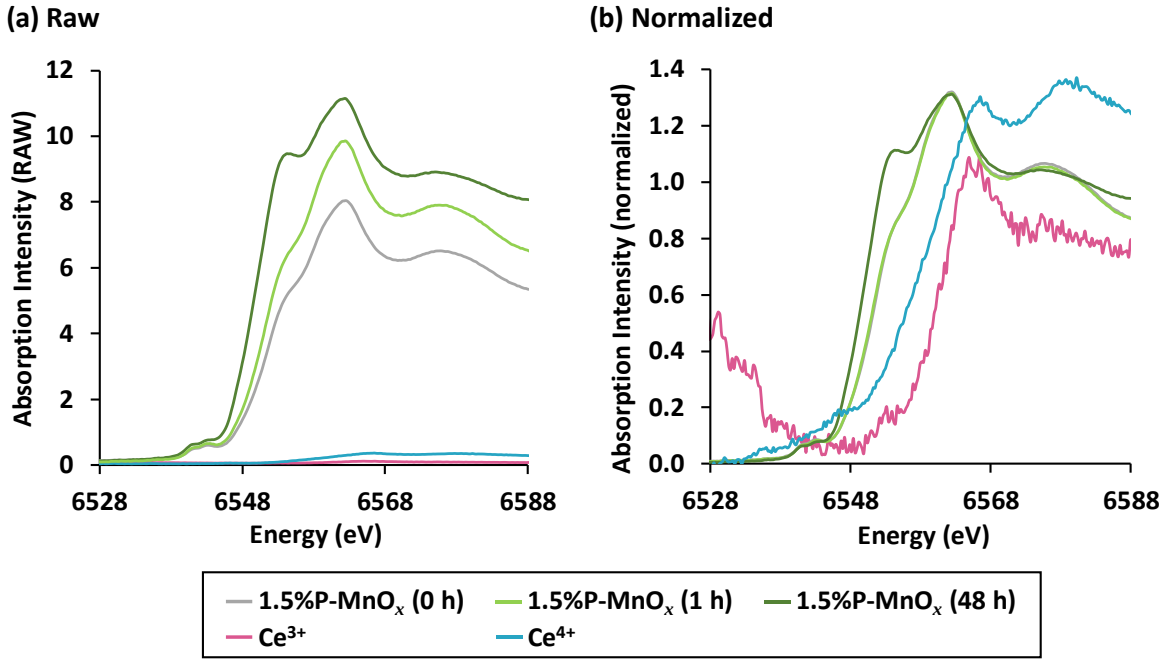

Figure 3.21: Ce L_1-edge data collected on Ce^{3+} and Ce^{4+} in the Mn K-edge region. Data is presented as: Ce^{3+} (*pink*), Ce^{4+} (*blue*), and Ce^{IV}/1.5%Pi-MnO_x (0 h – *grey*, 1 h – *light green*, 48 h – *dark green*).

The XAS analysis of the *ex situ* water oxidation experiment is given in **Figure 3.22**. The XANES of Ce^{IV}/K^+ birnessite do not show any indication of Mn^{2+} formation (**Figure 3.22a**), which indicates that K^+ birnessite does not reduce to Mn^{2+} during its limited activity in the *ex situ* water oxidation reaction. The XANES of the Ce^{IV}/0%Pi-MnO_x and Ce^{IV}/1.5%Pi-MnO_x samples (**Figure 3.22 b** and **c**, respectively) show the progressive contribution of Mn^{2+} to the edge position as defined by the fingerprint spectra presented in **Figure 3.19**. This indicates that the MnO_x phase was reduced to Mn^{2+} during the high activity of the *ex situ* water oxidation tests. The 1.5%Pi-MnO_x sample had a greater proportion of Mn^{2+} formed at the 48 h timepoint than 0%Pi-MnO_x, which is consistent with

1.5%Pi-MnO_x being more thermodynamically unstable. This XANES analysis provides strong evidence that the disordered 0%Pi-MnO_x and 1.5%Pi-MnO_x materials act -at least in part- as oxidants where Mn^{2+} is concomitantly formed as well as a catalysts in the Ce^{IV} mediated water oxidation reaction.

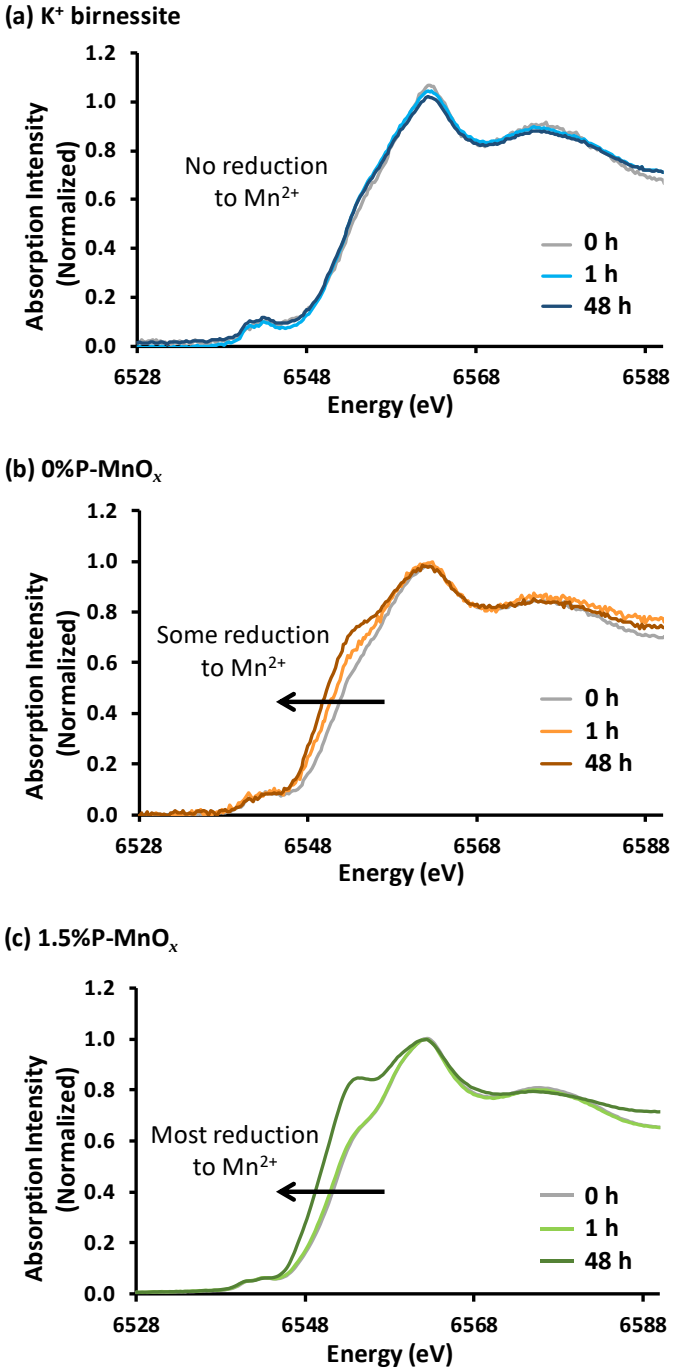

Figure 3.22: Mn K–edge XANES spectra collected on samples manganese oxide with Ce^{IV} samples. Data is presented as: **(a)** Ce^{IV}/K^+ birnessite, **(b)** Ce^{IV}/0%Pi-MnO_x, and **(c)** Ce^{IV}/1.5%Pi-MnO_x. The arrows in **(b)** and **(c)** indicate the shift in edge position to a lower energy value, which has been interpreted as the formation of Mn^{2+}.

3.4 Discussion

The study herein examined the functional effects of introducing nanoscale disorder and interlayer stacking disorder into a birnessite type manganese oxides. Both nanoscale and stacking disorder made birnessite more active for the water oxidation reaction, and made the birnessite phase less thermodynamically stable and a stronger chemical oxidant in reactions where MnO_x acted as an oxidant. This increase in activity was related to a decrease in thermodynamic stability and suggests that the disordered materials may be acting -at least in part- to directly oxidise water rather than catalyse the water oxidation reaction. Of the two disordered materials in this study; amorphous 1.5%Pi-MnO_x was the strongest oxidant but weakest catalyst, and 2D 0%Pi-MnO_x was a slightly weaker oxidant but a slightly stronger catalyst. Therefore, there is an optimisation between thermodynamic stability and reactivity for the water oxidation reaction; where a material can be too destabilised or too thermodynamically stable to effectively mediate the water oxidation reaction.

It was determined that there is an optimal level of disorder and thermodynamic stability to confer an advantage for catalytic water oxidation activity. It was also established that the propensity for oxidative activity systematically increases with increased disorder and decreased thermodynamic stability. This is summarized as a single graph in **Scheme 3.1**.

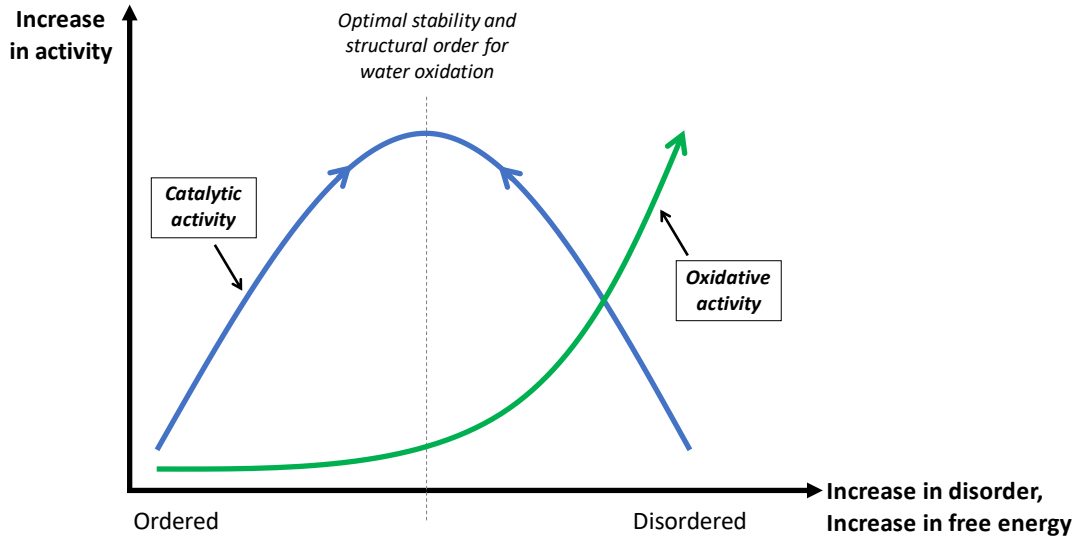

Scheme 3.1: A graphical representation of the relationship between catalytic activity, oxidative activity, thermodynamic stability and disorder.

The active birnessite-like manganese oxides appear to have a similar structure type and basic functional principles to active heterogenite-like cobalt oxides. Active forms of these materials have a similar layer structure, exhibit an increase in reactivity when structurally disordered or amorphous, are typically metastable, are stronger chemical oxidants than their crystalline counterparts, and they engage in a self-healing mechanism where the active phase is reformed from its own decomposition products (*i.e.* the M^{2+} state) under the Ph/Eh(V) conditions of water oxidation catalysis. Collectively, these properties distinguish disordered birnessite-like and heterogenite-like metal oxides from classical heterogenous catalysts as internal properties (*i.e.* properties beyond the catalyst surface) are critical for reactivity and the materials appear to be both consumed and reformed during catalytic cycles.

The synthetically formed birnessite-like manganese oxides are more closely related to naturally formed birnessite-type minerals in both structure and function, with both synthetic and natural birnessite-like materials having a disordered structure and dissolution/reformation reaction cycle. The chimie douce reaction conditions are important for synthesising these metastable phases and will be a key component in the continued development of redox active solid-state materials that can be thermodynamically turned to be better catalysts or better oxidants.

3.5 Conclusion

Herein, we examined the effects nanoscale disorder on the functionality of birnessite-type materials for both redox and catalytic reactions. Both the amorphous and 2D birnessite-like materials were less thermodynamically stable and stronger chemical oxidants than the ordered birnessite material. While it appeared that disorder conferred an advantage for water oxidation catalysis, we suggest that this increase in reactivity is due -at least in part- to direct oxidation of water rather than an increase in classical catalytic activity. The apparent self-healing mechanism is more similar in character to geochemical cycling of birnessite-type minerals than it is to heterogeneous surface catalysis.

3.6 Chapter 3 references

1. Pace, R., *An integrated artificial photosynthesis model, artificial photosynthesis: From basic biology to industrial application*. Wiley-VCH: Weinheim, 2005.
2. O'M. Bockris, J., *Energy: The solar hydrogen alternative*. Architectural Press: London, 1975; Vol. 123, p 365.
3. Najafpour, M. M.; Nayeri, S.; Pashaei, B., Nano-size amorphous calcium–manganese oxide as an efficient and biomimetic water oxidizing catalyst for artificial photosynthesis: back to manganese. *Dalton Trans.* **2011,** *40* (37), 9374-9378.
4. Chang, S. L. Y.; Singh, A.; Hocking, R. K.; Dwyer, C.; Spiccia, L., Nanoscale structural disorder in manganese oxide particles embedded in Nafion. *J. Mater. Chem. A* **2014,** *2* (11), 3730-3733
5. Lewis, N. S.; Nocera, D. G., Powering the planet: chemical challenges in solar energy utilization. *Proc. Natl. Acad. Sci.* **2006,** *103* (43), 15729-15735.
6. Armaroli, N.; Balzani, V., The future of energy supply: Challenges and opportunities. *Angew. Chem. Int. Ed. Engl.* **2007,** *46* (1-2), 52-66.
7. Bonke, S. A.; Wiechen, M.; Hocking, R. K.; Fang, X.-Y.; Lupton, D. W.; MacFarlane, D. R.; Spiccia, L., Electrosynthesis of highly transparent cobalt oxide water oxidation catalyst films from cobalt aminopolycarboxylate complexes. *ChemSusChem* **2015,** *8* (8), 1394-1403.
8. Cook, T. R.; Dogutan, D. K.; Reece, S. Y.; Surendranath, Y.; Teets, T. S.; Nocera, D. G., Solar energy supply and storage for the legacy and nonlegacy worlds. *Chem. Rev.* **2010,** *110* (11), 6474-502.
9. Zhou, F.; Izgorodin, A.; Hocking, R. K.; Spiccia, L.; MacFarlane, D. R., Electrodeposited MnO_x films from ionic liquid for electrocatalytic water oxidation. *Adv. Energy Mater.* **2012,** *2* (8), 1013-1021.
10. Yamashita, Y.; Tada, M.; Kakihana, M.; Osada, M.; Yoshida, K., Synthesis of RuO_2-loaded $BaTinO_{2n+1}$ (n = 1, 2 and 5) using a polymerizable complex method and its photocatalytic activity for the decomposition of water. *J. Mater. Chem.* **2002,** *12* (6), 1782-1786.
11. Frame, F. A.; Townsend, T. K.; Chamousis, R. L.; Sabio, E. M.; Dittrich, T.; Browning, N. D.; Osterloh, F. E., Photocatalytic water oxidation with nonsensitized IrO_2 nanocrystals under visible and UV light. *J. Am. Chem. Soc.* **2011,** *133* (19), 7264-7267.
12. Najafpour, M. M.; Ehrenberg, T.; Wiechen, M.; Kurtz, P., Calcium manganese (III) oxides ($CaMn_2O_4.xH_2O$) as biomimetic oxygen-evolving catalysts. *Angew. Chemie. Int. Ed.* **2010,** *49* (12), 2233-2237.
13. Hocking, R. K.; Brimblecombe, R.; Chang, L.-Y.; Singh, A.; Cheah, M. H.; Glover, C.; Casey, W. H.; Spiccia, L., Water-oxidation catalysis by manganese in a geochemical-like cycle. *Nat. Chem.* **2011,** *3* (6), 461-466.
14. Zaharieva, I.; Najafpour, M. M.; Wiechen, M.; Haumann, M.; Kurz, P.; Dau, H., Synthetic manganese–calcium oxides mimic the water-oxidizing complex of photosynthesis functionally and structurally. *Energy Environ. Sci.* **2011,** *4* (7), 2400-2408.
15. Wiechen, M.; Zaharieva, I.; Dau, H.; Kurz, P., Layered manganese oxides for water-oxidation: alkaline earth cations influence catalytic activity in a photosystem II-like fashion. *Chem. Sci.* **2012,** *3* (7), 2330-2339.
16. Frey, C. E.; Wiechen, M.; Kurz, P., Water-oxidation catalysis by synthetic manganese oxides – systematic variations of the calcium birnessite theme. *Dalton Trans.* **2014,** *43* (11), 4370-4379.

17. Zaharieva, I.; Chernev, P.; Risch, M.; Klingan, K.; Kohlhoff, M.; Fischer, A.; Dau, H., Electrosynthesis, functional, and structural characterization of a water-oxidizing manganese oxide. *Energy Environ. Sci.* **2012,** *5*, 7081-7089.
18. Iyer, A.; Del-Pilar, J.; King'ondu, C. K.; Kissel, E.; Garces, H. F.; Huang, H.; El-Sawy, A. M.; Dutta, P. K.; Suib, S. L., Water oxidation catalysis using amorphous manganese oxides, octahedral molecular sieves (OMS-2), and octahedral layered (OL-1) manganese oxide structures. *J. Phys. Chem. C* **2012,** *116* (10), 6474-6483.
19. Zhou, F.; Izgorodin, A.; Hocking, R. K.; Armel, V.; Spiccia, L.; MacFarlane, D. R., Improvement of catalytic water oxidation on MnO_x films by heat treatment. *ChemSusChem* **2013,** *6* (4), 643-651.
20. Najafpour, M. M.; Moghaddam, A. N., Nano-sized manganese oxide: A proposed catalyst for water oxidation in the reaction of some manganese complexes and cerium(IV) ammonium nitrate. *Dalton Trans.* **2012,** *41* (34), 10292-10297.
21. Jiao, F.; Frei, H., Nanostructured cobalt and manganese oxide clusters as efficient water oxidation catalysts. *Energy Environ. Sci.* **2010,** *3* (8), 1018-1027.
22. Gorlin, Y.; Lassalle-Kaiser, B.; Benck, J. D.; Gul, S.; Webb, S. M.; Yachandra, V. K.; Yano, J.; Jaramillo, T. F., *In situ* X-ray absorption spectroscopy investigation of a bifunctional manganese oxide catalyst with high activity for electrochemical water oxidation and oxygen reduction. *J. Am. Chem. Soc.* **2013,** *135* (23), 8525-8534.
23. Dinca, M.; Surendranath, Y.; Nocera, D., Nickel-borate oxygen-evolving catalyst that functions under benign conditions. *Proc. Natl. Acad. Sci.* **2010,** *23*, 10337-10341.
24. Singh, A.; Chang, S. L. Y.; Hocking, R. K.; Bach, U.; Spiccia, L., Highly active nickel oxide water oxidation catalysts deposited from molecular complexes. *Energy Environ. Sci.* **2013,** *6* (2), 579-586.
25. Risch, M.; Klingan, K.; Heidkamp, J.; Ehrenberg, D.; Chernev, P.; Zaharieva, I.; Dau, H., Nickel-oxido structure of a water-oxidizing catalyst film. *ChemComm* **2011,** *47* (43), 11912-11914.
26. Kanan, M. W.; Nocera, D. G., *In situ* formation of an oxygen-evolving catalyst in neutral water containing phosphate and Co^{2+}. *Science* **2008,** *321* (5892), 1072-1075.
27. Risch, M.; Khare, V.; Zaharieva, I.; Gerencser, L.; Chernev, P.; Dau, H., Cobalt−oxo core of a water-oxidizing catalyst film. *J. Am. Chem. Soc.* **2009,** *131* (20), 6936-6937.
28. Lutterman, D. A.; Surendranath, Y.; Nocera, D. G., A self-healing oxygen-evolving catalyst. *J. Am. Chem. Soc.* **2009,** *131* (11), 3838-3839.
29. Kanan, M. W.; Surendranath, Y.; Nocera, D. G., Cobalt–phosphate oxygen-evolving compound. *Chem. Soc. Rev.* **2009,** *38* (1), 109-114.
30. Surendranath, Y.; Dinca, M.; Nocera, D. G., Electrolyte-dependent electrosynthesis and activity of cobalt-based water oxidation catalysts. *J. Am. Chem. Soc.* **2009,** *131* (7), 2615-2620.
31. McAlpin, J. G.; Surendranath, Y.; Dinca, M.; Stich, T. A.; Stoian, S. A.; Casey, W. H.; Nocera, D. G.; Britt, R. D., EPR evidence for Co(IV) species produced during water oxidation at neutral pH. *J. Am. Chem. Soc.* **2010,** *132* (20), 6882-6883.
32. King, H. J.; Bonke, S. A.; Chang, S. L. Y.; Spiccia, L.; Johannessen, B.; Hocking, R. K., Engineering disorder into heterogenite-like cobalt oxides by phosphate doping: Implications for the design of water-oxidation catalysts. *ChemCatChem* **2017,** *9* (3), 511-521.
33. Kanan, M. W.; Yano, J.; Surendranath, Y.; Dinca, M.; Yachandra, V. K.; Nocera, D. G., Structure and valency of a cobalt-phosphate water oxidation catalyst determined by *in situ* X-ray spectroscopy. *J. Am. Chem. Soc.* **2010,** *132* (39), 13692-13701.

34. Surendranath, Y.; Kanan, M. W.; Nocera, D. G., Mechanistic studies of the oxygen evolution reaction by a cobalt-phosphate catalyst at neutral pH. *J. Am. Chem. Soc.,* **2010,** *132* (46), 16501-16509.
35. Gerken, J. B.; McAlpin, J. G.; Chen, J. Y. C.; Rigsby, M. L.; Casey, W. H.; Britt, R. D.; Stahl, S. S., Electrochemical water oxidation with cobalt-based electrocatalysts from pH 0-14: The thermodynamic basis for catalyst structure, stability and activity. *J. Am. Chem. Soc.* **2011,** *133* (36), 14431-14442.
36. Esswein, A. J.; Surendranath, Y.; Reece, S. Y.; Nocera, D. G., Highly active cobalt phosphate and borate based oxygen evolving catalysts operating in neutral and natural waters. *Energy Environ. Sci.* **2011,** *4* (2), 499-504.
37. Risch, M.; Klingan, K.; Ringleb, F.; Chernev, P.; Zaharieva, I.; Fischer, A.; Dau, H., Water oxidation by electrodeposited cobalt oxides - Role of anions and redox-inert cations in structure and function of the amorphous catalyst. *ChemSusChem* **2012,** *5* (3), 542-549.
38. Nocera, D., The artificial leaf. *Acc. Chem. Res.* **2011,** *45* (5), 767-776.
39. Cobo, S.; Heidkamp, J.; Jacques, P.-A.; Fize, J.; Fourmond, V.; Guetaz, L.; Jousselme, B.; Ivanova, V.; Dau, H.; Palacin, S. *et al.* A Janus cobalt-based catalytic material for electro-splitting of water. *Nat. Mater.* **2012,** *11*, 802-807.
40. Bediako, D. K.; Costentin, C.; Jones, E. C.; Nocera, D. G.; Savéant, J.-M., Proton–electron transport and transfer in electrocatalytic films. Application to a cobalt-based O_2-evolution catalyst. *J. Am. Chem. Soc.* **2013,** *135* (28), 10492-10502.
41. Risch, M.; Ringleb, F.; Kohlhoff, M.; Bogdanoff, P.; Chernev, P.; Zaharieva, I.; Dau, H., Water oxidation by amorphous cobalt-based oxides: *In situ* tracking of redox transitions and mode of catalysis. *Energy Environ. Sci.* **2015,** *8*, 661-674.
42. Seo, H.; Hee Cho, K.; Ha, H.; Park, S.; Hong, J.; Jin, K.; Nam, K. T., *Water Oxidation Mechanism for 3d Transition Metal Oxide Catalysts under Neutral Condition*. 2017; Vol. 54, p 1-8.
43. McCrory, C. C. L.; Jung, S.; Peters, J. C.; Jaramillo, T. F., Benchmarking heterogeneous electrocatalysts for the oxygen evolution reaction. *J. Am. Chem. Soc.* **2013,** *135* (45), 16977-16987.
44. Therese, G. H. A.; Kamath, P. V., Electrochemical synthesis of metal oxides and hydroxides. *Chem. Mater.* **2000,** *12* (5), 1195-1204.
45. Gopalakrishnan, J., Chimie douce approaches to the synthesis of metastable oxide materials. *Chem. Mater.* **1995,** *7* (7), 1265-1275.
46. Rein ten Wolde, P.; Frenkel, D., Homogeneous nucleation and the Ostwald step rule. *Phys. Chem. Chem. Phys.* **1999,** *1* (9), 2191-2196.
47. Van Santen, R. A., The Ostwald step rule. *J. Phys. Chem.* **1984,** *88* (24), 5768-5769.
48. Threlfall, T., Structural and thermodynamic explanations of Ostwald's rule. *Org. Process Res. Dev.* **2003,** *7* (6), 1017-1027.
49. Sanchez, C.; Rozes, L.; Ribot, F.; Laberty-Robert, C.; Grosso, D.; Sassoye, C.; Boissiere, C.; Nicole, L., "Chimie douce": A land of opportunities for the designed construction of functional inorganic and hybrid organic-inorganic nanomaterials. *Cr. Chim.* **2010,** *13* (1), 3-39.
50. Zaharieva, I.; Chernev, P.; Risch, M.; Klingan, K.; Kohlhoff, M.; Fischer, A.; Dau, H., Electrosynthesis, functional, and structural characterization of a water-oxidizing manganese oxide. *Energy Environ. Sci.* **2012,** *5* (5), 7081-7089.
51. Melghit, K., *Soft chemistry routes to new nanosize materials*. 2007; Vol. 12, p 87-100.

52. Bergmann, A.; Zaharieva, I.; Dau, H.; Strasser, P., *Electrochemical water splitting by layered and 3D cross-linked manganese oxides: correlating structural motifs and catalytic activity*. 2013.
53. Albering, J. H., *Handbook of battery materials*. 2nd ed.; Wiley-VCH Verlag GmbH: 2011; p 330.
54. Zhang, B.; Li, Y.; Valvo, M.; Fan, L.; Daniel, Q.; Zhang, P.; Wang, L.; Sun, L., Electrocatalytic water oxidation promoted by 3D nanoarchitectured turbostratic δ-MnO_x on carbon nanotubes. *ChemSusChem* **2017,** *10* (22), 4472-4478.
55. Hirata, K.; Shinzawa-Itoh, K.; Yano, N.; Takemura, S.; Kato, K.; Hananaka, M.; Muramoto, K.; Kawahara, T.; Tsukihar,a T.; Yamashita, E. *et al*. Determination of damage-free crystal structure of an X-ray sensitive protein using an XFEL. *Nat. Methods* **2014,** *11* (7), 734-736.
56. Post, J. E., Manganese oxide minerals: Crystal structures and economic and environmental significants. *Proc. Natl. Acad. Sci.* **1999,** *96*, 3447-3458.
57. Hocking, R. K.; Gummow, R. J.; King, H. J.; Sabri, M.; Kappen, P.; Dwyer, C.; Chang, S. L. Y., Direct formation of 2D-MnO_x under conditions of water oxidation catalysis. *ACS Appl. Nano Mater.* **2018**.
58. Geng, Z.; Sun, Y.; Zhang, Y.; Wang, Y.; Li, L.; Huang, K.; Wang, X.; Liu, J.; Yuan, L.; Feng, S., Architecture of biomimetic water oxidation catalyst with Mn_4CaO_5 clusterlike structure unit. *ACS Appl. Mater. Interfaces* **2018,** *10* (44), 37948-37954.
59. Ida, S.; Ishihara, T., Recent progress in two-dimensional oxide photocatalysts for water splitting. *J. Phys. Chem. Lett.* **2014,** *5* (15), 2533-2542.
60. Liu, H.; Gao, X.; Yao, X.; Chen, M.; Zhou, G.; Qi, J.; Zhao, X.; Wang, W.; Zhang, W.; Cao, R., Manganese(II) phosphate nanosheet assembly with native out-of-plane Mn centres for electrocatalytic water oxidation. *Chem. Sci.* **2019,** *10* (1), 191-197.
61. Wiechen, M.; Najafpour, M. M.; Allakhverdiev, S. I.; Spiccia, L., Water oxidation catalysis by manganese oxides: Learning from evolution. *Energy Environ. Sci.* **2014,** *7* (7), 2203-2212.
62. Zhang, G.; Dong, W.; Huang, X.; Zou, J., Oxygen vacancy induced enhancement of photochemical water oxidation on calcium manganese oxide catalyst. *Catal. Commun.* **2017,** *89*, 117-120.
63. Najafpour, M.; Rahimi, F.; Aro, E.-M.; Lee, C.-H.; Allakhverdiev, S., *Nano-sized manganese oxides as biomimetic catalysts for water oxidation in artificial photosynthesis: A review*. J. R. Soc. Interface: 2012; Vol. 9, p 2383-2395.
64. Kwon, K. D.; Refson, K.; Sposito, G., Defect-induced photoconductivity in layered manganese oxides: A density functional theory study. *Phys. Rev. Lett.* **2008,** *100* (14), 146601.
65. Zhang, R.; Zhang, Y.-C.; Pan, L.; Shen, G.-Q.; Mahmood, N.; Ma, Y.-H.; Shi, Y.; Jia, W.; Wang, L.; Zhang, X. *et al.* Engineering cobalt defects in cobalt oxide for highly efficient electrocatalytic oxygen evolution. *ACS Catal.* **2018,** *8* (5), 3803-3811.
66. Wang, J.; Liu, J.; Zhang, B.; Cheng, F.; Ruan, Y.; Ji, X.; Xu, K.; Chen, C.; Miao, L.; Jiang, J., Stabilizing the oxygen vacancies and promoting water-oxidation kinetics in cobalt oxides by lower valence-state doping. *Nano Energy* **2018,** *53*, 144-151.
67. Tian, T.; Gao, H.; Zhou, X.; Zheng, L.; Wu, J.; Li, K.; Ding, Y., Study of the active sites in porous nickel oxide nanosheets by manganese modulation for enhanced oxygen evolution catalysis. *ACS Energy Lett.* **2018,** *3* (9), 2150-2158.
68. Morgan Chan, Z.; Kitchaev, D. A.; Weker, J. N.; Schnedermann, C.; Lim, K.; Ceder, G.; Tumas, W.; Toney, M. F.; Nocera, D. G., Electrochemical trapping of metastable Mn^{3+} ions for activation of MnO_2 oxygen evolution catalysts. *Proc. Natl. Acad. Sci.* **2018,** *115* (23), E5261-E5268.

69. Chen, L.; Zhang, Y.; Li, D.; Wang, Y.; Duan, C., Magnesium-regulated oxygen vacancies of nickel layered double hydroxides for electrocatalytic water oxidation. *J. Mater. Chem. A* **2018,** *6* (38), 18378-18383.
70. Zhu, Y.; Liu, X.; Jin, S.; Chen, H.; Lee, W.; Liu, M.; Chen, Y., Anionic defect engineering of transition metal oxides for oxygen reduction and evolution reactions. *J. Mater. Chem. A* **2019,** *7* (11), 5875-5897.
71. Védrine, J. C., Heterogeneous catalysis on metal oxides. *Catalysts* **2017,** *7* (11), 341.
72. Mavrokefalos, C. K.; Patzke, G. R., Water oxidation catalysts: The quest for new oxide-based materials. *Inorganics* **2019,** *7* (3), 29.
73. Menezes, P. W.; Indra, A.; Gutkin, V.; Driess, M., Boosting electrochemical water oxidation through replacement of OH Co sites in cobalt oxide spinel with manganese. *ChemComm* **2017,** *53* (57), 8018-8021.
74. Post, J. E., Manganese oxide minerals: Crystal structures and economic and environmental significance. *Proc. Natl. Acad. Sci.* **1999,** *96* (7), 3447-3454.
75. Feng, Q.; Kanoh, H.; Ooi, K., Manganese oxide porous crystals. *J. Mater. Chem.* **1999,** *9* (2), 319-333.
76. Golden, D.; Dixon, J.; Kanehiro, Y., The manganese oxide mineral, lithiophorite, in an oxisol From Hawaii. *Soil Res.* **1993,** *31* (1), 51-66.
77. Taylor, R.; McKenzie, R.; Norrish, K., The mineralogy and chemistry of manganese in some Australian soils. *Soil Res.* **1964,** *2* (2), 235-248.
78. Onac, B. P., Minerals. In *Encyclopedia of caves (2nd Edition)*, White, W. B.; Culver, D. C., Eds. Academic Press: Amsterdam, 2012; pp 499-508.
79. Hocking, R. K.; Brimblecombe, R.; Chang, S. L. Y.; Singh, A.; Cheah, M. H.; Glover, C.; Casey, W. H.; Spiccia, L., Water-oxidation by manganese in a geochemical-like cycle. *Nat. Chem.* **2011,** *3*, 461-466.
80. Sunda, W. G.; Huntsman, S. A.; Harvey, G. R., Photoreduction of manganese oxides in seawater and its geochemical and biological implications. *Nature* **1983,** *301* (5897), 234-236.
81. Sunda, W. G.; Huntsman, S. A., Photoreduction of manganese oxides in seawater. *Mar. Chem.* **1994,** *46*, 133-152.
82. Najafpour, M. M.; Hołyńska, M.; Salimi, S., Applications of the "nano to bulk" Mn oxides: Mn oxide as a Swiss army knife. *Coord. Chem. Rev.* **2015,** *285*, 65-75.
83. Najafpour, M. M.; Sedigh, D. J., Water oxidation by manganese oxides, a new step towards a complete picture: simplicity is the ultimate sophistication. *Dalton Trans.* **2013,** *42* (34), 12173-12178.
84. Najafpour, M. M.; Haghighi, B.; Sedigh, D. J.; Ghobadi, M. Z., Conversions of Mn oxides to nanolayered Mn oxide in electrochemical water oxidation at near neutral pH, all to a better catalyst: catalyst evolution. *Dalton Trans.* **2013,** *42* (48), 16683-16686.
85. Lutterman, D. A.; Surendranath, Y.; Nocera, D. G., A self-healing oxygen-evolving catalyst. *J. Am. Chem. Soc.* **2009,** *131* (11), 3838-3839.
86. Hocking, R. K.; Malaeb, R.; Gates, W. P.; Patti, A. F.; Chang, S. L. Y.; Devlin, G.; MacFarlane, D. R.; Spiccia, L., Formation of a nanoparticulate birnessite-like phase in purported molecular water oxidation catalyst systems. *ChemCatChem* **2014,** *6* (7), 2028-2038.
87. Klingan, K.; Ringleb, F.; Zaharieva, I.; Heidkamp, J.; Chernev, P.; Gonzalez-Flores, D.; Risch, M.; Fischer, A.; Dau, H., Water oxidation by amorphous cobalt-based oxides: Volume activity and proton transfer electrolyte bases. *ChemSusChem* **2014,** *7* (5), 1301-1310.

88. Kim, S. H.; Kim, S. J.; Oh, S. M., Preparation of layered MnO_2 *via* thermal decomposition of $KMnO_4$ and its electrochemical characterizations. *Chem. Mater.* **1999,** *11*, 557-563.
89. Saratovsky, I.; Wightman, P. G.; Pasten, P. A.; Gaillard, J-F.; Poeppelmeier, K. R., Manganese oxides: Parallels between abiotic and biotic structures. *J. Am. Chem. Soc.* **2006,** *128*, 11188-11198.
90. U.S. EPA. 1996. "Method 3050B: Acid Digestion of Sediments, Sludges, and Soils," Revision 2. Washington, DC.
91. Kappen, P.; Ruben, G. *Sakura*, Australian Synchrotron: 2013.
92. Ravel, B.; Newville, M., Athena, Artemis, Hephaestus: Data analysis for X-ray absorption spectroscopy. *J. Synchrotron Radiat.* **2005,** *12*, 537-541.
93. Scott, R. A.; Hahn, J. E.; Doniach, S.; Freeman, H. C.; Hodgson, K. O., Polarized X-ray absorption spectra of oriented plastocyanin single crystals. Investigation of methionine-copper coordination. *J. Am. Chem. Soc.* **1982,** *104*, 5364-5369.
94. Brunauer, S.; Emmett, P. H.; Teller, E., Absorption of gases in mulimolecular layers. *J. Am. Chem. Soc.* **1938,** *60* (2), 309-319.
95. Wiechen, M.; Zaharieva, I.; Dau, H.; Kurz, P., Layered manganese oxides for water-oxidation: alkaline earth cations influence catalytic activity in a photosystem II-like fashion. *Chem. Sci.* **2012,** *3*, 2330-2339.
96. Najafpour, M. M.; Ehrenberg, T.; Wiechen, M.; Kurtz, P., Calcium manganese (III) oxides ($CaMn_2O_4.xH_2O$) as biomimetic oxygen-evolving catalysts. *Angew. Chemie. Int. Ed.* **2010,** *49* (12), 2233-2237.
97. Frey, C. E.; Kurtz, P., Water oxidation catalysis by synthetic manganese oxides with different structural motifs: A comparative study. *Chem. Eur. J.* **2015,** *21*, 14958-14968.
98. Sabri, M.; King, H. J.; Gummow, R. J.; Malherbe, F.; Hocking, R. K., The oxidation of peroxide by disordered metal oxides: A measurement of thermodynamic stability "by proxy". *ChemPlusChem* **2018,** *83* (7), 620-629.
99. Jin, K.; Chu, A.; Park, J.; Jeong, D.; Jerng, S. E.; Sim, U.; Jeong, H.-Y.; Lee, C. W.; Park, Y.-S.; Yang, K. D. *et al.* Partially oxidized sub-10 nm MnO nanocrystals with high activity for water oxidation catalysis. *Sci. Rep.* **2015,** *5*, 10279.
100. Indra, A.; Menezes, P. W.; Zaharieva, I.; Baktash, E.; Pfrommer, J.; Schwarze, M.; Dau, H.; Driess, M., Active mixed-valent MnO_x water oxidation catalysts through partial oxidation (corrosion) of nanostructured MnO particles. *Angew. Chem. Int. Ed. Engl.* **2013,** *52* (50), 13206-13210.
101. Izgorodin, A.; Hocking, R. K.; Winther-Jenson, O.; Hilder, M.; Winther-Jenson, B.; MacFarlane, D. R., Phosphorylated manganese oxide electrodeposted fron ionic liquid as a stable, high efficiency water oxidation catalyst. *Catal. Today* **2013,** *200*, 36-40.
102. Brimblecombe, R.; Swiegers, G. F.; Dismukes, G. C.; Spiccia, L., Sustained water oxidation photocatalysis by a bioinspired manganese cluster. *Angew. Chem. Int. Ed.,* **2008,** *47*, 7335-7338.
103. Manceau, A.; Marcus, M. A.; Grangeon, S.; Lanson, M.; Lanson, B.; Gaillot, A. C.; Skanthakumar, S.; Soderholm, L., Short-range and long-range order of phyllomanganate nanoparticles determined using high-energy X-ray scattering. *J. Appl. Cryst.* **2013,** *46*, 193-209.
104. Jurgensen, A.; Widmeyer, J. R.; Gordon, R. A.; Bendell-Young, L. I.; Moore, M. M.; Crozier, E. D., The structure of the manganese oxide on the sheath of bacterium Leptothrix discophora: An XAFS study. *Am. Mineral.,* **2004,** *89*, 1110-1118.

105. Silvester, E.; Manceau, A.; Drits ,V., Structure of synthetic monoclinic Na-rich birnessite and hexagonal birnessite: II. Results from chemical studies and EXAFS spectroscopy. *Am. Mineral.,* **1997,** *82*, 962-978.
106. Brimblecombe, R.; Bond, A. M.; Dismukes, G. C.; Swiegers, G. F.; Spiccia, L., Electrochemical investigration of Mn_4O_4-cubane water-oxidizing clusters. *Phys. Chem. Chem. Phys.* **2009,** *11*, 6441-6449.
107. Brimblecombe, R.; Dismukes, G. C.; Swiegers, G. F.; Spiccia, L., Molecular water-oxidation catalysts for photoelectrochemical cells. *Dalton Trans.* **2009**, 9374-9384.
108. Brimblecombe, R.; Kolling, D. R. J.; Bond, A. M.; Dismukes, G. C.; Swiegers, G. F.; Spiccia, L., Sustained water oxidation by $[Mn_4O_4]^{7+}$ core complexes inspired by oxygenic photosynthesis. *Inorg. Chem.* **2009,** *48* (15), 7269-7279.
109. Hocking, R. K.; Solomon, E. I. Ligand field and molecular orbital theories of transition metal X-ray absorption edge transitions *Struct. Bond.* [Online], 2012, p. 1-30.
110. Hocking, R. K.; King, H. J.; Hesson, A.; Bonke, S. A.; Johannessen, B.; Fekete, M.; Spiccia, L.; Chang, S. L. Y., Engineering disorder at a nanoscale: A combined TEM and XAS investigation of amorphous *versus* nanocrystalline sodium birnessite. *Aus. J. Chem* **2015,** *68* (11), 1715-1722.
111. Hocking, R. K.; Chang, S. L. Y.; MacFarlane, D. R.; Spiccia, L., Preparing and characterising catalyst for clean energy: a challenge for X-rays and electrons. *Aust. J. Chem.* **2012,** *65* (6), 608-614.
112. Gaillot, A. C.; Drits, V. A.; Manceau, A.; Lanson, B., Structure of the synthetic K-rich phyloomanganate birnessite obtained by high-temperature decomposition of $KMnO_4$: Substructures of K-rich birnessite from 1000°C experiment. *Microporous Mesoporous Mater.* **2007,** *98*, 267-282.
113. Post, J. E.; Bish, D. L., Rietveld refinement of the todorokite structure. *Am. Mineral.,* **1988,** *73*, 861-869.
114. Post, J. E.; Veblen, D. R., Crystal structure determinations of synthetic birnessite using TEM and the Rietveld method sample is Na-Birn. *Am. Mineral.,* **1990,** *75*, 477-489.
115. Villalobos, M.; Lanson, B.; Manceau, A.; Toner, B.; Sposito, G., Structural model for the biogenic Mn oxide produced by Pseudomonas putida. *Am. Mineral.,* **2006,** *91* (4), 489-502.
116. Drits, V.; Silvester, E.; Gorshkow, A. I.; Manceau, A., Structure of synthetic monoclinic Na-rich birnessite and hexagonal birnessite: I. Results from X-ray diffraction and selected-area electron diffraction. *82* **82**, 946-961.
117. Sun, H.; Xu K.; Huang, M.; Shang, Y.; She, P.; Yin, S.; Liu, Z., One-pot synthesis of ultrathin manganese dioxide nanosheets and their efficient oxidative degradation of Rhodamine B. *Appl. Surf. Sci.* **2015,** *357*, 69-73.
118. Meyer, J. C.; Geim, A. K.; Katsnelson, M. I.; Novoselov, K. S.; Booth, T. J.; Roth, S., The structure of suspended graphene sheets. *Nature* **2007,** *446*, 60-63.
119. Han, J. H.; Lee, S.; Cheon, J., Synthesis and structural transformations of colloidal 2D layered metal chalcogenide nanocrystals. *Chem Soc. Rev.* **2013,** *42*, 2581-2591.
120. Mei, J.; Liao, T.; Kou, L.; Sun, Z., Two-dimensional metal oxide nanomaterials for next-generation rechargeable batteries. *Adv. Mater.* **2017,** *29*, 1700176.
121. Nicolosi, V.; Chhowalla, M.; Kanatzidis, G.; Strano, M. S.; Coleman, J. N., Liquid exfoliation of layered materials. *Science* **2013,** *340*, 1226419.
122. Gupta, A.; Sakthivel, T.; Seal, S., Recent development in 2D materials beyond graphene. *Prog. Mater. Sci* **2015,** *73*, 44-126.
123. Navrotsky, A.; Mazeina, L.; Majzlan, J., Size-driven structural and thermodynamic complexity in iron oxides. *Science* **2008,** *319* (5870), 1635-1638.

124. Birkner, N.; Navrotsky, A., Thermodynamics of manganese oxides: Effects of particle size and hydration on oxidation-reduction equilibria among hausmannite, bixbyite, and pyrolusite. *Am. Mineral.,* **2012,** *97* (8-9), 1291-1298.
125. Birkner, N.; Nayeri, S.; Pashaei, B.; Najafpour, M. M.; Casey, W. H.; Navrotsky, A., Energetic basis of catalytic activity of layered nanophase calcium manganese oxides for water oxidation. *Proc. Natl. Acad. Sci.* **2013,** *110* (22), 8801-8806.
126. Gilbert, B.; Banfield, J. F., Molecular-scale processes involving nanoparticulate minerals in biogeochemical systems. *Revs. Min. Geo* **2005,** *59*, 109-155.
127. Gilbert, B.; Huang, F.; Zhang, H.; Waychunas, G. A.; Banfield, J. F., Nanoparticles: Strained and stiff. *Science* **2004,** *305*, 651-654.
128. Zhang, H.; Gilbert, B.; Huang, F.; Banfield, J. F., Water-driven structure transformation in nanoparticles at room temperature. *Nature* **2003,** *424*, 1025-1029.
129. Golden, D. C.; Chen, C. C.; Dixon, J. B., Synthesis of todorokite. *Science* **1986,** *231* (4739), 717-719.
130. Levar, C. E.; Hoffman, C. L.; Dunshee, A. J.; Toner, B. M.; Bond, D. R., Redox potential as a master variable controlling pathways of metal reduction by Geobacter sulfurreducens. *ISME J.* **2017,** *11* (3), 741-752.
131. Do, S-H.; Batchelor, B.; Lee, H-K.; Kong, S-H., Hydrogen peroxide decomposition on manganese oxide (pyrolusite): Kinetic intermediates and mechanism. *Chemosphere* **2009,** *75*, 8-12.
132. Broughton, D. B.; Wentworth, R. L., Mechanism of decomposition of hydrogen peroxide solutions with manganese dioxide. *J. Am. Chem. Soc.* **1947,** *69* (4), 741-744.
133. Zhou, H.; Shen, Y. F.; Wang, J. Y.; Chen, X.; O'Young, C-L.; Suib, S. L., Studies of decomposition of H_2O_2 over manganese oxide octahedral molecular sieve materials. *J. Catal.* **1998,** *176*, 321-328.
134. Elprince, A. M.; Mohamed, W. H., Catalytic decomposition kinetics of aqueous hydrogen peroxide and solid magnesium peroxide by birnessite. *Soil Sci. Soc. Am. J.* **1997,** *56* (6), 1784-1788.
135. Latimer, W. M., The oxidation states of the elements and their potentials in aqeous solution. *J. Chem. Educ.* **1940**.
136. Roy, C. B., Catalytic decomposition of hydrogen peroxide on some oxide catalysts. *J. Catal.* **1968,** *12*, 129-133.
137. Kanungo, S. B.; Parida, K. M.; Sant, B. R., Studies on MnO_2-III. The kinetics and the mechanism for the catalytic decomposition of H_2O_2 over different crystalline modifications of MnO_2. *Electrochim. Acta* **1981,** *26* (8), 1157-1167.
138. Kitajima, N.; Fukuzumi, S-I.; Ono, Y., Formation of superoxide ion during the decomposition of hydrogen peroxide on supported metal oxides. *J. Phys. Chem.* **1978,** *82* (13), 1505-1509.

Chapter 4 –

Photon-induced, timescale and electrode effects critical for the *in situ* X-ray spectroscopic analysis of electrocatalysts: The water oxidation case

ABSTRACT

In situ experiments combining X-ray absorption spectroscopy (XAS) and electrochemistry have become an indispensable tool for understanding the mechanisms of operation, structure and the modes of degradation of electrocatalysts under operational conditions. Herein, the design of a gas- and liquid-tight spectroelectrochemical cell (SEC) is introduced, and the effects of the working electrode, loading of active material, and X-ray damage are demonstrated and interpreted by an example of a well-known heterogenite-like cobalt oxide water oxidation catalyst. The SEC permitted reproducible XANES to be collected with a resolution of at least 0.05 eV (equivalent to approximately 0.02 oxidation state units), and allowed X-ray mediated photoeffects to be examined in detail. The potential-dependent Co oxidation state changes of the cobalt oxide catalyst were tracked with high precision and reproducibility and were used to investigate the mechanism of the catalyst.

To ensure the active state of the catalyst was measured, the *in situ* XAS analysis was coupled to a recent electrokinetic study and to an evaluation of timescale differences between the probed electron transfer events and the XAS analysis. It was concluded that metal oxidation states higher than IV are not involved in the catalytic mechanism.

Chapter 4 – Publications

This chapter is based on the largely unedited version of the first author peer-reviewed and published manuscript described below:

Title: Photon-induced, timescale and electrode effects critical for the *in situ* X-ray spectroscopic analysis of electrocatalysts: the water oxidation case

Publisher: Journal of Physical Chemistry C

Year: 2019

Details: volume 123, issue 47, pages 28533-28549

Authors: Hannah J. King, Maxime Fournier, Shannon A. Bonke, Enrico Seeman, Manjunath Chatti, Askhat N. Jumabekov, Bernt Johannessen, Peter Kappen, Alexandr N. Simonov, Rosalie K. Hocking

Chapter 4 – Table of contents

4.1 Introduction

Diverting renewable electricity towards electrosynthesis of commodity products is broadly considered and actively studied as a promising approach to decarbonising the chemicals industry and producing clean energy-rich fuels.[1-3] Implementation of these strategies on a global scale will require cheap, efficient and stable electrocatalysts.[2, 4-5] Significant progress has been made in a number of relevant technologies, such as those involving the oxygen evolution reaction (OER),[6-13] the hydrogen evolution reaction (HER),[14-20] CO_2 reduction,[21-25] and most recently, N_2 reduction.[26-28] However, most of these systems require improvements in long-term stability and activity to become fiscally and/or energetically competitive with the fossil fuels industry.[29-31]

The pathway to electrocatalyst improvement has been led by experimental and theoretical studies that focus on resolving the exact structures of active sites within a material, and investigating the structure *versus* function relationships.[2, 32-33] *In situ* experimental studies that couple electroanalytical methods to direct characterisation techniques have become increasingly valuable in determining the nature of a material under operational conditions.[34-38] These studies are crucial as active catalyst structures during operation can differ from their rest state. X-ray absorption spectroscopy (XAS) has many advantages over other direct characterisation methods used to analyse heterogeneous electrocatalyst materials.[39-42] One of its greatest strengths is its ability to provide information on both electronic and geometric structures under operational conditions irrespective of the crystallinity of a material.[41, 43-45] This is significant for electrocatalysts as these materials are often amorphous and/or disordered thin films and are difficult to characterise by other techniques.

An X-ray absorption spectroelectrochemical cell (SEC) – the device utilised for *in situ* studies – should provide high quality XAS without compromising the electrochemical data. Many SECs have been designed and used for *in situ* experimentation[12, 36-37, 41, 43, 46-55], though a number of designs suffer from insufficiently high signal-to-noise ratios. Spectroscopic data particularly experiences low signal-to-noise when the sample loading

on the electrode is not high. Analysing low sample loadings of heterogeneous electrocatalysts is required to increase the proportion of the electrochemically "active" to "inactive" material. That is, decreasing the sample loading should increase the proportion of the XAS signal attributable to the active component (shown in **Scheme 4.1**). Low electrocatalyst loadings typically require measurement by fluorescence detection.[56] The need for a low sample loading should, however, be considered in parallel with the need to minimise photoeffects, which are more pronounced under such conditions.[57]

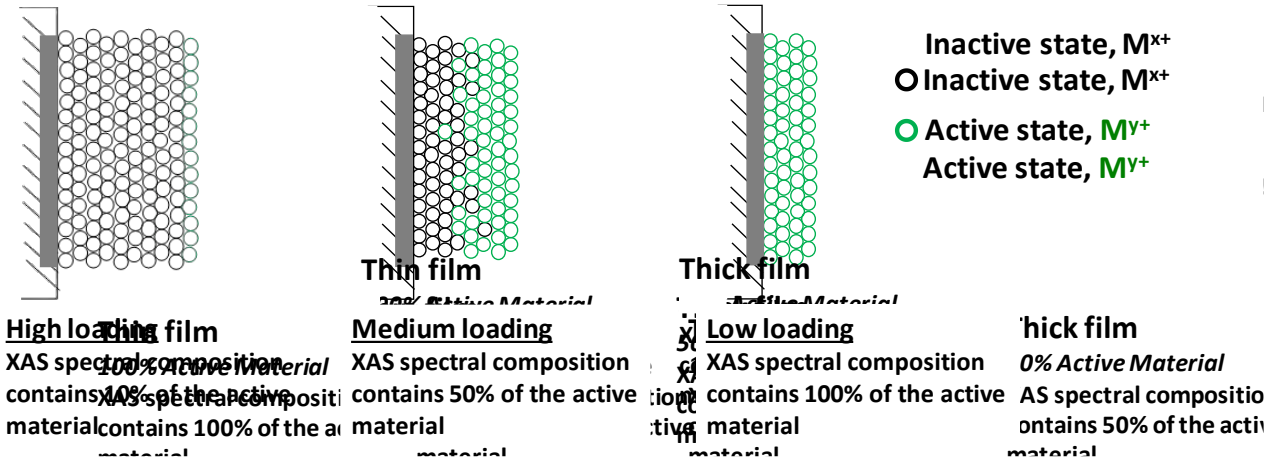

Scheme 4.1: Idealised effects of the electromaterial film thickness on the XAS signal assuming no indirect or secondary effects.

Photoeffects is the collective term used to describe the phenomenological changes occurring within a sample upon interaction with X-rays.[58-62] The most commonly encountered photoeffect phenomena include *photoreduction* (*i.e.* an oxidation state decrease),[63-67] *photooxidation* (*i.e.* an oxidation state increase),[64, 68] *beam damage* (*e.g.* phase decomposition), and gas bubble formation from solvent ionisation.[64, 68-69] These changes can be caused by direct photoelectrochemical effects to the sample from ionising X-ray radiation, or by indirect changes affecting the sample matrix. Examples of the latter include chemical perturbations in the sample environment (*e.g.* ionisation of the solvent),[58-59, 61, 64, 70-71] or a change to the adhesion between the sample material and the electrode substrate. As photoeffects can result in the misinterpretation of XAS data[72-73], it is important to mitigate photodamage effects where possible (*vide infra*) and to investigate whether other photoeffects are unduly influencing the spectroscopic data.

Ex situ and quasi *in situ* XAS experiments are frequently performed at liquid nitrogen (77 K) or liquid helium (4 K) temperatures to reduce photoeffects.[74] *Quasi in situ* approaches have involved rapidly freezing a specially designed spectroelectrochemical cells under potential control to "trap" a catalyst in its operational state and have been demonstrated to be an efficient tool in electrocatalysis research.[75-77] One major limitation of the method is that each electrode can be analysed at one potential only, rendering the mandatory reproducibility studies more challenging and time-consuming. For dynamic *in situ* electrochemical experiments, cryogenic cooling is not possible as these measurements require efficient ion-conductivity through an electrolyte. In this case, the effects of X-ray radiation on a given sample (and its wider electrochemical environment) require consideration so that the spectroscopic data reliably represent the sample and photoeffects are not misconstrued as real changes to the sample under operational conditions.

While photoeffects can be qualitatively identified in the XAS data of any *ex situ* or *in situ* sample, an *in situ* SEC configuration provides the opportunity to quantify the susceptibility of a sample to undergo photooxidation and photoreduction at a given potential. In conventional XAS analysis, photoeffects are typically identified as differences between replicate spectra collected for a single position on the sample,[64, 68] and can often be visually identified as discolouration in the localised footprint of the beam. A SEC enables the susceptibility of photooxidation and photoreduction effects to be measured by quantifying the photocurrent induced by the X-ray beam, and correlating them with different redox states of the material (as defined by the electrode potential) and monitored by XAS. For example, the material could be analysed in a rest state, in an oxidised form where it is susceptible to photoreduction, or in a reduced form where it is susceptible to photooxidation. To the best of our knowledge, no published work has demonstrated the use of a SEC to measure photoeffect phenomena intentionally.

Another critically important aspect of an *in situ* spectroelectrochemical experiment, the significance of which is often overlooked, is the difference in the timescales of analysis and the charge-transfer processes that are coupled to rapid catalytic reactions. XAS and most other spectroscopic methods used for *in situ* experiments require a notable amount of time for the data collection, which is much slower than typical electrocatalytic turnover frequencies (TOF). The implications of this mismatch are exemplified for the simplest electrocatalytic model involving a ground state (**G**) and an active state (**A**) of an

electrocatalyst and several hypothetical scenarios in **Scheme 4.2**, which presents two ways in which the catalytic cycle can be viewed. The first way views a catalytic cycle from the perspective of an isolated group of atoms, *viz.* the way researchers often think about a catalytic mechanism (solid lines in **Scheme 4.2 a-d).** The second way views a catalytic cycle as the average state of the entire material over time (dotted lines in **Scheme 4.2 a-d**), which is the way XAS "sees" a catalytic mechanism.

It is clear from **Scheme 4.2** that both the lifetime (how long state **A** exists for) and TOF (the frequency with which state **A** is made and consumed) of the catalyst matter in terms of what can be detected by XAS. The effect of TOF on the average state of the material is shown from a comparison of **Scheme 4.2 a** and **b**, and the effects of lifetime are shown by comparisons of **Scheme 4.2 a, c** and **d**. Unless the conditions of the *in situ* spectroelectrochemical experiment are optimised based on the kinetic data, the actual active state (**A** in **Scheme 2**) might remain invisible for spectroscopy.[78-79] In other words, for some systems, short-lived states may never be detectable in an XAS experiment.

The present work aims to further highlight and undertake an extended analysis of the phenomena discussed above, including sample loading effects, photoeffects, considerations of XAS and electron transfer timescale differences, and the importance of electrokinetic modelling to a spectroelectrochemical experiment. To this end, an *in situ* SEC and relevant protocols for the simultaneous collection of high quality XAS and electrochemical data are introduced and implemented for the analysis of electrocatalytic oxidation of water to dioxygen.

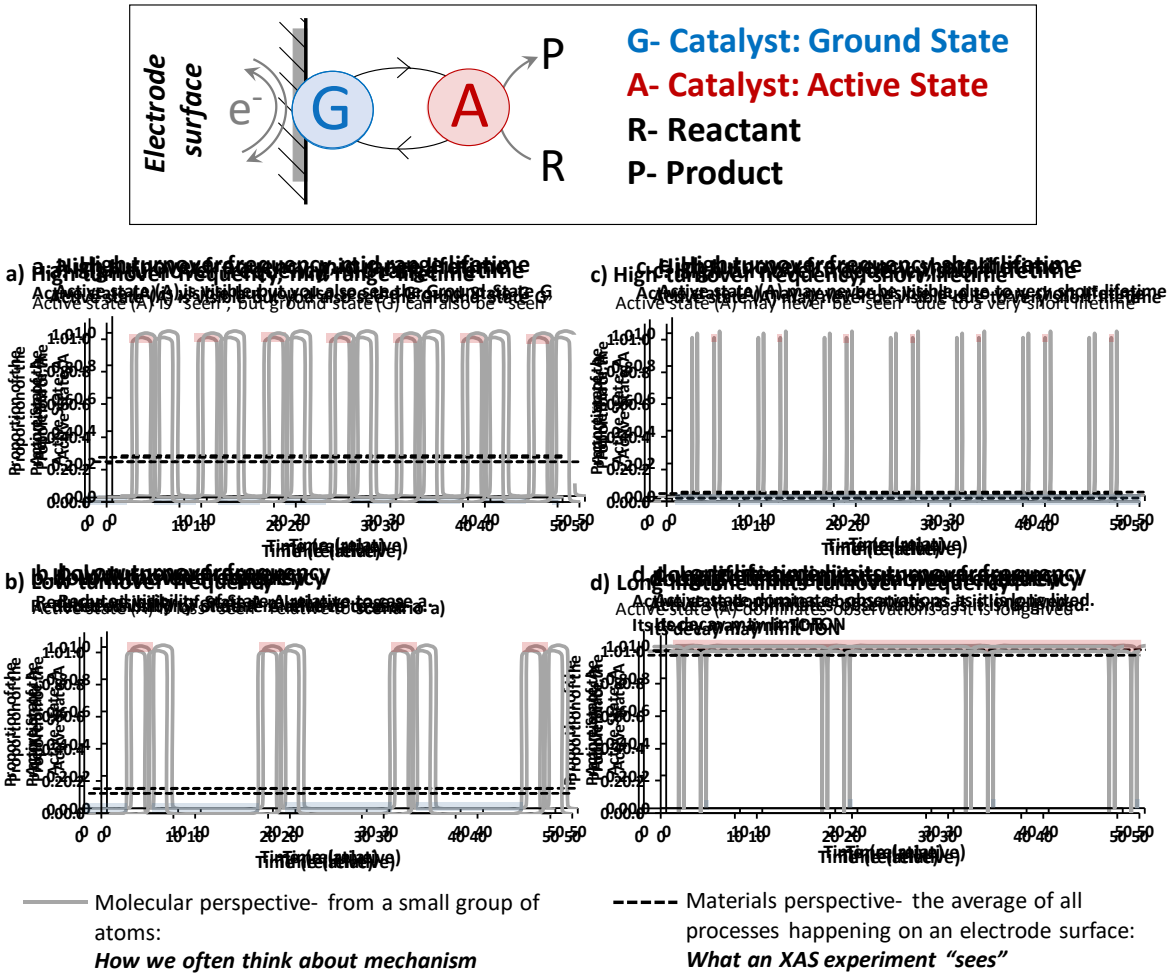

Scheme 4.2: A schematic presentation of how electrochemical timescales can effect spectrochemical measurements for the simplified heterogeneous electrocatalytic mechanism summarised in the top panel (**G** and **A** are the ground and active states of the electrocatalyst, respectively; **R** is a reactant, and **P** is a product). Plots in panels **(a-d)** depict different combinations of TOF and lifetime of state **A**. *Grey* lines represent the molecular perspective (*i.e.* as catalysis would be observed from an isolated group of atoms). *Dashed black* line represent the average of the material detected by XAS. *Light blue* and *light red* shadings show the periods when the catalyst is in the state **G** and **A**, respectively.

The mechanism of the OER was hypothesised by several groups to be of the kind depicted in **Scheme 4.2**.[80-82] Among different modes of the OER, the reaction in near neutral solutions catalysed by electrodeposited heterogenite-like cobalt oxides (CoO_x) received special attention[83] and was investigated by a range of techniques, including *in situ* electron paramagnetic resonance[84] and *in situ* XAS[12, 74]. Based on these previous experimental findings, the oxidation of $Co^{III}(OH)$ to $Co^{IV}(O)$ or even Co^{V} (reaction **G** ⇄ **A** in **Scheme 4.2**) coupled to a proton withdrawal by dissolved base (reaction **A** + **R** → **G** + **P** in **Scheme 4.2**) was suggested to be a rate limiting step of the CoO_x-catalysed OER.[12, 85]

This mechanism was used by Ahn and Bard,[80] Savéant and co-workers[81], as well as Dau and colleagues[82] in their electrokinetic analysis to derive the key parameters of the reaction. Following these insightful studies, a further detailed experimental and theoretical electrokinetic investigation of the OER was conducted by Bonke et al..[78] Among other findings, this work demonstrated that the reversible potential of the presumptive $Co^{n+/(n+1)+}$ process for such a mechanism should be as positive as 2 V *vs.* reversible hydrogen electrode (RHE).[78]

However, the link between these electrokinetic data and *in situ* spectroscopic analysis of the CoO_x active state was missing. Thus, the OER catalysed by heterogenite-like CoO_x presents a thoroughly investigated benchmark electrocatalytic system[75-76, 86-88], with several interesting unresolved mechanistic questions. As such, this reaction was investigated herein using the extended protocols and the new SEC.

The following research is segmented into two major parts. The first part describes the new SEC and outlines the design solutions employed to overcome common experimental problems associated with *in situ* XAS analysis. The second part benchmarks the new SEC, provides an extended analysis of the photoeffects phenomena, and reports a detailed analysis of heterogenite-like cobalt oxide catalysts during the water oxidation reaction. The conclusions of our studies are supported by consideration of all the challenges of *in situ* spectroelectrochemical analysis (*i.e.* sample loading effects, photoeffects, considerations of XAS and electron transfer timescale differences, and correlation with electrokinetic modelling).

4.2 Experimental

4.2.1 Materials

All chemicals were purchased from Sigma Aldrich. High-purity deionised water (*Milli-Q*, 18 MΩ cm at 23 ± 1°C) was used in all experimental procedures. Prior to use, all glassware was cleaned by soaking in NaOH + isopropanol mixture for at least 5 hours, washed with water, soaked in H_2SO_4(conc.) : 30 wt.% H_2O_2 (1 : 1 vol.) mixture for at least 1 hour, again washed copiously with water, and dried under a strong flow of N_2. High purity N_2 (O_2 < 0.01%) and Ar (O_2 < 0.003%) were used.

4.2.2 Fabrication of gold electrodes on a plastic substrate

To begin the fabrication process, 30 mm × 60 mm polyethylene terephthalate (PET) supports were cleaned by sequential sonication in an aqueous surfactant solution, pure water, acetone and isopropanol for 15 min in each media. After drying with compressed air, a *ca* 2 μm thick photoresist layer (AZ 1512SH, *Clariant*) was spin coated onto the clean PET substrates and kept at 110°C for 2 min. The substrates were then exposed to UV light through a photo-mask with the electrode pattern. The UV-exposed section of the photoresist layer was removed by washing the substrate in a developer solution AZ 726MIF mixed with water (3 : 1 vol.). In the next step, 5 nm Ti and 60 nm Au layers were sequentially evaporated onto the substrates using an electron beam evaporator (*Nanochrome II, Intlvac*) at $<10^{-6}$ Torr. At the final stage, the remainder of the polymer mask was removed by gently washing the substrates in acetone (lift-off process). A photograph of a typical electrode is shown in **Figure 4.1**.

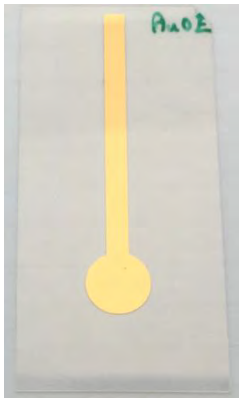

Figure 4.1: Photograph of a gold on PET working electrode.

4.2.3 Electrochemical procedures

Electrochemical experiments were performed using either a VSP (*Bio-Logic*) or an Autolab PGSTAT101 (*Metrohm*) electrochemical workstation in a three-electrode configuration. A "leak-free" Ag|AgCl|KCl (3.4 M) LF-1-100 reference electrode (1 mm diameter, *Innovative Instruments, Inc.*) was used throughout. However, all potentials were recalculated to a reversible hydrogen electrode (RHE) scale using Nernst equation and $E^0_{\text{LF-1-100}}$ = 0.210 V *vs.* normal hydrogen electrode, unless otherwise stated. A *ca* 20 cm^2 surface area nickel wire was used as an auxiliary electrode. Teflon fabric reinforced Nafion N324 membrane embedded into a homemade flexible frame (urethane polymer, *Smooth-on*) was used to separate the working and auxiliary electrode compartments. Three types of working electrodes were employed: (i) a glassy carbon plate (1 mm thickness, *AlfaAesar*), (ii) a PET plastic sheet (0.5 mm thickness) covered with a thin layer of indium-tin oxide (ITO), and (iii) gold on PET. Prior to use, the glassy carbon electrode was polished with a 0.3 μm Al_2O_3 (*AlfaAesar*) aqueous paste, flushed with water, wiped with a clean polishing pad, flushed with water again, and finally, cleaned by ultra-sonication in water. ITO and gold electrodes were not subjected to any pre-treatment.

Currents reported in this paper are normalised to the geometric surface area of the electrodes, unless stated otherwise. The active surface area of the working electrodes was *ca* 0.79 cm^2 (maximal value for the employed modification of the cell) for glassy carbon and Au, and typically between 0.6-0.7 cm^2 for ITO (defined by the isolation applied). Given the imperfect and sometimes inhomogeneous conductivity of the commercially available ITO electrodes, it was not possible to laser-engrave these substrates with a precisely defined active surface area (*e.g.* similarly to the Au electrode pattern) as this resulted in very poor electrochemical response. To minimise the unfavourable effects of ITO electrode resistance, a wide "U" pattern was employed, and electrical contact was provided with copper tape (sealed with *Kapton* tape) as close as possible to the electroactive area (**Figure 4.2c**). There were no indications of copper leaching, even when using acidic solutions.

Experiments with cobalt-based electrodes were undertaken using air-saturated solutions. Except for the electrodeposition of thick Ni coating, measurements with nickel-based electrodes used deoxygenated solutions. This was achieved by purging Ar for more than 2 hours through *ca* 300 mL of electrolyte solutions inside gas-tight bottles connected to the

cell with tubing, and then filling the cell with the Ar-saturated solution completely leaving no headspace. The flow of solutions in and out of the SEC was provided by a peristaltic pump (*ISMATEC*) through Teflon tubing (internal diameter 1 mm).

The surface concentration of electroactive cobalt (Γ) reported herein was calculated as a specific charge (mC cm^{-2}) of the cobalt oxidation peak prior to the onset of water oxidation, which can be assumed to correspond to the one electron $Co^{2+/3+}$ process based on the previous reports[77, 80-81] and the *in situ* XAS data herein. The Γ values are also reported as a concentration per surface area of electroactive cobalt (nmol cm^{-2}) calculated using Faraday's law.

4.2.4 Deposition of cobalt oxides

As precursors, either 1.0 mM $CoSO_4$ or 10 mM $[Co(NTA)(OH_2)_2]^-$ (NTA = nitrilotriacetate)[77] dissolved in 0.1 M borate buffer (pH 9.2) were used to produce materials further denoted as CoO_x and CoO_x^{NTA}, respectively. In all cases, the deposition solutions were air-saturated. Electrodeposition of CoO_x was conducted at a constant potential of 2.148 V *vs*. RHE. CoO_x^{NTA} was electrodeposited using cyclic voltammetry within 0.748 – 2.148 V *vs.* RHE range at a sweep rate of 0.020 V s^{-1}; the number of cycles was varied to achieve the desired concentration of electroactive cobalt species. Both CoO_x and CoO_x^{NTA} were also photodeposited onto ITO and Au electrodes by irradiating with X-rays. After deposition, the precursor solution was replaced with pure 0.1 M borate buffer (pH 9.2), which was then additionally flowed through the cell for 20 min. During further analysis, the electrodes were in contact with still 0.1 M borate buffer.

4.2.5 Fabrication of nickel-based electrodes

Low loadings of nickel were electrodeposited onto gold electrodes from Ar-saturated 0.01 M $NiSO_4$ solution in 0.2 M Na_2SO_4 (pH 7) at a constant potential of -1.223 V *vs*. Ag|AgCl|KCl (3.4 M KCl) (LF-1-100) for 2 min. The potential was then maintained at -0.977 V *vs*. Ag|AgCl|KCl (3.4 M KCl) (LF-1-100) while the precursor solution was replaced with Ar-saturated 0.1 M NaOH (pH 13). The analysis was then performed in the same solution with no flow. Thick nickel metal plating of Au electrodes was undertaken using air-saturated 1 M $NiSO_4$ solution and by applying -1 V *vs*. Ag|AgCl|KCl (3.4 M KCl) (LF-1-100) for 5 min; the electrode was copiously washed with water before being analysed in Ar-saturated 0.1 M NaOH.

4.2.6 Synthesis of XAS reference compounds

Four cobalt oxide materials were used herein as reference materials for XAS: delithiated $LiCoO_x$ (a $Co^{3.7+}$ reference), heterogenite (a Co^{3+} reference), $LiCoO_2$ (a Co^{3+} reference) and CoO (a Co^{2+} reference); in all cases, the cobalt sites are in an octahedral geometry. $LiCoO_2$ and CoO were purchased from Sigma Aldrich and their phase was confirmed with X-ray diffraction (XRD).

Heterogenite was synthesised using a procedure adapted from Myers and Penn.[82] In this adaption, the addition (at a rate of 8 mL min^{-1}) of NaOH (200 mL, 1 M, 60°C) to a stirred solution of Co^{II} (cobalt sulphate heptahydrate, 200 mL, 0.1 M, 60°C) was followed by the addition of 80 mL of sodium hypochlorite (NaOCl, 4 w/v%, pH 12) at approximately 3 mL min^{-1}. The suspension was heated and continuously stirred for further 2 hours and then cooled down to ambient temperature (23 ± 1°C) naturally. The precipitate was isolated and washed with water using a centrifuge, washed once with acetone, and dried in an oven in air at 110°C for approximately 10 hours. The purity was confirmed by XRD.

The delithiated $LiCoO_x$ reference material was synthesised using a procedure outlined by Basch and White.[83] In this procedure, commercially available $LiCoO_2$ was treated with concentrated HCl, and the resulting product was separated and washed copiously with water. The lithium : cobalt ratio was confirmed by inductively coupled plasma mass spectrometry and the crystal structure by XRD, giving the final product $Li_{0.3}CoO_2$.

4.2.7 X-ray absorption spectroscopy (XAS)

Co K-edge XAS data were collected on the multipole wiggler XAS beamline (12-ID), operating with an electron beam energy of 3.0 GeV and beam current of 200 mA (maintained in top-up mode), at the Australian Synchrotron, Melbourne. The XAS beamline was operated in "mode 1" with a Si(111) monochromator and focusing optics. The data were collected in fluorescence mode using a solid-state 100-element germanium detector. The SEC was bolted to the beamline sample table with the electrode aligned 45° to the fluorescence detector. An *OKEN* ionisation chamber was used to measure the incident radiation. All the data were collected at ambient temperature (23 ± 1°C).

The sample environment was kept under a helium atmosphere (to reduce air absorption of fluorescent X-rays) by connecting a flight tube between the beamline and the cell and providing an overpressure of helium between the cell and the fluorescence detector. Collection of a single XANES and EXAFS (k = 15) spectrum required *ca* 15 and 30 min, respectively. The XAS data presented below were collected as single spectra (*i.e.* not an average of replicate spectra), except where stated otherwise. XAS data were collected on multiple spots to ensure homogeneity of the samples. The raw data collected from the beamline were initially read into Sakura,[84] deglitched in Microsoft Excel, and then processed (normalisation and background subtraction) in Pyspline[85] or Athena.[86]

4.3 Cell design and operation

4.3.1 Electrochemical and spectroscopic requirements

An *in situ* XAS-electrochemical cell must satisfy the requirements of spectroscopy and electrochemistry to enable the simultaneous collection of reliable data from both. While a simple SEC can be employed for studies that solely prioritise the collection of high quality spectroscopic data, a more sophisticated design is necessary when further capabilities are required, such as high quality electrochemical data collection, long-term electrochemical stability, maintaining a specific atmosphere (*e.g.* O_2 exclusion), as well as liquid and gas-tightness. The SEC introduced hereafter meets all of these requirements through the employment of a functionalised modular layered architecture and by favouring fluorescence detection over transmission detection in XAS. Fluorescence detection not only provides better signal-to-noise for low sample loadings of first row transition metal electrocatalysts, but also affords a better electrochemical design.

The SEC has been designed to produce high quality spectroscopic and electrochemical data and to maintain a specific electrochemical environment for an extended length of time (hours). Spectroscopic signal-to-noise was maximised by minimising beam attenuation caused by the passage of incident and outgoing X-rays through the components of the cell. This has been achieved through the common design practice of using an "X-ray transparent" working electrode (WE) as a window to the cell, *i.e.* the WE serves as a separator between the electrolyte solution and the X-ray chamber.[36, 41, 50-51] In such configuration, the collection of high quality spectroscopic and electrochemical data depends heavily on the choice of WE substrate, as discussed in more detail in **§ 4.3.3** and **§ 4.4.1**.

To produce high quality electrochemical data, the SEC offers all the functionalities of a conventional three-electrode electrochemical cell with additional considerations for minimising uncompensated resistance, potential drifts, electromagnetic noise, as well as charge and mass transport limitations. The electrochemical environment of the SEC can be maintained long-term due to the modular construction, which provides chemical and spatial separation of the WE and auxiliary electrode (AE) compartments as well as liquid- and

gas-tightness. The SEC can be used to study a wide variety of electrochemical processes and is suitable for long-term operation. Further details of the cell architecture and the WE selection criteria are discussed below.

4.3.2 Spectroelectrochemical cell architecture

The SEC is comprised of three polytetrafluoroethylene (PTFE) main body components (**Figure 4.2a**, parts **III**, **V** and **VII**) that are held tightly together with a stainless-steel housing (**Figure 4.2a**, parts **I** and **VIII**). The stainless-steel housing functions to both compress the PTFE main body components, and to firmly attach the cell to the motorised XY beamline optical-board/stage *via* screws through the base of part **I** (**Figure 4.2a**). Connecting the cell directly to the beamline reduces the effects of ambient vibrations, assists in XAS sample alignment, and allows the X-ray path to be kept under a helium atmosphere to minimise incident beam and fluorescence signal attenuation.

The leak-proof WE compartment has no headspace, and its conical design mitigates the accumulation of gases by funnelling any bubbles formed during an experiment towards the outlet at the top (**Figure 4.2a**, part **V**). The captured gas can then be removed from the WE chamber by pumping the solution through the external tubing system that connects to the cell *via* the inlet and outlet orifices at the bottom and the top, respectively (**Figure 4.2a**, part **V**). This pumping system additionally allows the WE and AE compartments to be filled and emptied without dismantling the cell. The absence of a headspace in the fully sealed leak-proof WE compartment significantly facilitates experiments under controlled atmosphere. In such an experiment, solutions are saturated with the required gas outside of the cell using sealed containers and are pumped into the cell without contacting air. An example of voltammetric analysis undertaken in such manner for nickel (Ni^0)-modified gold electrodes in deoxygenated solutions is provided in **Figure 4.3**. Cyclic voltammograms recorded with a nickel-plated Au electrode in the SEC are in a perfect agreement with those reported in the literature for nickel metal.[87-88]

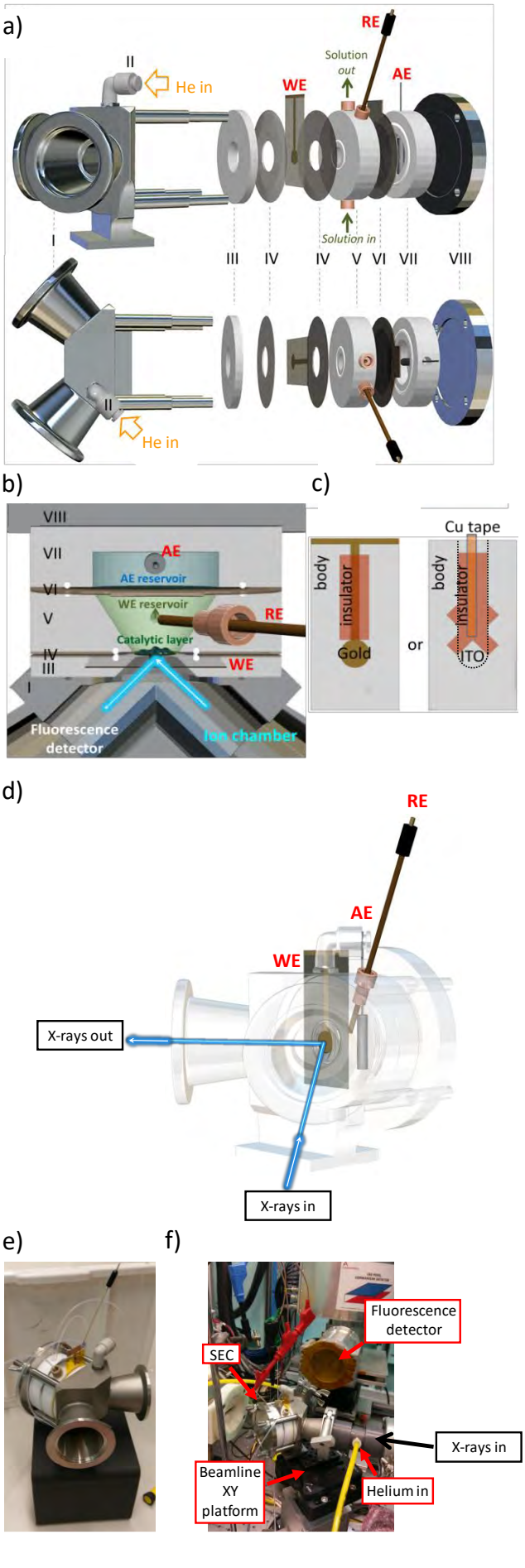

Figure 4.2: Schematics of the SEC. Information is presented as: **(a)** key components of the *in situ* SEC, **(b)** cross-sectional view of the electrochemical and ion chambers, and **(c)** working electrode configurations. WE, AE and RE are working, auxiliary and reference electrodes, respectively. **I** and **VIII** – stainless-steel housing, **II** – helium inlet, **III**, **V**, **VII** – PTFE body of the cell, **IV** – polyurethane gaskets, **VI** – Nafion N324 membrane embedded into a polyurethane gasket. The WE is positioned between the polyurethane gaskets (components **IV**) at the smaller end of the cone-shaped WE chamber. The stainless-steel chamber **I** (panel **(a)**) has two KF40 flanges, which are positioned at 90° with respect to each other. A flexible gasket **IV** sandwiches the WE and O-rings between parts **III** and **V** (panel **(a)**) and is highly effective at preventing leaks between/from the gas- and liquid-filled compartments. A transparent perspective view of the SEC is given in **(d).** A photograph of the free-standing SEC is given in panel **(e)**, and an annotated photograph of the SEC mounted to the beamline XY platform is given in panel **(f)**.

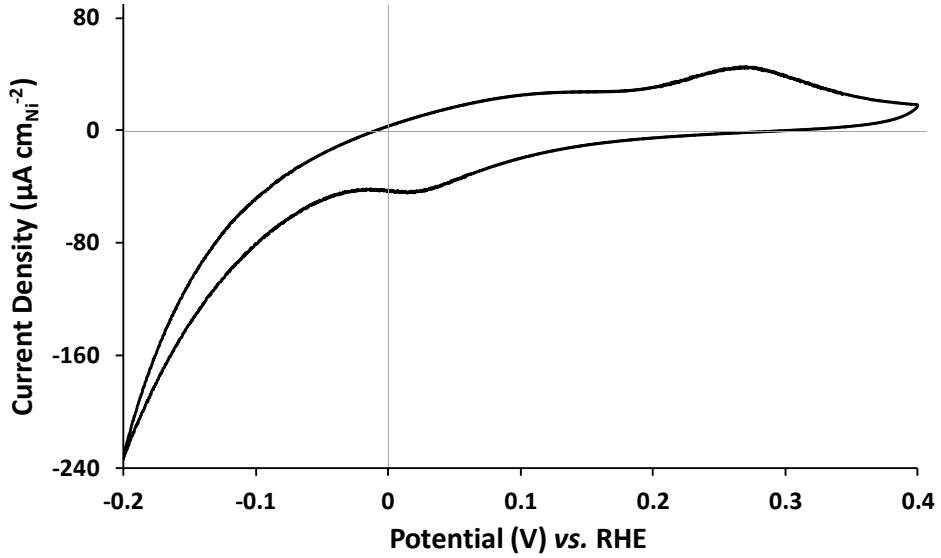

Figure 4.3: Cyclic voltammetry (v = 0.020 V s^{-1}; quasi-stabilized fifth cycle shown) of a nickel (Ni^0)-modified gold electrode in contact with an Ar-saturated 0.1 M NaOH. Currents are normalized to the electroactive surface area of nickel. The latter was calculated using the conversion coefficient 0.514 mC cm^{-2} and the charge corresponding to the formation of a monolayer of α-$Ni(OH)_2$, which was derived from the integration of the anodic sweep of the cyclic voltammogram in the range from -0.06 to 0.40 V *vs.* RHE.[S1]

4.3.3 Working electrode requirements

The working electrode has a critical function in the SEC as the X-ray window to the cell and as the support for the electrocatalyst sample. To satisfy the spectroscopic requirements, the WE and its substrate/support must be physically stable and X-ray "transparent". Specifically, incident and outbound radiation should be able to pass through the body of the electrode with minimal interference. Thus, the WE material(s) should not significantly absorb, reflect or diffract photons within the energy range relevant to the element of interest in the sample. The WE must also act as a physical component of the cell, *i.e.* separate parts **I** and **III** from part **V** (**Figure 4.2b**), and must therefore be mechanically robust and impermeable to gases and liquids. To satisfy the electrochemical requirements, the WE needs to exhibit high electrical conductivity as well as minimal and highly reproducible electrochemical activity within the potential range relevant to the analysed sample/solvent system.

Given the requirements above, three types of working electrode substrates were examined herein: a 1 mm thick glassy carbon sheet, a 0.5 mm thick PET plastic sheet coated with ITO (denoted as ITO/PET), and a 0.5 mm thick PET plastic sheet covered with a 60 nm thick gold layer (denoted as Au/PET). Polyimide (*Kapton*) tape (as well as laser engraving for the ITO electrodes) was used to additionally restrict the electrochemically active area to a region accessible by the synchrotron beam (**Figure 4.2c**). Copper tape was applied to the ITO/PET sheets to lower the ohmic resistance between the edge of the electroactive area and the external circuit (**Figure 4.2c**).

4.4 Results and discussion

Heterogenite-like cobalt oxide water oxidation catalysts were used to benchmark the spectroelectrochemical cell. Supplementary data was also collected on nickel-based materials to demonstrate key capabilities of the SEC and to provide extended insights into the photoeffects phenomena. In this section, the new SEC is benchmarked (**§ 4.4.1** and **§ 4.4.2**), provide an analysis of photoeffects phenomena (**§ 4.4.3** and **§ 4.4.4**), and undertake an analysis of heterogenite-like (CoOOH) cobalt oxides as catalysts for the water oxidation reaction (**§ 4.4.5**).

The cobalt oxide materials were electrodeposited onto glassy carbon or ITO/PET using either aqueous Co^{2+} derived from $Co(SO_4)_2$[98] or $[Co(NTA)(OH_2)_2]^-$ (NTA = nitrilotriacetate) complex[86] (samples referred to as CoO_x and CoO_x^{NTA}, respectively) in borate buffer (0.1 M, pH 9.2). While the CoOOH structures of CoO_x and CoO_x^{NTA} are indistinguishable, highly active CoO_x^{NTA} materials can be easily deposited at very low loadings,[86] therefore making them ideal for benchmarking the sample loading detection limit of the SEC. XAS analysis of the cobalt oxide catalysts was undertaken at three potentials based on voltammetrically observed features: (i) 1.153 and (ii) 1.653 V *vs*. RHE, prior to and after the first well-defined oxidative process in voltammetry; and (iii) 2.153 V *vs*. RHE, where the material is very active for water oxidation (**Figure 4.4**). The use of the very positive third potential to probe the catalytically active state of cobalt oxide was motivated by a Fourier transformed ac voltammetric (FTacv) study,[78] which predicted the stabilisation of an active, higher oxidation state species (further discussions are provided in **§ 4.4.5**). Cyclic voltammetry was used to calculate the amount of the electrochemically active cobalt in the cobalt oxide samples presented herein (**Figure 4.4**).

Nickel-based materials were electrodeposited potentiostatically onto Au/PET from near-neutral Ni^{2+} aqueous solutions. Two types of the samples were analysed – one with a loading comparable to that used for CoO_x samples, and another with a very thick nickel metal deposit that could be easily seen by a naked eye. Nickel-modified electrodes were analysed at both reductive and oxidative potentials.

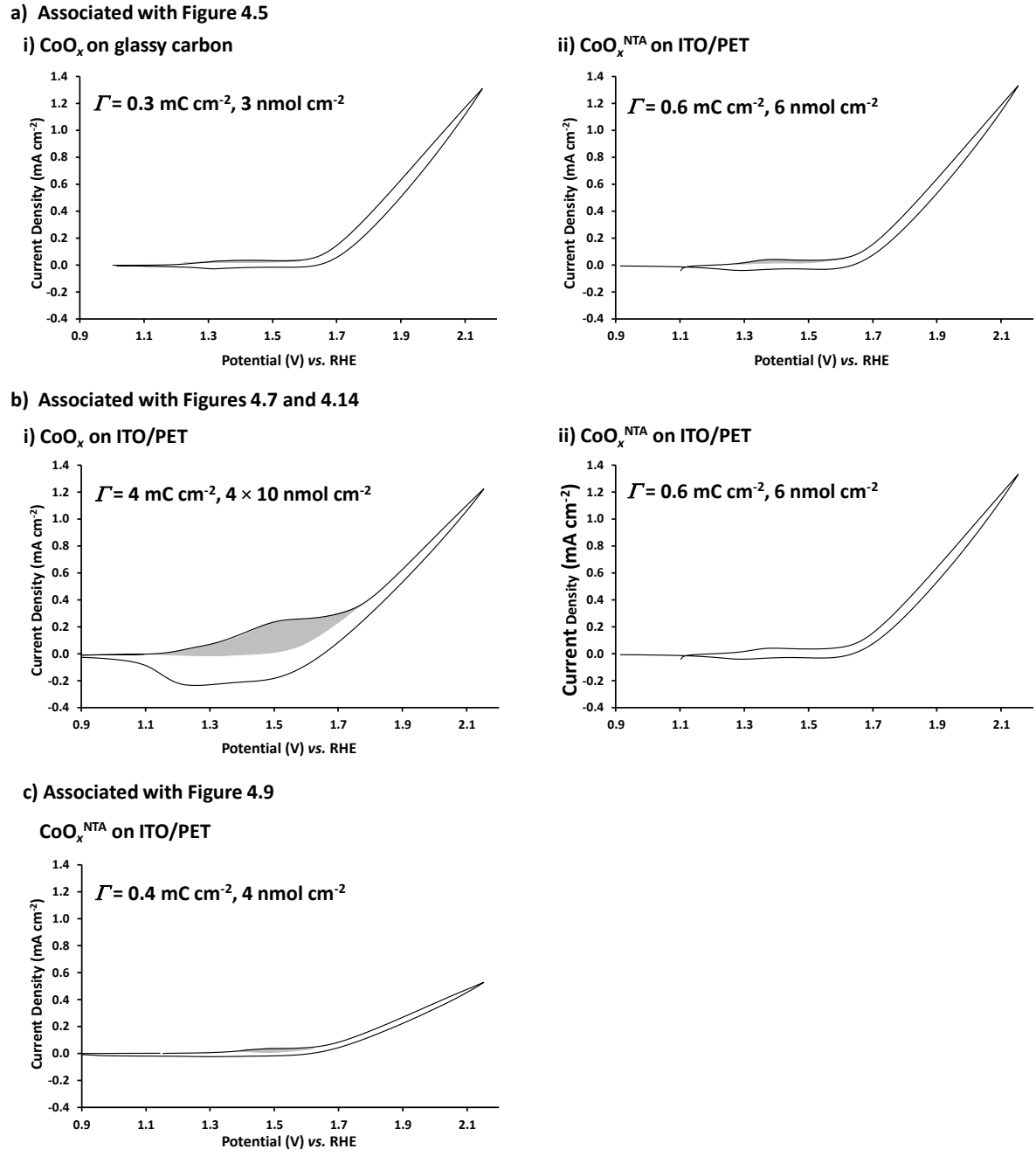

Figure 4.4: Cyclic voltammetry of each CoO_x and CoO_x^{NTA} modified electrode. Electrodes were analysed in air-saturated 0.1 M borate buffer (pH 9.2). Cyclic voltammetry data corresponds to the XAS data presented in: **(a) Figure 4.5** (**a** – glassy carbon support; **b** – ITO/PET support), **(b) Figures 4.7** and **4.14** (**a** – higher loading; **b** – lower loading; both supported on ITO/PET), and **(c) Figure 4.9** (supported on ITO/PET). *Grey* shading shows the peak area used to quantify the concentration of electrochemically active cobalt oxide.

4.4.1 Working electrode selection

The choice of WE substrate greatly influences the quality of both the electrochemical and spectroscopic data. For example, this is evident in the comparison of single X-ray absorption spectrum obtained with either a 1 mm thick glassy carbon sheet or an ITO coated 0.5 mm thick PET sheet (**Figure 4.5**). Both electrodes had similar surface concentrations of electroactive cobalt oxide and were maintained at an applied potential of 2.153 V *vs.* RHE while in contact with air saturated 0.1 M borate buffer during analysis (**Figures 4.4a**).

While both substrate types showed excellent quality electrochemical data (**Figures 4.4a**), the glassy carbon substrate produced poorer quality spectroscopic data as compared to ITO/PET (**Figure 4.5**). The poor quality of the XAS with glassy carbon electrode is most pronounced in the pre-edge region where a signal-to-noise ratio is very low, and in the extended X-ray analysis fine structure (EXAFS) region where monochromator glitches (deliberately not removed) manifest. Although glassy carbon is an amorphous and low atomic number material, the thickness of the substrate attenuated the X-ray beam and resulted in a comparably poor signal-to-noise ratio. In contrast, good quality electrochemical and XAS data were obtained with CoO_x-modified ITO/PET (**Figure 4.4a-ii**) and also from Au/PET electrodes that were functionalized with nickel oxyhydroxide/oxide (**Figure 4.6a**). The provided examples demonstrate the critical importance of the judicious choice of a working electrode and its support for the quality *in situ* spectroelectrochemical measurements.

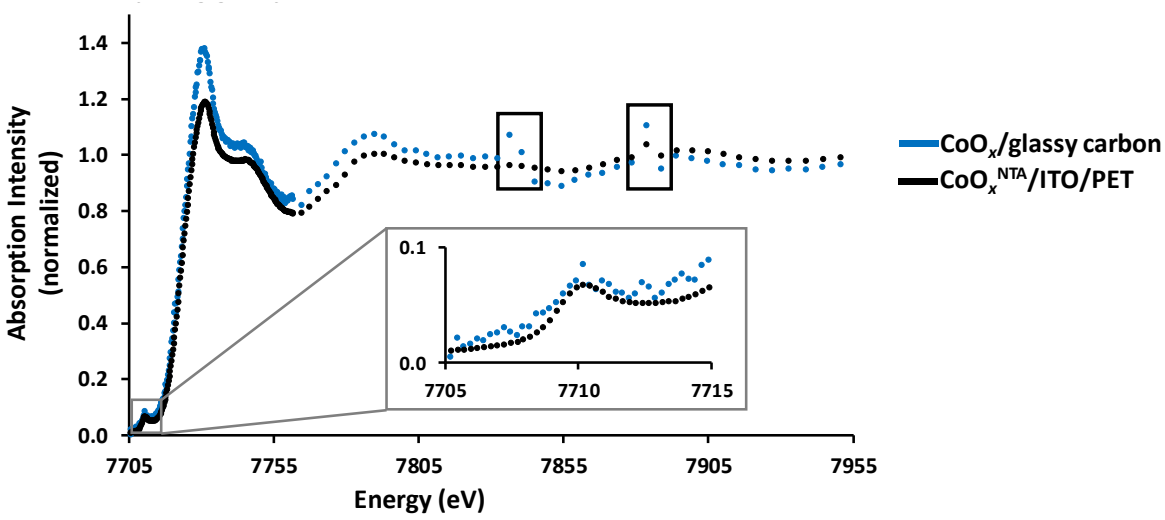

Figure 4.5: Single Co K-edge X-ray absorption spectra collected *in situ* for cobalt oxides on 1 mm thick glassy carbon (*red* trace; Γ = 0.3 mC cm^{-2} ≈ 3 nmol cm^{-2}) and CoO_x^{NTA} on 0.5 mm thick ITO/PET (*black* trace; Γ = 0.6 mC cm^{-2} ≈ 6 nmol cm^{-2}). Electrodes were

analysed at 2.153 V *vs.* RHE in air-saturated aqueous 0.1 M borate buffer (pH 9.2) electrolyte solution. The pre-edge region is expanded in the inset. The single monochromator glitches outlined with black boxes in the main plot (occurring at 7835.5 and 7882.9 eV in I_0) have not been removed to highlight the differences between signal-to-noise ratios in the spectra.

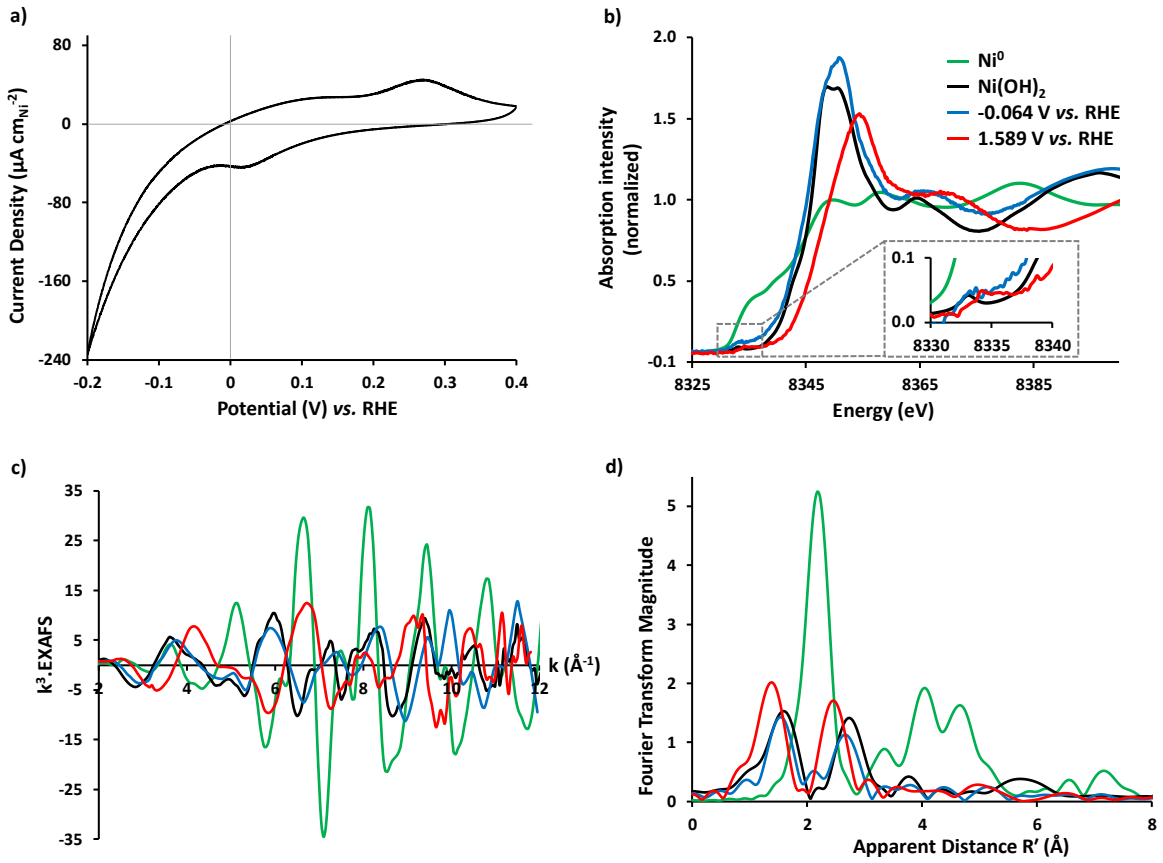

Figure 4.6: Electrochemical and spectroscopic data collected on nickel-based materials. Data is presented as: **(a)** Cyclic voltammetry in the HER and pre-OER regions (0.020 V s^{-1}, *quasi*-stabilized third cycles are shown) and **(b-d)** *in situ* Ni K-edge XAS data for electrodeposited nickel-based material on Au/PET in contact with 0.1 M NaOH. XAS data is presented as: **(b)** full range XANES, **(c)** k^3-weighted EXAFS, and **(d)** Fourier transform of the EXAFS. *In situ* XAS data were obtained at -0.064 (*blue*) and 1.589 V *vs.* RHE (*red*) (marked with crosses in panel **(a)**). *Green* traces show *in situ* data collected for the thick Ni^0 coating on Au/PET (voltammetry shown in **Figure 4.3**) with no potential applied. *Black* traces show data collected for the Ni(OH)$_2$ reference.

4.4.2 Data reproducibility

A SEC should allow quality XAS data to be collected in a single measurement to facilitate rapid collection of reliable and reproducible datasets. Moreover, successive registration of replicate spectra from the same sample may not be feasible for some systems that are labile or susceptible to the effects of X-rays. From this perspective, the cell should enable the collection of high signal-to-noise X-ray absorption near edge structure (XANES) and EXAFS single spectra that can be interpreted unambiguously. The cell should also provide an electrochemical environment that is unaltered on the timescale of hours so that replicate spectra can be collected to assess the reproducibility. Additionally, high quality single spectrum measurements should allow sample changes and/or beam damage to be evaluated before assessing the suitability for replicate spectra to be averaged.

As the ITO/PET substrate facilitates the collection of high signal-to-noise spectra, it was chosen as the WE material for both the CoO_x and CoO_x^{NTA} samples examined herein. To assess the spectral reproducibility obtainable by the SEC using these two materials, X-ray absorption spectra were collected stepwise at 1.153, 1.653 and 2.153 V *vs.* RHE, with the sequence of potentials then repeated without changing the beam-spot (**Figure 4.7**; experimental protocol depicted in **Figure 4.7a-i** and **4.7b-i** for CoO_x/ITO/PET and CoO_x^{NTA}/ITO/PET, respectively). This protocol allowed for a direct comparison between the spectra collected at different potentials, and any effects of the beam to be assessed. The beam-spot position was then changed, and a single spectrum was collected at each potential to demonstrate that the observable changes were homogeneous throughout the material. A chronoamperogram (CA) was recorded during the collection of each XAS spectrum to ensure a stable electrochemical response over time (**Figure 4.8**). The amount of electrochemically active cobalt in the samples in **Figure 4.7** is calculated in **Figure 4.4b**.

Each individual XAS spectrum shows excellent data quality, with the replicate spectra illustrating almost perfect reproducibility (**Figure 4.7 iii** and **iv**). The difference between the edge positions in the replicate XANES measurements is less than 0.1 eV in beam energy, and as such, does not indicate any irreversible X-ray beam damage to the samples. This high level of reproducibility allows any difference between the edge positions for the spectra collected at 1.153, 1.653, and 2.153 V *vs.* RHE to be analysed with a high degree of certainty (**§ 4.4.5**). The CAs recorded during the collection of each spectrum were reproducible aside from typical discrepancies at positive potentials due to bubble formation (**Figure 4.8**).

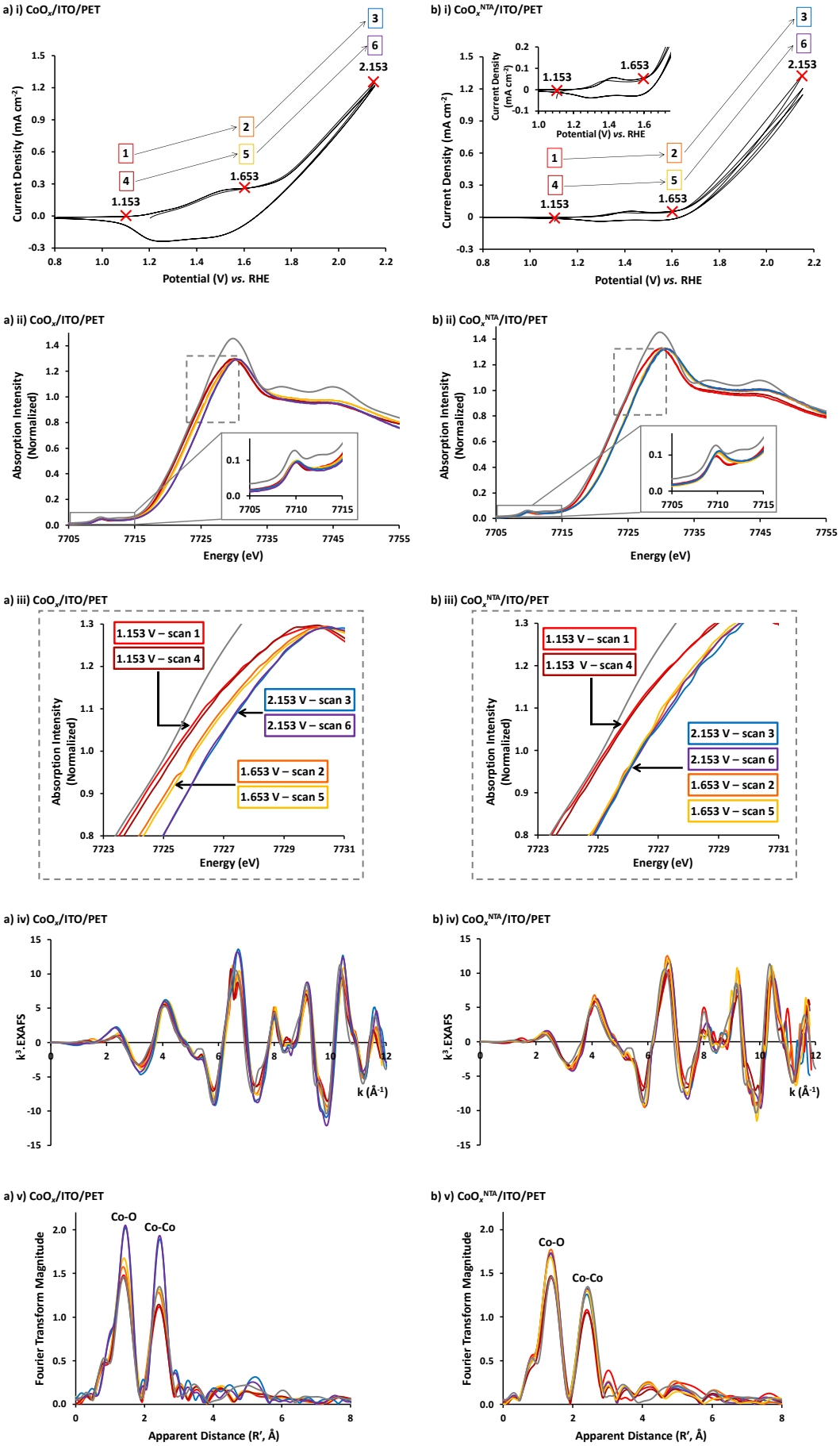

(Figure caption over page)

Figure 4.7: Electrochemical and *in situ* Co K-edge XAS data collected on CoO_x/ITO/PET and CoO_x^{NTA}/ITO/PET. Data is presented as: **(a)** CoO_x/ITO/PET (Γ = 4 mC cm^{-2} ≈ 4 × 10 nmol cm^{-2}) and **(b)** CoO_x^{NTA}/ITO/PET (Γ = 0.6 mC cm^{-2} ≈ 6 nmol cm^{-2}) in contact with 0.1 M borate buffer (pH 9.2): **(i)** cyclic voltammetry (v = 0.020 V s^{-1}; first three cycles; inset shows peaks prior to the onset of water oxidation), **(ii)** full range XANES (the pre-edge region is expanded in the inset), **(iii)** expanded maxima of XANES (outlined by dashed grey boxes in panels **ii**), **(iv)** k^3-weighted EXAFS, and **(v)** Fourier transform of the EXAFS. *In situ* XAS data were obtained at: 1.153 (*red* – replicate 1; *dark red* – replicate 2), 1.653 (*orange* – replicate 1, *yellow* – replicate 2), and 2.153 V *vs.* RHE (*blue* – replicate 1, *purple* – replicate 2). *Grey* traces show *in situ* data collected for the CoOOH reference.

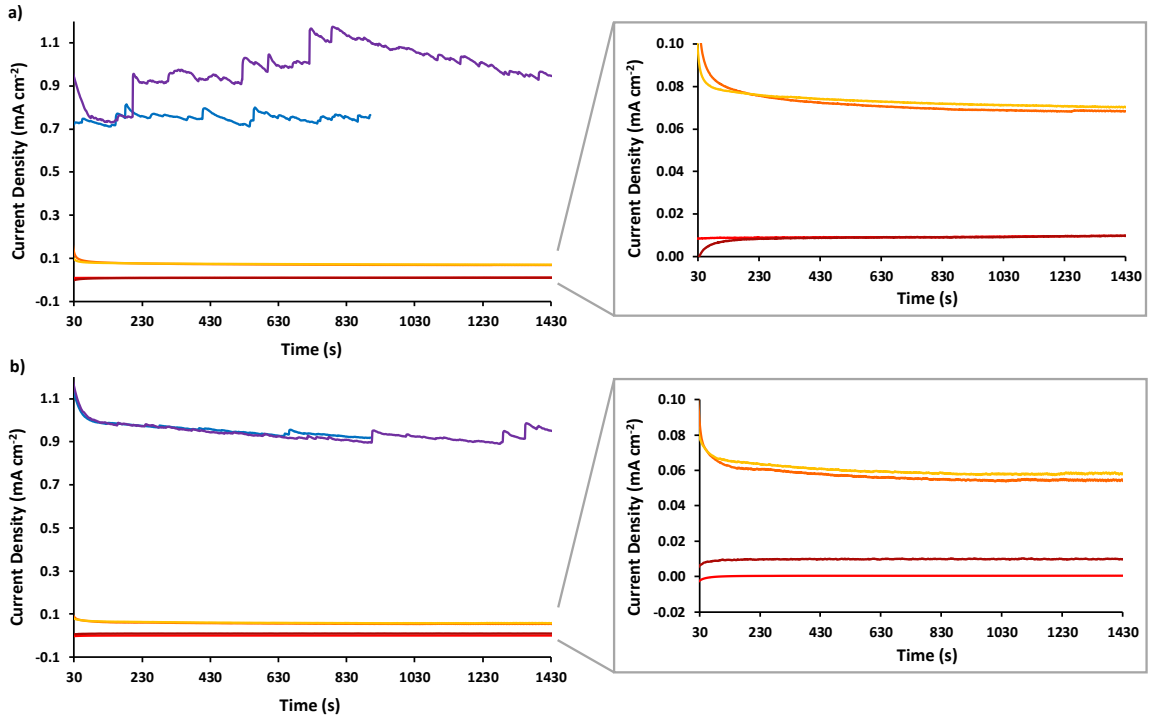

Figure 4.8: Chronoamperomograms recorded on CoO_x/ITO/PET and CoO_x^{NTA}/ITO/PET during spectroscopic data collection. Chronoamperomograms are associated with the *in situ* XAS spectra collected in the cycling sequence shown in **Figure 4.7i**. Data is presented as: **(a)** CoO_x/ITO/PET (Γ = 4 mC cm^{-2} ≈ 4 × 10 nmol cm^{-2}) and **(b)** CoO_x^{NTA}/ITO/PET (Γ = 0.6 mC cm^{-2} ≈ 6 nmol cm^{-2}). Chronoamperometric data for the potentials generating a low current density is expanded on the right hand side. *In situ* XAS data were obtained at: 1.153 (*red* – replicate 1; *dark red* – replicate 2), 1.653 (*orange* – replicate 1, *yellow* – replicate 2), and 2.153 V *vs.* RHE (*blue* – replicate 1, *purple* – replicate 2). Note that some of the replicate data are hard to distinguish at the resolution of this figure.

4.4.3 The observation of X-ray induced photoeffects as a function of potential

In general, all samples are susceptible to photodamage during X-ray absorption analysis to a certain degree. When electromaterials are probed in an *in situ* mode, the magnitude of the photoeffects will be additionally affected by the material film thickness and electrode potential, meaning that these variables need to be considered during the design of experiments and data analysis. While low sample loadings on the electrode surface (thin films) are preferred for the *in situ* characterisation of heterogeneous electrocatalysts (**Scheme 4.1**), a lower sample loading often increases the susceptibility to photodamage. In terms of X-ray cross-sections, the damage caused to thick and thin samples should be similar since hard X-rays will likely penetrate the full depth of both sample types. However, the secondary reactions involving X-rays penetrating through the sample and into the electrolyte solution can be distinguishably different (**Scheme 4.3**), both in terms of photodamage and *in situ* regeneration of the sample (*vide infra*).

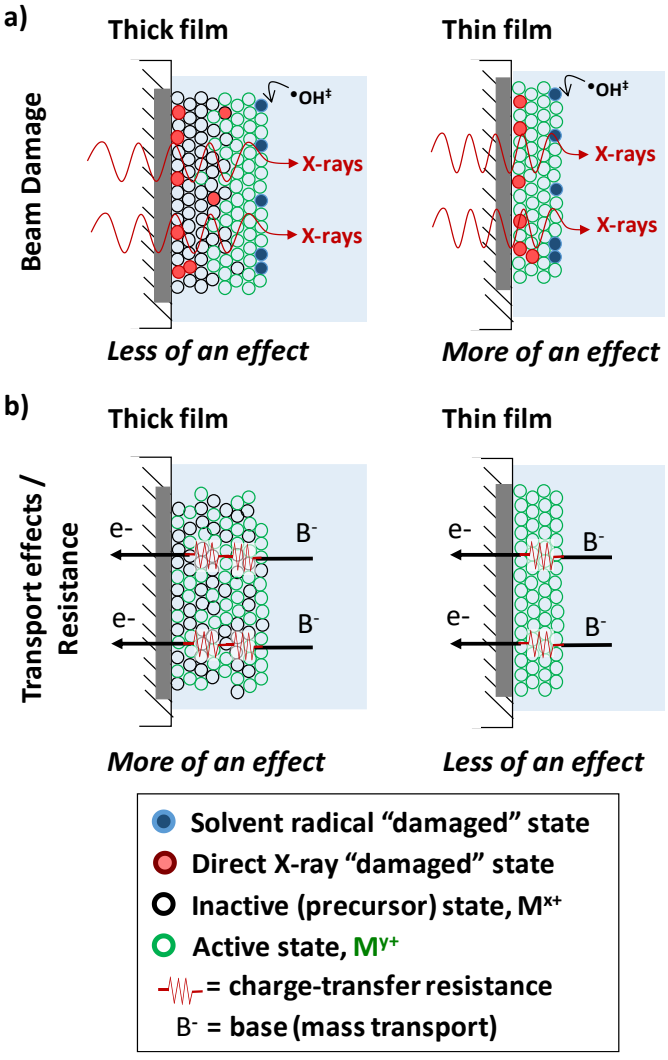

Scheme 4.3: A visual guide describing the interplay of X-ray photoeffects and resistance/transport effects. Note that the X-rays enter *via* the working electrode as the WE is the window of the SEC. The direction of the effect could be reversed depending on the cell configuration. ‡Note that X-ray damage can be caused directly to the material, or through interaction with ionised solvent. Ionised solvent will affect sites in contact with that solvent directly in the system described.

The effect of film thickness on photodamage susceptibility can be determined by comparison of successive *in situ* XANES spectra collected from electrodes with differing sample loadings. This is exemplified herein with spectra taken with a two low loading CoO_x^{NTA} catalysts on ITO/PET with Γ = 0.6 mC cm^{-2} ≈ 6 nmol cm^{-2} (**Figure 4.7b**) and Γ = 0.4 mC cm^{-2} ≈ 4 nmol cm^{-2} (**Figure 4.9**). Note that the two successive XANES spectra were collected on the same beam-spot to ensure any observable change in the spectra was a function of X-ray damage and not sample inhomogeneity. The electrochemical solution was not flowed during this photoeffects analysis as the solution was not flowed during the mechanistic study (further details provided in **§4.4.5 Interpretation of the *in situ* XAS data: the water oxidation case**), and therefore, the photoeffects analysis is examined as a function of one variable (*i.e.* sample loading) and not multiple variables (*i.e.* sample loading and mixing). While no evidence of photodamage was observed for CoO_x^{NTA} at Γ = 0.6 mC cm^{-2}, nor for higher sample loadings, the lower sample loading of 0.4 mC cm^{-2} appeared to undergo photooxidation at 1.153 V *vs.* RHE (**Figure 4.9a**) and photoreduction at 2.153 V *vs.* RHE (**Figure 4.9b**). Thus, the photodamage processes occurring within the CoO_x materials are influenced by sample loading.

Although the exact causes of such photodamage are not always clear, the photooxidation and photoreduction processes show potential dependence. This indicates that the photochemical reactions act to make a more thermodynamically stable product. Thus, a reduced metal centre is more likely to be photooxidised, while an oxidised metal centre is more likely to be photoreduced. Under our experimental conditions these processes clearly manifest for the thinnest CoO_x^{NTA} films (**Figure 4.9**). Moreover, application of a potential cannot restore the expected state of the cobalt oxide (*i.e.* electrochemical processes cannot compensate for the beam damage.) For example, at very positive potential of 2.153 V *vs.* RHE, the CoO_x^{NTA} sample with lowest loading examined (Γ = 0.4 mC cm^{-2}) appeared to become sequentially more reduced than the CoOOH standard with each subsequent XANES spectrum collected (**Figure 4.9b**). A less pronounced though similar photooxidation effect was observed for this sample at 1.153 V *vs.* RHE (**Figure 4.9a**).

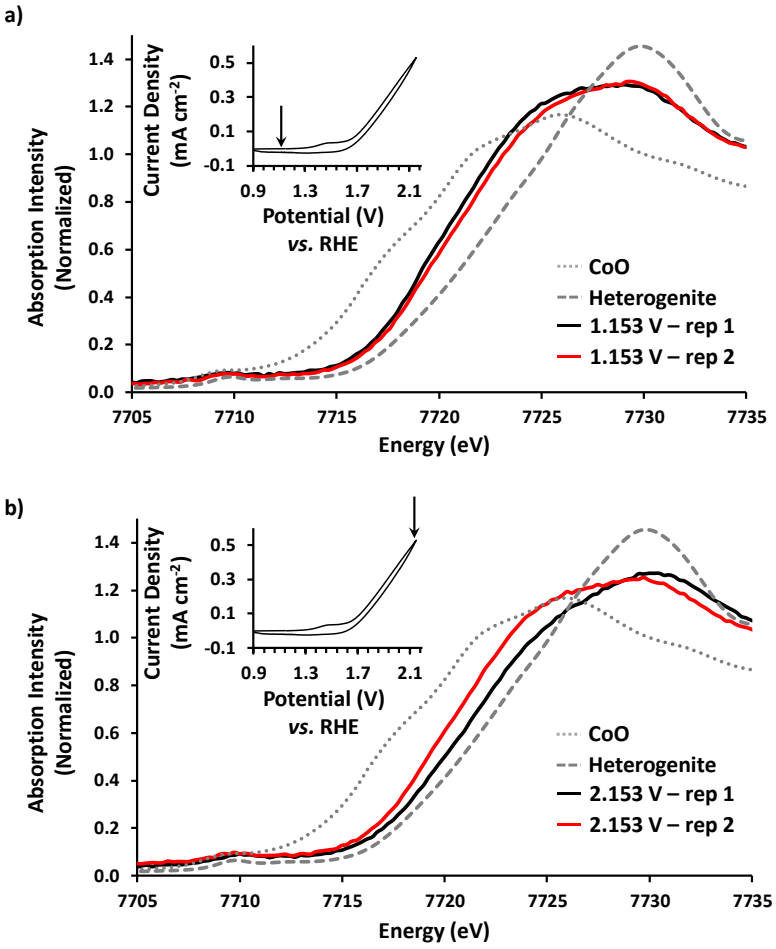

Figure 4.9: *In situ* Co K-edge XANES data collected on a very low loading of CoO_x^{NTA}. CoO_x^{NTA} (Γ = 0.4 mC cm^{-2} ≈ 4 nmol cm^{-2}) was electrodeposited onto ITO/PET in contact with 0.1 M borate buffer (pH 9.2). Data were obtained at: **(a)** 1.153 and **(b)** 2.153 V *vs.* RHE. A cyclic voltammogram of the material is shown in each inset with arrows indicating the potential applied during XANES collection.

Very significant effects of the X-ray beam were also observed during the analysis of the reductively electrodeposited nickel onto Au/PET electrodes (**Figure 4.6**). The materials were obtained in aqueous Ni^{2+} solutions at -1.013 V *vs.* NHE (-0.6 V *vs.* RHE at pH 7), which is significantly more negative than E^0 = -0.257 V *vs.* NHE for the $Ni^{2+/0}$ redox process, and the corresponding cyclic voltammograms in the hydrogen evolution/oxidation range were in a good agreement with that of Ni^0 metal (**Figure 4.3**). However, *in situ* XANES spectra recorded for such electrodeposits at -0.15 V *vs.* RHE, where nickel metal exhibits pronounced catalytic activity for the hydrogen evolution reaction, indicated that the dominating state is $Ni(OH)_2$ (**Figure 4.6 b-d**).

A plausible rationalisation of the discrepancy between electrochemical and spectroscopic data is quantitative photooxidation of Ni^0 to Ni^{II} in a comparatively small irradiated area probed by XAS. At the same time, cyclic voltammetry probes the whole electrode surface, most of which remained in a dominating metallic state because it was not affected by the X-ray beam. When a very thick nickel metal plating was applied to the Au/PET electrode, the XANES data were in a perfect agreement with that of Ni^0 (**Figure 4.6 b-d**) and corresponding voltammetry (**Figure 4.3**). However, the extremely high thickness of this sample prevented meaningful *in situ* spectroelectrochemical analysis as the XANES spectra always demonstrated Ni^0 irrespective of the potential applied, presumably due to the effects of film thickness summarised in **Scheme 4.1**.

When analysing photoeffects in an *in situ* cell, it is important to consider the possible chemical changes to not only the analysed electromaterial, but also to the surrounding electrolyte solution. X-ray induced perturbations in the solution can cause direct and indirect changes to the sample material given that all SEC components are in a physical contact. Of direct relevance to the experiments described herein and many other *in situ* spectroelectrochemical studies is the interaction between water and ionising radiation.[58-60] One of the major products of the water photolysis are hydroxyl radicals, produced *via* a mechanistically complicated process that can be described by **reactions 4.1** and **4.2**:[58-59, 64, 70-71]

$$H_2O + h\nu \rightarrow H_2O^{\bullet+} + e^-_{aq} \qquad \textbf{(4.1)}$$

$$H_2O^{\bullet+} + H_2O \rightarrow H_3O^+ + OH^{\bullet} \qquad \textbf{(4.2)}$$

Under ambient conditions, hydroxyl radicals are highly-reactive species that can interact with the sample during the *in situ* XAS analysis and change the oxidation states of elements of interest.[57-59, 64, 68, 70-71] For example, hydroxyl radical formation might contribute to the indirect photooxidation of CoO_x^{NTA} (Γ = 0.4 mC cm^{-2}) which was observed at 1.153 V *vs.* RHE (**Figure 4.9a**) by oxidising Co^{II} at the cobalt oxide surface to Co^{III} (Co^{II} is present prior to the first oxidative wave) as summarised in **reaction 4.3a**. Similar effects of $OH^{\bullet}$ could also contribute to the oxidation of Ni^0 to Ni^{II}.

$$Co^{II}O_xH_y + OH^{\bullet} \longrightarrow Co^{III}O_{x+1}H_{y+1} \qquad \textbf{(4.3a)}$$

$$Co^{2+} + OH^{\bullet} + 2OH^- \longrightarrow Co^{III}(OH)_3 \downarrow \qquad \textbf{(4.3b)}$$

The oxidation of Co^{II} by hydroxyl radicals is also concordant with the observations of another series of experiments, where blank ITO/PET electrodes were kept in contact with Co^{2+} or $[Co(NTA)(OH_2)_2]^-$ precursor solution (in borate buffer, pH 9.2) and analysed by successive XANES (*i.e.* the sample was irradiated by X-rays) without an applied potential; **Figure 4.10 a** and **b**, respectively. The heterogenite-like cobalt oxide formation is evident from a progressive shift in the edge position to higher energy through the successive XANES spectra. The shift towards a higher average Co oxidation state was accompanied by an increase in raw fluorescence intensity (**Figure 4.11**). The photodeposited materials were electrochemically (**Figure 4.12a**) and spectroscopically (**Figure 4.12b**) indistinguishable from samples synthesised by electrodeposition. Subsequent analysis of the electrodes confirmed that the materials were immobilised on the electrode surface and localised to the beam footprint (**Figure 4.10c**). This localisation is probably because $OH^{\bullet}$ radicals are too unstable and short-lived to migrate from the beamspot.[58-59, 64, 70-71] The overall photodeposition process can be described by **reaction 4.3b**.

The photooxidation, photoreduction and photodeposition phenomena observed herein highlight the importance of photoeffects in spectroelectrochemical studies. Such beam phenomena can result in direct phase transformation that might be erroneously ascribed to purely electrochemical transformations.

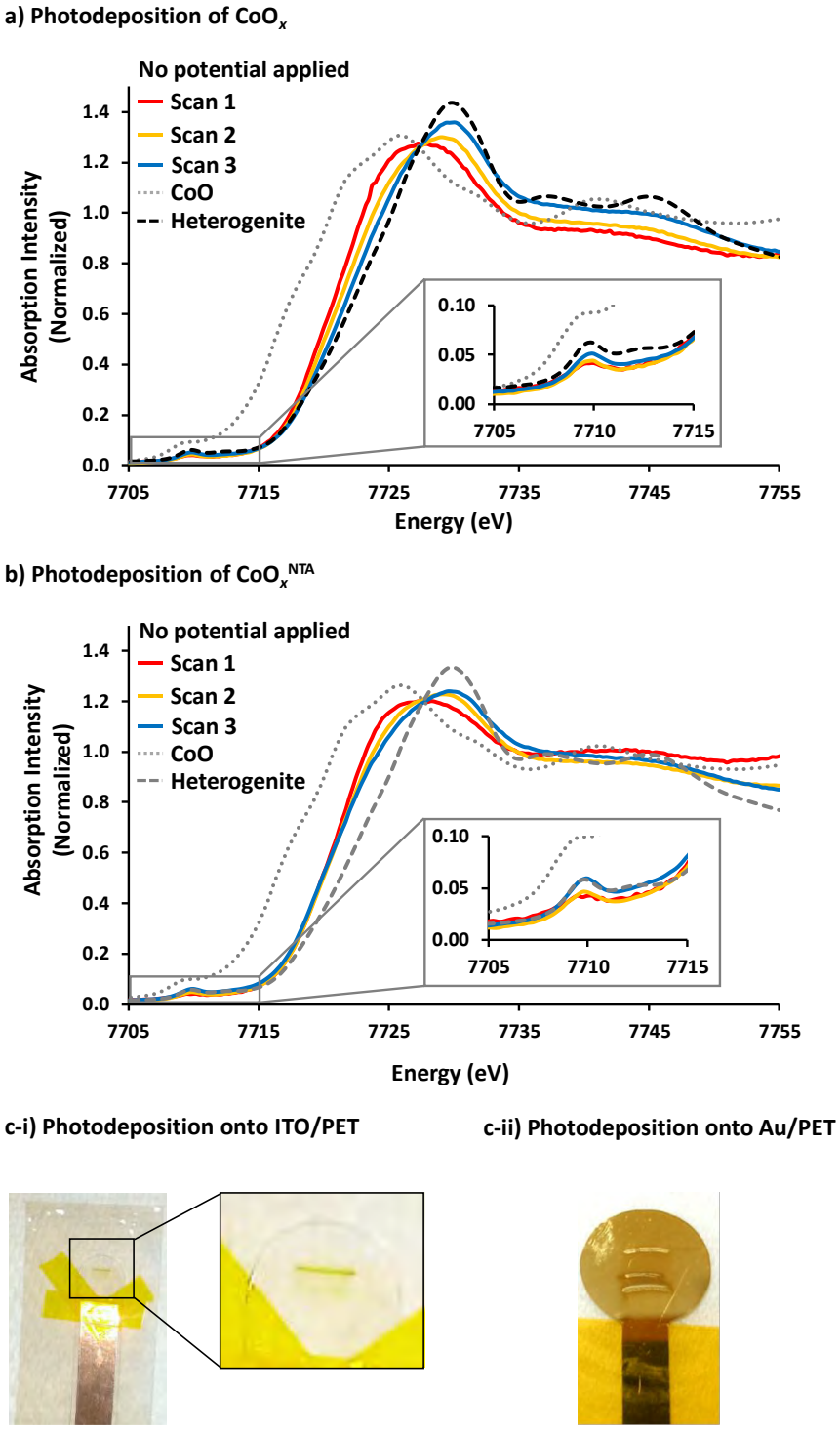

Figure 4.10: Normalized XAS data collected during the spontaneous photodeposition of the cobalt oxide materials. *In situ* Co K-edge XANES spectra collected consecutively for a blank ITO/PET electrode in contact with **(a)** the CoO_x deposition solution (1 mM Co^{2+} in 0.1 M borate buffer, pH 9.2), and **(b)** CoO_x^{NTA} deposition solution ($[Co(NTA)(OH_2)_2]^-$ in borate buffer, pH 9.2); both with no potential applied. *Dotted* and *dashed grey* data were obtained from CoO and CoOOH references, respectively. **(c)** Photographs of the photodeposited CoO_x materials onto **(i)** ITO/PET and **(ii)** Au/PET electrodes.

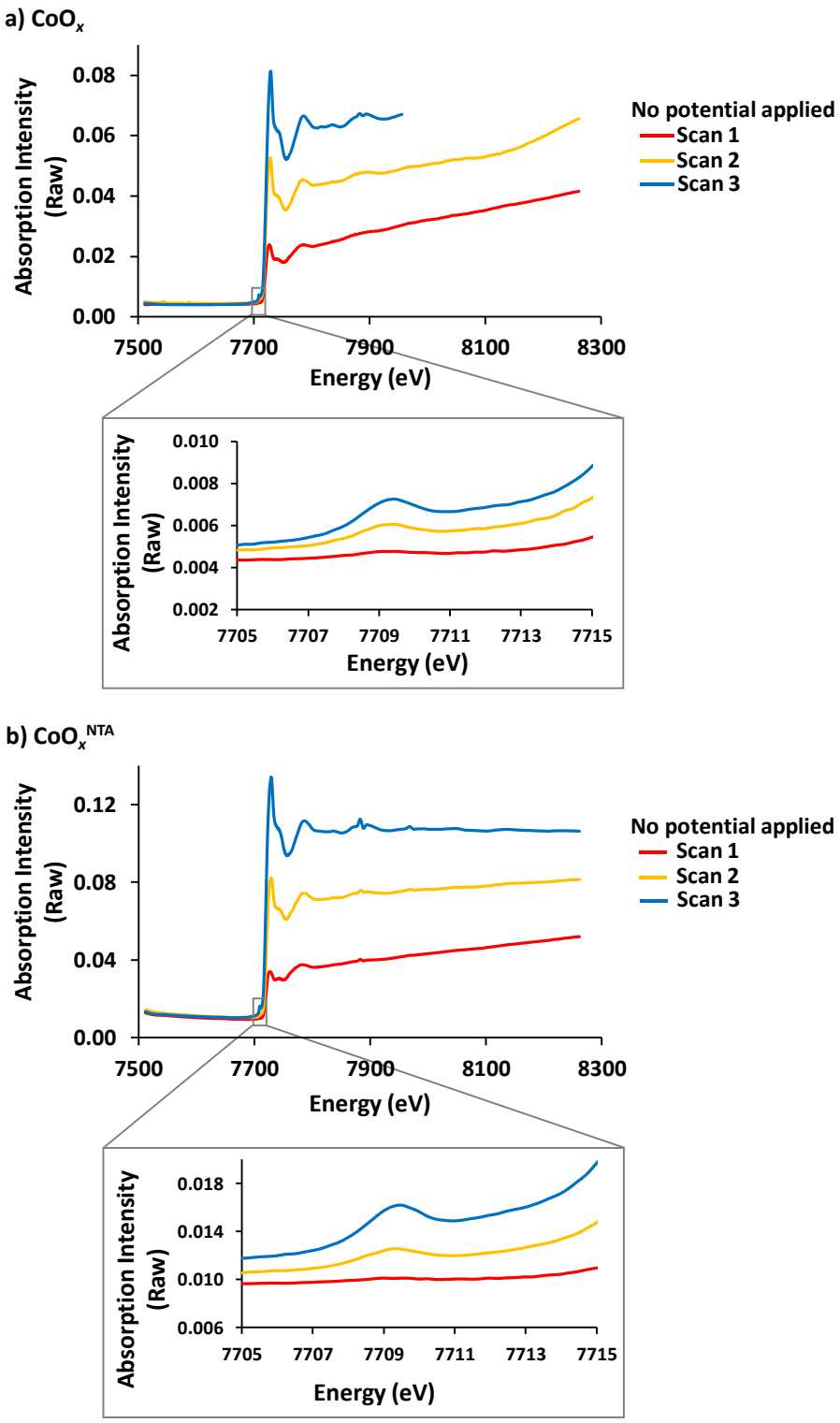

Figure 4.11: Raw XAS data collected during the spontaneous photodeposition of the cobalt oxide materials. Data is presented as: **(a)** CoO_x and **(b)** CoO_x^{NTA}. The three successive Co K-edge spectra (*red* –spectrum 1, *yellow* –spectrum 2, and *blue* –spectrum 3) were collected using a blank ITO/PET electrode in contact with **(a)** CoO_x^{NTA} deposition solution ($[Co(NTA)(OH_2)_2]^-$ in borate buffer, pH 9.2) or **(b)** CoO_x deposition solution (1 mM Co^{2+} in 0.1 M borate buffer, pH 9.2), with no potential applied.

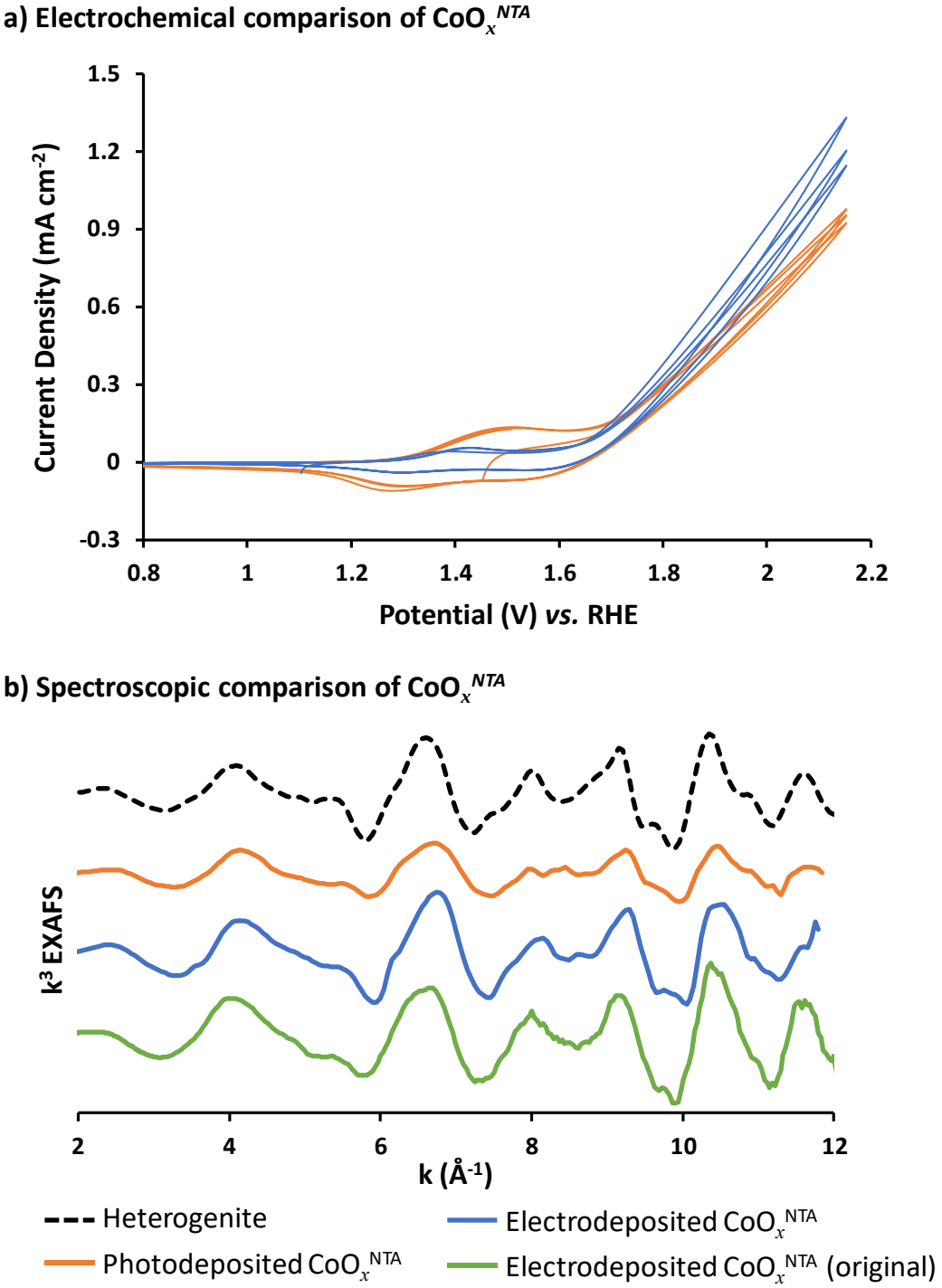

Figure 4.12: Comparison of electrochemically deposited and photodeposited CoO_x^{NTA}. Data is presented as: **(a)** cyclic voltammograms (v = 0.020 V s^{-1}; first three cycles shown) for electrodeposited CoO_x^{NTA} (**Figure 4.7**) (*blue*) and photodeposited CoO_x^{NTA} (**Figure 4.10b**) (*orange*), and **(b)** k^3-weighted EXAFS for heterogenite (*black*), electrodeposited CoO_x^{NTA} (*blue*), photodeposited CoO_x^{NTA} (*orange*), and the original publication[S2] of electrodeposited CoO_x^{NTA} (*green*). All of these samples are considered structurally identical within experimental inconsistencies.

4.4.4 Quantification of the photoelectrochemical effects of X-rays

While XANES analysis can quantitatively identify beam-damage over the course of multiple spectra, the SEC configuration can be used to measure effects immediately upon irradiation. The occurrence of photooxidation and photoreduction processes can be dependent on whether a sample is in an oxidised or reduced state (*vide supra*). As such, a SEC can measure the susceptibility of a sample to photoeffects by using applied potential to maintain an oxidised or reduced state and quantifying the associated X-ray derived photocurrent.

In practice, this is achieved by recording a CA as the beamline shutter is opened and closed. The resulting CA will contain the superposition of the current associated with the sample (which is recorded when the shutter is closed) and the current associated with the interaction between the beam and the sample/electrode/solution (which is recorded when the shutter is open). The susceptibility of a system to photooxidation or photoreduction can then be quantified by examining the amplitude and polarity (*i.e.* whether the current is oxidative or reductive) of the photocurrent contribution as compared to the baseline current contribution from the sample.

The susceptibility of CoO_x^{NTA} on Au/PET sample to photoeffects was examined by conducting the aforementioned CA experiment at the potentials of 1.635 (an oxidative potential), 0.005 (an intermediate potential) and -0.395 V *vs.* RHE (a reductive potential). CAs recorded under such conditions confirmed that the polarity of the photocurrent was dependent on the potential applied (**Figure 4.13**). Indeed, the oxidative current at 1.635 V *vs.* RHE became even more positive during X-ray irradiation (**Figure 4.13a**), and the cathodic current at -0.395 V *vs.* RHE became increasingly negative (**Figure 4.13c**). For an intermediate potential of 0.005 V *vs.* RHE, the effect was less pronounced but still clear enhancement of the reduction current was observed (**Figure 4.13b**).

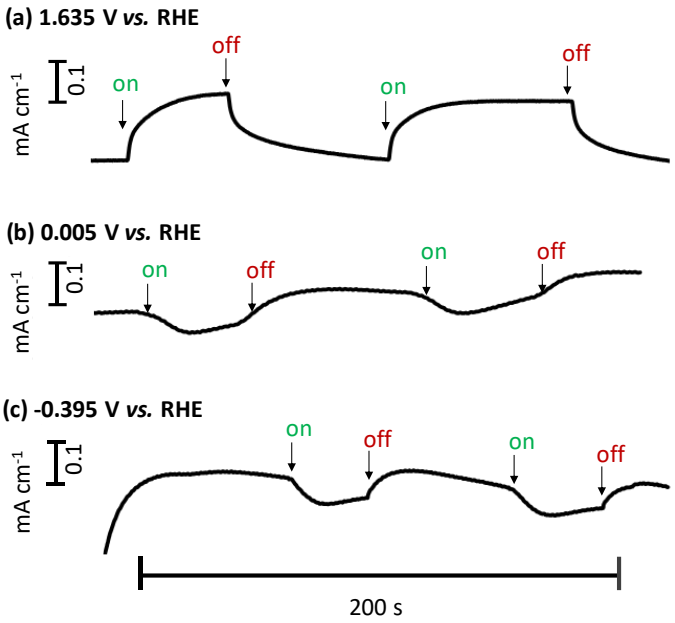

Figure 4.13: The interaction of the synchrotron beam (8000 eV) with cobalt oxide materials. Effects of switching the beam "on" and "off" (*i.e.* opening and closing the shutter) on the current were recorded during potentiostatic experiments at: **(a)** 1.653, **(b)** 0.005 and **(c)** -0.395 V *vs.* RHE. CoO_x was deposited onto Au/PET electrode in contact with 0.1 M borate buffer (pH 9.2). Note that currents are normalised to the beam area in this figure.

By correlating the conclusions drawn from **Figure 4.9** to these results, it is suggested that positive photocurrent is spectroscopically associated with a tendency for photoreduction of the electrocatalyst (**Figure 4.9b**), and that negative photocurrent is spectroscopically associated with a tendency for photooxidation of the electrocatalyst (**Figure 4.9a**). The chemical processes occurring during the *in situ* XAS analysis at oxidative potentials can be simplistically summarised as follows:

Photoreduction: $Co^{m+} + h\nu \rightleftarrows Co^{(m-x)+}$ **(4.4)**

Electrooxidation: $Co^{(m-x)+} \rightleftarrows Co^{m+} + xe^-$ **(4.5)**

The chemical processes occurring during the *in situ* XAS analysis at reductive potentials can be summarised as follows:

Photooxidation: $Co^{m+} + h\nu \rightleftarrows Co^{(m+x)+}$ **(4.6)**

Electroreduction: $Co^{(m+x)+} + xe^- \rightleftarrows Co^{m+}$ **(4.7)**

As photooxidation and photoreduction are essentially redox reactions caused by the X-ray beam, these effects might be theoretically corrected for by applying a potential to compensate for the current generated through the processes in **reactions 4.4-4.7**. However, doing this quantitatively can be challenging as processes beyond electron transfer are involved in photooxidation/photoreduction. For example, the photooxidation of Co^{II} to Co^{III} (**Figure 4.10 a** and **b**) or Ni^0 to Ni^{II} (**Figure 4.6**) could be a purely redox electron transfer process (*e.g.* $Ni^0 \rightarrow Ni^{2+} + 2e^-$), or it could involve radiologically generated species like hydroxyl radical produced through **reactions 4.1** and **4.2** (*e.g.* $Ni^0 + 2OH^\bullet \rightarrow Ni(OH)_2$).

If a sample is being photooxidised or photoreduced during an *in situ* experiment, there are two strategies to reduce these effects. Firstly, the sample loading can be increased until photoeffects are no longer apparent in the XAS data. The sample loading should not be increased to the extent that the system becomes insensitive to the electrochemical processes of interest (*i.e.* the 'high loading' scenario in **Scheme 4.1**). Secondly, our research suggests that the electrochemical cell could be used to estimate the potential correction required to offset the photoreduction/photooxidation effects using the aforementioned CA experiment (**Figure 4.13**). However, further research is needed to better understand the kinetic and thermodynamic mechanisms of this protection method.

4.4.5 Interpretation of the *in situ* XAS data: the water oxidation case

Further discussions focus on the heterogenite-like cobalt oxide catalysts that were not subject to significant X-ray photodamage and differed significantly in the amount of electroactive metal: CoO_x^{NTA} with Γ = 0.6 mC cm^{-2} ≈ 6 nmol cm^{-2} and CoO_x with Γ = 4 mC cm^{-2} ≈ 4 × 10 nmol cm^{-2} (**Figure 4.7**). These samples produce the same water oxidation current density per geometric surface area, but differ in their specific activity (activity per electroactive cobalt centre) by a factor of 10 (**Figure 4.4b**). As XAS indicates these materials are chemically identical, the catalytic turnover per active site must be limited in the higher loading sample to account for the differences in specific activity. While it is possible for electron transport to be limited in the "thicker" sample due to a higher charge-transfer resistance, mass transport of the base and water is also likely to be slowing the catalytic turnover rate (**Scheme 4.3**).

As mentioned above, the mechanism of the CoO_x-catalysed OER has been previously analysed under the assumption that key steps are described by the reactions in **Scheme 4.2a**. In the terms of this scheme, **G** and **A** are the lower and higher oxidation states of cobalt, while **R** and **P** are the deprotonated and protonated base. The electrochemical conditions employed herein for the *in situ* XAS analysis of cobalt oxide water oxidation catalysts were selected to suppress the mass transport of deprotonated base, *viz.* the experiments were undertaken with no convection and using a low concentration of proton acceptors (0.1 M borate buffer, pH 9.2). This was done to suppress the abstraction of protons from the catalytic surface (reaction **A** + **R** → **G** + **P** in **Scheme 4.2**), which was expected to increase the lifetime of the highly oxidised state of CoO_x (state **A** in **Scheme 4.2**) according to the previous electrokinetic modelling.[78, 81]

Another key requirement for the stabilisation of active state **A** is the polarisation of the electrode at potential beyond the reversible potential for the **G** ⇄ **A** ± $\mathbf{e^-}$. Specifically, if the mechanism in **Scheme 4.2** would apply to a CoO_x-catalysed water electrooxidation, the corresponding effective reversible potential would be approximately 1.9-2.0 V *vs.* RHE.[78] Hence by definition, any *in situ* spectroelectrochemical analysis undertaken at potentials that are more negative would not be able to detect the active state. It is also important to recognise that high catalytic current is often achievable at potentials significantly less positive (electrooxidation) or less negative (electroreduction) than the actual reversible potential of an electron transfer (**G** ⇄ **A** in **Scheme 4.2**) when the latter is coupled to a chemical reaction (**R** → **P** in **Scheme 4.2**) in a catalytic mechanism. However, a significant rate of the catalytic reaction does not guarantee that the catalyst is continuously present in the state **A**.[79]

Bonke *et al.* utilised Fourier transformed alternating current voltammetry[99-100] to identify two clear redox events important to the function of cobalt water oxidation electrocatalysts.[78] By undertaking simulation[101] to experiment comparisons, it was demonstrated therein that the electrochemical process detected at *ca* 1.42 V *vs.* RHE is very slow and is not coupled to catalytic water oxidation (*Process I*), while a second significantly faster electron transfer process manifests at potentials where the oxygen evolution reaction rate is high (*Process II*). Key FTacv data collected on these systems are reproduced herein and presented as the 1st and 4th ac harmonics alongside XAS data focused on three critical potentials: 1.153 (before *Process I*), 1.653 (after *Process I* but before *Process II*), and 2.153 V *vs.* RHE (after *Process II*) (**Figure 4.14**).

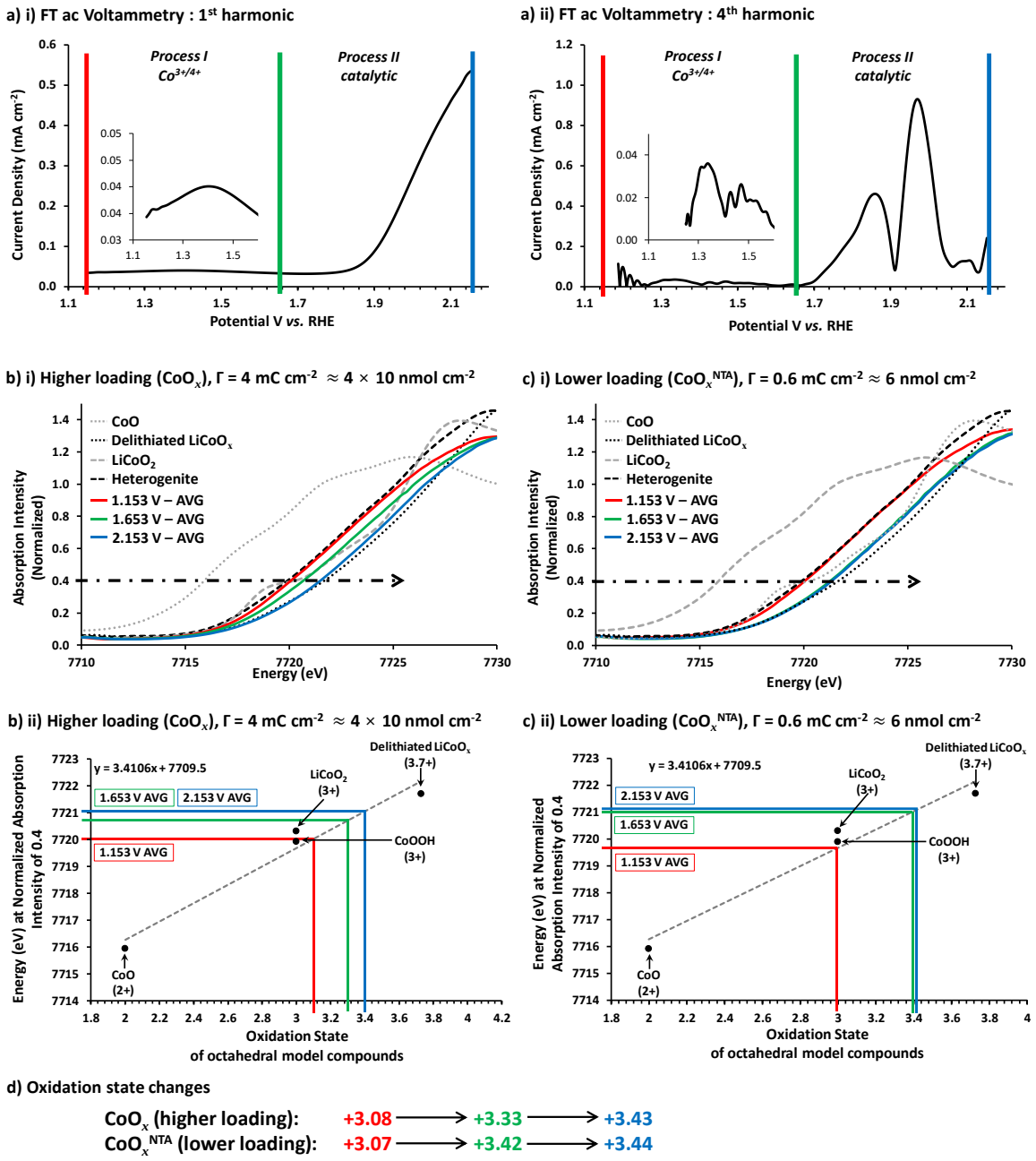

Figure 4.14: Oxidation state calculation for CoO_x^{NTA} and CoO_x. Data is presented as: **(a)** First and fourth harmonic components of Fourier transformed ac voltammogram of the cobalt oxide electrocatalyst (deposited on glass coated with F-doped SnO_2; activity similar to that of CoO_x^{NTA}) recorded in air-saturated 0.1 M borate buffer (pH 9.2) at fundamental frequency of 9.02 Hz, amplitude of 0.08 V and scan rate of 0.07541 V s^{-1} (see reference 78 for details on the experimental procedure). **(b-c)** Oxidation state calculation for **(b)** CoO_x/ITO/PET and **(c)** CoO_x^{NTA}/ITO/PET from the average of 2 replicate XANES scans (average spectra are shown in **b-i** and **c-i**) at 3 reference positions of 0.4, 0.8 and 1.0 at 1.153 (*red*), 1.653 (*green*) and 2.153 V *vs.* RHE (*blue*). Reference data include CoO (a Co^{2+}

reference) (*grey* short dash), $LiCoO_2$ (a Co^{3+} reference) (*grey* long dash), heterogenite (a Co^{3+} reference) (*black* long dash), and $Li_{0.3}CoO_2$ (a $Co^{3.7+}$ reference) (*black* short dash). Panels **(b-ii)** and **(c-ii)** show an interpolation calculation of the oxidation state based on the normalised absorption of 0.4. *Black* dots show the reference data, while *dashed* line is a linear fit to these data; coloured lines show results from the *in situ* analysis of **(b)** CoO_x and **(c)** CoO_x^{NTA}. Note that many transitions affect the edge structure and shape, rendering this calculation only an estimate of the actual redox state.

The XANES data collected from the lower (CoO_x^{NTA}) and higher loading (CoO_x) cobalt oxide samples at 1.153, 1.653, and 2.153 V *vs.* RHE (**Figure 4.14 b-c**) were used to calculate the oxidation states of the materials at these potentials so that their electronic structure during *Process I* and *Process II* could be examined. The oxidation states were calculated by comparing the edge positions in the XANES spectra to those of closely related and structurally similar octahedral cobalt oxide reference compounds.[102] While this method does not provide an absolute measurement of oxidation state (as many factors influence the position and shape of the edge), is does allow the two materials to be considered relative to each other (**Figures 4.15** and **4.16**, and **Table 4.1**).[102]

The precision of the oxidation state values was calculated by measuring how reproducible the replicate spectra were at 3 edge positions in the spectra of the 2 different samples. The overall precision of the oxidation state values was measured to be ± 0.02 oxidation state units. This is the estimated calibration error for the oxidation state values for the 2 samples quoted below. A precision of ± 0.02 oxidation state units indicates that replicate spectra collected using our SEC cell is highly reproducible.

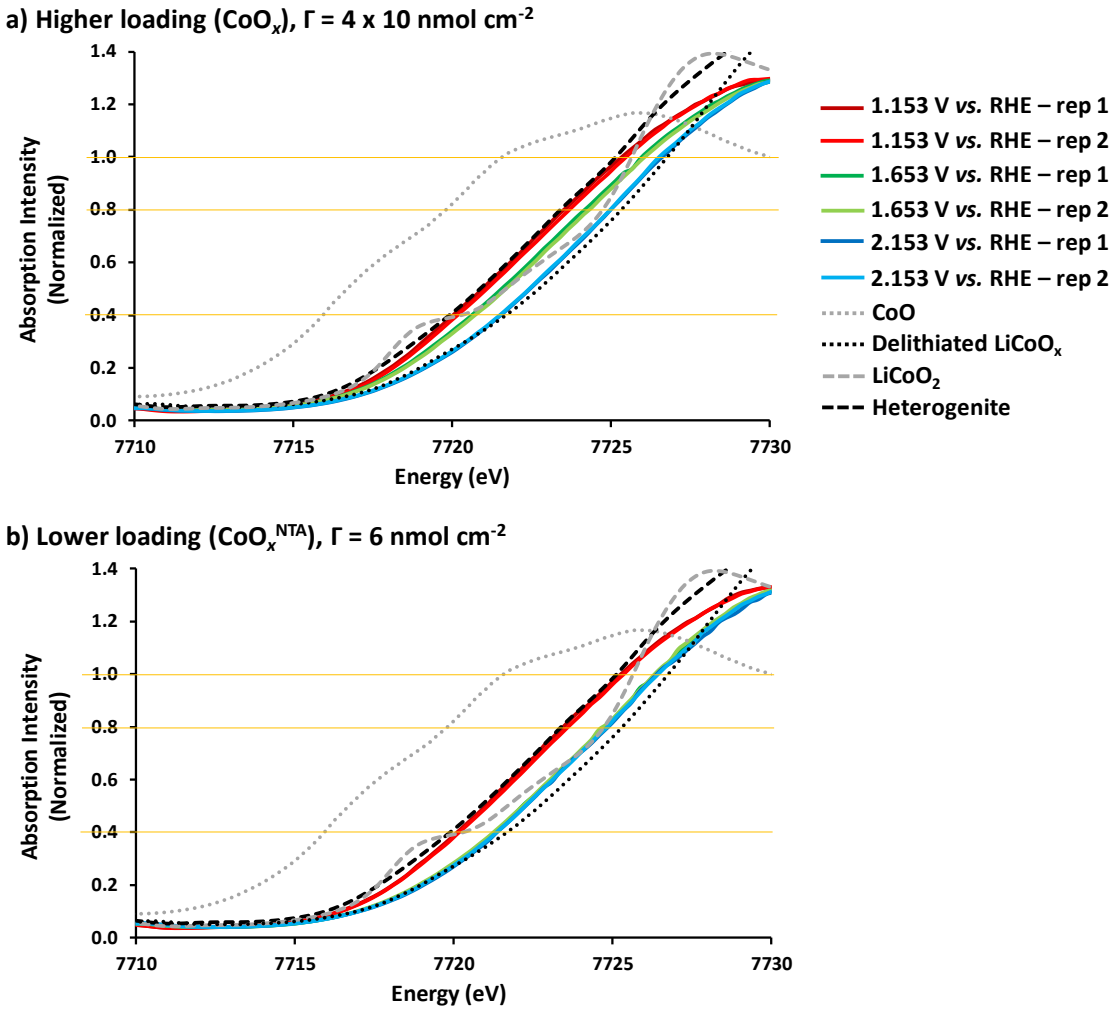

Figure 4.15: Expanded Co K-edge XANES data used in oxidation state calculation. Data presented as: **(a)** CoO_x/ITO/PET and **(b)** CoO_x^{NTA}/ITO/PET. These samples are associated with **Figures 4.7** and **4.14**. This figure is associated with **Figure 4.16** and **Table 4.1**. **(a)** and **(b)** are reproduced from **Figure 4.7 a-iii** and **4.7b-iii**, and show the 2 replicate XANES spectra and full set of reference data used to calculate the oxidation state for each material at the potentials of: 1.153 (*red*), 1.653 (*green*) and 2.153 V *vs.* RHE (*blue*). The first replicate at each potential (*vs.* RHE) is the darker trace colour, and produces a full ledged as follows: 1.153 – replicate 1 (*dark red*), 1.153 – replicate 2 (*red*), 1.653 – replicate 1 (*dark green*), 1.653 – replicate 2 (*green*), 2.153 – replicate 1 (*dark blue*), and 2.153 – replicate 2 (*blue*). Reference data include CoO (a Co^{2+} reference) (*grey* short dash), $LiCoO_2$ (a Co^{3+} reference) (*grey* long dash), heterogenite CoOOH (a Co^{3+} reference) (*black* long dash), and $Li_{0.3}CoO_2$ (a $Co^{3.7+}$ reference) (*black* short dash). Due to the almost perfect reproducibility of the replicate data, it is difficult to distinguish each replicate spectrum in this figure. The *orange* horizontal lines highlight the absorption intensities of 0.4, 0.8 and 1 at which the oxidation state calculation is based upon.

Table 4.1: Energy data used in the oxidation state calculation. The energy values (eV) for CoO_x/ITO/PET and CoO_x^{NTA}/ITO/PET at the absorption intensities of 0.4, 0.8 and 1. This table is associated with **Figures 4.15** and **4.16**. Energy values were accurately determined to 2 decimal places (as presented). Potentials are given *vs.* RHE.

		0.4 abs	**0.8 abs.**	**1 abs.**
Reference materials	**CoO**	7715.92	7719.81	7721.60
	Heterogenite	7719.90	7723.40	7725.10
	$LiCoO_2$	7720.30	7724.73	7725.60
	Delithiated $LiCoO_x$	7721.69	7725.32	7726.80
(a) CoO_x/ITO/PET	**1.153 V - rep 1**	7719.95	7723.47	7725.40
	1.153 V - rep 2	7720.19	7723.67	7725.41
	1.653 V - rep 1	7720.57	7724.16	7725.93
	1.653 V - rep 2	7720.73	7724.34	7726.10
	2.153 V - rep 1	7721.52	7724.51	7726.53
	2.153 V - rep 2	7721.55	7724.54	7726.64
(b) CoO_x^{NTA}/ITO/PET	**1.153 V - rep 1**	7720.11	7723.46	7725.30
	1.153 V - rep 2	7720.17	7723.60	7725.30
	1.653 V - rep 1	7721.30	7724.80	7726.40
	1.653 V - rep 2	7721.26	7724.69	7726.30
	2.153 V - rep 1	7721.36	7724.87	7726.40
	2.153 V - rep 2	7721.34	7724.84	7726.40

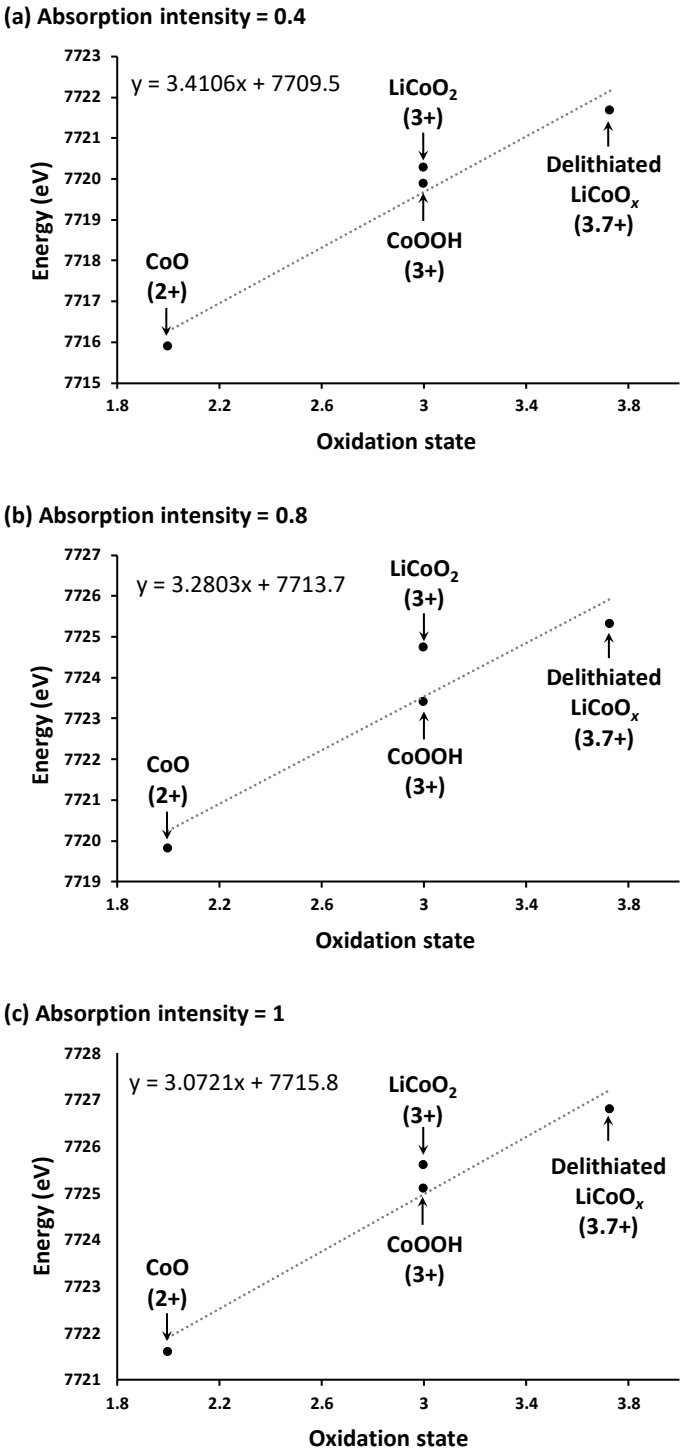

Figure 4.16: Calibration curves used in the oxidation state calculation. The calibration curves were generated at the absorption intensities of **(a)** 0.4, **(b)** 0.8 and **(c)** 1. This figure is associated with **Figure 4.15** and **Table 4.1**. The calibration curves in **(a-c)** are common to both CoO_x and CoO_x^{NTA}. Reference data include CoO (a Co^{2+} reference), $LiCoO_2$ (a Co^{3+} reference), heterogenite CoOOH (a Co^{3+} reference), and $Li_{0.3}CoO_2$ (a $Co^{3.7+}$ reference). *Black* dots indicate the reference data, and the dashed line indicates the linear fit to this reference data.

The average cobalt oxidation state at 1.153, 1.653, and 2.153 V *vs.* RHE for the lower loading CoO_x^{NTA} sample was +3.07, +3.42 and +3.44, and for the higher loading CoO_x was +3.08, +3.33 and +3.43, respectively. The two samples had the same oxidation states (within 0.01 units of each other) at 1.153 and 2.153 V *vs.* RHE, but had a significant oxidation state difference of +0.1 units at 1.653 V *vs.* RHE. Crucially, the differences observed were reproducible even after cycling the same electrode for hours (**Figure 4.7**). In general, the oxidation states found herein are within the range of values reported for disordered heterogenite materials studied *ex situ*[12, 44, 103] and *in situ*.[12, 75]

Thus, the CoO_x and CoO_x^{NTA} catalysts are chemically identical prior to oxidation, as has been noted previously.[86] When the potential was augmented from 1.153 to 1.653 V *vs.* RHE, the higher loading CoO_x sample experienced less of an oxidation state change (+3.08 to +3.33) as opposed to a more pronounced change (+3.07 to +3.42) for the lower loading CoO_x^{NTA} material. This difference in the oxidation states at 1.653 V *vs.* RHE may be due to the increased charge-transfer resistance of the thicker CoO_x film. Hampered charge-transfer would have likely caused the rate of the cobalt electrooxidation in the bulk of the catalyst film (**reaction 4.5**) to be insufficiently fast to fully compensate for the effects of photoreduction (**reaction 4.4**). In comparison, most of the cobalt species in the thinner film were electrochemically active and readily underwent electrochemically-induced transformations (**Scheme 4.1**), which allowed the rate of **reaction 4.5** to be competitive with that of **reaction 4.4** and resulted in a higher oxidation state detected by XAS.

At 2.153 V *vs.* RHE (*i.e.* beyond the catalytically relevant *Process II* (**Figure 4.14a**) the oxidation states of the lower loading CoO_x^{NTA} and higher loading CoO_x samples were essentially identical. This observation can be interpreted in two ways. Firstly, it is reasonable to suggest that higher oxidation states of cobalt are not directly involved in the final electrochemical step of water oxidation, as has been proposed previously by some researchers.[78-79] In other words, the reactions of the type shown in **reactions 4.8** and **4.9** (hypothesised for the $O^{II/I}$ transformation) do not make any significant contribution to the electrocatalytic mechanism of water oxidation.

$$[Co^{4+}]\text{-}O^{II}H_y^* \rightleftarrows [Co^{5+}]\text{-}O^{II}H_y^* + e^- \quad \textbf{(4.8)}$$

$$[Co^{5+}]\text{-}O^{II}H_y^* + B^- \rightleftarrows [Co^{4+}]\text{-}O^{I}H_{y-1}^* + HB \quad \textbf{(4.9)}$$

The second possible explanation is based on the very significant difference in the lifetimes of the electrochemically generated species in **reactions 4.8** and **4.9**. As XAS "sees" the average of an entire material and not the mechanism of an individual group of atoms (as outlined in **Scheme 4.2**), it is important to consider the presence/visibility of the active state (**A**) during an XAS experiment. The visibility of **A** is generally dependent on two important timescale aspects; the lifetime of **A** and the TOF of **A**. **Scheme 4.2c** demonstrates the extreme example in which an active species has both a sufficiently short lifetime and a sufficiently low TOF that it could never be measured in an XAS experiment. The classical effect of TOF is exemplified in the comparison of **Scheme 4.2a** and **Scheme 4.2b**, where it is illustrated that lowering the TOF reduces the contribution of **A** to the XAS data. The effect of lifetime is illustrated in the comparison of **Scheme 4.2c** and **Scheme 4.2a**, where it is shown that despite a reasonable TOF a very short-lived active species will not be visible in the XAS data.

If the mechanism in **reactions 4.8** and **4.9** is valid, then it is most likely that the lifetime of the active species in the heterogenite-like cobalt oxides is too short to be visible by XAS. Under this assumption and based on the FTacv experiment-simulation comparisons,[78] the heterogeneous rate constant of the electron transfer process coupled to the water oxidation reaction (**reaction 4.8**; *Process II* in **Figure 4.14**) should not be very high (10^2 s^{-1} order of magnitude), but the rate constant for the subsequent chemical **reaction 4.9** should be reasonably fast (10^5 M^{-1} s^{-1} order of magnitude).[72]

Simulations to determine the concentration of the active state under these conditions predicts that the active state has a minimal contribution to the overall CoO_x composition when the proton-withdrawing base is continiously supplied to the electrode surface,[78] *i.e.* scenario in **Scheme 4.2c** applies. In terms of the mechanism in **Scheme 4.2**, this means steady supply of **R** to the electrode surface results in rapid quenching of **A** as soon as it is produced which makes spectroscopic detection of this active state impossible. However, if the mass-transport of **R** towards the electrode is restricted, the ground state **G** should be quantitatively converted into state **A** as soon as the potential is sufficiently positive (for the catalytic electrooxidation) or negative (for the catalytic electroreduction).

However, detailed electrokinetic analysis and modelling are not usually undertaken, the effective redox potentials of the key electron transfers coupled to the catalytic processes are

often unknown and the differences in the timescales of the electrochemical events and XAS analysis are often overlooked. This might result in undertaking *in situ* spectroelectrochemical studies under the conditions where the formation of the true active state of the electrocatalyst of interest might be physically impossible. The discussions above highlight the importance of using multiple analytical techniques to study processes within *in situ* XAS-electrochemical experiments.

4.5 Conclusion

The present work outlines the general requirements for undertaking a reliable *in situ* X-ray absorption spectroelectrochemical analysis of electrocatalysts and introduces a detailed design of a gas- and liquid-tight SEC for the simultaneous collection of high quality XAS and electrochemical data. The high quality electrochemical and spectroscopic data allowed for a quantitative analysis of X-ray beam induced photoeffects and demonstration of their strong dependence on the potential. It was found that cobalt oxides photooxidise and photoreduce at negative and positive potentials, respectively. When no potential was applied, photodeposition of cobalt oxides was demonstrated and found to produce exactly the same materials as those formed by conventional electrodeposition. Furthermore, photooxidation of nickel electrodeposits at low loadings by the X-ray beam was revealed. These and other effects of the beam can significantly affect the interpretation of the *in situ* XAS data and should always be considered and preferably quantified for any spectroelectrochemical experiment.

Another critical aspect to considered in the design of an *in situ* XAS analysis of high-performance electrocatalysts operating at high TOF is the lifetime of the active state under the employed conditions. Comparatively high and stable catalytic reaction rates do not guarantee that the dominating state is actually the active one. Preliminary modelling of the available electrochemical data using plausible models should be undertaken to predict the conditions required for the stabilisation of the active state in the context of a considered hypothesis. For the heterogenite-like cobalt oxide electrocatalysts considered here, the initial hypothesis was based on the key role of very high oxidation states of cobalt (>4+), but the analysis undertaken herein suggests that those are not directly involved in the catalytic cycle. It is also possible that these changes could be caused by a ligand centred oxidation reaction. Many others have investigated alternative ways to study this system including by EPR and Raman spectroscopy.[94,95] The timescale effects we outline in **Scheme 4.2** may complicate the study of these materials.

This conclusion would not be possible if the conditions of the *in situ* XAS analysis were not guided by preliminary electrokinetic modelling. At the same time, the formation of a $Co^{>4+}$

species cannot be excluded because such a species might remain so short lived that it cannot be detected. In a more general case, experimentalists should always consider the very significant differences in the timescales of the electron-transfer events and the spectra collection and aim to correlate the observations from the *in situ* spectroelectrochemical analysis with the kinetic modelling to support the interpretations.

4.6 Chapter 4 references

1. Zinola, C. F.; Martins, M. E.; Tejera, E. P.; Neves, N. P., Electrocatalysis: Fundamentals and applications. *Int. J. Electrochem. Sci.* **2012**.
2. Seh, Z. W.; Kibsgaard, J.; Dickens, C. F.; Chorkendorff, I.; Nørskov, J. K.; Jaramillo, T. F., Combining theory and experiment in electrocatalysis: Insights into materials design. *Science* **2017,** *355* (6321).
3. Sapountzi, F. M.; Gracia, J. M.; Weststrate, C. J.; Fredriksson, H. O. A.; Niemantsverdriet, J. W., Electrocatalysts for the generation of hydrogen, oxygen and synthesis gas. *Prog. Energy Combust. Sci.* **2017,** *58*, 1-35.
4. Cowan, A. J., Intermediate identification. *Nat. Chem.* **2016,** *8*, 740-741.
5. Nocera, D. G., Chemistry of personalized solar energy. *Inorg. Chem.* **2009,** *48* (21), 10001-10017.
6. Pittkowski, R.; Krtil, P.; Rossmeisl, J., Rationality in the new oxygen evolution catalyst development. *Curr. Opin. Electrochem.* **2018,** *12*, 218-224.
7. Suen, N.-T.; Hung, S.-F.; Quan, Q.; Zhang, N.; Xu, Y.-J.; Chen, H. M., Electrocatalysis for the oxygen evolution reaction: Recent development and future perspectives. *Chem. Soc. Rev.* **2017,** *46* (2), 337-365.
8. Chatti, M.; Glushenkov, A. M.; Gengenbach, T.; Knowles, G. P.; Mendes, T. C.; Ellis, A. V.; Spiccia, L.; Hocking, R. K.; Simonov, A. N., Highly dispersed and disordered nickel–iron layered hydroxides and sulphides: robust and high-activity water oxidation catalysts. *Sustain. Energy Fuels* **2018,** *2* (7), 1561-1573.
9. McCrory, C. C. L.; Jung, S.; Peters, J. C.; Jaramillo, T. F., Benchmarking heterogeneous electrocatalysts for the oxygen evolution reaction. *J. Am. Chem. Soc.* **2013,** *135* (45), 16977-16987.
10. Dau, H.; Limberg, C.; Reier, T.; Risch, M.; Roggan, S.; Strasser, P., The mechanism of water oxidation: From electrolysis *via* homogeneous to biological catalysis. *ChemCatChem* **2010,** *2* (7), 724-761.
11. Zaharieva, I.; Chernev, P.; Risch, M.; Klingan, K.; Kohlhoff, M.; Fischer, A.; Dau, H., Electrosynthesis, functional, and structural characterization of a water-oxidizing manganese oxide. *Energy Environ. Sci.* **2012,** *5* (5), 7081-7089.
12. Kanan, M. W.; Yano, J.; Surendranath, Y.; Dinca, M.; Yachandra, V. K.; Nocera, D. G., Structure and valency of a cobalt-phosphate water oxidation catalyst determined by *in situ* X-ray spectroscopy. *J. Am. Chem. Soc.* **2010,** *132* (39), 13692-13701.
13. Chatti, M.; Gardiner, J. L.; Fournier, M.; Johannessen, B.; Williams, T.; Gengenbach, T. R.; Pai, N.; Nguyen, C.; MacFarlane, D. R.; Hocking, R. K., et al. Intrinsically stable *in situ* generated electrocatalyst for long-term oxidation of acidic water at up to 80°C. *Nat. Catal.* **2019,** *2* (5), 457-465.
14. Chatti, M.; Gengenbach, T.; King, R.; Spiccia, L.; Simonov, A. N., Vertically aligned interlayer expanded MoS_2 nanosheets on a carbon support for hydrogen evolution electrocatalysis. *Chem. Mater.* **2017,** *29* (7), 3092-3099.
15. Laursen, A. B.; Patraju, K. R.; Whitaker, M. J.; Retuerto, M.; Sarkar, T.; Yao, N.; Ramanujachary, K. V.; Greenblatt, M.; Dismukes, G. C., Nanocrystalline Ni_5P_4: A hydrogen evolution electrocatalyst of exceptional efficiency in both alkaline and acidic media. *Energy Environ. Sci.* **2015,** *8* (3), 1027-1034.
16. Zou, X.; Zhang, Y., Noble metal-free hydrogen evolution catalysts for water splitting. *Chem. Soc. Rev.* **2015,** *44* (15), 5148-5180.
17. Laursen, A. B.; Kegnæs, S.; Dahl, S.; Chorkendorff, I., Molybdenum sulfides—Efficient and viable materials for electro- and photoelectrocatalytic hydrogen evolution. *Energy Environ. Sci.* **2012,** *5* (2), 5577-5591.

18. Li, Y.; Wang, H.; Xie, L.; Liang, Y.; Hong, G.; Dai, H., MoS_2 nanoparticles grown on graphene: An advanced catalyst for the hydrogen evolution reaction. *J. Am. Chem. Soc.* **2011,** *133* (19), 7296-7299.
19. Yang, Y.; Zhang, K.; Lin, H.; Li, X.; Chan, H. C.; Yang, L.; Gao, Q., MoS_2–Ni_3S_2 heteronanorods as efficient and stable bifunctional electrocatalysts for overall water splitting. *ACS Catal.* **2017,** *7* (4), 2357-2366.
20. Chung, D. Y.; Jun, S. W.; Yoon, G.; Kim, H.; Yoo, J. M.; Lee, K.-S.; Kim, T.; Shin, H.; Sinha, A. K.; Kwon, S. G., et al. Large-scale synthesis of carbon-shell-coated FeP nanoparticles for robust hydrogen evolution reaction electrocatalyst. *J. Am. Chem. Soc.* **2017,** *139* (19), 6669-6674.
21. Li, F.; Zhao, S.-F.; Chen, L.; Khan, A.; MacFarlane, D. R.; Zhang, J., Polyethylenimine promoted electrocatalytic reduction of CO_2 to CO in aqueous medium by graphene-supported amorphous molybdenum sulphide. *Energy Environ. Sci.* **2016,** *9* (1), 216-223.
22. Li, F.; Xue, M.; Li, J.; Ma, X.; Chen, L.; Zhang, X.; MacFarlane, D. R.; Zhang, J., Unlocking the electrocatalytic activity of antimony for CO_2 reduction by two-dimensional engineering of the bulk material. *Angew. Chem. Int. Ed.* **2017,** *56* (46), 14718-14722.
23. Kortlever, R.; Shen, J.; Schouten, K. J. P.; Calle-Vallejo, F.; Koper, M. T. M., Catalysts and reaction pathways for the electrochemical reduction of carbon dioxide. *J. Phys. Chem. Lett.* **2015,** *6* (20), 4073-4082.
24. Velasco-Vélez, J.-J.; Jones, T.; Gao, D.; Carbonio, E.; Arrigo, R.; Hsu, C.-J.; Huang, Y.-C.; Dong, C.-L.; Chen, J.-M.; Lee, J.-F., et al. The role of the copper oxidation state in the electrocatalytic reduction of CO_2 into valuable hydrocarbons. *ACS Sustain. Chem. Eng.* **2019,** *7* (1), 1485-1492.
25. Wang, L.; Nitopi, S.; Wong, A. B.; Snider, J. L.; Nielander, A. C.; Morales-Guio, C. G.; Orazov, M.; Higgins, D. C.; Hahn, C.; Jaramillo, T. F., Electrochemically converting carbon monoxide to liquid fuels by directing selectivity with electrode surface area. *Nat. Catal.* **2019**, *2*, 702-708.
26. Wang, L.; Xia, M.; Wang, H.; Huang, K.; Qian, C.; Maravelias, C. T.; Ozin, G. A., Greening ammonia toward the solar ammonia refinery. *Joule* **2018,** *2* (6), 1055-1074.
27. Foster, S. L.; Bakovic, S. I. P.; Duda, R. D.; Maheshwari, S.; Milton, R. D.; Minteer, S. D.; Janik, M. J.; Renner, J. N.; Greenlee, L. F., Catalysts for nitrogen reduction to ammonia. *Nat. Catal.* **2018,** *1* (7), 490-500.
28. Zhou, F.; Azofra, L. M.; Ali, M.; Kar, M.; Simonov, A. N.; McDonnell-Worth, C.; Sun, C.; Zhang, X.; MacFarlane, D. R., Electro-synthesis of ammonia from nitrogen at ambient temperature and pressure in ionic liquids. *Energy Environ. Sci.* **2017,** *10* (12), 2516-2520.
29. Zhang, M.; de Respinis, M.; Frei, H., Time-resolved observations of water oxidation intermediates on a cobalt oxide nanoparticle catalyst. *Nat. Chem.* **2014,** *6*, 362-367.
30. Cipriani, G.; Di Dio, V.; Genduso, F.; La Cascia, D.; Liga, R.; Miceli, R.; Ricco Galluzzo, G., Perspective on hydrogen energy carrier and its automotive applications. *Int. J. Hydrog. Energy* **2014,** *39* (16), 8482-8494.
31. Suryanto, B. H. R.; Du, H.-L.; Wang, D.; Chen, J.; Simonov, A. N.; MacFarlane, D. R., Challenges and prospects in the catalysis of electroreduction of nitrogen to ammonia. *Nat. Catal.* **2019,** *2* (4), 290-296.
32. Weckhuysen, B. M., Determining the active site in a catalytic process: *Operando* spectroscopy is more than a buzzword. *Phys. Chem. Chem. Phys.* **2003,** *5* (20), 4351-4360.

33. Deng, Y.; Yeo, B. S., Characterization of electrocatalytic water splitting and CO_2 reduction reactions using *in situ*/*operando* raman spectroscopy. *ACS Catal.* **2017,** *7* (11), 7873-7889.
34. Pastor, E.; Le Formal, F.; Mayer, M. T.; Tilley, S. D.; Francàs, L.; Mesa, C. A.; Grätzel, M.; Durrant, J. R., Spectroelectrochemical analysis of the mechanism of (photo)electrochemical hydrogen evolution at a catalytic interface. *Nat. Commun.* **2017,** *8*, (14280).
35. Bard, A. J.; Faulkner, L. R., *Electrochemical methods: Fundamentals and applications*. John Wiley & Sons, Inc.: United States of America, 2000; p 864.
36. Binninger, T.; Fabbri, E.; Patru, A.; Garganourakis, M.; Han, J.; Abbott, D. F.; Sereda, O.; Kötz, R.; Menzel, A.; Nachtegaal, M., et al. Electrochemical flow-cell setup for *in situ* X-ray investigations: I. Cell for SAXS and XAS at synchrotron facilities. *J. Electrochem. Soc.* **2016,** *163* (10), H906-H912.
37. Best, S. P.; Levina, A.; Glover, C.; Johannessen, B.; Kappen, P.; Lay, P. A., XAS spectroelectrochemistry: Reliable measurement of X-ray absorption spectra from redox manipulated solutions at room temperature. *J. Synchrotron Radiat.* **2016,** *23* (3), 743-750.
38. Sharpe, L. R.; Heineman, W. R.; Elder, R. C., EXAFS spectroelectrochemistry. *Chem. Rev.* **1990,** *90* (5), 705-722.
39. Francke, R.; Schille, B.; Roemelt, M., Homogeneously catalyzed electroreduction of carbon dioxide— Methods, mechanisms, and catalysts. *Chem. Rev.* **2018,** *118* (9), 4631-4701.
40. Hocking, R. K.; Chang, S. L. Y.; MacFarlane, D. R.; Spiccia, L., Preparation and characterization of catalysts for clean energy: A challenge for X-rays and electrons. *Aust. J. Chem.* **2012,** *65* (6), 608-614.
41. Lassalle-Kaiser, B.; Gul, S.; Kern, J.; Yachandra, V. K.; Yano, J., *In situ*/*operando* studies of electrocatalysts using hard X-ray spectroscopy. *J. Electron Spectros. Relat. Phenomena* **2017,** *221*, 18-27.
42. Farmand, M.; Landers, A. T.; Lin, J. C.; Feaster, J. T.; Beeman, J. W.; Ye, Y.; Clark, E. L.; Higgins, D.; Yano, J.; Davis, R. C., et al. Electrochemical flow cell enabling *operando* probing of electrocatalyst surfaces by X-ray spectroscopy and diffraction. *Phys. Chem. Chem. Phys.* **2019,** *21* (10), 5402-5408.
43. Fabbri, E.; Abbott, D. F.; Nachtegaal, M.; Schmidt, T. J., *Operando* X-ray absorption spectroscopy: A powerful tool toward water splitting catalyst development. *Curr. Opin. Electrochem.* **2017,** *5* (1), 20-26.
44. Risch, M.; Ringleb, F.; Khare, V.; Chernev, P.; Zaharieva, I.; Dau, H., Characterisation of a water-oxidising Co-film by XAFS. *J. Phys.* **2009,** *190,* 1-4.
45. Lassalle-Kaiser, B.; Merki, D.; Vrubel, H.; Gul, S.; Yachandra, V. K.; Hu, X.; Yano, J., Evidence from *in situ* X-ray absorption spectroscopy for the involvement of terminal disulfide in the reduction of protons by an amorphous molybdenum sulfide electrocatalyst. *J. Am. Chem. Soc.* **2015,** *137* (1), 314-321.
46. Watanabe, N.; Morais, J.; Alves, M. C. M., Design of an electrochemical cell for *in situ* XAS studies. *J. Electron Spectros. Relat. Phenomena* **2007,** *156-158*, 164-167.
47. Erickson, E. M.; Thorum, M. S.; Vasić, R.; Marinković, N. S.; Frenkel, A. I.; Gewirth, A. A.; Nuzzo, R. G., *In situ* electrochemical X-ray absorption spectroscopy of oxygen reduction electrocatalysis with high oxygen flux. *J. Am. Chem. Soc.* **2012,** *134* (1), 197-200.
48. Saadi, F. H.; Carim, A. I.; Drisdell, W. S.; Gul, S.; Baricuatro, J. H.; Yano, J.; Soriaga, M. P.; Lewis, N. S., *Operando* spectroscopic analysis of CoP films electrocatalyzing the hydrogen-evolution reaction. *J. Am. Chem. Soc.* **2017,** *139* (37), 12927-12930.

49. Bak, S.-M.; Shadike, Z.; Lin, R.; Yu, X.; Yang, X.-Q., *In situ*/*operando* synchrotron-based X-ray techniques for lithium-ion battery research. *NPG Asia Mater.* **2018,** *10* (7), 563-580.
50. Browne, M. P.; Domínguez, C.; Colavita, P. E., Emerging trends in metal oxide electrocatalysis: Bifunctional oxygen catalysis, synergies and new insights from *in situ* studies. *Curr. Opin. Electrochem.* **2018,** *7*, 208-215.
51. Gorlin, Y.; Lassalle-Kaiser, B.; Benck, J. D.; Gul, S.; Webb, S. M.; Yachandra, V. K.; Yano, J.; Jaramillo, T. F., *In situ* X-ray absorption spectroscopy investigation of a bifunctional manganese oxide catalyst with high activity for electrochemical water oxidation and oxygen reduction. *J. Am. Chem. Soc.* **2013,** *135* (23), 8525-8534.
52. Friebel, D.; Louie, M. W.; Bajdich, M.; Sanwald, K. E.; Cai, Y.; Wise, A. M.; Cheng, M.-J.; Sokaras, D.; Weng, T.-C.; Alonso-Mori, R., et al. Identification of highly active Fe sites in (Ni,Fe)OOH for electrocatalytic water splitting. *J. Am. Chem. Soc.* **2015,** *137* (3), 1305-1313.
53. Lewerenz, H.-J.; Lichterman, M. F.; Richter, M. H.; Crumlin, E. J.; Hu, S.; Axnanda, S.; Favaro, M.; Drisdell, W.; Hussain, Z.; Brunschwig, B. S.; Liu, Z., et al. *Operando* analyses of solar fuels light absorbers and catalysts. *Electrochim. Acta* **2016,** *211*, 711-719.
54. Frydendal, R.; Seitz, L. C.; Sokaras, D.; Weng, T.-C.; Nordlund, D.; Chorkendorff, I.; Stephens, I. E. L.; Jaramillo, T. F., *Operando* investigation of Au-MnO_x thin films with improved activity for the oxygen evolution reaction. *Electrochim. Acta* **2017,** *230*, 22-28.
55. Hoffman, A. S.; Debefve, L. M.; Bendjeriou-Sedjerari, A.; Ouldchikh, S.; Bare, S. R.; Basset, J.-M.; Gates, B. C., Transmission and fluorescence X-ray absorption spectroscopy cell/flow reactor for powder samples under vacuum or in reactive atmospheres. *Rev. Sci. Instrum.* **2016,** *87* (7), 073108.
56. Bediako, D. K.; Lassalle-Kaiser, B.; Surendranath, Y.; Yano, J.; Yachandra, V. K.; Nocera, D. G., Structure–activity correlations in a nickel–borate oxygen evolution catalyst. *J. Am. Chem. Soc.* **2012,** *134* (15), 6801-6809.
57. Gunter, T. E., Electron paramagnetic resonance studies of the radiolysis of H_2O in the solid state. *J. Chem. Phys.* **1967,** *46* (10), 3818-3829.
58. Garrett, B. C.; Dixon, D. A.; Camaioni, D. M.; Chipman, D. M.; Johnson, M. A.; Jonah, C. D.; Kimmel, G. A.; Miller, J. H.; Rescigno, T. N.; Rossky, P. J., et al. Role of water in electron-initiated processes and radical chemistry: Issues and scientific advances. *Chem. Rev.* **2005,** *105* (1), 355-390.
59. El Omar, A. K.; Schmidhammer, U.; Jeunesse, P.; Larbre, J.-P.; Lin, M.; Muroya, Y.; Katsumura, Y.; Pernot, P.; Mostafavi, M., Time-dependent radiolytic yield of OH• radical studied by picosecond pulse radiolysis. *J. Phys. Chem. A* **2011,** *115* (44), 12212-12216.
60. Yano, J.; Kern, J.; Irrgang, K.-D.; Latimer, M. J.; Bergmann, U.; Glatzel, P.; Pushkar, Y.; Biesiadka, J.; Loll, B.; Sauer, K., et al. X-ray damage to the Mn_4Ca complex in single crystals of photosystem II: A case study for metalloprotein crystallography. *Proc. Natl. Acad. Sci. U.S.A.* **2005,** *102* (34), 12047-12052.
61. Kubin, M.; Kern, J.; Guo, M.; Källman, E.; Mitzner, R.; Yachandra, V. K.; Lundberg, M.; Yano, J.; Wernet, P., X-ray-induced sample damage at the Mn L-edge: A case study for soft X-ray spectroscopy of transition metal complexes in solution. *Phys. Chem. Chem. Phys.* **2018,** *20* (24), 16817-16827.
62. Penner-Hahn, J. E., Characterization of "spectroscopically quiet" metals in biology. *Coord. Chem. Rev.* **2005,** *249* (1), 161-177.
63. George, G. N.; Pickering, I. J.; Pushie, M. J.; Nienaber, K.; Hackett, M. J.; Ascone, I.; Hedman, B.; Hodgson, K. O.; Aitken, J. B.; Levina, A., et al. X-ray-induced photo-

chemistry and X-ray absorption spectroscopy of biological samples. *J. Synchrotron Radiat.* **2012,** *19* (Pt 6), 875-886.
64. Corbett, M. C.; Latimer, M. J.; Poulos, T. L.; Sevrioukova, I. F.; Hodgson, K. O.; Hedman, B., Photoreduction of the active site of the metalloprotein putidaredoxin by synchrotron radiation. *Acta Crystallogr. D* **2007,** *63* (9), 951-960.
65. Clay, M. D.; Jenney, F. E.; Hagedoorn, P. L.; George, G. N.; Adams, M. W. W.; Johnson, M. K., Spectroscopic studies of pyrococcus furiosus superoxide reductase: Implications for active-site structures and the catalytic mechanism. *J. Am. Chem. Soc.* **2002,** *124* (5), 788-805.
66. Mesu, J. G.; Beale, A. M.; de Groot, F. M. F.; Weckhuysen, B. M., Probing the influence of X-rays on aqueous copper solutions using time-resolved *in situ* combined video/X-ray absorption near-edge/ultraviolet−visible spectroscopy. *J. Phys. Chem. B* **2006,** *110* (35), 17671-17677.
67. Hackett, M. J.; Smith, S. E.; Paterson, P. G.; Nichol, H.; Pickering, I. J.; George, G. N., X-ray absorption spectroscopy at the sulfur K-edge: A new tool to investigate the biochemical mechanisms of neurodegeneration. *ACS Chem. Neurosci.* **2012,** *3* (3), 178-185.
68. Nan, J., Electron beam damage in oxides: A review. *Rep. Prog. Phys.* **2016,** *79* (1), 016501.
69. Symons, M. C. R., Conversion of OH radicals into O– ions on cooling: A radiation–e.s.r. study. *J. Chem. Soc., ChemComm* **1980,** (14), 675-676.
70. Plonka, A.; Szajdzinska-Pietek, E.; Bednarek, J.; Hallbrucker, A.; Mayer, E., Unexpected radical generation on γ-irradiating metastable forms of water at 77 K. Invited Lecture. *Phys. Chem. Chem. Phys.* **2000,** *2* (8), 1587-1593.
71. Bissardon, C.; Proux, O.; Bureau, S.; Suess, E.; Winkel, L. H. E.; Conlan, R. S.; Francis, L. W.; Khan, I. M.; Charlet, L.; Hazemann, J. L., et al. Sub-ppm level high energy resolution fluorescence detected X-ray absorption spectroscopy of selenium in articular cartilage. *Analyst* **2019**, *144*, 3488−3493.
72. Risch, M.; Ringleb, F.; Kohlhoff, M.; Bogdanoff, P.; Chernev, P.; Zaharieva, I.; Dau, H., Water oxidation by amorphous cobalt-based oxides: *In situ* tracking of redox transitions and mode of catalysis. *Energy Environ. Sci.* **2015,** *8,* 661-674.
73. González-Flores, D.; Sánchez, I.; Zaharieva, I.; Klingan, K.; Heidkamp, J.; Chernev, P.; Menezes, P. W.; Driess, M.; Dau, H.; Montero, M. L., Heterogeneous water oxidation: Surface activity *versus* amorphization activation in cobalt phosphate catalysts. *Angew. Chem. Int.* **2015,** *127* (8), 2502-2506.
74. Bergmann, A.; Martinez-Moreno, E.; Teschner, D.; Chernev, P.; Gliech, M.; de Araújo, J. F.; Reier, T.; Dau, H.; Strasser, P., Reversible amorphization and the catalytically active state of crystalline Co_3O_4 during oxygen evolution. *Nat. Commun.* **2015,** *6*, 8625.
75. Bonke, S. A.; Bond, A. M.; Spiccia, L.; Simonov, A. N., Parameterization of water electrooxidation catalyzed by metal oxides using Fourier transformed alternating current voltammetry. *J. Am. Chem. Soc.* **2016,** *138* (49), 16095-16104.
76. Tesch, M. F.; Bonke, S. A.; Jones, T. E.; Shaker, M. N.; Xiao, J.; Skorupska, K.; Mom, R.; Melder, J.; Kurz, P.; Knop-Gericke, A., et al. Evolution of oxygen–metal electron transfer and metal electronic states during manganese oxide catalyzed water oxidation revealed with *in situ* soft X-ray spectroscopy. *Angew. Chem. Int.* **2019,** *131* (11), 3464-3470.
77. Bonke, S. A.; Wiechen, M.; Hocking, R. K.; Fang, X.-Y.; Lupton, D. W.; MacFarlane, D. R.; Spiccia, L., Electrosynthesis of highly transparent cobalt oxide water

oxidation catalyst films from cobalt aminopolycarboxylate complexes. *ChemSusChem* **2015,** *8* (8), 1394-1403.
78. Liu, Y.; Nocera, D. G., Spectroscopic studies of nanoparticulate thin films of a cobalt-based oxygen evolution catalyst. *J. Phys. Chem. C* **2014**, 17060-17066.
79. Surendranath, Y.; Lutterman, D. A.; Liu, Y.; Nocera, D. G., Nucleation, growth, and repair of a cobalt-based oxygen evolving catalyst. *J. Am. Chem. Soc.* **2012,** *134* (14), 6326-6336.
80. Burke, M. S.; Kast, M. G.; Trotochaud, L.; Smith, A. M.; Boettcher, S. W., Cobalt–iron (oxy)hydroxide oxygen evolution electrocatalysts: The role of structure and composition on activity, stability, and mechanism. *J. Am. Chem. Soc.* **2015,** *137* (10), 3638-3648.
81. Chang, J.-K.; Wu, C.-M.; Sun, I. W., Nano-architectured $Co(OH)_2$ electrodes constructed using an easily-manipulated electrochemical protocol for high-performance energy storage applications. *J. Mater. Chem.* **2010,** *20* (18), 3729-3735.
82. Myers, J. C.; Penn, R. L., Controlling heterogenite particle morphology and microstructure by varying synthetic conditions. *Mater. Res. Bull.* **2011,** *46* (5), 649-657.
83. Basch, A.; de Campo, L.; Albering, J. H.; White, J. W., Chemical delithiation and exfoliation of Li_xCoO_2. *J. Solid State Chem.* **2014,** *220*, 102-110.
84. Kappen, P.; Ruben, G. *Sakura*, Australian Synchrotron: 2013.
85. Tenderholt, A.; Hedman, B.; Hodgson, K. O. *In Pyspline: A modern, cross-platform program for the processing of raw averaged XAS edge and EXAFS data, XAFS13*, Stanford, California, 2007.
86. Ravel, B.; Newville, M. *Athena, Artemis, Hephaestus: Data analysis for X-ray absorption spectroscopy using IFEFFIT*, J. Synchrotron Radiat.: 2005.
87. Oshchepkov, A. G.; Simonov, P. A.; Cherstiouk, O. V.; Nazmutdinov, R. R.; Glukhov, D. V.; Zaikovskii, V. I.; Kardash, T. Y.; Kvon, R. I.; Bonnefont, A.; Simonov, A. N., et al. On the effect of Cu on the activity of carbon supported Ni nanoparticles for hydrogen electrode reactions in alkaline medium. *Top. Catal.* **2015,** *58* (18), 1181-1192.
88. Oshchepkov, A.; Bonnefont, A.; Saveleva, V.; Papaefthimiou, V.; Zafeiratos, S.; Pronkin, S.; N. Parmon, V.; R. Savinova, E., Exploring the influence of the nickel oxide species on the kinetics of hydrogen electrode reactions in alkaline media. *Top. Catal.* **2016,** *59* (15-16), 1319–1331.
89. Esswein, A. J.; Surendranath, Y.; Reece, S. Y.; Nocera, D. G., Highly active cobalt phosphate and borate based oxygen evolving catalysts operating in neutral and natural waters. *Energy Environ. Sci.* **2011,** *4* (2), 499-504.
90. Costentin, C.; Porter, T. R.; Savéant, J.-M., Conduction and reactivity in heterogeneous-molecular catalysis: New insights in water oxidation catalysis by phosphate cobalt oxide films. *J. Am. Chem. Soc.* **2016,** *138* (17), 5615-5622.
91. Jin, K.; Chu, A.; Park, J.; Jeong, D.; Jerng, S. E.; Sim, U.; Jeong, H.-Y.; Lee, C. W.; Park, Y.-S.; Yang, K. D., et al. Partially oxidized sub-10 nm MnO nanocrystals with high activity for water oxidation catalysis. *Sci. Rep.* **2015,** *5*, 10279.
92. King, H. J.; Bonke, S. A.; Chang, S. L. Y.; Spiccia, L.; Johannessen, B.; Hocking, R. K., Engineering disorder into heterogenite-like cobalt oxides by phosphate doping: Implications for the design of water-oxidation catalysts. *ChemCatChem* **2017,** *9* (3), 511-521.
93. Kanan, M.; Junko, Y.; Surendranath, Y.; Dinca, M.; Yachandra, V.; Nocera, D., Structure and valency of a cobalt-phosphate water oxidation catalyst determined by *in situ* X-ray spectroscopy. *J. Am. Chem. Soc.* **2010,** *132*, 13692-13701.

94. McAlpin, J. G.; Surendranath, Y.; Dinca, M.; Stich, T. A.; Stoian, S. A.; Casey, W. H.; Nocera, D. G.; Britt, R. D., EPR evidence for Co(IV) species produced during water oxidation at neutral pH. *J. Am. Chem. Soc.* **2010,** *132* (20), 6882-6883.
95. Eom, C. J.; Suntivich, J., *In situ* stimulated Raman spectroscopy reveals the phosphate network in the amorphous cobalt oxide catalyst and its role in the catalyst formation. J. Phys. Chem. C **2019**, 123 (48), 29284-29290.

Thesis Conclusions

Cobalt oxides and manganese oxides synthesised through Chimie douce methods are often amorphous, disordered, and/or ordered on the nano-scale. The implications of this disorder to catalytic mechanism was examined herein for heterogenite-like cobalt oxides and birnessite-like manganese oxides.

The cobalt oxide study in Chapter 2 established that phosphate doping introduces nanoscale and atomic-level disorder into the heterogenite phase. Although it is conventionally thought that amorphous materials are more catalytically active for water oxidation, the most disordered materials in the CoO_x (*x* %P) series (*i.e.* the samples with the highest loadings of phosphate) were the least catalytically active for water oxidation. To determine why the phosphate doped materials were not the most catalytically active, the oxidative strength of the CoO_x (*x* %P) series was examined. It was found that the most disordered materials were the most thermodynamically unstable and were more active as chemical oxidants than as surface catalysts. This conclusion suggested that thermodynamic stability was important to the self-healing mechanism of cobalt oxide catalysts, and that the functionality of the heterogenite phase could be tuned toward oxidative or catalytic activity by tuning the stability or redox potential of the phase. The similarity in activity between the undoped and doped materials further suggested that phosphate did not play a direct role in increasing the activity of the heterogenite-like phase but rather acted to destabilise the phase and allow the catalytically active (undoped) cobalt oxide material to form under the conditions of water oxidation catalysis. The in-depth characterisation of the CoO_x (*x* %P) series suggested that phosphate was located in the interlayer.

In the manganese oxide study in Chapter 3, the disordered birnessite-like materials were the most catalytically active, the strongest oxidants, and the most thermodynamically unstable materials. The significant increase in oxidative strength and the XAS evidence for Mn^{2+} during catalysis for the disordered materials suggested that these materials acted to directly

oxidise water. This strongly suggests that synthetic manganese oxides undergo a dissolution/reformation process as part of their 'catalytic' cycle, in a similar manner to mineral birnessite phases in nature.

The conclusions from Chapters 2 and 3 have be graphically summarised in **Scheme 3.1 (reproduced)**. The graph in **Scheme 3.1 (reproduced)** illustrates that there is an optimal level of disorder and thermodynamic stability to confer an advantage for catalytic water oxidation activity and that the propensity for oxidative activity increases proportionally with disorder and inversely with thermodynamic stability. Therefore, the catalytic activity of heterogenite-like and birnessite-like materials can be increased by synthesizing metastable materials that have a high enough redox potential to directly oxidize water but are thermodynamically destabilized enough to reform *in situ* under the conditions for water oxidation (*i.e.* engage in the self-healing mechanism). In our research, ordered forms of heterogenite and K^+ birnessite were destabilized by introducing structural disorder through phosphate doping and 2D nano-structuring methods. This research explains why very ordered and very disordered forms of heterogenite and K^+ birnessite are not the most catalytically active materials, and why metastable materials confer the best advantage as redox-type catalysts.

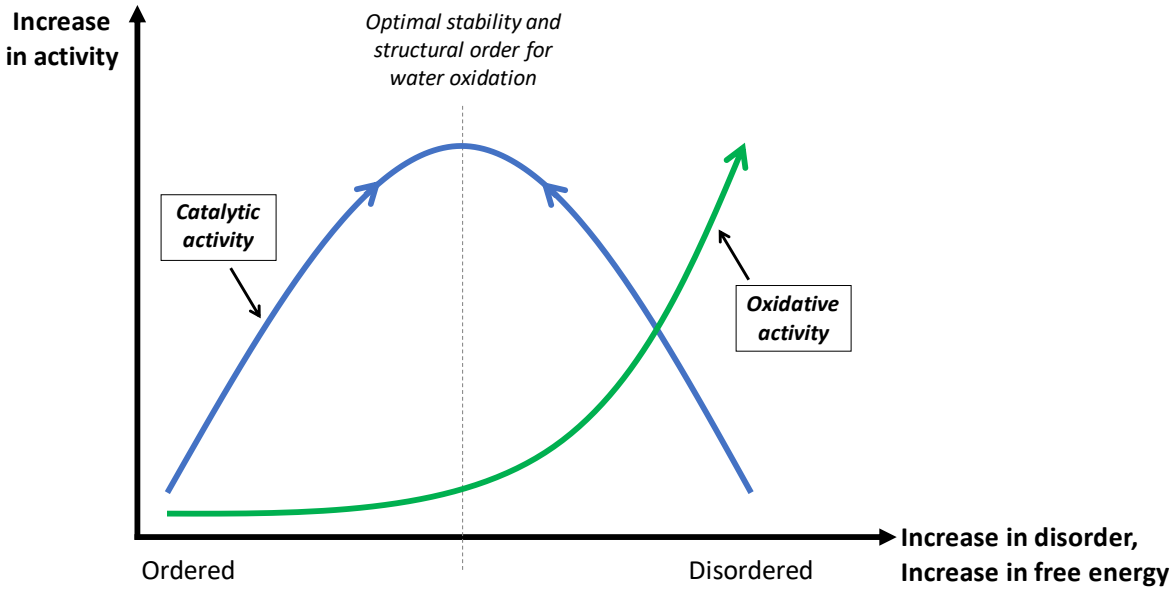

Scheme 3.1 (reproduced): A graphical representation of the relationship between catalytic activity, oxidative activity, thermodynamic stability and disorder.

The primary finding from the *in situ* XAS/electrochemical study in Chapter 4 was that very high oxidation states of cobalt (>4+) are unlikely to be directly involved in the catalytic cycle of heterogenite-like cobalt oxides. However, the in-depth analysis of TOF and lifetimes determined that the formation of a $Co^{>4+}$ species cannot be excluded because such a species might remain so short lived that it cannot be detected by XAS. The study additionally highlighted the X-ray beam induced photoeffects have strong dependence on the applied potential and that beam effects could significantly influence the XAS data. Specifically, it was found that cobalt oxides photooxidise and photoreduce at negative and positive potentials, respectively, and that photodeposition occurred when there was no applied potential. The study demonstrates the importance of preliminary electrokinetic modelling prior to *in situ* XAS/electrochemical experimentation.